

# Temporal and spectral pattern recognition for detection and combined network and array waveform coherence analysis for location of seismic events

Von der Fakultät für Bau- und Umweltingenieurwissenschaften  
der Universität Stuttgart zur Erlangung der Würde eines  
Doktor-Ingenieurs (Dr.-Ing.) genehmigte Abhandlung

Vorgelegt von  
**Benjamin SICK**  
aus Heilbronn

Hauptberichter: Prof. Dr. Manfred JOSWIG  
Mitberichter: Prof. Dr. Götz BOKELMANN

Tag der mündlichen Prüfung: 12. April 2017

Institut für Geophysik der Universität Stuttgart

2017



*The story so far: In the beginning the Universe was created. This has made a lot of people very angry and been widely regarded as a bad move.*

— Douglas Adams, *The Restaurant at the End of the Universe*

*Simplicity is prerequisite for reliability*

— Edsger W. Dijkstra



---

## ACKNOWLEDGEMENTS

---

My special thanks goes to the following people, organizations and everybody who I forgot but would deserve to be thanked:

My sincere gratitude goes to my advisor, Prof. Manfred Joswig who gave me the opportunity for this PhD thesis. Thank you for your trust and the freedom you gave me to be independent during the whole time of the thesis. I am thankful to Prof. Götz Bokelmann who was so kind to be the second reviewer. Thanks to my colleague Rudolf Widmer-Schmidrig for proof reading the thesis and giving me detailed feedback. Special thanks also to the colleagues of the institute for a nice atmosphere and open ears for any problems. Especially: Patrick Blascheck (also for proof reading parts of the thesis), Marco Walter, Sabrina Rothmund and Rolf Häfner.

I would like to thank the [CTBTO](#) for financing my research position at the institute for the development of the [OSI SAMS](#) software. This allowed me to have a very meaningful programming project and I could apply outcomes of the thesis there. The [CTBTO](#) also gave me the Young Scientist award and the possibility to attend various very interesting UN training exercises, especially the [IFE14](#). Peter Labak together with Gregor Malich of the [CTBTO](#) were always good partners who trusted me with the development of the software.

The thesis could not have been possible without the people deploying and maintaining the seismic stations and creating the ground truth data:

1. Basel dataset: Martin Häge and Marco Walter deployed the stations. Martin Häge and Patrick Blascheck did the manual analysis with an extensive ground truth of multiple thousand events by Patrick Blascheck. The external data with an additional ground truth was recorded and made available by the [SED](#).

2. [DGMK](#) dataset: Ulrich Schwaderer with the help of Patrick Blascheck, Gregor Mokolke, Marc Schmid, Alexander Kicherer, Tom Rohloff and Juan-Carlos Santoyo deployed the initial DGMK network. Later maintenance and extensions were done by Zaneta Gurbisz and Gregor Mokolke supported mainly by Marc Schmid, Alexander Kicherer, Marco Walter and me. Uwe Niethammer generated the synthetic seismograms for this dataset. The funding for the project came from [DGMK](#), Project 761: ExxonMobil Production Deutschland GmbH, DEA Deutsche Erdoel AG, GDF SUEZ E&P Deutschland GmbH, Wintershall Holding GmbH. External data was provided by [BGR](#) and [WEG](#).
3. [IFE14](#) dataset: The [CTBTO](#) organized the training exercise and made the data available. Network deployment, maintenance and data screening was done by the [OSI SAMS](#) team. Special thanks goes to the team members Nicolai Gestermann and Martin Häge.
4. [PISCO](#) dataset: The [GFZ](#) made the data available publicly with an accompanying ground truth ([GEOFON, 2010](#)). Günter Asch provided the dataset initially together with additional information.
5. The data of the nuclear test of North Korea is available from IRIS.

Although I re-implemented most of the algorithms from scratch during this thesis, I would like to thank all the software developers whose open-source libraries I used. I used Python to create most of the plots with mainly the libraries NumPy, SciPy, matplotlib and seaborn. I used ObsPy ([Megies et al., 2011](#)) for MiniSEED reading, acquisition of external data via SeedLink and FDSN webservices and to test some of my trigger implementations. I used the Generic mapping tools (GMT, [Wessel & Smith 1998](#)) to create the [PISCO](#) map. Scikit-learn ([Pedregosa et al., 2011](#)) was used for the Random Forest and Naive Bayes classifiers. Keras ([Chollet, 2015](#)) was used for the conventional, recurrent and convolutional neural networks. The

PCA plots were created with the JFreeChart Java plotting library. The thesis was written in  $\text{\LaTeX}$  and the PGF and TikZ packages were used to combine Figures and add explanations.

Last but certainly not least I would like to thank my wife Alice for being such a wonderful partner during all these years.



---

## CONTENTS

---

1	INTRODUCTION	31
2	CHALLENGES OF AUTOMATIC PROCESSING	37
3	OUTLINE OF TEST DATASETS	41
3.1	Basel . . . . .	42
3.2	DGMK . . . . .	43
3.3	IFE14 . . . . .	45
3.4	PISCO . . . . .	48
4	ALGORITHMIC BUILDING BLOCKS	51
4.1	Single stations . . . . .	52
4.1.1	Single station event detection and phase picking . . . . .	52
4.1.2	Single station event classification by pattern recognition . . . . .	66
4.2	Coincidence processing . . . . .	89
4.3	Coherence analysis . . . . .	91
4.3.1	Beamforming . . . . .	92
4.3.2	Combined array spectrograms . . . . .	105
4.3.3	Comparison of array algorithms at one mini-array . . . . .	105
5	CLUSTERING BY UNSUPERVISED PATTERN RECOGNITION	111
5.1	Feature extraction . . . . .	114
5.1.1	Interpretation . . . . .	115
5.2	Application of clustering algorithms . . . . .	117
5.3	PCA . . . . .	118
5.3.1	Cluster analysis with PCA . . . . .	118
5.3.2	Feature reduction . . . . .	119
5.3.3	Visualization by back-transformation . . . . .	125
5.3.4	Variations along principal components . . . . .	125
5.4	SOM . . . . .	127
5.4.1	Visualization of SOM nodes . . . . .	133
5.4.2	Event locations of SOM nodes . . . . .	133

5.4.3	Amplitude invariance . . . . .	135
5.4.4	Supervised classification with SOM . . . . .	136
6	WAVEFORM-COHERENCE FOR SEISMIC EVENT LOCA- TION	145
6.1	Conventional processing . . . . .	146
6.2	Source scanning . . . . .	148
6.2.1	Characteristic function (CF) . . . . .	153
6.2.2	Weighting with Fisher ratio . . . . .	157
6.2.3	Normalization of characteristic functions . . . . .	158
6.2.4	Final stacking of travel time corrected char- acteristic functions . . . . .	161
6.3	Application . . . . .	164
6.3.1	Basel Deep Heat Mining project monitoring	164
6.3.2	Gas field monitoring in northern Germany	166
6.3.3	CTBTO on-site inspection Integrated Field Exercise 2014 . . . . .	172
7	CONCLUSIONS AND OUTLOOK	181
7.1	Outlook . . . . .	185
7.2	Algorithm implementations . . . . .	188
	References	189
	Appendices	207
A	COMBINED REAL-TIME DETECTOR	209
B	NOISE REMOVAL BY SIMPLIFIED SOURCE SCANNING	211
C	VISUAL SEISMIC EVENT SCREENING BY SUPER-SONO- GRAMS	215
c.1	Abstract . . . . .	215
c.2	Introduction . . . . .	216
c.2.1	Nanoseismic Monitoring . . . . .	217
c.2.2	Heumoes slope example dataset . . . . .	219
c.3	Super-sonogram event screening and classification	219
c.3.1	Sonogram calculation steps . . . . .	221
c.3.2	Super-sonograms . . . . .	223
c.3.3	Signal classification . . . . .	225
c.4	Software . . . . .	227
c.5	Conclusions and discussions . . . . .	232
c.6	Acknowledgements . . . . .	233

D	LANDSLIDE AND SINKHOLE MONITORING BY SONO-	
	GRAM SCREENING	239
D.1	Abstract . . . . .	239
D.2	Introduction . . . . .	240
D.3	Visualization of continuous seismic data with super-sonograms . . . . .	241
D.4	Noise forensics . . . . .	243
D.5	Discovered signals-of-interest . . . . .	247
D.6	Conclusions . . . . .	250
D.7	Acknowledgements . . . . .	254
E	WORDCLOUD	257
F	LIST OF PUBLICATIONS	259



---

## LIST OF FIGURES

---

Figure 3.1	Overview of Basel network layout . . . . .	44
Figure 3.2	Overview of northern Germany DGMK network layout . . . . .	46
Figure 3.3	Topographic map of IFE14 with stations .	47
Figure 3.4	Map of seismic events of the PISCO project	49
Figure 4.1	Comparison of STA/LTA detections be- tween surface and borehole stations . . .	56
Figure 4.2	Comparison of STA/LTA detections be- tween surface and borehole stations, sec- ond time frame . . . . .	57
Figure 4.3	Comparison of characteristic functions for first Basel event . . . . .	62
Figure 4.4	Comparison of characteristic functions for second Basel event . . . . .	63
Figure 4.5	Comparison of characteristic functions for third Basel event . . . . .	64
Figure 4.6	Three-component polarization analysis . .	67
Figure 4.7	Trade-off between detection threshold and restriction to known events . . . . .	68
Figure 4.8	Comparison of North Korean nuclear tests	71
Figure 4.9	Raw waveform cross-correlation example	72
Figure 4.10	Processing steps of sonogram calculation	73
Figure 4.11	Sonogram detection (SonoDet) amplitude adaptation steps . . . . .	74
Figure 4.12	Walsrode cluster event overview . . . . .	76
Figure 4.13	Cross-correlation example of Walsrode events . . . . .	77
Figure 4.14	SonoDet example of Walsrode events . . .	78
Figure 4.15	Confusion matrix of cross-correlation fit between 9 events of the Walsrode cluster .	79

Figure 4.16	Confusion matrix of SonoDet fit between 9 events of the Walsrode cluster . . . . .	80
Figure 4.17	STA/LTA and SonoDet comparison with scenario explosion events from IFE14 . . . . .	81
Figure 4.18	Single station precision recall plot for Basel monitoring . . . . .	82
Figure 4.19	Comparison of spectrograms and the continuous wavelet transform . . . . .	84
Figure 4.20	Event examples with further processing of sonograms . . . . .	87
Figure 4.21	Noise examples with further processing of sonograms . . . . .	88
Figure 4.22	Comparison of STA/LTA coincidence detections between surface and borehole stations . . . . .	90
Figure 4.23	Comparison of STA/LTA coincidence detections between surface and borehole stations, second time frame . . . . .	91
Figure 4.24	Slowness grid for beamforming . . . . .	93
Figure 4.25	DGMK network array layouts . . . . .	96
Figure 4.26	Coherence at LOEV array . . . . .	97
Figure 4.27	Coherence at WIED array . . . . .	98
Figure 4.28	Coherence at BELL array . . . . .	99
Figure 4.29	Cross-correlation on beam . . . . .	100
Figure 4.30	Vespagram at LOEV ten element array with local event . . . . .	102
Figure 4.31	Simplified explanation of the Fisher ratio	104
Figure 4.32	Comparison of array coherency detection algorithms . . . . .	106
Figure 4.33	Fisher detection comparison with different array setups, first time frame . . . . .	107
Figure 4.34	Fisher detection comparison with different array setups, second time frame . . . . .	107
Figure 4.35	Compilation of super-sonogram . . . . .	108
Figure 4.36	Mini-array precision recall plot for Basel monitoring . . . . .	110
Figure 5.1	PISCO events SNR histogram . . . . .	114

Figure 5.2	Example of a <i>CENTER</i> event from the catalog . . . . .	115
Figure 5.3	Five exemplary events of each of the five classes . . . . .	116
Figure 5.4	1-D velocity model for P-waves in the measurement area . . . . .	117
Figure 5.5	Station A04 input data along first two principal components clustered by regional classes . . . . .	119
Figure 5.6	Station A04 input data along first two principal components clustered by epicentral distance . . . . .	120
Figure 5.7	Station A04 input data along first two principal components clustered by depth . . . . .	121
Figure 5.8	Station A07 input data along first two principal components clustered by regional classes . . . . .	122
Figure 5.9	Station A07 input data along first two principal components clustered by epicentral distance . . . . .	123
Figure 5.10	Station A07 input data along first two principal components clustered by depth . . . . .	124
Figure 5.11	PCA forward and back transformed sonogram . . . . .	126
Figure 5.12	Five exemplary events of each of the five classes back transformed with 80 principal components . . . . .	126
Figure 5.13	Visualization of events in the PCA space . . . . .	128
Figure 5.14	Initialization of the SOM . . . . .	131
Figure 5.15	A trained SOM . . . . .	132
Figure 5.16	Locations of events for SOM nodes . . . . .	134
Figure 5.17	Amplitudes of events for SOM nodes . . . . .	135
Figure 5.18	Confusion matrices for stations A04 and A07 . . . . .	138
Figure 5.19	Random forest feature importance . . . . .	140
Figure 5.20	Confusion matrices with additional machine learning classifiers . . . . .	143

Figure 6.1	Automatic phase picking with low-SNR event . . . . .	147
Figure 6.2	Overview of source scanning steps . . . . .	149
Figure 6.3	Flowchart of source scanning location . . . . .	154
Figure 6.4	Calculation of back azimuth and incidence grid . . . . .	156
Figure 6.5	Calculation of CF for Basel monitoring . . . . .	159
Figure 6.6	Calculation of CF for northern Germany monitoring . . . . .	160
Figure 6.7	Source scanning CF overview for Basel monitoring . . . . .	167
Figure 6.8	Source scanning comparison with and without array methods for Basel monitoring . . . . .	168
Figure 6.9	XY-grid showing the stack energy at the time and depth of the overall maximum for Basel . . . . .	169
Figure 6.10	Source scanning CF overview for northern Germany monitoring . . . . .	173
Figure 6.11	Source scanning comparison with and without array methods for northern Germany monitoring . . . . .	174
Figure 6.12	XY-grid showing the stack energy for northern Germany monitoring . . . . .	175
Figure 6.13	Iteration of x-y grids of source scanning energy over source times . . . . .	176
Figure 6.14	Comparison of automatic locations for IFE14 monitoring without and with array methods . . . . .	178
Figure 6.15	Influence from topography and array methods on source scanning energy distribution	179
Figure A.1	Flowchart of coincidence processing with various detectors for DGMK network . . . . .	210
Figure B.1	Acoustic noise from artillery practice . . . . .	213
Figure B.2	Acoustic noise from artillery practice removed with source scanning detector . . . . .	213

Figure C.1	Heumoes slope, sliding velocities and location of the three seismic mini-arrays . . .	220
Figure C.2	Processing steps of sonogram calculation for a local earthquake . . . . .	223
Figure C.3	Layout of mini-array and compilation of super-sonogram . . . . .	224
Figure C.4	Comparison of super-sonogram compilation of ordinary spectrograms . . . . .	226
Figure C.5	Screenshot of the software module SonoView with recurring anthropogenic noise . . . .	228
Figure C.6	Examples of natural seismicity and noise	229
Figure C.7	NanoseismicSuite overview of components and interfaces . . . . .	230
Figure D.1	Step-by-step sonogram generation . . . .	244
Figure D.2	Generation of super-sonograms . . . . .	245
Figure D.3	Screenshot of SonoView showing frost heave event and natural noise transient .	246
Figure D.4	SonoView screenshot showing two local earthquakes . . . . .	247
Figure D.5	Comparison of seismogram and super-sonogram view . . . . .	249
Figure D.6	Slidequake generation at Heumoes slope	251
Figure D.7	Slidequake generation at the Super-Sauze mudslide . . . . .	252
Figure D.8	Schematic diagram of a sinkhole . . . . .	253
Figure D.9	SonoView screenshot of rockfall registration	254



---

## LIST OF TABLES

---

Table 1	Overview of test datasets . . . . .	42
Table 2	Confusion matrix of prediction outcomes	53
Table 3	Number of events per class . . . . .	113
Table 4	Overview of source scanning steps for single and array stations . . . . .	163
Table 5	Event bulletin from monitoring in north- ern Germany . . . . .	171



---

## ACRONYMS

---

<b>AC<sub>2</sub>TC</b>	Advanced Course 2nd Training Cycle
<b>AIC</b>	Akaike information criterion
<b>AR</b>	auto-regressive
<b>BGR</b>	Federal Institute for Geosciences and Natural Resources
<b>CF</b>	characteristic function
<b>CCF</b>	cross-correlation function
<b>CNN</b>	convolutional neural network
<b>CTBT</b>	Comprehensive Nuclear Test-Ban Treaty
<b>CTBTO</b>	Comprehensive Nuclear Test-Ban Treaty Organization
<b>DGMK</b>	Deutsche Wissenschaftliche Gesellschaft für Erdöl, Erdgas und Kohle e.V.
<b>FK</b>	frequency wavenumber
<b>GFZ</b>	GeoForschungsZentrum Potsdam
<b>IFE<sub>14</sub></b>	Integrated Field Exercise 2014
<b>IfG</b>	Institute for Geophysics, University of Stuttgart
<b>IMS</b>	International Monitoring System
<b>ML</b>	local magnitude
<b>NN</b>	neural network
<b>OSI</b>	on-site inspection
<b>PCA</b>	principal component analysis

<b>PISCO</b>	Proyecto de Investigación Sismológica de la Cordillera Occidental - Project for the seismological investigation of the western cordillera
<b>PMCC</b>	Progressive Multi Channel Correlation
<b>RNN</b>	recurrent neural network
<b>SAMS</b>	seismic aftershock monitoring system
<b>SED</b>	Swiss Seismological Service
<b>SNR</b>	signal-to-noise ratio
<b>SOM</b>	self-organizing map
<b>STA/LTA</b>	short term average / long term average
<b>WEG</b>	Wirtschaftsverband Erdöl- und Erdgasgewinnung e. V.

---

## ABSTRACT

---

The reliable automatic detection, location and classification of seismic events still poses great challenges if only few sensors record an event and/or the signal-to-noise ratio is very low. This study first examines, compares and evaluates the most widely used algorithms for automatic processing on a diverse set of seismic datasets (e.g. from induced seismicity and nuclear-test-ban verification experiments). A synthesis of state-of-the-art algorithms is given. Several single station event detection and phase picking algorithms are tested followed by a comparison of single station waveform cross-correlation and spectral pattern recognition. Coincidence analysis is investigated afterwards to demonstrate up to which level false alarms can be ruled out in sensor networks of multiple stations. It is then shown how the use of seismic (mini) arrays in diverse configurations can improve these results considerably through the use of waveform coherence.

In a second step, two concepts are presented which combine the previously analysed algorithmic building blocks in a new way.

The first concept is seismic event signal clustering by unsupervised learning which allows event identification with only one sensor. The study serves as a base level investigation to explore the limits of elementary seismic monitoring with only one single vertical-component seismic sensor and shows the level of information which can be extracted from a single station. It is investigated how single station event signal similarity clusters relate to geographic hypocenter regions and common source processes. Typical applications arise in local seismic networks where reliable ground truth by a dense temporal network precedes or follows a sparse (permanent) installation. The test dataset comprises a three-month subset from a field campaign

to map subduction below northern Chile, project for the seismological investigation of the western cordillera (PISCO). Due to favourable ground noise conditions in the Atacama desert, the dataset contains an abundance of shallow and deep earthquakes, and many quarry explosions. Often event signatures overlap, posing a challenge to any signal processing scheme. Pattern recognition must work on reduced seismograms to restrict parameter space. Continuous parameter extraction based on noise-adapted spectrograms was chosen instead of discrete representation by, e.g. amplitudes, onset times, or spectral ratios to ensure consideration of potentially hidden features. Visualization of the derived feature vectors for human inspection and template matching algorithms was hereby possible. Because event classes shall comprise earthquake regions regardless of magnitude, signal clustering based on amplitudes is prevented by proper normalization of feature vectors. Principal component analysis (PCA) is applied to further reduce the number of features used to train a self-organizing map (SOM). The SOM arranges prototypes of each event class in a 2D map topologically. Overcoming the restrictions of this black-box approach, the arranged prototypes can be transformed back to spectrograms to allow for visualization and interpretation of event classes. The final step relates prototypes to ground-truth information, confirming the potential of automated, coarse-grain hypocenter clustering based on single station seismograms. The approach was tested by a two-fold cross-validation whereby multiple sets of feature vectors from half the events are compared by a one-nearest neighbour classifier in combination with an euclidean distance measure resulting in an overall correct geographic separation rate of 95.1% for coarse clusters and 80.5% for finer clusters (86.3% for a more central station).

The second concept shows a new method to combine seismic networks of single stations and arrays for automatic seismic event location. After exploring capabilities of single station algorithms in the section before, this section explores capabilities of algorithms for small local seismic networks. Especially traffic light systems for induced seismicity monitoring rely on

the real-time automated location of weak events. These events suffer from low signal-to-noise ratios and noise spikes due to the industrial setting. Conventional location methods rely on independent picking of first arrivals from seismic wave onsets at recordings of single stations. Picking is done separately and without feedback from the actual location algorithm. With low signal-to-noise ratios and local events, the association of onsets gets error prone, especially for S-phase onsets which are overlaid by coda from previous phases. If the recording network is small or only few phases can be associated, single wrong associations can lead to large errors in hypocenter locations and magnitude. Event location by source scanning which was established in the last two decades can provide more robust results. Source scanning uses maxima from a travel time corrected stack of a characteristic function of the full waveforms on a predefined location grid. This study investigates how source-scanning can be extended and improved by integrating information from seismic arrays, i.e. waveform stacking and Fisher ratio. These array methods rely on the coherency of the raw filtered waveforms while traditional source scanning uses a characteristic function to obtain coherency from otherwise incoherent waveforms between distant stations. The short term average to long term average ratio (STA/LTA) serves as the characteristic function and single station vertical-component traces for P-phases and radial and transverse components for S-phases are used. For array stations, the STA/LTA of the stacked vertical seismogram which is furthermore weighted by the STA/LTA of the Fisher ratio, dependent on back azimuth and slowness, is utilized for P-phases. In the chosen example, the extension by array-processing techniques can reduce the mean error in comparison to manually determined hypocenters by up to a factor of 2.9, resolve ambiguities and further restrain the location.



---

## ZUSAMMENFASSUNG

---

### **Spektrale und zeitliche Mustererkennung zur Detektion und kombinierte Netzwerk- und Array-Kohärenz zur Lokalisierung von seismischen Ereignissen**

Die verlässliche automatische Detektion, Lokalisierung und Klassifikation von seismischen Ereignissen birgt noch immer große Herausforderungen wenn nur wenige Sensoren ein Ereignis registrieren und/oder das Signal-Rausch-Verhältnis sehr niedrig ist. Diese Studie untersucht und vergleicht zuerst vorhandene Algorithmen der Automatisierung anhand diverser seismischer Datensätze (z.B. der induzierten Seismizität und der Überwachung des Kernwaffen-Test-Stop Vertrages). Es wird eine Synthese der Algorithmen die auf dem neuesten Stand der Technik sind gegeben. Mehrere Detektions- und Phasenpickalgorithmen von Einzelstationen werden getestet, gefolgt von einer Analyse der zeitlichen Korrelation mit Mustern und spektraler Mustererkennung. Die Koinzidenzanalyse wird im nächsten Schritt untersucht um zu zeigen, wie Fehldetektionen in einem Sensornetzwerk aus mehreren Stationen ausgeschlossen werden können. Es wird dargestellt, wie die Einbeziehung von seismischen (Mini-)Arrays in unterschiedlichen Konfigurationen diese Resultate weiter verbessern kann, indem die Wellenformkohärenz ausgenutzt wird.

In einem zweiten Schritt werden zwei Ansätze vorgestellt, welche die vorgestellten Algorithmen-Bausteine in einer neuen Weise verknüpfen.

Der erste Ansatz ist eine seismische Ereignis-Clusterung durch unüberwachtes Lernen welche es ermöglicht, Ereignisse mit nur einem Sensor zu identifizieren. Diese Studie dient als Basisuntersuchung um die Grenzen der elementaren seismischen Überwachung, mit nur einem vertikalen seismischen Sensor,

auszuloten. Sie zeigt die Tiefe an Information, die von einzelnen Stationen extrahiert werden kann. Es wird untersucht inwiefern die Ereignisähnlichkeit in Beziehung zu geografischen Regionen von Hypozentren und ähnlichen Quellprozessen steht. Typische Anwendungen sind lokale seismische Netzwerke bei denen verlässliches Vorwissen durch dichte temporäre Netzwerke vorhanden ist und davor oder danach ein (permanentes) Netzwerk mit wenigen Stationen verbleibt. Als Testdatensatz dient ein dreimonatiger Teil einer Feldkampagne um die Subduktionszone unterhalb Nordchiles zu kartieren, Project for the Seismological Investigation of the Western Cordillera (PISCO). Durch vorteilhafte Rauschbedingungen in der Atacamawüste beinhaltet der Datensatz eine Vielzahl an flachen und tiefen Erdbeben und auch viele Minenexplosionen. Ereignissignaturen überlappen oft, was eine Herausforderung für jedes Signalverarbeitungssystem darstellt. Eine Mustererkennung muss auf reduzierten Seismogrammen arbeiten um die Parameterdimensionalität einzuschränken. Kontinuierliche Parameterextraktion basierend auf rauschadaptierten Spektrogrammen wurde gewählt anstatt einer diskreten Repräsentation von zum Beispiel Amplituden, Einsatzzeiten oder spektralen Verhältnissen, um sicher zu stellen, dass auch potentielle versteckte Merkmale berücksichtigt werden. Hierdurch war es möglich die abgeleiteten Merkmalsvektoren für eine manuelle Untersuchung und die Algorithmen der Mustervergleiche zu visualisieren. Da Ereignisklassen die Erdbebenregionen unabhängig von der Magnitude repräsentieren sollen, wird eine Clusterung basierend auf Amplituden durch eine geeignete Normalisierung der Merkmalsvektoren verhindert. Eine Hauptkomponentenanalyse wird benutzt um die Anzahl der Merkmale weiter zu reduzieren um dann eine selbstorganisierende Karte zu trainieren. Die selbstorganisierende Karte ordnet Prototypen der Ereignisklassen in einer 2D-Karte topologisch an. Um diesen Black-Box-Ansatz zu überwinden, können die geordneten Prototypen wieder zurück zu Spektrogrammen transformiert werden um eine Visualisierung und Interpretation der Ereignisklassen zu erlauben. Der letzte Schritt ordnet Prototypen den wahren Klassen zu. Dies

bestätigt das Potential der automatisierten, grobskaligen Clustering von Hypozentren basierend auf Seismogrammen von Einzelstationen. Der Ansatz wurde mittels einem zweigeteilten Kreuzvalidierungsverfahren getestet bei dem mehrere Sätze von Merkmalsvektoren der Hälfte der Ereignisse mittels einem One-Nearest-Neighbour Klassifizierer in Kombination mit einer euklidischen Distanzmetrik verglichen werden. Dies ergibt eine korrekte geographische Separierungsrate von 95.1% für grobe Cluster und 80.5% für feinere Cluster (86.3% für eine zentralere Station).

Der zweite Ansatz zeigt einen Weg um seismische Netzwerke aus Einzel- und Array-Stationen zu kombinieren um Ereignisse automatisch zu lokalisieren. Nach der Untersuchung der Möglichkeiten von Einzelstationen im vorigen Abschnitt, untersucht dieser Abschnitt die Möglichkeiten der nächsten Stufe, kleine lokale seismische Netzwerke. Speziell Ampelsysteme für induzierte Seismizität beruhen auf der automatischen Echtzeitlokalisierung von schwachen Ereignissen. Diese Ereignisse beinhalten niedrige Signal-Rausch-Verhältnisse und Rauschstörungen durch die industrielle Umgebung. Konventionelle Lokalisierungsmethoden basieren auf dem unabhängigen auswählen von Ersteinsatzzeiten seismischer Wellenzüge an Einzelstationen. Der Auswählvorgang findet hierbei getrennt und ohne Rückkopplung der eigentlichen Lokalisierung statt. Dieses auswählen wird bei niedrigen Signal-Rausch-Verhältnissen und lokalen Ereignissen oft fehlerhaft, vor allem für S-Phaseneinsätze welche von Coda vorheriger Phasen überlagert sind. Wenn das Netzwerk zur Aufzeichnung nun klein ist oder es nur möglich ist wenige Phasen zu bestimmen, dann können einzelne Fehlpicks zu großen Fehlern im Hypozentrum und der Magnitude führen. Ereignislokalisierung durch Source-Scanning, welches in den letzten beiden Jahrzehnten etabliert wurde kann hierbei robustere Resultate erzielen. Source-Scanning benutzt Maxima einer laufzeitkorrigierten Stapelung von charakteristischen Funktionen der Wellenformen auf einem zuvor definierten Lokalisierungsgitter. Diese Studie untersucht, in wie weit Source-Scanning erweitert und verbessert werden kann, indem

Informationen von seismischen Arrays, das heißt Stapelung und Fisher-Verhältnis, integriert werden. Diese Array Methoden beruhen auf der Kohärenz der gefilterten aber sonst unprozedierten Wellenformen wohingegen traditionelles Source-Scanning die charakteristische Funktion benutzt um eine Kohärenz von ansonsten inkohärenten Wellenformen zwischen entfernten Stationen zu erreichen. Das Verhältnis aus Kurzzeit-Mittelwert zu Langzeit-Mittelwert (STA/LTA) dient als charakteristische Funktion. Vertikalkomponenten von Einzelstationen für P-Phasen und radiale und transversale Komponenten für S-Phasen werden benutzt. Für Arraystationen und P-Phasen wird STA/LTA auf den gestapelten vertikalen Seismogramm benutzt welches zusätzlich mittels STA/LTA des Fisher-Verhältnisses gewichtet ist (basierend auf Rückazimut und Langsamkeit). In dem gezeigten Beispiel ergibt die Erweiterung mittels Techniken der Arrayprozessierung eine durchschnittliche Reduktion des Fehlers zu manuell bestimmten Hypozentren um einen Faktor von 2.9. Die Erweiterung löst Doppeldeutigkeiten auf und Lösungen werden besser einschränkt.

# 1

---

## INTRODUCTION

---

In the last decades, many research projects addressed automatic processing of seismic signals and by now it is used routinely in multiple scenarios. In some cases, as for the detection of repeating very similar seismic events it surpasses manual detection capabilities (see section 4.1.2). In many other cases, especially if data to train algorithms is rare and new event types need to be detected, manual analysis is still superior. If only few stations record seismic signals, the gap between manual and automatic analysis increases in the favour of manual analysis. This study tries to further reduce this gap in such cases and thereby hopes to enable the usage of automatic processing in additional areas of monitoring. To provide a clarification of typical terms used in seismology for readers from other scientific fields, this introduction will explain basic seismological concepts first and then give a short history of seismic automatic processing.

Seismology examines earthquakes, explosions and the propagation of seismic waves inside the earth. These waves are recorded by seismometers which measure usually ground displacement or velocity (this study only uses recorded velocity). Based on the distance of an seismic event from the recording station or network it can be classified as teleseismic (more than 1000 km), regional (between 100 and 1000 km) or local (less than 100 km). Recording is done digitally in global networks and with arrays since the mid 1970s (Joswig, 1987). Main developments like these global networks are driven by the need to monitor the earth for underground nuclear explosions which led to the United Nations Comprehensive Nuclear Test-Ban Treaty Organization (CTBTO) and its International Monitoring Sys-

tem (IMS). Seismic wave types can be divided broadly in body and surface waves (Shearer, 1999). While body waves travel through the interior of the Earth, surface waves travel along its surface. Body waves in turn can be divided into two types: compressional waves (longitudinal polarization of particle motion) which are named primary waves (P-waves), and shear waves (transverse polarization of particle motion) which are named secondary waves (S-waves). P-waves as opposed to S-waves can travel in any kind of material and are faster. As fluids do not support shear stress, S-waves can only travel through solid material. Surface waves can be divided into Rayleigh and Love waves.

The most detailed information about earth's deep interior comes from seismology. The largest signals for this endeavor come from naturally occurring quakes. At the onset both time and place of a quake is unknown as well as the speed with which the waves travel through the earth (depending on the interior structure). However, since seismology is a mature science, a good idea of the velocity with which seismic waves propagate through the earth exists. The focus can therefore be on the earthquake detection and location problem. This will be done in the following but bear in mind that the velocity distribution based on the underground structure is unknown as well to some extent.

To investigate the interior of the earth it is mandatory to locate registered seismic events. Seismic networks with multiple sensors which each record an event are primarily used (Lay & Wallace, 1995; Lee & Stewart, 1981). Time difference of arrivals of different wave types at one station and of the same wave type at different stations (multilateration) are utilized. Body waves that are reflected and refracted at velocity boundaries inside the earth can be utilized. For body waves dispersion is almost negligible so that a seismogram consists of discrete pulses, so called phases. The estimated arrival time of a wave type is named phase pick and at least four phase picks are necessary to constrain a seismic event in time and space ( $t, x, y, z$ ). Because of errors in phase picking and unknown velocity distribution,

more than four phase picks are usually needed to constrain a location well. The resulting over-determined system can be posed as an optimization problem and can be solved by, for example, least squares minimization of errors. An earthquake location is usually given by latitude, longitude and depth and is called hypocenter. Its projection onto the surface of the earth is called epicenter.

An additional way of registering signals is by using seismic arrays. These can be used instead or as an extension to seismic networks (Harjes & Henger, 1973). Seismic arrays consist of multiple sensors which are arranged in a specific geometry to allow the analysis of the seismic wave field. The size of an array is given by its aperture, the largest distance between two of its sensors. Depending on the targeted signal, geometries and apertures vary greatly between different arrays. In many cases seismic networks can be also used as arrays. Important for most array processing techniques is the coherence of seismic signals between individual stations. This requires certain spatial limitations and similar geology below each station. A commonly used technique is the so called beamforming, which consists of delaying signals at single stations and stacking them. This improves signal-to-noise ratios (SNRs) due to constructive interference of signals and suppression of incoherent background noise. Beamforming is based on back azimuth (station-to-event azimuth) and slowness (reciprocal of apparent wave velocity) determination which can help in event location.

Once an event is located, its actual size or magnitude can be evaluated by estimating the released energy. Different magnitude “recipes” exist which range from more accurate (e.g. moment magnitude scale) to more practical (e.g. local magnitude scale). The moment magnitude scale ( $M_W$ ) relies on estimates of the seismic moment of events which can often not be estimated reliably for weak events. Therefore this study uses the local magnitude scale ( $M_L$ ) also known as Richter magnitude scale (Richter, 1956). It consists of a simple logarithmic dependence from recorded amplitude at a station and its distance to the event. The seismic intensity on the other hand classifies the

energy arriving at a particular location, for example a city and is used to classify possible damage. The intensity therefore varies between different places for the same seismic event. While the magnitude has no physical unit, it still has some very practical advantages: it allows an operator of a single seismic station to estimate the size of an event. This was especially important in the early days of seismology.

Some decades ago, all of the processing steps to detect and locate seismic events were done manually by experienced seismologists, but a continuously increasing number of seismological measurement networks and the employment of high-resolution seismometers with continuous recordings led to a rapidly growing amount of seismological data. As a consequence rapid and automatic processing schemes have become an essential component of early warning systems for seismic hazards or the verification of the Comprehensive Nuclear Test-Ban Treaty (CTBT). As an example for scale and importance, the preparatory commission which will be responsible to enforce the CTBT once it enters into force will need to process worldwide seismic data (amongst other geophysical techniques) from 50 primary and 120 auxiliary seismic stations in near real-time (many stations being seismic arrays). Any delay in processing of this data will delay on-site inspections (OSIs) in countries of potential violators and thereby reduce the chance of conviction.

As mentioned, automatic detection of seismic events and further characterization with respect to location and magnitude is a standard procedure in seismic data centres worldwide for events which are recorded at many stations. A coincidence analysis of phase picks from variations of the short term average / long term average (STA/LTA) trigger algorithm (see section 4.1.1) are used dominantly for detection (Withers et al., 1998). If recordings of sufficiently high SNR are available, these algorithms are very robust and events can be located automatically and thereby discriminated with respect to hypocenter latitude, longitude, depth and magnitude. Joswig (1987) was the first to use spectral pattern recognition to detect events with only one or few stations.

However for local seismicity measurements, dense networks are realized only as temporary installations for reasons of flexibility and/or costs, manpower or accessibility of the area. More ruggedized sensors and data loggers, longer lasting batteries and increasing hard-disk capacities make it easier to deploy dense *temporal* seismic networks with many stations on a small grid to monitor weak local seismic events. These station setups are cheap in comparison to *permanent* network stations, which require a complex and costly infrastructure. Permanent networks for local seismic monitoring are therefore often under-equipped, as e.g. in the case of permanent monitoring of induced seismology (Beyreuther et al., 2012), seismicity monitoring on the sea floor with Ocean Bottom Seismometers (D'Alessandro et al., 2013) and permanent monitoring of volcanic activity with only one station per volcano in some cases (e.g. Alaska Volcano Observatory - Google Map<sup>1</sup>, accessed August, 2015). Other examples include sinkhole monitoring (Wust-Bloch & Joswig, 2006) and permanent landslide monitoring (Walter et al., 2011b; Sick et al., 2013). Signals additionally suffer from low SNRs because sensor sites can not be chosen optimally due to restrictions. Sought-after events in these cases are often only detected at one or two stations and can therefore not be located reliably by conventional means. Furthermore, the location of an event does not always permit conclusions on event type.

This study tries to push the boundaries of automatic processing to these less researched areas of seismic monitoring by an extensive examination of existing techniques and, based on this examination, a new combination thereof will be tried. It is thus split into two main parts. After a short treatment of the main challenges of seismic signal processing in chapter 2 and an introduction to the test datasets in chapter 3, the first part in chapter 4 examines currently available state of the art algorithms for automated processing. It starts by looking into single station detection and phase picking algorithms and continues with an analysis of single station pattern recognition techniques. Afterwards network coincidence procedures and

---

<sup>1</sup> <http://www.avo.alaska.edu/map/>

array techniques are explored. The second part is following in the next two chapters where two new techniques are introduced. The first of these shows the capabilities and limits of using only a single station to categorize events in geographic clusters and distinguish between quarry explosions and natural earthquakes from a subduction zone in the central Andes in chapter 5. It establishes a basic understanding of what algorithms can provide if only the information from a single station is available. The second new technique introduces a new location procedure which combines seismic networks and arrays in chapter 6. The source scanning technique is phase pick independent and relies on time shifted stacking of characteristic functions (CFs). By including array techniques into the CF, the robust and reliable location of low SNR events recorded at only few stations is possible.

# 2

---

## SEISMIC SIGNALS AND THE CHALLENGES OF AUTOMATIC PROCESSING

---

Automatic processing of seismic signals is often compared to speech recognition and both disciplines utilize methods from each other, see e.g. [Ohrnberger \(2001\)](#). The comparison suggests itself by the similarities from both areas. Spoken words, recorded by a microphone and seismic signals of earthquakes, recorded by a seismometer are both time series with distinctive characteristics. Particular words on the one hand and particular earthquake types on the other hand have both certain time dependant features. The equivalent for phonemes of words (units of sound) are the different seismic phases of earthquake recordings. By comparing both research areas with each other, this chapter tries to show the main challenges of automatic processing of seismic signals and how this study attempts to solve them.

Seismology possesses some specialities which don't exist in speech recognition. Speech recognition relies mainly on a clearly defined corpus of possible words or phonemes. This corpus is known and difficulties arise mainly from varying speakers pronouncing words differently depending on their origin, anatomy and mood. Furthermore the same word can have different meanings depending on the given context. In seismology, similar to words, basic types of earthquakes exist which are defined by their source parameters. The main difficulty here is that signals travel through only vaguely known heterogeneous underground material between source and sensor which acts as a transfer function for the signal. For local signals this travel path is often dominated by mostly unknown local underground

heterogeneities which vary greatly between different monitoring regions. This means that especially high frequencies of signals (above a few Hertz) can not be simulated realistically in most cases. The transfer function for speech signals on the other hand is mainly dependant on the anatomy and heritage of the speaker which allows at least to learn speaker dependant models.

Another difference is that speech recognition needs to cope with low SNRs only in very specific tasks (e.g. in car voice recognition) while in most applications the recorded voice signal has a high SNR because the speaker talks directly into a microphone. Many applications allow also a re-recording if SNR was bad or unclear by asking the speaker to repeat the text. This brings us to the main challenge for learning models in local seismology. While for speech recognition we can train models for each speaker by asking him or her to record test sentences, this is not possible for new seismic monitoring areas. We can only rely on very basic features which do not change considerably in different monitoring areas and use the information from whatever signals were recorded previously there. If the area has only a low rate of seismicity it might take weeks or months to record a first actual event. Until then only general simple statistical models can be applied to detect events. By introducing knowledge from different measurement areas, one risks to exclude events with novel characteristics. On the other hand by using only simple statistical features it is often impossible to exclude events from noise sources. Even after registering events for a long time in a certain region, one can never be sure if a new event type will occur in the future due to its low recurrence frequency or change of the local ground stress regime.

Finding the “needle in a haystack” is a great challenge and applies especially to the nuclear test-ban monitoring where the seismic event of an underground nuclear explosion must be found in the “noise” of the permanently ongoing background natural seismicity and industrial quarry blasts. This poses especially a challenge during aftershock sequences from strong earthquakes (magnitudes greater than seven to eight). At the

moment an algorithm based on phase onsets and beamforming, the Global Association algorithm (Bras et al., 1994) is used there. However it is planned to introduce a new algorithm based on Bayesian statistics which includes a global prior probability of seismic events (Arora et al., 2013). This algorithm has proven to lower the false positive rate significantly. The prior distribution for the algorithm has an above zero value for the whole globe and an increased value for known nuclear test sites in anticipation of potential future tests. The question remains if the system is appropriate to detect underground nuclear tests at a priori unknown test sites and therefore also unknown detailed signal characteristics.

An additional difficulty in machine learning of seismic models in comparison to other disciplines like speech recognition is the never completely known ground truth. This means it is never known how many actual seismic events happened during a monitoring campaign. The Gutenberg Richter law (Gutenberg & Richter, 1954) postulates that the occurrence frequency of seismic events increases exponentially with decreasing magnitude. Therefore we can never truly estimate the false positive rate of detected events because each detected signal might actually be an event hidden in noise. An example of this is shown in section 4.1.2 where the detection algorithm outperforms the manual detection and thereby introduces questions on how to verify such detected events.

A further fundamental problem of developing seismic automation algorithms is the lack of few common established benchmark datasets which are used by most algorithm developers to compare the performance of new algorithms. Many areas of machine learning as for example speech or image recognition have well documented benchmark datasets as for example the TIMIT dataset (Garofolo et al., 1993). New algorithms are routinely tested on these datasets and can therefore be compared easily. While this comparison is surely not perfect and algorithms might be tuned for a certain specific sub-field, this still allows a rough fast benchmarking. If algorithms in seismology are not released open-source or are not well documented it is

impossible to make comparisons. Many research papers even omit exact values of parameters which makes a reproduction of results difficult. Even if a method is publicly available, it takes a tremendous time of work to reproduce results and compare them to self-developed algorithms. A reason for the lack of such a reference dataset might be the extreme diversity of monitoring campaigns. Most measurements are fundamentally different. This includes the recording region, sensor locations and measurement equipment.

This study tries to overcome the mentioned challenges by investigating both, algorithms without (section 4.1.1) and with extensive prior knowledge of expected signals (section 4.1.2). Various algorithms were re-implemented to allow an unbiased comparison on the same datasets. Subsets of stations are used for training and compared to manual detections using the whole set of stations. This allows to lower the likelihood of false positive detections which are actual events which were not found in a manual analysis. An example of this is the processing of the Basel monitoring dataset (section 3.1). A borehole station near the hypocenter of events is used to establish a reliable ground truth of events. Detection algorithms are then evaluated at more distant surface stations. Furthermore multiple datasets from diverse locations and network setups are used to compare algorithms. This allows to not be biased by optimized algorithms for only one particular monitoring setup.

---

## OUTLINE OF TEST DATASETS

---

The emphasis of this study lies on the automation algorithms and the explanation of them. This chapter therefore provides only a short overview in advance of the monitoring campaigns which provided the data to test the algorithms. The datasets are carefully chosen and comprise four campaigns with varying objectives, network designs and event characteristics. They allow to test individual properties of the automatic algorithms. Strong biases which might arise if an algorithm is only tuned for one particular dataset are eliminated. The short overview of the used datasets in table 1 shows how monitoring durations, deployed stations and the number of events varies greatly between datasets. One dataset is for example from a short term two day additional surface monitoring of the Basel Deep Heat Mining Project where thousands of microseismic events occurred. Another one is from a long term two and a half year long monitoring of gas fields in northern Germany (DGMK) with only few events but plenty of noise and a heterogeneous recording network.

Three of the campaigns (Basel, DGMK and IFE14) are so called Nanoseismic Monitoring (Joswig, 2008) campaigns. Typical for these campaigns is the use of so called mini-arrays (Sick et al., 2012). These are flexible and fast to deploy seismic arrays with one central three-component sensor and three satellite vertical component sensors with an aperture of approximately 200 m. The use of these arrays allows to use beamforming and thereby estimate apparent velocities and back azimuths of an incoming wave field. Nanoseismic Monitoring focuses on forensic seismology (Zucca, 1998; Douglas, 2007) with manual screening

Table 1: Overview of test datasets with significant statistics.

Name	Basel	DGMK	IFE14	PISCO
Duration	2 days	2.5 years	20 days	100 days
Mini-arrays	2	3 <sup>*</sup>	12	0
Surface stations	0	5	4	25
Borehole stations	1 (3) <sup>**</sup>	0 (2) <sup>***</sup>	0	0
Order of events	1000s	10s	10s	1000s
Installation by	IfG & SED	IfG	CTBTO	GFZ

<sup>\*</sup> One of the arrays was extended to a ten component array

<sup>\*\*</sup> Borehole stations from [SED](#). Two of the three borehole stations have only overlapping data of 9.5 h with the surface mini-arrays

<sup>\*\*\*</sup> Two borehole stations from the [WEG](#) network are in the vicinity of the [DGMK](#) network and data was available

of data and sought after events just above the ambient noise level. Apart from [CTBTO OSI](#) (see IFE14 dataset), further applications are sinkhole monitoring ([Wust-Bloch & Joswig, 2006](#)), active fault mapping ([Häge & Joswig, 2009](#)), monitoring of slope dynamics ([Walter et al., 2009](#); [Walter & Joswig, 2009](#); [Walter et al., 2011a](#); [Sick et al., 2013](#)), hydraulic stimulation monitoring ([Häge et al. 2012](#), see Basel dataset), oil and gas field monitoring (see [DGMK](#) dataset) and radioactive waste deposit monitoring ([Blascheck et al. 2015](#), monitoring of rock laboratory which is only used to test techniques).

### 3.1 BASEL DEEP HEAT MINING MONITORING (BASEL)

The Basel Deep Heat Mining project monitoring dataset (Basel) is from an additional surface monitoring of the Basel hydraulic stimulation Deep Heat Mining Project ([Häge et al., 2012](#)). The project was well monitored by an extensive network of borehole stations from the company Geothermal Explorers and Swiss Seismological Service ([SED](#)). To test and compare the accuracy capabilities of surface monitoring, two surface mini-arrays (SNS1 and SNS2) were temporarily deployed at a distance of 2.1 and 4.8 km to the stimulation for two days during the time of the maximum number of events by the Institute for Geophysics,

University of Stuttgart (Häge et al., 2012). This data is combined here with data from three three-component borehole stations of the SED which are publicly available (JOHAN, MATTE and OTER1), see Figure 3.1. However for two of the three borehole stations (JOHAN and MATTE), only 9.5 hours which overlap with the surface monitoring were available.

### 3.2 INDUCED SEISMICITY MONITORING OF GAS FIELDS IN NORTHERN GERMANY (DGMK)

The Induced seismicity monitoring of northern Germany gas fields dataset (DGMK) is from a two and a half year monitoring research network in northern Germany funded by Deutsche Wissenschaftliche Gesellschaft für Erdöl, Erdgas und Kohle e.V. (DGMK) and deployed by the Institute for Geophysics, University of Stuttgart. It combines five single three-component sensors, two four-element mini-arrays and one ten-element array (Figure 3.2). Natural and potentially induced seismicity in the region is infrequent. Detection and location of seismic events is difficult due to several man made noise sources (e.g. army artillery practice) in combination with soft sedimentary surface layers in which high amplification and scattering results in high noise levels. Between November 2013 and February 2016 only nine seismic events in a radius of 30 km around the network were registered by multiple stations. Additional events were found by cross-correlation but these events are too weak to be located reliably without relative location techniques (mostly only detected at one station). Data transfer of this network was realized live to the institute over mobile network (LTE) by the use of Raspberry Pi single board computers at the sensor sites. Around 6.3 Gigabyte of uncompressed data per day are transmitted to a local server at the institute and processed there by the algorithms developed in this study. Stations from two additional monitoring networks are nearby. The networks are from Wirtschaftsverband Erdöl- und Erdgasgewinnung e. V. (WEG) and Federal Institute for Geosciences and Natural Resources (BGR). The WEG network includes multiple borehole

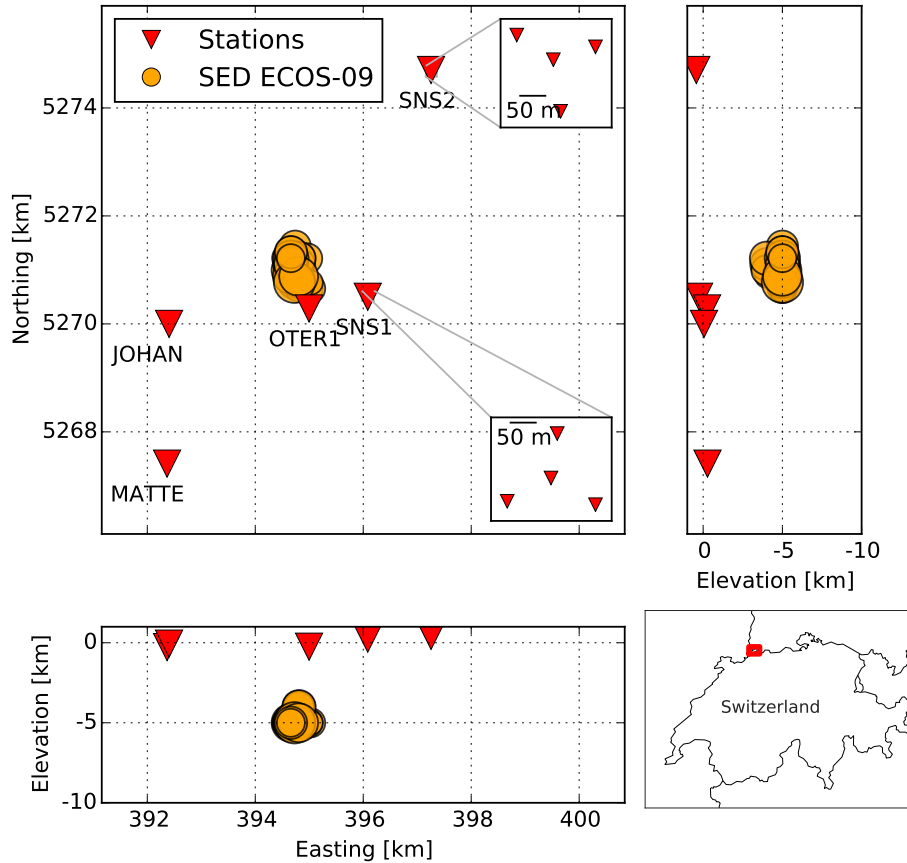


Figure 3.1: Overview of Basel network layout. Stations OTER<sub>1</sub>, JOHAN and MATTE are borehole stations from the SED. SNS<sub>1</sub> and SNS<sub>2</sub> are temporary surface mini-arrays deployed by the Institute for Geophysics, University of Stuttgart to test the accuracy and capabilities of surface monitoring. Thousands of micro-seismic events were registered during the two day additional surface monitoring and are used to test detection algorithms. The shown events (orange symbols, scaled by magnitude) here are stronger ones ( $M_L = 0.8 - 2.6$ , scaled by magnitude) included in the public bulletin from the SED and are used to test location algorithms. All events cluster closely in epicenter and depth near the borehole casing shoe.

stations with one being 200 m below the central element of the WIED mini-array.

### 3.3 CTBTO ON-SITE INSPECTION EXERCISE (IFE14)

The Comprehensive Nuclear Test-Ban Treaty Organization (CTBTO) monitors the globe for nuclear explosions which would violate its treaty once it comes into force. The final verification measure for this treaty will be on-site inspections (OSIs) where up to 40 inspectors travel into the country which is suspected of illegal testing. They monitor the area, among other techniques, for seismic aftershocks from a possible underground nuclear explosion. The treaty states that this verification regime must be ready shortly after the CTBT enters into force which is why regular exercises are being held to practice such an OSI. The last one of those extensive exercises was the Integrated Field Exercise 2014 (IFE14) from November to December 2014 in Jordan.

The seismic aftershock monitoring system (SAMS) of an OSI consists of up to 50 mini-arrays which can be deployed in the 1000 km<sup>2</sup> inspection area. The official SAMS software is developed by the author of this study and uses several ideas and algorithms from it. During IFE14, SAMS was tested by triggering three small near surface explosions unknown to the inspectors. The inspectors had the task of detecting and locating these explosions between the various natural seismic events and additional quarry explosions in the monitored region east of the Dead Sea. The yields of the explosions were 3, 5 and 10 kg (corresponding to local magnitudes of 0.0, -0.2 and -0.6) and they were buried in few meter deep boreholes. The SAMS network of IFE14 consisted of twelve mini-arrays and four three-component stations. Strong safety restrictions and the extreme topography in the inspection area made a larger number of deployed stations impossible. The map in Figure 3.3 shows the stations and the underlying topography.

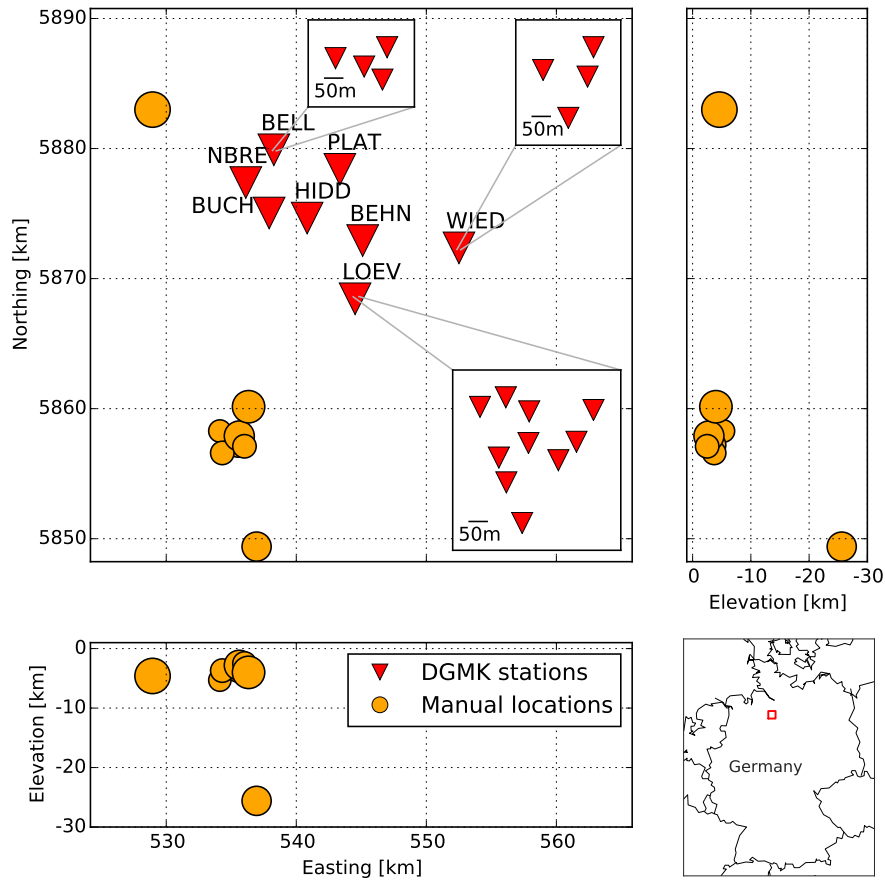


Figure 3.2: Overview of northern Germany **DGMK** network layout. The network was deployed to study seismic monitoring techniques for hydrocarbon extraction. Stations **BELL** and **WIED** are mini-arrays, station **LOEV** was consecutively built into a 10-station array with one three-component station in the center and the other nine stations with one component each. The other network stations are three-component single stations. Events (orange symbols, scaled by magnitude) in a region of 30x30 km are infrequent. All registered events which were visible at multiple stations during a two and a half year permanent measurement campaign are shown and comprise mainly the cluster including one outlier in the south of the network near the city of Walsrode and one event in the north-west near the city of Rotenburg. Manual location of these events has benefited from two additional **WEG** borehole stations in the region and up to four additional **BGR** surface stations.

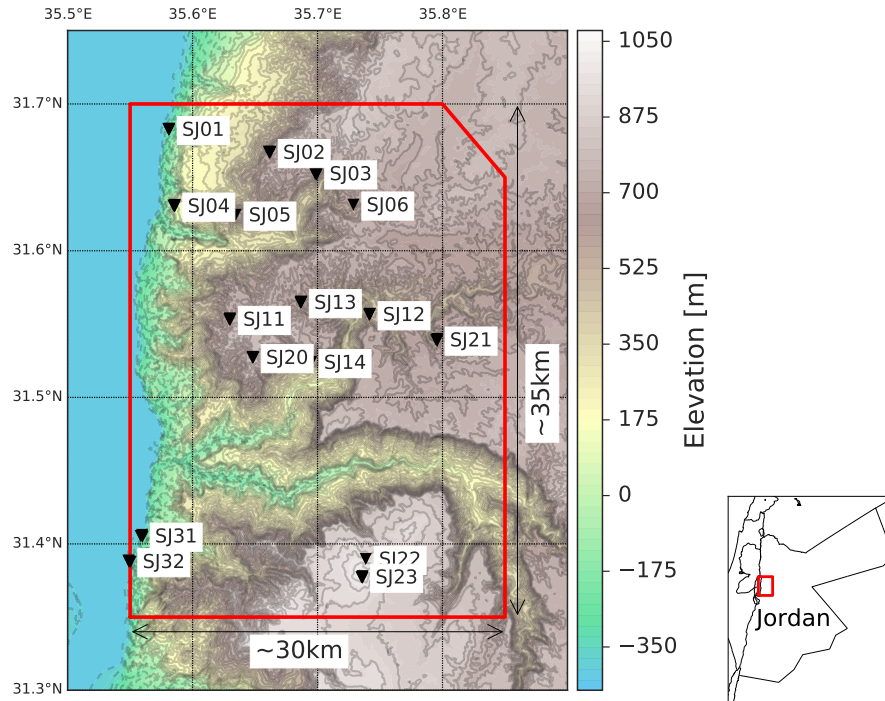


Figure 3.3: Topographic map of IFE14 with seismic aftershock monitoring system stations. Stations SJ05, SJ06, SJ14 and SJ23 are three-component stations, the others are mini-arrays. The topography ranges from around  $-400$  m at the dead sea in the west to more than  $1000$  m in the mountains which made deployment and maintenance of the temporary network extremely difficult. The red line indicates the on-site inspection area which comprises  $1000$  km<sup>2</sup>. The base of operations where inspectors analysed the data was north of station SJ01 at the coast of the Dead Sea. During the 20 days monitoring, multiple natural events from the Dead Sea Transform fault system were registered. The control team of the training exercise detonated three low-yield near-surface explosions unknown to the inspection team. The explosions were set up near station SJ02 to test the seismic aftershock monitoring system capabilities.

### 3.4 SUBDUCTION ZONE MAPPING BELOW NORTHERN CHILE (PISCO)

The Proyecto de Investigación Sismológica de la Cordillera Occidental - Project for the seismological investigation of the western cordillera (**PISCO**) project was a large seismological field campaign conducted in a 100 days period in spring 1994. The campaign itself was a part of the Collaborative Research Center (SFB 267) "Deformation processes in the Andes" and included a network of 25 seismic stations in the Atacama desert of the central Andes of north Chile for continuous recording of seismic activity. The dataset is freely available on the website of the German Research Centre for Geosciences (**GEOFON**, 2010). Access to an accompanying bulletin with epicentre time, localization and depth is available for 764 events (**Graeber**, 1997). A comprehensive statistical analysis of hypocenters yielded 377 events which could be assigned to distinctive event types which allow a cluster analysis (Figure 3.4). Since the measurement area was on top of the subduction zone between the oceanic Nasca Plate and the continental South-American Plate, the recorded data contains a wealth of seismic events with hypocenter depth increasing from west to east (with the exception of the *QUARRY* and *CRUST* events).

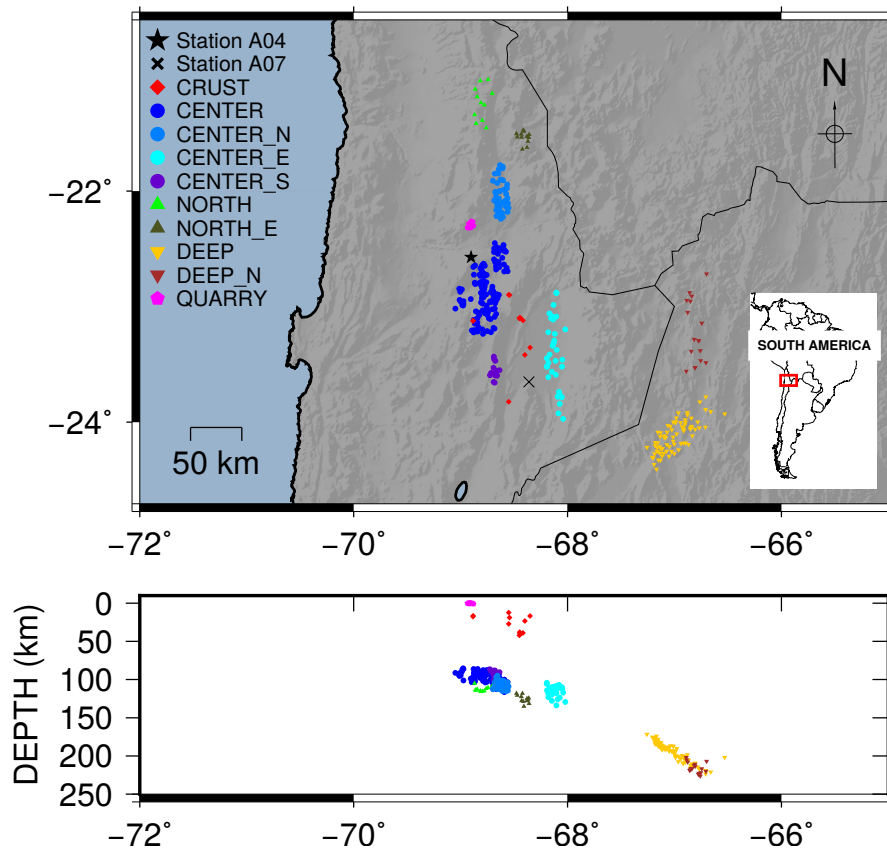


Figure 3.4: Map of seismic events and single stations A04 and A07 of the PISCO project (spring 1994). Each event sub-class is depicted in a different color. Event depths are generally increasing from west to east along the subducting Nazca plate with the exception of *QUARRY* explosions from a copper quarry and *CRUST* events.



# 4

---

## ALGORITHMIC BUILDING BLOCKS

---

This chapter examines available techniques of automatic seismic event detection and extensions thereof. Each of the techniques was reimplemented or newly developed in algorithmic form in Java and/or Python based on the available literature. This allows a direct unprecedented comparison. Based on algorithm objective, each one is applied to the appropriate datasets. The cross-correlation pattern matching for example is only helpful for repeating seismicity.

The first two sections of this chapter cover single station detectors based on waveform statistics and pattern recognition respectively. The following section treats coincidence analysis in seismic networks between single stations. Arrays and the analysis of coherence are the topic afterwards. Coincidence methods can be applied between single array elements as well but improved results can be obtained by utilizing the coherency of incoming waveforms. A conventional single trace or coincidence detector can then be applied to the output of the coherence analysis. The last section shows a possible combination of all approaches for a reliable real-time event detection scheme which is used for multiple projects.

Joswig (1987) divides automated processing in two distinct categories: “voting” where multiple independent decisions are combined in a second step (e.g. single station detection and coincidence analysis) and “integral” where information is combined before decision making (e.g. array coherence analysis). Another important classification of algorithms is the exclusive detection of seismic events by event detectors versus the actual phase picking where single phases must be as exact as possible.

Often event detection algorithms are the basis for later phase picking algorithms where the area around the maximum of the detection  $CF$  is analyzed further.

A luxury nowadays is the abundance of available processing power, fast access times and large band-widths to record and transfer data. As a rule, today real-time systems can operate on the full waveforms instead of pre-determined triggered events from single stations. This makes on-site trigger algorithms which can only use limited hardware resources unnecessary. Powerful servers can be used to process the continuous raw waveforms in real-time with advanced detection algorithms most of the time.

#### 4.1 SINGLE STATIONS

##### 4.1.1 *Single station event detection and phase picking*

###### *Detector theory*

Freiberger (1963) proposed the so called Neyman-Pearson filter and signal averaging to improve the  $SNR$  in an optimal way. Freiberger assumed Gaussian signals of length  $T$  and stationary noise with a Gaussian distribution. Many state-of-the-art detectors are still based on this scheme of comparison of power in a short term window versus a long term window. Preprocessing can include waveform filtering in frequency bands depending on the expected dominant frequencies of events.

Event detector results can be compared to ground truth information mostly from a manual event detection. Table 2 shows the confusion matrix of prediction outcomes from detectors. Based on these definitions, detection statistic metrics and corresponding plots can be used to compare the performance of different algorithms. Based on the used dataset and corresponding number of events, different plots will be used in this study. For the datasets  $DGMK$  and  $IFE_{14}$  where only very few events are available, the complete detections over time will be plotted. For the Basel dataset on the other hand, where the number of events

Table 2: Confusion matrix of prediction outcomes. True negatives are used only seldom in seismology due to comparatively low occurrence of seismic events.

		Predicted condition	
		Positive	Negative
True condition	Positive	True positive (TP)	False negative (FN)
	Negative	False positive (FP)	True negative (TN)

is very high, this study will use the precision recall (PR) curve as explained below. The PISCO dataset analysis is focused on clustering and classification instead of detection and confusion matrices with all event classes will be used. Another widely used detection benchmarking plot, the receiver operator curve (ROC), is usually not applicable in seismology because of the extremely few true positive detections in comparison to true negatives. ROC uses the false positive rate which is defined by  $\frac{FP}{FP+TN}$ , whereas true negative in seismology is the common state of background noise. The PR curve on the other hand shows precision  $\frac{TP}{TP+FP}$  over recall (also known as sensitivity)  $\frac{TP}{TP+FN}$  and is therefore more useful in a seismological context.

After simple power based detectors, Goforth & Herrin (1981) introduced the Walsh transform for detection purposes which is similar to the Fourier transform. Later Joswig (1987, 1990) introduced short-time Fourier transform (spectrograms) and a positive logic for event detection. Previous algorithms applied a negative logic where stationary background noise was regarded as the normal state. Each deviation from this state was seen as a possible detection. High false alarm rates are usually the norm with negative logic detectors as only the non-detection, the background noise is defined. The positive detection of Joswig is based on a spectral pattern recognition with template events, see section 4.1.2. Classification based on these sonograms is used in chapter 5.

Positive logic algorithms are often computationally expensive. If large amounts of data need to be reprocessed a combination of a very sensitive but fast detection algorithm based on negative

logic with a second stage positive logic algorithm can be used. The advantages of both algorithms can be combined by using the positive logic to reduce the large false positive number from the previous step.

Allen (1978) coined the name of the characteristic function (CF) which is a (non-linearly) filtered waveform used to generate the binary detector output.

#### *Short term average / long term average (STA/LTA)*

The short term average / long term average (STA/LTA) algorithm or adaptations thereof are the most widely used CFs in automatic seismic data processing. STA/LTA is calculated by the ratio of a short term over a long term window of (bandpass filtered) squared seismic amplitudes. See equation 1 for a recursive implementation where  $N_{STA}$  and  $N_{LTA}$  are the lengths of the short and long term window respectively and  $x$  is the seismogram. The recursive formula is only valid for  $t \geq N_{LTA}$  and is only an approximation of the arithmetic mean. It is however much faster than the exact formula.

$$\begin{aligned} STA(t) &= \frac{1}{N_{STA}} \cdot x^2 + \left(1 - \frac{1}{N_{STA}}\right) \cdot STA(t-1) \\ LTA(t) &= \frac{1}{N_{LTA}} \cdot x^2 + \left(1 - \frac{1}{N_{LTA}}\right) \cdot LTA(t-1) \end{aligned} \quad (1)$$

$$CF = \frac{STA}{LTA}$$

Multiple adaptations of the STA/LTA concept were developed over the years but the general concept remained similar. The advantage of the algorithm is its simplicity and generalization. It is applicable to all kinds of seismic datasets from local to teleseismic. Its only parameters are the two window lengths and optionally the corner frequencies of a bandpass which is applied to the seismic data a priori. Detectors can use multiple frequency bands and window lengths to adapt to different event types. Withers et al. (1998) showed that STA/LTA incorporat-

ing adaptive window lengths controlled by the non-stationary seismic spectral characteristics performs best.

To show the capabilities and problems with false positive detections with *STA/LTA*, Figure 4.1 and 4.2 show a comparison of *STA/LTA* detections for two surface stations of the *DGMK* network and one borehole station of the *WEG* network. Detections are declared when the value of the *CF* reaches a certain detection threshold. The Figures only show the maximum value in 60 second windows. The detection threshold is chosen individually for each station and time frame so that all events in the time frame are detected with the lowest possible number of false positives. Traces are filtered with a four pole Butterworth band-pass filter with corner frequencies of 5 and 40 Hz. *STA* window length is 0.5 s and *LTA* 10 s. The borehole station outperforms the *WIED* station which sits on top of the borehole station in both time frames due to advantageous noise conditions 200 m below the ground. The *LOEV* central station at a more quiet surface location outperforms the borehole station in the first time frame where events additionally come from the south-west closer to the *LOEV* station (14 instead of 22 km). In the second time frame with events from multiple directions, no station can detect all events with the chosen minimum threshold of 5 for the *STA/LTA* algorithm. Both surface stations have considerably more false positive detections than the borehole station. Section 4.3 shows how the usage of surface arrays can outperform borehole stations.

#### *Allen and Baer-Kradolfer phase pickers*

Phase-pickers are optimized for most accurate onset time determination but mostly do not handle wrong phase associations or noise peaks. Early implementations of phase-pickers use a combination of the seismic signal and its time derivative (Allen, 1978; Baer & Kradolfer, 1987). The time derivative is more sensitive to high frequency changes. Additional widely applied algorithms use the fit of auto regressive modeling of the noise and the seismic signal to calculate a *CF*. Akaike information criterion (*AIC*) is then used to refine actual phase onset time



Figure 4.1: Comparison of *STA/LTA* detections between two stations of the *DGMK* network (LOEV and WIED) and a borehole station from the *WEG* network (IO<sub>3</sub>CB). In the given time frame of two months, the surface station LOEV outperforms the borehole station which in turn outperforms the station WIED. The epicentral distance of the events to LOEV is 14 km while to WIED/IO<sub>3</sub>CB it is 22 km. The borehole station is 200 m directly below the WIED central station. Circles mark maximum *STA/LTA* detection in a 60 s window. Vertical lines in cyan mark times of five confirmed events (two events only five minutes apart on October 20). A dotted line is used if the event is local but was only found by cross-correlation. Dashed lines mark regional events which are not the main scope of the recording network. The line is solid if the event is local and strong enough to be generally detectable. Detections are true positives at all cyan markers but only false negatives for a non-detection at a solid cyan marker. The red horizontal line marks the minimum detection threshold for the solid markers. Detection circles are painted in light gray for true negatives (under the threshold line), dark gray for false positives (above the threshold line) and red for true positives.

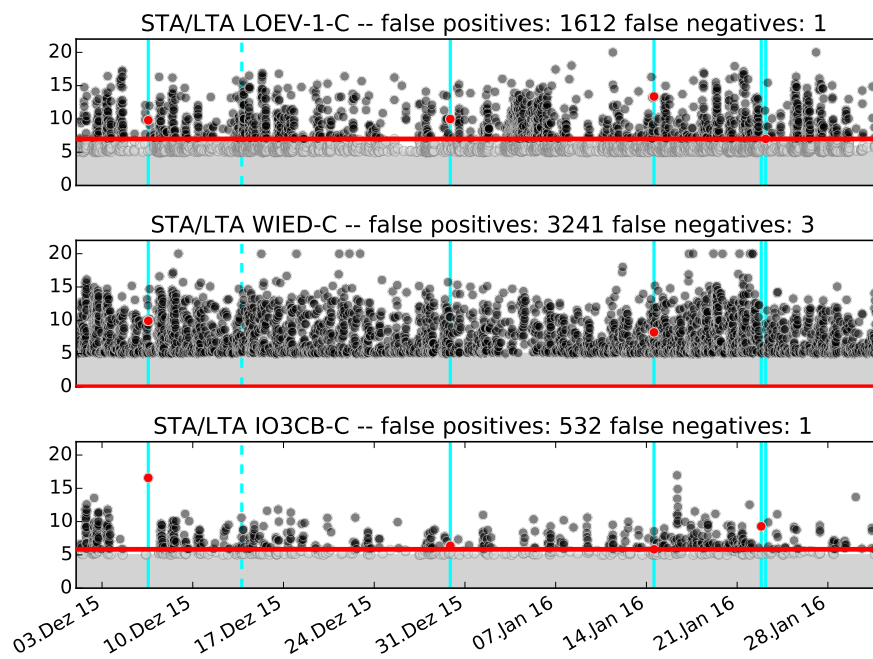


Figure 4.2: Comparison of [STA/LTA](#) detections between two stations of the [DGMK](#) network (LOEV and WIED) and a borehole station from the WEG network (IO<sub>3</sub>CB), similar to [Figure 4.1](#) but for a different time frame. In this time frame the borehole station outperforms both surface stations considerably.

(Sleeman & van Eck, 1999; Leonard, 2000), see also section 4.1.1. Neural networks for phase picking were studied by Gentili & Michelini (2006) but are used in this study only for classification of events (chapter 5).

The study of individual phase pickers is kept short here because as will be shown in section 6, phase picking for low SNR local events does not yield satisfying results. Most phase picking algorithms try to optimize the exact onset time while the problem with the studied events is to detect the right onset at all among the multiple noise peaks. Even manual phase picking can often not define the exact sample accurate phase onset time.

Equation 2 shows the CF calculation for the Allen-picker (Allen, 1978, 1982) where  $E(t)$  is the envelope function,  $x$  is the seismic trace and  $x'$  its time derivative.  $K$  is a weighting constant. This picker is used for example in the software Earthworm (Johnson et al., 1995).

$$E(t) = x(t)^2 + K \cdot x'(t)^2 \quad (2)$$

The Baer-Kradolfer picker (Baer & Kradolfer, 1987) is another widely used phase picking routine. It is a modification of Allens' envelope function. The software PITSA (Scherbaum & Johnson, 1992) as well as the picking routine Manneken-Pixs (Aldersons, 2004) are based on the Baer-Kradolfer picker. Manneken-Pixs uses a Wiener filter and a statistical estimate of uncertainty from a weighting engine to improve results. The threshold to set a pick can be set dynamically by a combination of the mean and standard deviation of the CF.

A more recent adaptation of the Allen and Baer-Kradolfer pickers is the FilterPicker Lomax et al. (2012). It is tuned for real-time and early warning applications and includes a realistic time uncertainty of picks. FilterPicker is used in chapter 6 with an example of a low SNR event to show the general problems of phase pickers with these events.

### *Higher order statistics and auto-regressive models*

Apart from the power detection approaches discussed before, higher order statistics (HOS) and auto-regressive (AR) models are additional statistical approaches which operate directly on the filtered waveform data.

From higher order statistics, the skewness and kurtosis (scaled third and fourth moment) which detect deviations from the normal (Gaussian) distribution were established in multiple studies [Saragiotis et al. \(2002\)](#); [Küperkoch \(2010\)](#). Skewness measures the asymmetry of a distribution and kurtosis measures how strong its peak is in relation to its tails. Skewness  $S$  and kurtosis  $K$  are defined in equation 3 with  $E$  being the expectation and  $X$  the distribution. The idea behind using these statistics is that the distribution of amplitudes changes considerably at the phase onset of a seismic event.

$$\begin{aligned} S &= \frac{E[X - E[X]]^3}{E[X - E[X]]^{\frac{3}{2}}} \\ K &= \frac{E[X - E[X]]^4}{E[X - E[X]]^{\frac{4}{2}}} \end{aligned} \quad (3)$$

The next approach is based on the theory that a seismic signal  $x$  can be seen as a stochastic process where each sample is a linear combination of its  $n$  predecessors. This allows to model the time series with an autoregressive process with order  $n$ . See equation 4 with  $a$  as process coefficients and  $\epsilon$  as Gaussian white noise. One crucial parameter is the order  $n$  and various methods exist to estimate the optimal length. First work was done by [Morita & Hamaguchi \(1984\)](#).

$$x(t) = \sum_{m=1}^M a_m x(t-m) + \epsilon(t) \quad (4)$$

The AR models are often used for the determination of an accurate pick time after an initial detection of a phase onset ([Sleeman & van Eck, 1999](#); [Leonard et al., 1999](#)). The idea behind using AR models is again that a time window with a signal has

different statistical properties than a window with noise. The onset time of a phase is the time which separates the model of noise and signal from the model of only noise. Similarly this can be done with multiple models for noise and events. All model fits are compared continuously and a detection can be declared if the best fitting model belongs to an event. This technique can be already seen as a pattern recognition which is shown in section 4.1.2. It is included in this section nevertheless because the comparison is done on general models of events instead of specific events. A simplified approach is to only model the noise and detect points in time where the model does not fit well anymore because signal energy is present. If only stationary noise is recorded, the model will fit the seismic time series well. Upon arrival of an seismic event, the model fit will decrease rapidly as for example frequency content and variance of the signal change. Measuring the misfit of the model results in a CF which can be used for detection purposes.

Takanami & Kitagawa (1988) were the first to combine AR models with the AIC Akaike (1971, 1974) to further refine the onset time. Küperkoch (2010) applied the AIC on higher-order statistics with the formula from equation 5 with L as the length of the CF).

$$AIC(k) = (k-1) \log\left(\frac{1}{k} \sum_{j=1}^k CF_j^2\right) + (L-k+1) \log\left(\frac{1}{L-k+1} \sum_{j=k}^L CF_j^2\right) \quad (5)$$

#### *Comparison of single station characteristic functions*

Figures 4.3,4.4 and 4.5 show comparisons of the discussed single station detection and phase picking algorithms for three events of the Basel dataset with different SNRs. Similar to before, the waveforms are filtered with a four pole Butterworth bandpass filter with corner frequencies of 5 and 40 Hz. STA window length is 0.1 s and LTA 2 s. The Kurtosis, Skewness and AR CFs

are calculated on 0.625 s long windows with a time step size of 0.05 s. The high SNR event in Figure 4.3 can be best detected by the AR CF. However all other CFs show also clear peaks at the P-onset. The event from Figure 4.4 can be best detected from the STA/LTA, Kurtosis and Skewness CFs. The AR CF shows only a peak at the S-onset. The STA/LTA CF is the only method which shows peaks at the P- and S-onset. The low SNR event from Figure 4.5 can be best detected by the STA/LTA CF. Only the STA/LTA and AR CF show peaks at the S-onset. In the studied datasets, no significant improvement over the ordinary STA/LTA could be found by using more sophisticated methods. Algorithm parameters strongly influence the results and each algorithm can be tuned optimally to detect events in a reference dataset. During this study it turned out that empirically STA/LTA provides the most robust results using the same parameters on multiple datasets. Due to the fact that at the beginning of a monitoring campaign often only little information is available about existing seismicity, STA/LTA is chosen for further tests as the reference detector in this thesis. Cesca & Grigoli (2015) also find that STA/LTA is advantageous over Kurtosis for source scanning location as discussed in chapter 6.

### *Three-component analysis*

Many single stations in local seismological monitoring networks are in fact three-component sensors which record ground motion in three orthogonal directions. If sensors are deployed on the surface those directions are usually vertical, north-south and east-west. Borehole seismometers on the other hand can not be aligned to the north reliably. Multiple studies exist however to obtain the offset from true north for these sensors by analysing strong earthquakes with known locations (Grigoli et al., 2012). If the offset is known, a coordinate transformation can be applied to get the typical three directions.

The three component recording allows to use integral methods for detection of events. Most common are the rotation of seismograms into vertical, radial and transverse components for visual inspection and (automatic) phase picking. Another

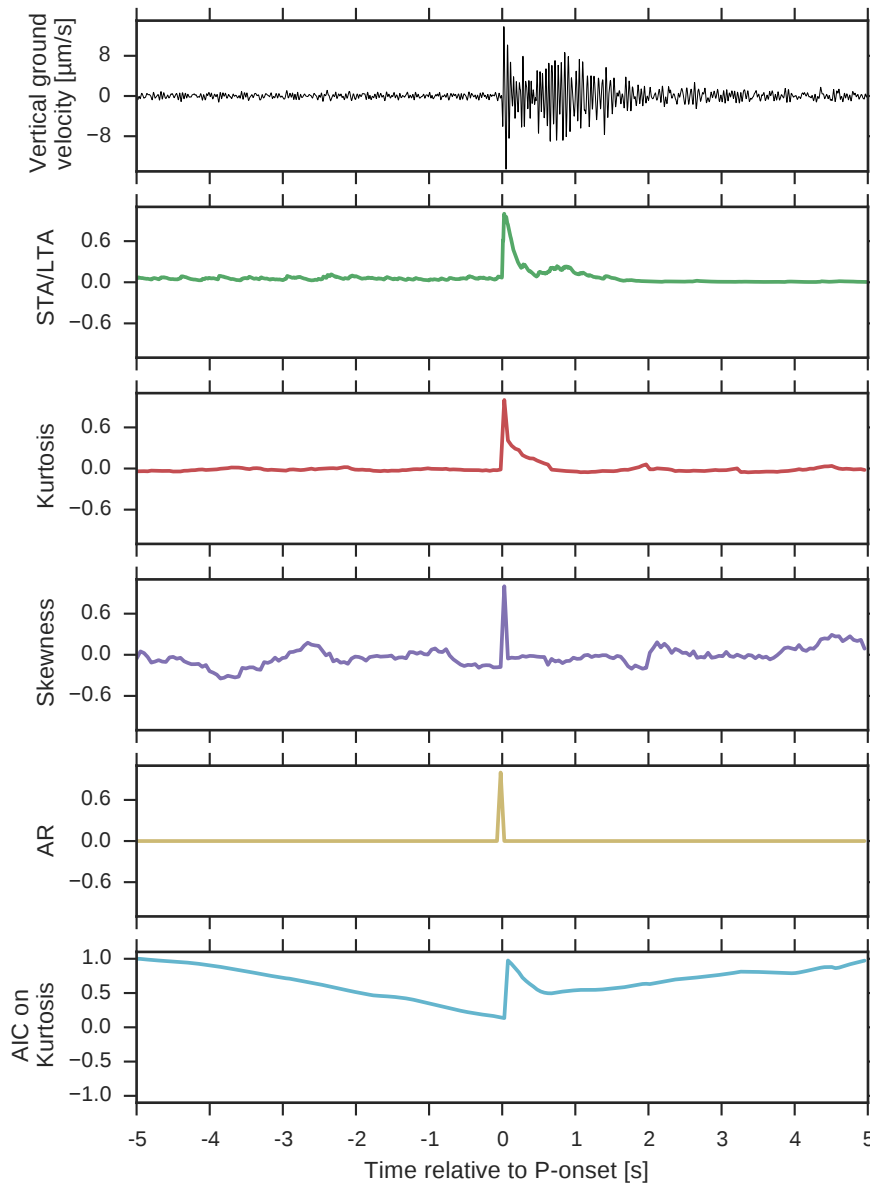


Figure 4.3: Comparison of characteristic functions for Basel event from 2006/12/06 14:52:27 UTC ( $M_L = 1.0$ ). The seismogram is bandpass filtered between 5 and 40 Hz. All characteristic functions show a clear peak at the P-onset of the high SNR event. Theoretical onset times for this station can be calculated from the known event location. AR=auto-regressive model, AIC=Akaike information criterion.

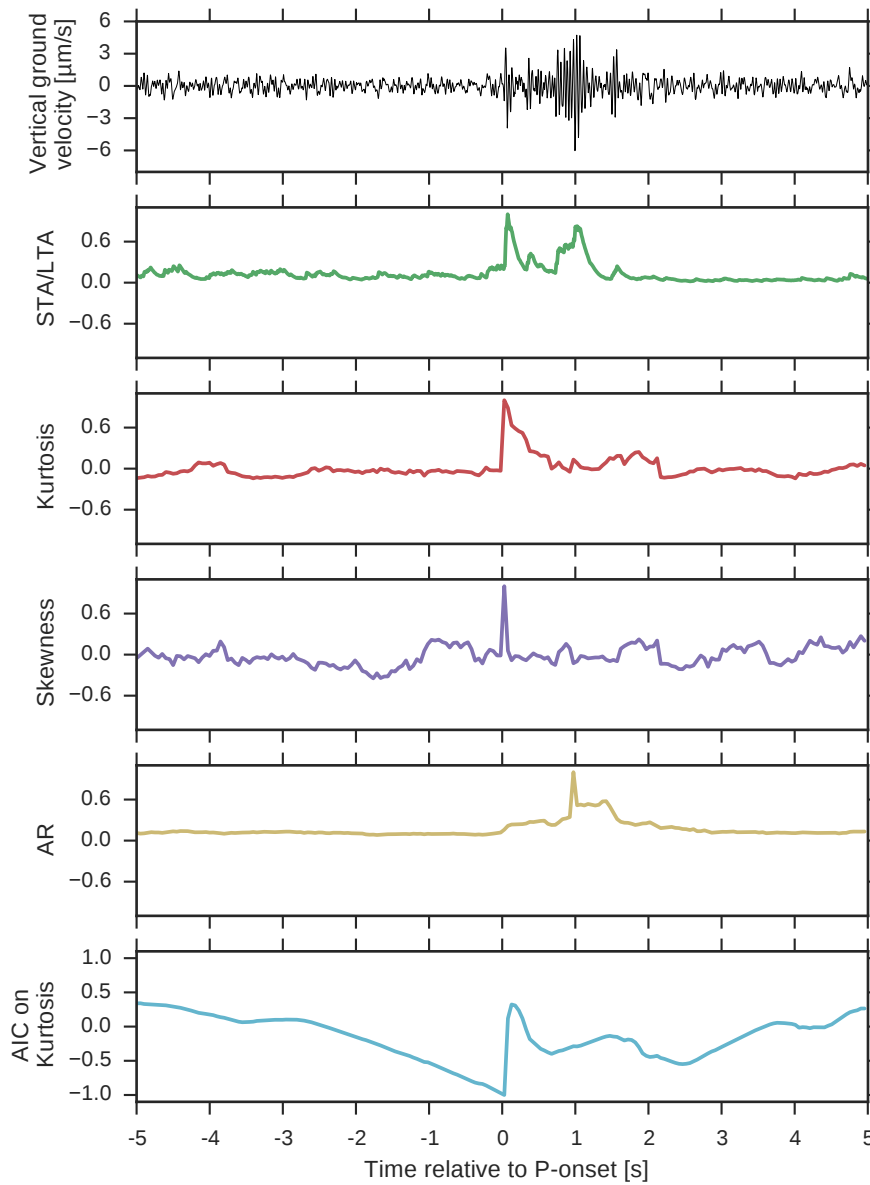


Figure 4.4: Comparison of characteristic functions for Basel event from 2006/12/06 14:55:47 UTC ( $M_L = 0.6$ ). The seismogram is bandpass filtered between 5 and 40 Hz. All but the AR model show a peak at the P-onset of the weaker event. Theoretical onset times for this station can be calculated from the known event location. AR=auto-regressive model, AIC=Akaike information criterion.

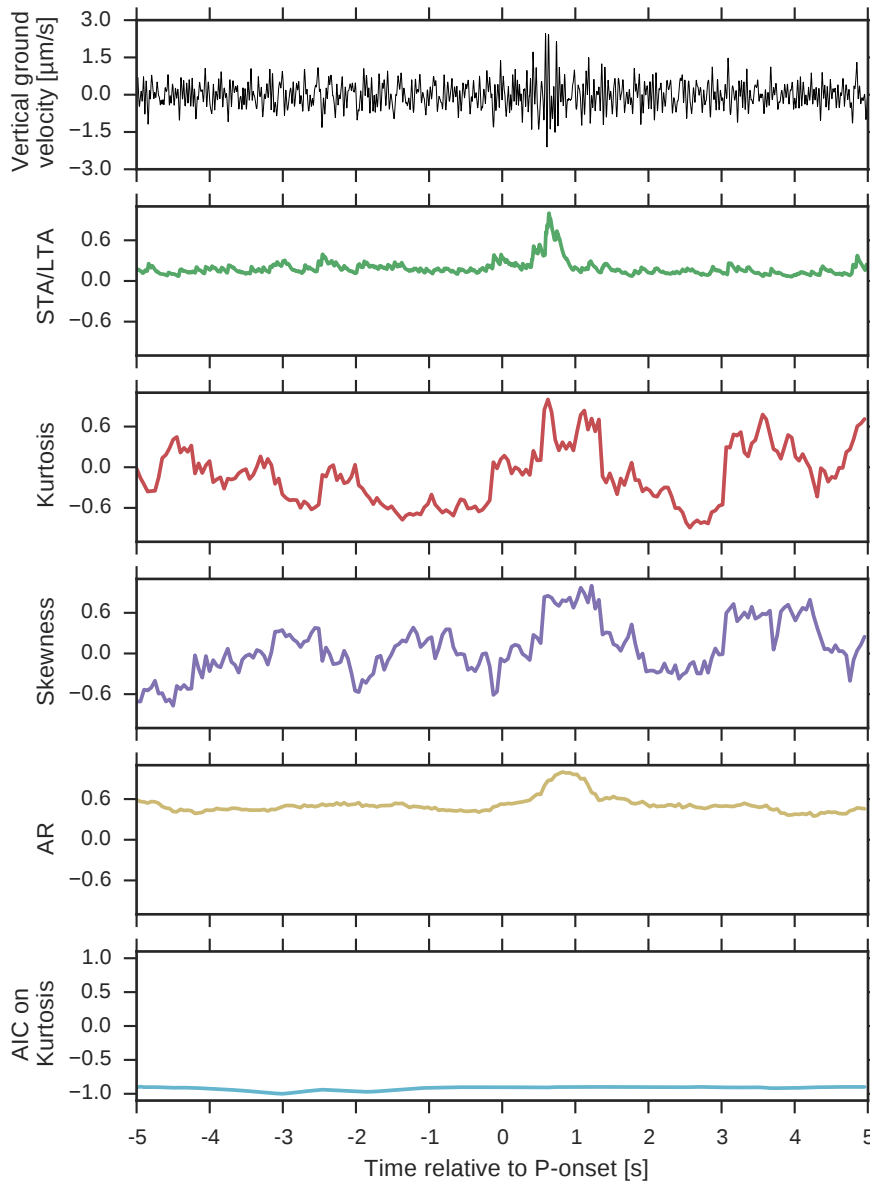


Figure 4.5: Comparison of characteristic functions for Basel event from 2006/12/06 14:52:00 UTC ( $M_L = 0.2$ ). The seismogram is bandpass filtered between 5 and 40 Hz. No characteristic function shows a peak at the P-onset of the low SNR event. STA/LTA and AR model show small peaks at the S-onset. Theoretical onset times for this station can be calculated from the known event location. AR=auto-regressive model, AIC=Akaike information criterion.

technique is the calculation of the eigenvalues and eigenvectors of the covariance matrix over a moving time window (Vidale, 1986; Jurkevics, 1988). This method allows to get a first estimate of incidence angle and back azimuth of incoming signals. Equation 6 shows the calculation of the 3x3 covariance matrix  $S$  with  $X$  being a matrix containing one seismic trace in each row with  $N$  samples.

$$S_{jk} = \frac{XX^T}{N} = \frac{1}{N} \sum_{i=1}^N x_{ij}x_{ik} \quad (6)$$

The resulting covariance matrix  $S$  describes the polarization ellipsoid which fits the three component data best with a least-squares metric. Solving the eigenvalue problem of  $S$  results in the principal axes (eigenvectors) and their lengths (eigenvalues,  $\lambda$ ) of this ellipsoid. After ordering the eigenvalues by size, the rectilinearity ( $1 - \frac{\lambda_2 + \lambda_3}{2\lambda_1}$ ) and planarity ( $1 - \frac{2\lambda_3}{\lambda_1 + \lambda_2}$ ) can be calculated. Rectilinearity reaches 1 for pure body waves and planarity reaches 1 for pure Rayleigh waves.

The back azimuth angle of an incoming P-wave can be determined by the horizontal orientation of the largest eigenvalue corresponding to the rectilinear motion.

Empirical tests in this study with local events however showed that these methods are not reliable in such cases. The overlap of phases at short distances and the heterogeneity of the underground prohibits clear polarization patterns. Figure 4.6 shows that even with a high SNR event from the Basel monitoring, the rectilinearity and planarity do not show significant peaks at phase onsets. The Figure also shows the CF of an S-phase picker by Cichowicz. It calculates three parameters: deflection angle, degree of polarization and the ratio between transverse energy and total energy (Cichowicz, 1993). The CF consists of the product of these three parameters. However as shown in the Figure, a conventional simple STA/LTA on the horizontal components is superior to the S-phase picker of Cichowicz in this case. Traces are unfiltered and STA/LTA as before are 0.1 and 2 s. Rectilinearity, planarity and the Cichowicz statistic are

calculated on Hamming windowed data with a window length of 0.64 s and with a time step size of 0.05 s.

Chapter 5 section 5.4.4 provides a comparison of three-component back azimuth estimation to pattern recognition for regional clustering of events. It shows that the pattern recognition approach is superior.

#### 4.1.2 *Single station event classification by pattern recognition*

The previous algorithms described systems which detect any signal deviating from stationary noise. This has the advantage that previously unknown events, if their power exceeds the stationary noise power considerably or if the statistical properties change, can be detected reliably. However if weak events with low SNRs and only few recording stations need to be detected, the number of false positive detections rises dramatically with these algorithms because thresholds need to be set extremely low. If we can assume that events possess some kind of similarity between each other, the approach of pattern recognition with templates from previously detected events can yield significant improvements.

An eased form of pattern recognition would be the creation of statistical models based on previously detected events. Detections are based on comparisons of data between noise and event model. Established methods contain the AR models discussed in section 4.1.1 or Hidden Markov Models (Ohrnberger, 2001; Beyreuther et al., 2012; Hammer et al., 2012b). This work however discusses “direct” pattern recognition where detections are made by comparison of continuous data to templates of previously detected events. A step in the direction of the statistical model generation is done in chapter 5 where the unsupervised methods include a prototype generation from multiple templates which are then used for classification. Each prototype can be seen as a model for a certain signal type.

An obvious limitation of the pattern recognition approach is the restriction to find only a priori known or similar events. This limitation is especially strong in the cross-correlation approach

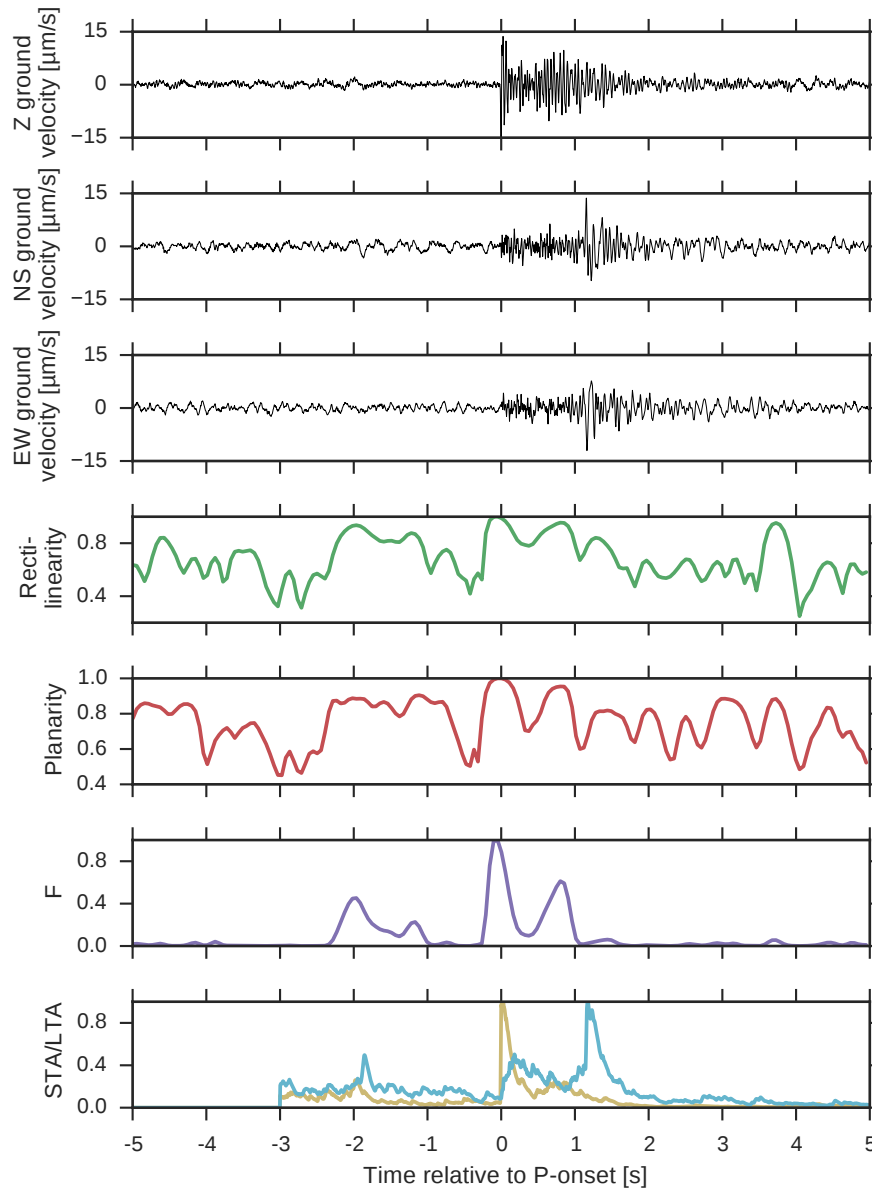


Figure 4.6: Three-component polarization analysis for event from Figure 4.3. The polarization analysis is often cited as particularly useful for S-phase picking. However rectilinearity and planarity do not show clear peaks for local events with low SNR. The F statistic after Cichowicz (1993) shows clear peaks at the P- and S-onset but in comparison to the STA/LTA function (brown on vertical component, blue on horizontal component) it is still inferior.

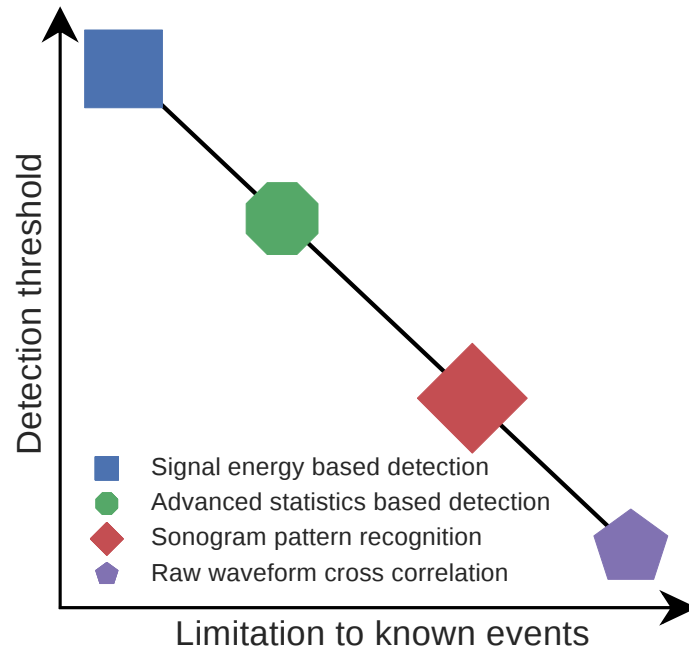


Figure 4.7: Trade-off between detection threshold and restriction to known events. Lower detection thresholds can be acquired by the limitation on previously recorded events.

(section 4.1.2) but less so in the sonogram detection (section 4.1.2) as shown later. On the other hand pattern recognition can provide much lower detection thresholds in comparison to power based approaches. Another advantage is the classification and relative location based on the template event. Figure 4.7 shows a simple illustration of the trade-off between detection threshold and restriction to known events.

#### *Raw waveform cross-correlation*

Signal detection by cross-correlation, also known as matched filter, dates back to the beginnings of signal processing, see e.g. [van Trees \(1968\)](#). First applications to detect a synthetic signal in noise were done by [Anstey \(1964\)](#). It operates on the raw waveforms which might be filtered to increase SNR and is the most reliable way to detect a recurring signal in a time series. In seismology however this means that to detect an event by cross-correlation it has to occur very close to the template hypocenter

and the source mechanism has to be similar as well. Furthermore it needs to be recorded at the same location preferably by the same sensor. Waveform similarity is theoretically existent up to a quarter of the wavelength in hypocenter distance between template and event (Geller & Mueller, 1980). Increased inter-event separation introduces different earth structure of seismic travel paths. Furthermore time differences between successive phases in the seismogram will be changed (e.g. tS-tP travel time). Schulte-Theis & Joswig (1990) tried to overcome this issue by using dynamic waveform matching (DWM). DWM is a non-linear correlation which allows stretching and shortening of the waveform, similar to the dynamic time warp algorithm.

Equation 7 shows how the normalized cross-correlation ( $r$ , Pearson's cross-correlation Pearson 1895) is calculated between a template signal  $x$  and current time frame signal  $y$ . Both continuous data frames have the length  $N$ .  $\bar{x}$  and  $\bar{y}$  denote the mean. The value of  $r$  can vary between  $-1$  and  $1$ , the former indicating a polarity flipped signal and the latter indicating an identical signal.

$$r = \frac{\sum_{i=1}^N (x_i - \bar{x})(y_i - \bar{y})}{\sqrt{\sum_{i=1}^N (x_i - \bar{x})^2 \sum_{i=1}^N (y_i - \bar{y})^2}} \quad (7)$$

The vast accumulation of digital archives of not only triggered seismic recordings but also continuous recordings in combination with improved hard disk and processor speeds has allowed the reprocessing of this data by cross-correlation with large template databases in the last decade on a world-wide scale. This led to the detection of thousands of new events in existing datasets. Recent advances in distributed processing by frameworks as for example Apache Hadoop<sup>1</sup> allow further improvements in processing speed to calculate statistics of seismic data (Magana-Zook et al., 2016).

Due to its properties of finding very similar events, cross-correlation is especially useful for seismic aftershock and cluster analysis. A problem for aftershock detection can be the large

<sup>1</sup> <http://hadoop.apache.org/>

differences in magnitude between the original event and its aftershock and therefore large discrepancies between event waveforms. [Schaff & Waldhauser \(2010\)](#) however found a correlation of 0.5 for an event with a magnitude difference of 2.3 to its template.

A comparison of actual correlation values is however difficult as it is highly dependent on correlation length and applied filters. In general, shorter correlation lengths and narrow filter bands at low frequencies can lead to higher correlation values. This study mostly uses correlation lengths of 10 s and filter bands of either 4 – 50, 4 – 30 or 10 – 30 Hz. Correlation templates are always starting at the P-onset of the template event.

For [CTBT](#) purposes, correlation allows to lower the detection threshold for known nuclear test sites significantly. See [Figure 4.8](#) for a comparison of the four supposed underground nuclear explosions at the Punggye-ri Test Site in North Korea. The seismograms are from a nearby station in China (MDJ) and show extremely strong similarities. A disputed study by [Zhang & Wen \(2015b\)](#) claimed to have found another nuclear test on 12 May 2010 by combining cross-correlation with the source scanning method (see also [chapter 6](#)). An objective discussion of their results is provided in [Ford & Walter \(2015\)](#).

The application of cross-correlation in the monitoring of local seismicity of the [DGMK](#) network is shown with the help of a small cluster of events near the German city of Walsrode. Events were clustered both in time (October - November 2014) and in space (apart from one outlier on November 2). [Figure 4.9](#) shows how a template event from this cluster is compared over time to a continuous recording. The traces are filtered with a four pole Butterworth bandpass filter with corner frequencies of 10 and 30 Hz. The window length for the cross-correlation is 10 s and the time step size is one sample (0.002 s). The continuous daily cross-correlation at the [DGMK](#) network found multiple new extremely low-SNR events which could not be detected by manual analysis. A comparison of cross-correlation to other techniques is done in the following sections.

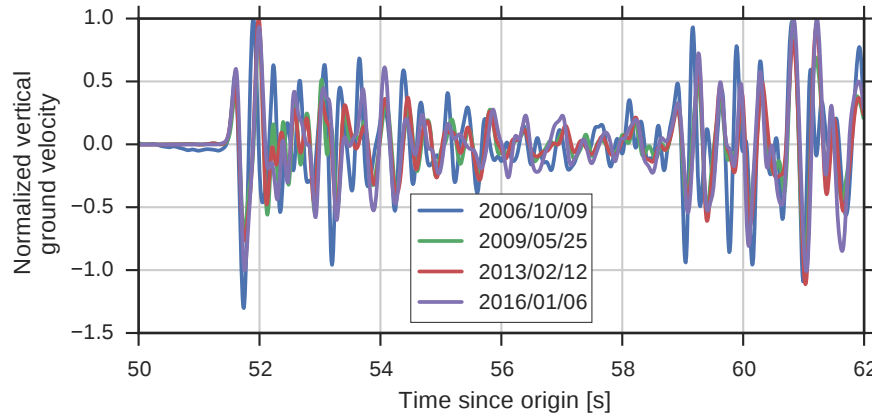


Figure 4.8: The comparison of the North Korean nuclear tests with seismograms from GSN station IC.MDJ.oo.BHZ, 371 km from the epicenter shows a strong similarity. This is a strong indication that all events took place in the same region and had a similar source process. Here, cross-correlation can be used reliably to detect consecutive events.

#### *Adaptive spectrogram pattern recognition*

To decrease the dependence on the waveform similarity while still preventing large numbers of false positive detections, pattern recognition on spectrograms can be used. Spectrograms show the average signal power binned in time and frequency and similar event classes show similar two-dimensional patterns. Spectrograms reduce the information of seismograms and thereby allow a more general comparison between events. The phase information is lost and only dominant frequencies and amplitudes are preserved.

#### SONODET

Joswig (1990, 1995) introduced the sonogram for pattern recognition. The sonogram uses half-octave frequency binning and an adaptive noise removal. Further details and examples for the sonogram calculation can also be found in the attached publications (Sick et al., 2012, 2013).

Sonograms consist of the power spectral density ( $A(\omega, t)$  with frequency  $\omega$  and time  $t$ ) computed by short-term-Fourier-transformation (STFT) with 256 samples which are tapered

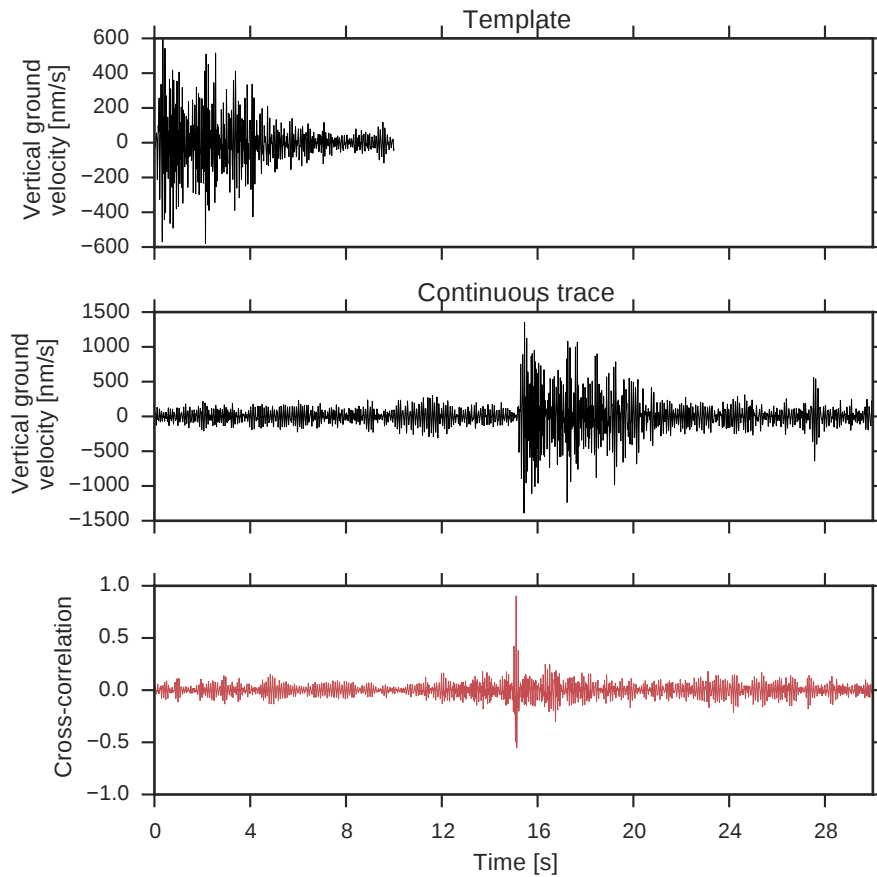


Figure 4.9: Raw waveform cross-correlation example at station LOEV of DGMK network. The waveform of a template event (top) is normalized, bandpass filtered and cropped so that it starts with the P-onset. It is then cross-correlated over time with equally normalized and filtered sections of the continuous seismogram of the same station (middle). The resulting cross-correlation function ranging from  $-1$  to  $1$  can be seen at the bottom with a clear peak at the P-onset of the event (due to the fact that the template starts at the P-onset as well).

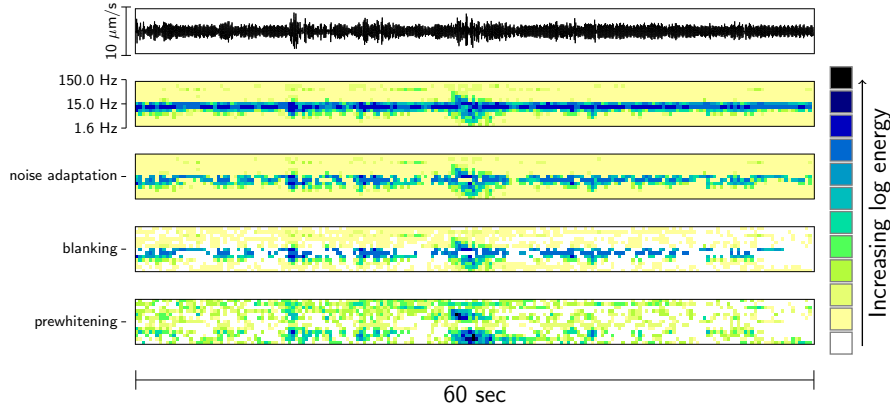


Figure 4.10: Processing steps of sonogram calculation for a local earthquake in a noisy environment, from top to bottom: seismogram, power spectral density spectrogram with logarithmic amplitudes and half-octave frequency bands, noise adaptation, blanking and pre-whitening ( $M_L$  1.0, distance 7.7 km)

with a  $\sin^2$  windowing function and a segment overlap of approximately 50%. Frequencies are filtered in 13 half-octave wide passbands and amplitudes are scaled logarithmically. Furthermore noise adaptation, muting and prewhitening is performed. The noise adaptation is outlier-resistant as it uses the more robust median  $M(\omega) = M_{50}$  instead of the mean and  $S(\omega) = M_{75} - M_{50}$  instead of the variance.  $M(\omega)$  and  $S(\omega)$  are both calculated for each frequency band of the power spectral density, allowing an individual adaptation (see Equation 8 and Figure 4.10). Both are calculated as the minimum from a stride with 20 pixel long time windows and a stride length of 5 pixels. For the visual representation, a special color palette that facilitates visual detection of seismic event candidates is used (see Figure 4.10 on the right).

$$\text{SONO}(\omega, t) = \begin{cases} \log_2 \left( \frac{A(\omega, t) - 2^{M(\omega)}}{2^{M(\omega) + S(\omega)} - 2^{M(\omega)}} \right), & A(\omega, t) > 2^{M(\omega) + S(\omega)} \\ 0, & \text{else} \end{cases} \quad (8)$$

The SonoDet algorithm (Joswig, 1995) compares a reference sonogram template to a continuously calculated sonogram from

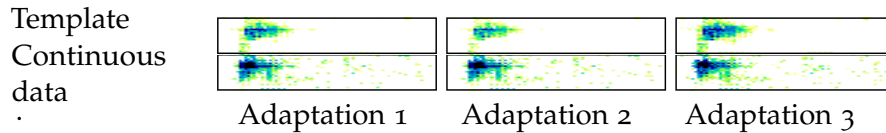


Figure 4.11: Sonogram detection (SonoDet) amplitude adaptation steps. The noise level of the template event (top) is adapted at each time step and compared to the continuous data. Comparison is calculated by a two-dimensional cross-correlation of the energy in each spectrogram pixel. This allows for example the detection of weak aftershocks from stronger event templates. The comparison on spectrograms instead of the raw waveforms furthermore eases the strong similarity constraints from waveform cross-correlation. This allows to also detect events from a broader range.

a data stream with a two-dimensional cross-correlation. At each time step values are adapted to account for different SNRs between template and data stream, see Figure 4.11. The SonoDet algorithm was re-implemented in Java during this thesis. The pattern adaptation contains multiple steps, a detailed explanation of each step would be too long to be included here and can be found in Joswig (1995).

Figure 4.12 shows seismograms and sonograms of the Walrode cluster mentioned in section 4.1.2. The hypocenter outlier is shown in the second row from the bottom (2014/11/02). It occurred at a depth of around 27 km in comparison to a depth of less than 5 km for the rest of the events. Furthermore the epicenter of the event was around 5 km to the south of the main cluster. Figure 4.13 shows that the outlier event from 2014/11/02 compared to the event from 2014/10/16 has pronounced differences. The comparison between the same event from 2014/10/16 and the event from 2014/11/15 shows on the other hand how similar events can be also in the seismograms. The same comparison with sonograms contains many similarities for all three events (Figure 4.14). This allows a pattern recognition detection of the outlier event by SonoDet. On the other hand, the weak events in row three and five can only be detected by cross-correlation. Visually they can not be seen in the seismograms. The sono-

grams allow to identify the event from the third row visually, the event from the fifth row is only barely visible. Similarity matrices between all events by cross-correlation and SonoDet can be seen in Figure 4.15 and 4.16 respectively. Both Figures confirm the already visually obtained results.

Figure 4.17 shows a comparison of SonoDet to STA/LTA for the IFE14 campaign to detect the three explosions at a single station (training scenario events). STA/LTA can only find the explosions in a 38 hour window with 84 false positive detections. Using the first explosion as a template, both succeeding explosions could be found by SonoDet with only 4 false positive detections. Note that each of the three explosions took place at a different location which is also the reason why cross-correlation did not yield any usable results here. It is also investigated if it is possible to do a pattern recognition with patterns from different campaigns for the SonoDet detection. For this purpose, patterns from the CTBTO Advanced Course 2nd Training Cycle (AC2TC) campaign were used successfully. The AC2TC campaign took place in Hungary (instead of Jordan for the IFE14 campaign) and included several near-surface training explosions. Nevertheless with the different campaign patterns, only 13 false positive detections were necessary to detect all three explosions by SonoDet.

To get more reliably statistics, the Basel monitoring campaign with thousands of events can be used to compare different single station algorithms. Figure 4.18 shows a comparison of STA/LTA, cross-correlation and SonoDet of a five hour time frame in a precision recall plot. For recalls below 0.7, cross-correlation and SonoDet perform similarly. Both outperform STA/LTA for recalls below 0.82. For higher recalls, the precision for SonoDet and STA/LTA drop rapidly while the cross-correlation precision only decreases slowly. This shows that the cross-correlation does not even yield small similarities for non-events.

#### ALTERNATIVE TIME-FREQUENCY REPRESENTATIONS

One weakness of spectrograms is the fixed time window used for the power spectrum calculation for all frequencies (sono-

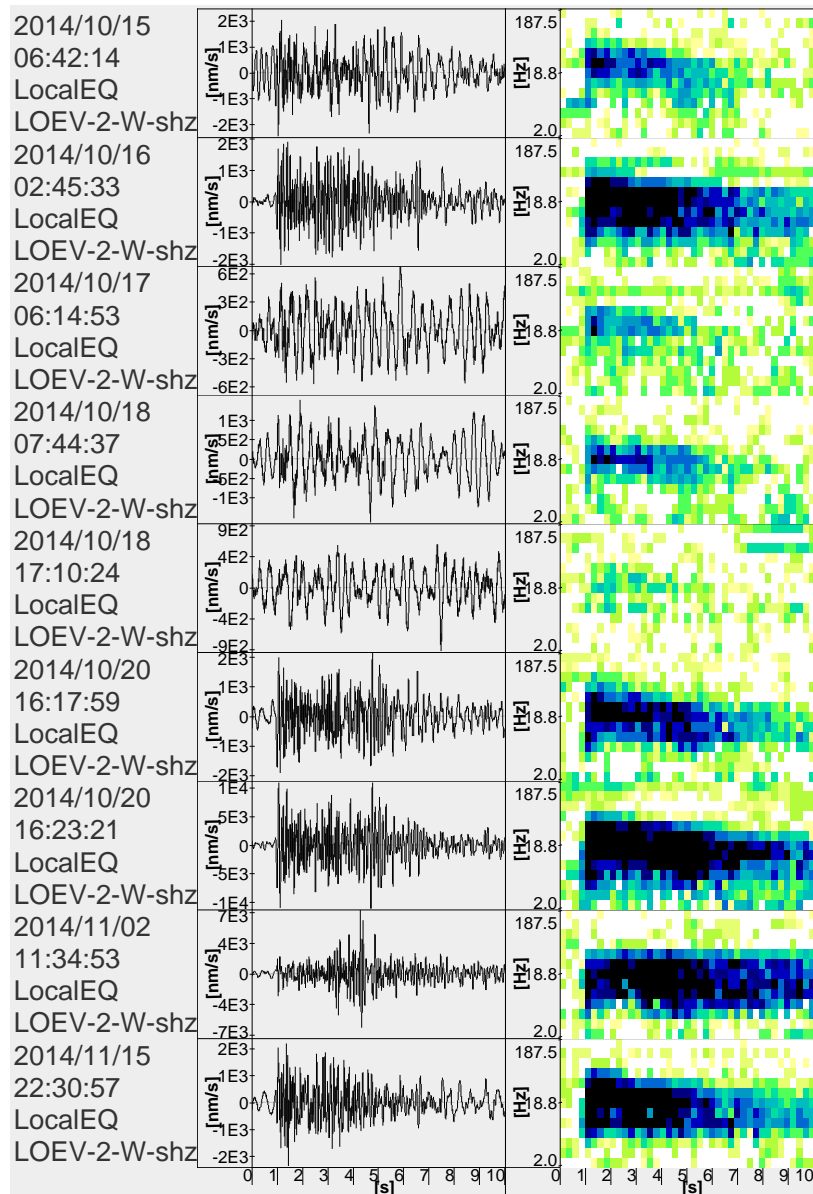


Figure 4.12: Walsrode cluster event overview. The cluster consists of 9 events clustered in time with local magnitudes between 0.3 and 1.7. All events apart from the one from 02/11/14 are also clustered closely in space. The epicenter of the outlier event is around 5 km to the south of the main cluster and its depth is around 27 km while the other events are shallower than 5 km. Sonogram similarity can be seen on the stronger events including the outlier while the cross-correlation was able to detect the two weak events in row 3 and 5.

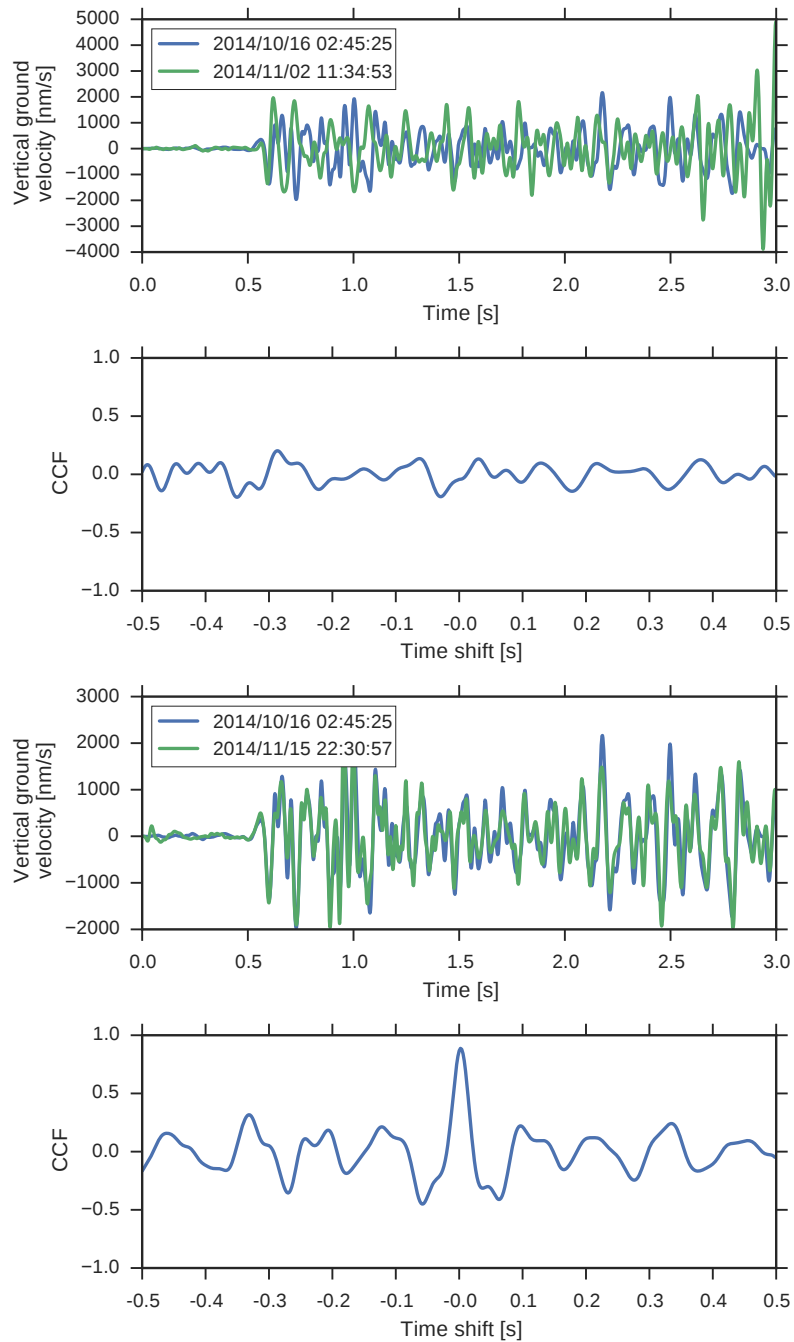


Figure 4.13: Cross-correlation example of Walsrode events. Two events are compared to the event from 2014/10/16. The outlier event from 2014/11/02 shows no significant correlation while the event from 2014/11/15 has a high correlation peak at the time of zero time shift between P-onsets.

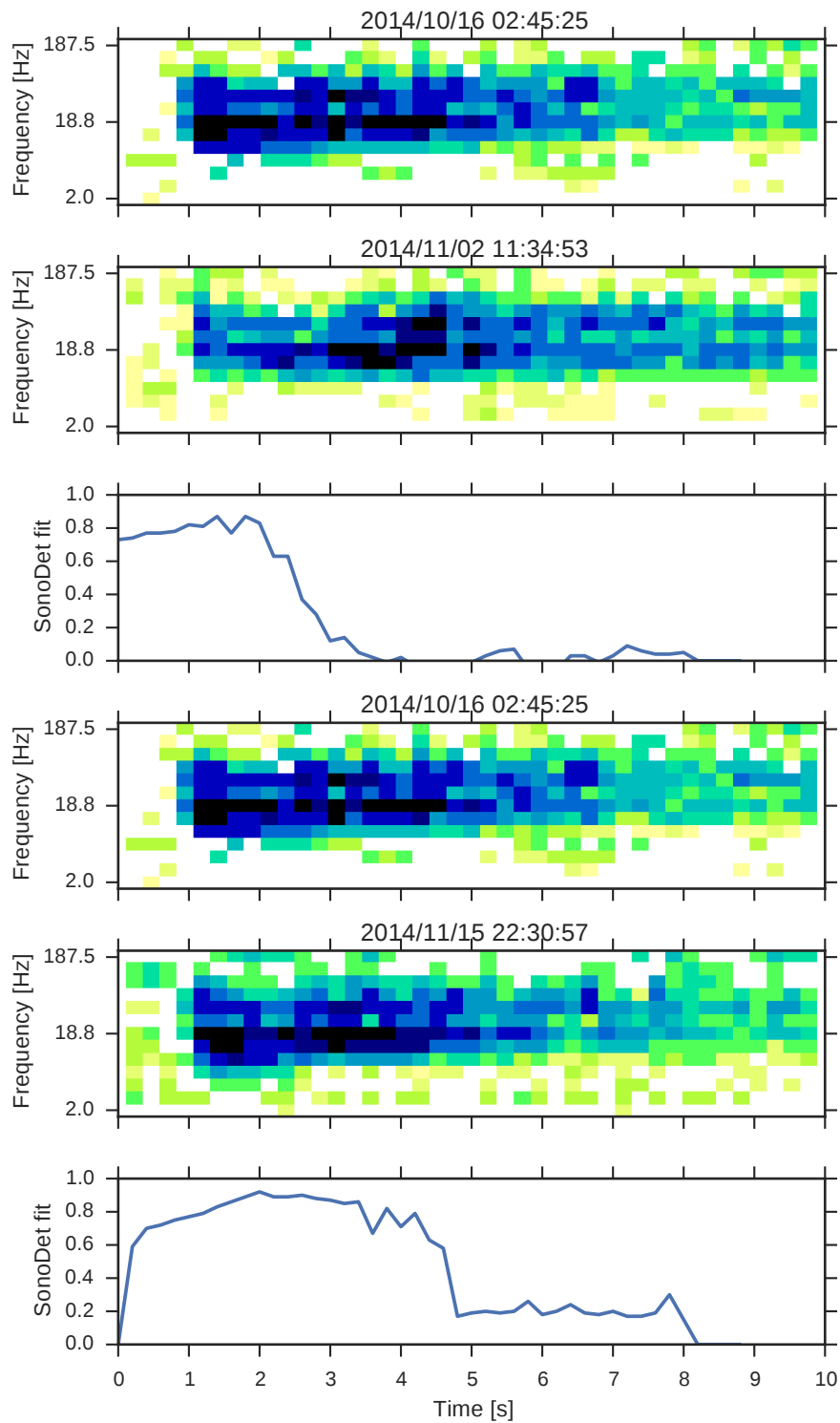


Figure 4.14: SonoDet example of the same Walsrode events from Figure 4.13. In contrary to the cross-correlation, the outlier event from 2014/11/02 can be detected with SonoDet. Both events show high SonoDet fits.

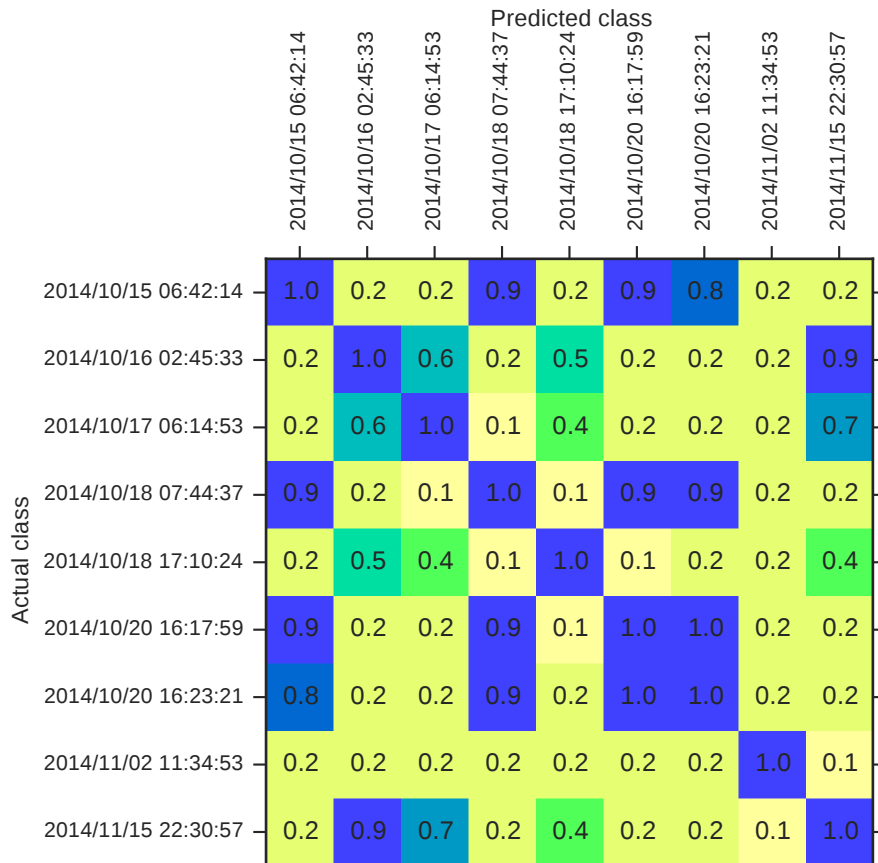


Figure 4.15: Confusion matrix of cross-correlation fit between 9 events of the Walsrode cluster. Similarities are high between the events of two subclusters (lines 1,4,6 and 7; lines 2,3,5 and 9). The event from 02/11/2014 is a clear outlier with no fit above 0.2 for any other event. It turned out that this event is located considerably deeper then the rest.

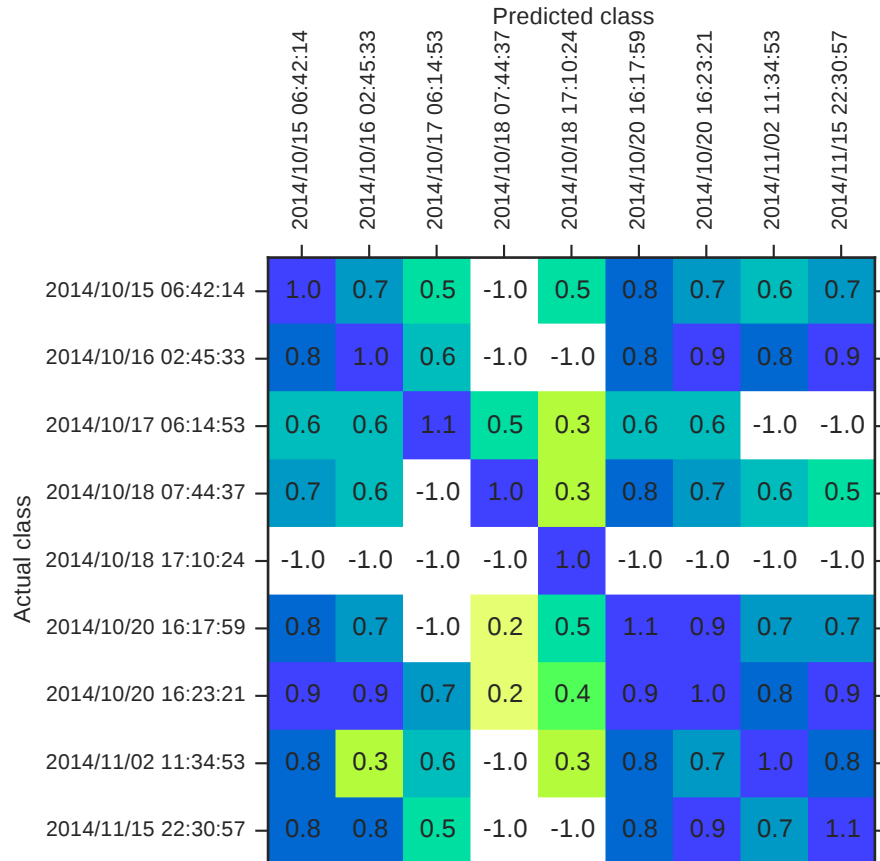


Figure 4.16: Confusion matrix of SonoDet fit between 9 events of the Walsrode cluster. Small events as for example the event from 18/10/2014 are not considered in SonoDet because of missing considerable energy above the background noise level. The outlier event from 02/11/2014 shows high similarities with other events and can thereby be detected with previous patterns.

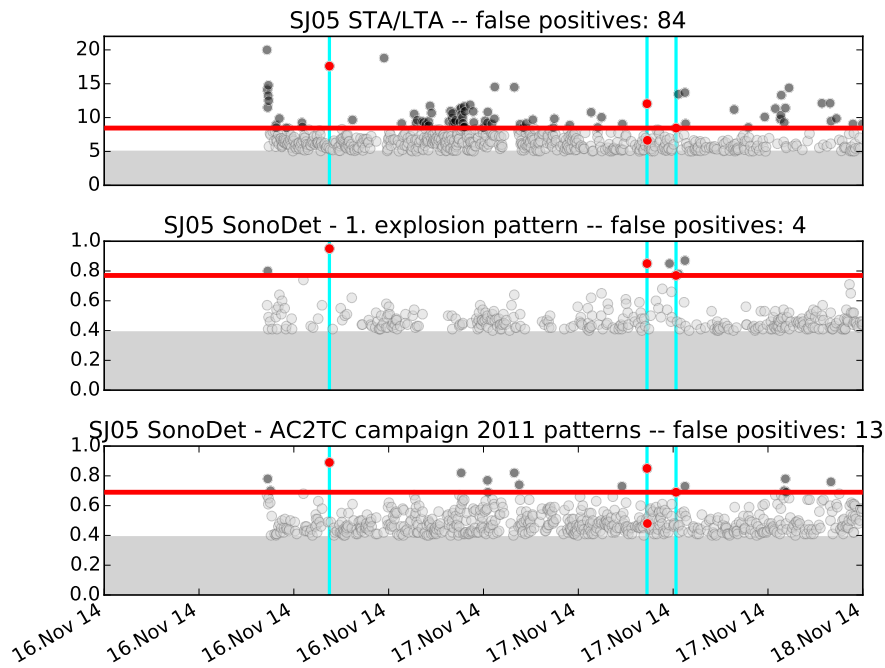


Figure 4.17: [STA/LTA](#) and SonoDet comparison with scenario explosion events from IFE14. Each dot represents the maximum detection level in a 60 s window similar to Figure 4.1. Scenario events are marked with vertical lines in cyan. To focus on the scenario events, detections of the multiple natural seismic events from the Dead Sea Transform fault zone are removed. The [STA/LTA](#) algorithm has 84 false positive detections if all three events need to be detected (top). The SonoDet algorithm with the first scenario event as a template has only 4 false positives (middle). Using explosion event templates from a different campaign from Hungary ([AC2TC](#)) results in 13 false positives (bottom).

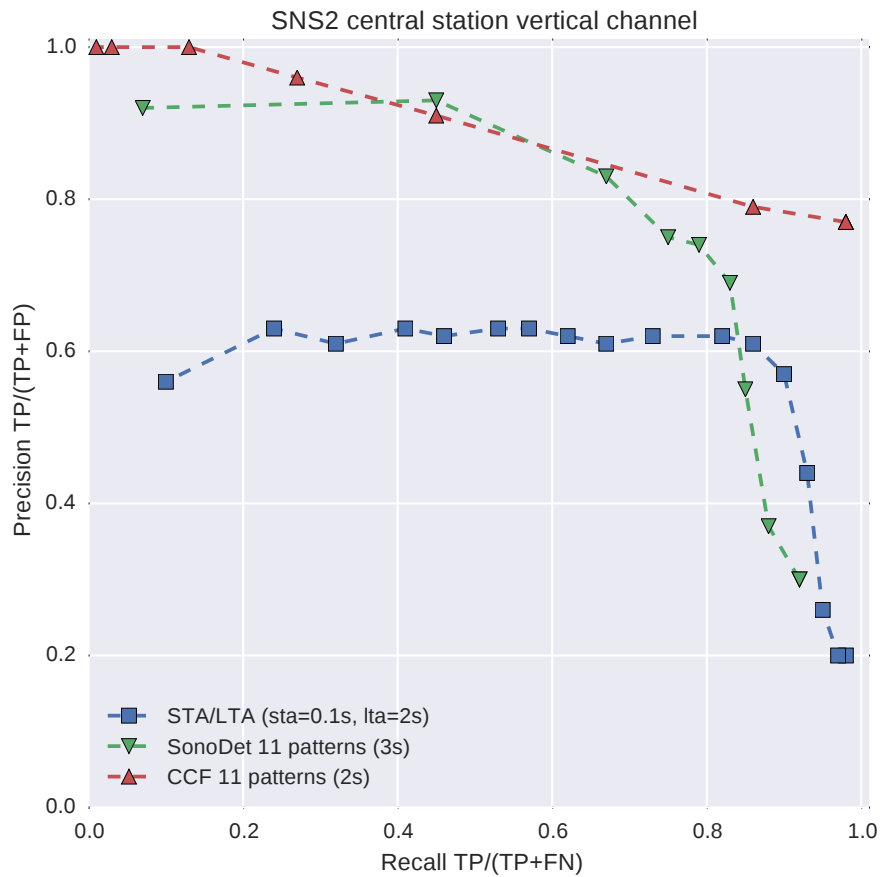


Figure 4.18: Single station precision recall plot (percentage of valid detections over percentage of detected events) for Basel monitoring and different detection algorithms. Detection was done in a 5 hour window between 2006/12/06 14:50:00 and 19:50:00 UTC. Patterns for SonoDet and CCF are from the time frame 19:50-20:00 of the same day (11 patterns). For a low recall, SonoDet and CCF detection have a similar high precision while STA/LTA has a precision of only around 0.6. For higher recalls above 0.8, the SonoDet precision drops fast in comparison to the CCF precision.

grams use 256 samples with 500 Hz data which results in a time window of 0.512 s). The general problem is that spectral and temporal precision can not be increased at the same time. Either a high spectral or a high temporal precision is possible. Wavelets allow an improvement in that the time window decreases for higher frequencies. It allows thereby a higher time resolution for high frequencies while keeping the lower frequency limit fixed. Figure 4.19 shows a comparison of sonograms to Wavelets (largest scale 40 s). As can be seen, the Wavelet transform introduces only minor changes. Improvements to resolve lower frequencies by using wider time windows with Wavelets can not be used because typical seismometers in local monitoring campaigns have a lower corner frequency of 1 Hz which means not much energy below that frequency is recorded. On the other hand higher time resolution at high frequencies by using smaller time windows with Wavelets is also not very helpful because signal energies for typical local events only reach up until around 30 Hz. The sonograms with the half-octave frequency binning already provide an adapted resolution along the frequency axis which together with the small bandwidth of expected signals explains the small differences between sonograms and Wavelets. Sonograms feature an easy implementation of pattern shift due to the constant column width which is not true for Wavelets.

Based on the versatile results of SonoDet, multiple sonogram extensions inspired by conventional image recognition were tested for improvements in seismic event detection in this thesis. Additional features like including the first and second derivative of the sonogram in time and frequency were tested. Another approach was to emphasize the tS-tP onset time difference by including sums of all rows from the sonogram matrix at each frequency step. More advanced image processing techniques as the Histogram of Oriented Gradients (N. Dalal, 2005) object detector or the Speeded Up Robust Feature (SURF, Bay et al. 2006) were also investigated. For SURF it was important to discard rotation invariance a property which is often needed for image object recognition but which is clearly not applicable for spectrograms of seismic events. Another technique is the image

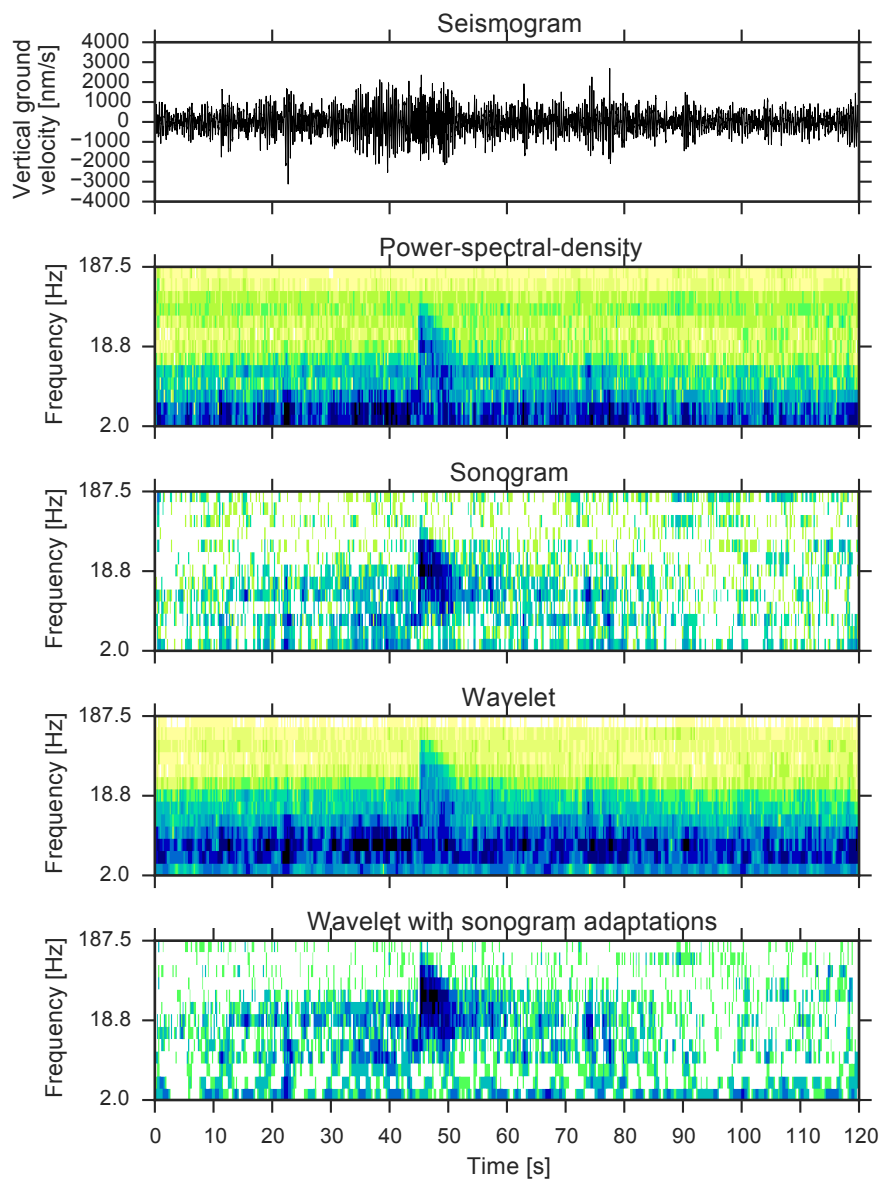


Figure 4.19: Comparison of spectrograms and the continuous wavelet transform. The Wavelet transform provides only minor improvements due to the small bandwidth of local events and the high background noise in the low frequency bands. The improved time resolution at high frequencies is not necessary for the pure detection of events.

segmentation and use of super-pixels of regions and groups as a feature vector (Fulkerson et al., 2009). A widely used feature extraction technique in speech recognition, the Mel Frequency Cepstral Coefficients (MFCC, Mermelstein 1976) is actually very similar to the sonogram feature extraction.

Most promising was an extension of SonoDet which was newly developed in this study, named SegmentDet with further processing steps mainly from morphological image processing as seen in Figure 4.20 and 4.21. The first Figure shows event examples while the second picture shows false positive detections from a SonoDet detection run. The intention was to figure out if certain features could be found in the false positives to exclude them from further detections. The first step is to use a Gaussian filter with variance  $\sigma^2 = 2$ . This introduces a blur between single sonogram pixels. The intention behind it is that neighbouring pixels contain similar information and a detection algorithm comparing single pixels at the same time and frequency position should take into account neighbouring pixels. The next step is a morphological gradient rank filter with a disk size of 3. This filter indicates the contrast intensity in the given region and thereby highlights edges. Afterwards only values above the 80th percentile are kept and used for a binary closing algorithm which closes small holes between individual sections and removes small parts. In the last step, further holes are closed and small objects are removed. The pattern recognition between templates and the data stream is done at consecutive time steps. Each template only consists of the extracted (black) region. The top and lower frequency band is stored with each template. This allows a two-dimensional cross-correlation at only the important frequency bands of the template. The processing steps of SegmentDet are inspired by a competition for the IEEE International Workshop on Machine Learning for Signal Processing which was hosted on Kaggle<sup>2</sup>. The task was to recognise different bird species from audio recordings. Results from a comparison of SegmentDet to SonoDet and other detection algorithms are shown in Figure 4.36.

<sup>2</sup> <https://www.kaggle.com/c/mlsp-2013-birds>

Overall the detection could not be made more reliable compared to SonoDet. Nevertheless the results showed some interesting characteristics of certain false positives as e.g. the noise bursts from rows 4, 5 and 7 of Figure 4.21 which have very similar patterns as actual events from Figure 4.20.

### *Neural networks*

Neural networks have been used in multiple studies for seismic detection (Dowla et al., 1990; Dysart & Pulli, 1990; Murat & Rudman, 1992; Hsu & Alexander, 1993; Wang & Teng, 1995; Dai & MacBeth, 1995; Romeo et al., 1995; Zhao & Takano, 1999; Esposito et al., 2003; Giudicepietro et al., 2005; Esposito et al., 2006, 2012). Section 3.4 discusses self-organizing maps (SOMs) which are a neural network and are used there to cluster seismic events for classification. Furthermore a conventional, recurrent and convolutional neural network with so called deep architectures are applied there on sonograms. Wiszniowski et al. (2014) used a recurrent neural network (RNN) to detect small earthquakes in Poland. The state of an RNN depends on the previous state which makes it ideal for time series analysis. Recent breakthroughs in image processing by using convolutional neural network (CNN) with deep architectures inspired the use of them for sonogram pattern recognition. Problems are usually that these algorithms require an enormous amount of training data until they are able to classify unseen data correctly. To circumvent that, studies in speech and image recognition artificially increase the number of available training data by deforming training images according to certain rules. One approach to extend training data could be to use the SonoDet amplitude adaptation rules to create multiple patterns from single events. Thereby the results from feature engineering are trained into the neural network. RNNs and CNNs to classify events are compared to other machine learning algorithms in chapter 5.

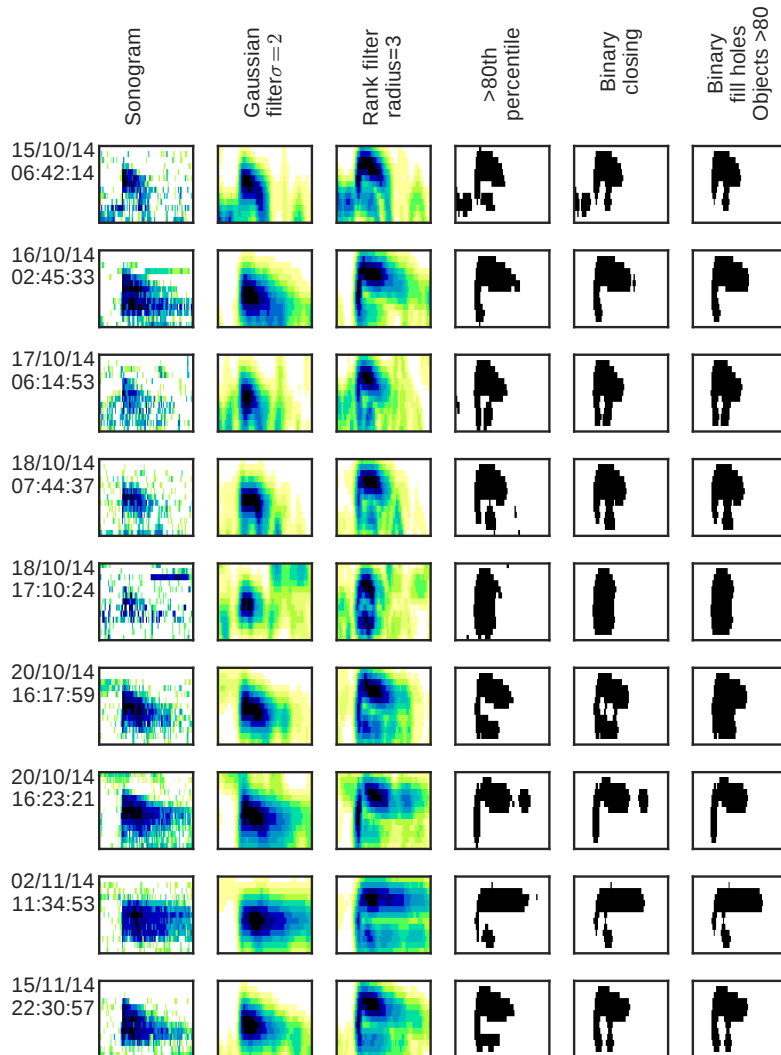


Figure 4.20: Event examples with further processing of sonograms. Each row shows the processing of one event. From left to right, additional processing is applied. The last column shows the templates used for the SegmentDet detection algorithm. Most patterns at the last processing step show a similar corner like shape. One or two broadband vertical strips over multiple frequency bands at the beginning and a high frequency horizontal strip.

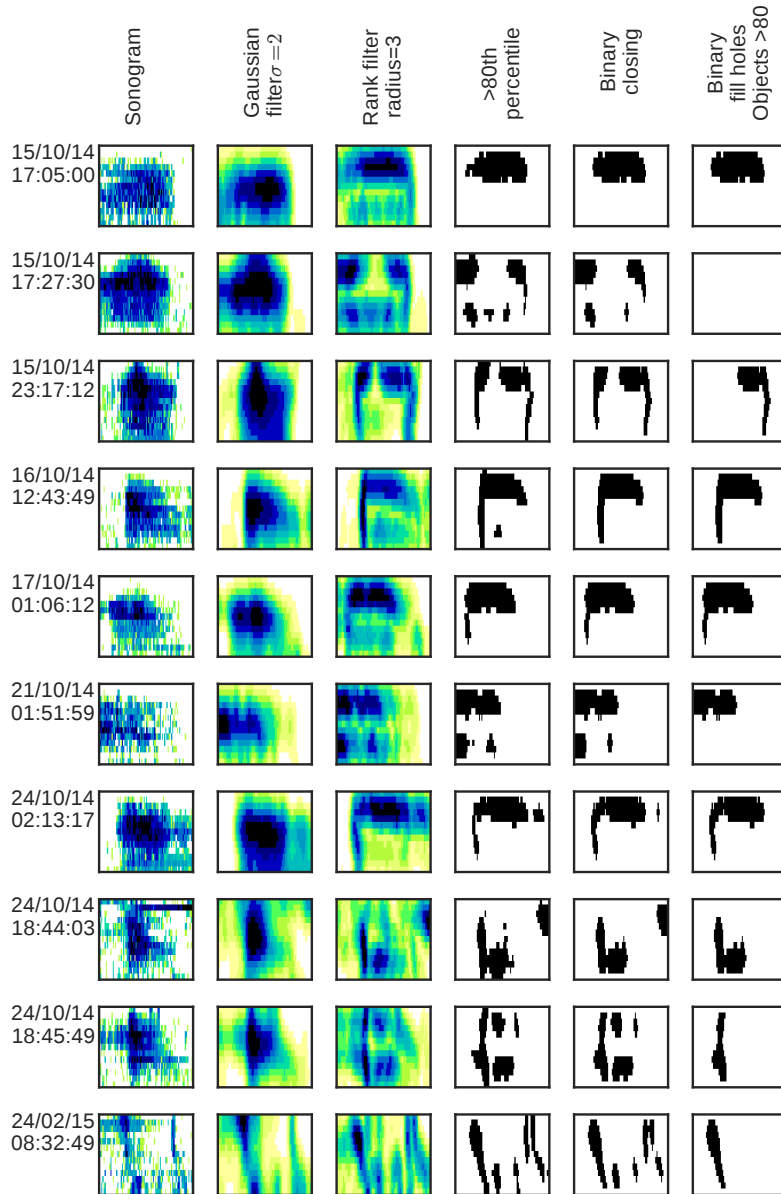


Figure 4.21: Noise examples with further processing of sonograms. Each row shows the processing of one noise burst (similar to Figure 4.20 but false positives instead of true positives). Rows 4, 5 and 7 show patterns after the last processing step on the right which are similar to events. It was therefore not possible to find features for these noise bursts which make a distinction to actual events prominent. However it can not be ruled out completely that the patterns are actually seismic events which can just not be identified by visual analysis.

## 4.2 COINCIDENCE PROCESSING IN SEISMIC NETWORKS

The previous sections used only single station data to detect events. However many monitoring campaigns make use of seismic networks with multiple sensors. This allows to exclude false positive detections from local noise disturbances which are only visible at a single station. Coincidence analysis is done in time windows whose length is chosen to account for inter station distances, local seismic velocities and depths of expected events. The further apart the stations are and the slower the local seismic velocity is, the longer the coincidence windows have to be. Stations can be weighted additionally by their quality depending on previous registrations and each station can have individual detection thresholds and detection parameters. An important factor is the depth of the expected events. Near surface events have generally larger time delays between stations and steeper amplitude decay over epicentral distance and therefore require different coincidence statistics from deep events. If events are near the surface and weak they might be only seen at few stations. Most coincidence processing algorithms separate the detection in two steps: the single station detection followed by a separate coincidence analysis where only detections above a certain threshold are considered. An exception is the source scanning approach shown in chapter 6.

Figure 4.22 and 4.23 show detections from a [STA/LTA](#) coincidence analysis of the [DGMK](#) network for two time frames respectively. As the required number of stations for a coincidence detection increases, the number of false positive detections decreases. However if too many stations are needed, events might be missed which is especially problematic if only few events per year are registered. Stations of the [DGMK](#) network in northern Germany are too noisy for a reliable low magnitude event detection by a [STA/LTA](#) coincidence analysis without allowing the detection of multiple false positives. In fact it is typical that noise sources are either so common that they happen coincidentally at the same time at multiple stations or are so strong that multiple stations register them. This leads to falsely

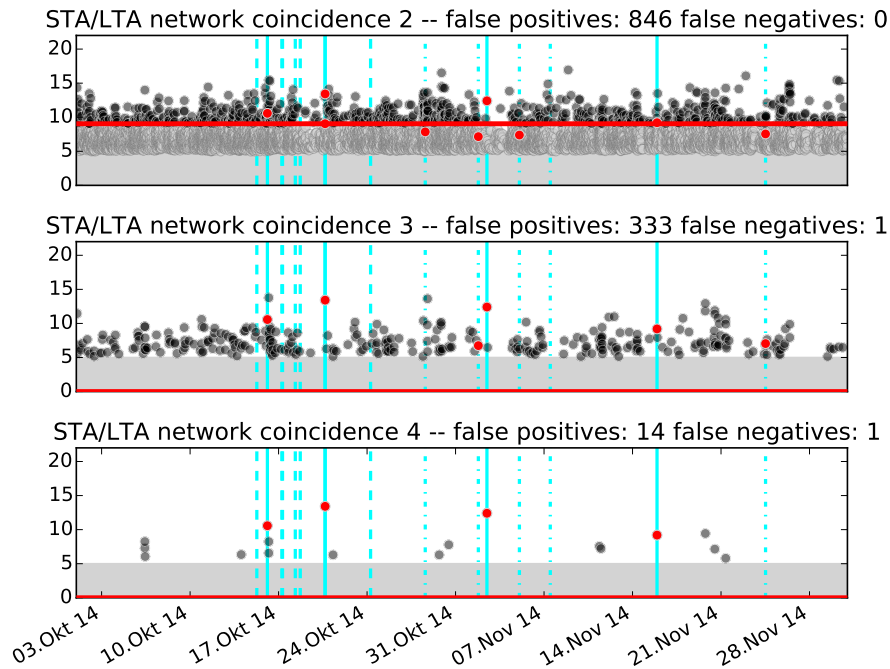


Figure 4.22: Same as in Figure 4.1 but with a network coincidence of at least two, three and four stations. Even the STA/LTA coincidence detector of the whole DGMK network can not detect all weak events without a high number of false positives.

triggered events. Zero false negatives can only be obtained with a coincidence of two stations for the first time frame of the DGMK dataset. However 846 false positive detections are detected in that way. If one false negative can be tolerated, a coincidence with four stations for the first time frame gives only 14 false positives. The best results for the second time frame are with a coincidence of three stations with one false negative and 74 false positives.

Mini-arrays can already be used to employ coincidence processing on a small scale. Figure 4.36 shows a STA/LTA coincidence algorithm at a single mini-array compared to multiple other detectors tuned for the mini-array. Results are discussed in section 4.3.3.

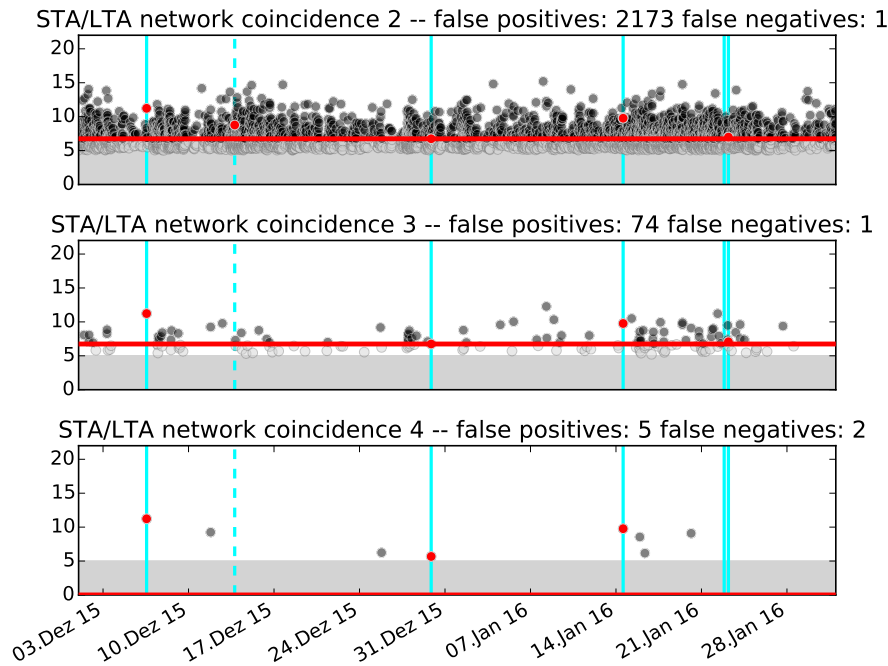


Figure 4.23: Same as in Figure 4.22 but for different time frame. The second last event can not be found in any configuration.

#### 4.3 COHERENCE ANALYSIS WITH SEISMIC ARRAYS

Many advantages of the Nanoseismic Monitoring (Joswig, 2008) technique used for multiple datasets in this study come from the application of seismic mini-arrays which are suited for azimuth and slowness determination of an incoming signal. Seismic arrays have a long-standing history in CTBT monitoring (e.g. Ringdal & Husebye, 1982; Ringdal, 1990) and much work was done on fundamental array design (e.g. Haubrich, 1968; Mykkeltveit et al., 1983; Harjes, 1990). However, sparse arrays with three or four stations are rarely considered (e.g. Suyehiro, 1967; Ward & Gregersen, 1973; Chiu et al., 1991; Kvaerna & Ringdal, 1992; Kennett et al., 2003) although they offer great improvement for automated processing at minor investment costs (e.g. Sokolowski & Miller, 1967; Joswig, 1990, 1993a). In fact, mini-arrays are the standard on the Moon, see Apollo Lunar Surface Experiments Package of the Apollo 17 mission. Mini-arrays consist of three vertical seismometers and one three-component seismometer. Each mini-array is arranged as having the three-

component station in the center and the three one-component vertical stations in a tripartite array around (e.g. Figure 4.25 bottom). Depending on the epicentral distance of the expected signals, the array aperture is usually chosen between around 50 and 200 m. The use of these mini-arrays combines array processing with three component processing and thus provides calculation of back azimuths, apparent velocities and particle motion. Furthermore, the mini-arrays are designed for a fast and easy installation by two persons.

For automatic detection, the mini-arrays offer multiple options ranging from an inner-array coincidence analysis to the usage of signal coherence by delay and sum of seismograms. The inner-array coincidence analysis can use a single station trigger at each array station. The coincidence is then done in very small time frames depending on the array aperture.

#### 4.3.1 *Beamforming*

The power of array analysis comes from using the waveform coherence between the different array elements. Depending on the array design and the direction of incoming signals, wave onsets arrive at each element with different time delays. To time shift each signal, an initial direction and apparent velocity of an incoming wave must be assumed. Signals are assumed to be by plane waves. The direction of propagation is described by the two-dimensional apparent slowness vector of the signal where slowness is defined as the inverse of velocity. Beamforming is the search through slowness space in order to maximise a certain function. Most beamforming algorithms rely on the coherency of the waveforms between single array elements. Alternatively one can think of a slowness and back azimuth grid where for each grid point the relative time offsets between single array stations are calculated. The waveforms are then time shifted accordingly. The used slowness grid for the following examples is shown in Figure 4.24. It is tuned for expected slowness values for incoming signals from local events.

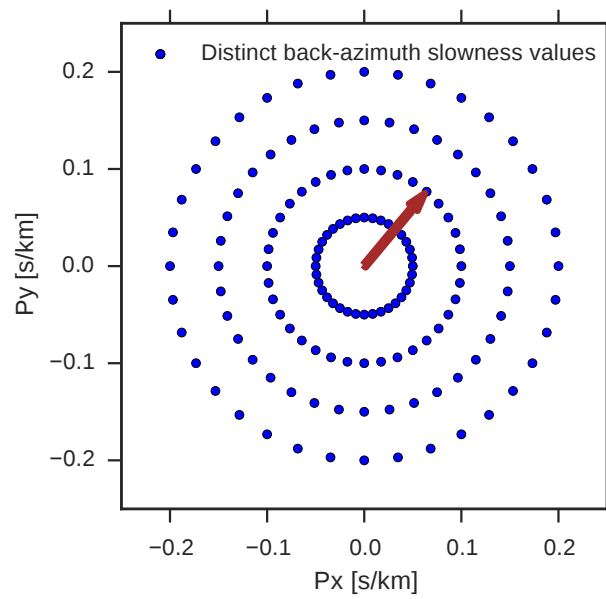


Figure 4.24: Slowness grid for beamforming. Each grid point represents a distinctive two dimensional slowness vector or alternatively a back azimuth slowness pair. Slowness values are chosen in the range of typical seismic signals. This grid is used in the following tests for different array processing methods and is tuned for expected slowness values for incoming signals from local events.

The time delay  $t$  for horizontal slowness  $s_h$  and back azimuth  $\alpha$  for two stations is calculated by equation 9 where  $d$  contains the locations of all  $n$  stations. This is valid for horizontally flat array layouts and homogeneous seismic velocities inside the array.  $\alpha$  is measured in the seismological notation starting with 0 degrees in the north direction and increasing clock-wise.  $d_{x0}$  and  $d_{y0}$  are the locations in  $x$  and  $y$  of the central array element.

$$\begin{aligned} t_n &= (d_{xn} - d_{x0}) \cdot s_{hx} + (d_{yn} - d_{y0}) \cdot s_{hy} \\ s_{hx} &= s_h \cdot \cos(\alpha) \\ s_{hy} &= s_h \cdot \sin(\alpha) \end{aligned} \quad (9)$$

To account for uneven array layouts as for the subsequently used mini-array SNS2 on a hill-slope near Basel, a correction based on the surface seismic velocities is introduced, see equation 10 where  $t_h$  is the introduced time offset,  $i$  the incidence angle,  $h$  the elevation difference and  $s$  the slowness in the upper layer.

$$\begin{aligned} t_h &= \cos(i) \cdot h \cdot s \\ i &= \sin\left(\frac{s_h}{s}\right) \\ t_n &= t_n + t_h \end{aligned} \quad (10)$$

The stacked seismogram  $z$  is then the mean of all time corrected array element vertical seismograms  $x$  at each time step  $t$  where  $N$  is the total number of stations, see equation 11.

$$z(t) = \frac{1}{N} \sum_N x_n(t - t_n) \quad (11)$$

Figure 4.25 shows the array configuration of the DGMK network. Both BELL and WIED are classical mini-arrays. Their layout is not optimal due to local constraints at the sites. The LOEV array contains ten stations and is located at a quiet former bunker site. Figures 4.26, 4.27 and 4.28 show the magnitude squared coherence  $C_{xy}$  of seismograms  $x$  and  $y$  for these three

arrays for a local seismic event as a function of frequency. The individual traces are shifted in time according to the apparent slowness of a wave coming from the event hypocenter to allow a best fit. The coherence is calculated using Welch's method with  $C_{xy} = \frac{|P_{xy}|^2}{P_{xx}P_{yy}}$ .  $P_{xx}$  and  $P_{yy}$  are power spectral densities of  $x$  and  $y$  respectively and  $P_{xy}$  is the cross-spectral density estimate of  $x$  and  $y$ . A Hanning taper with a segment length of 256 samples and overlap of 50% is used. Frequencies below 5 Hz are excluded from the plot because segment lengths are too short to calculate meaningful statistics in that range. Frequencies above 50 Hz are excluded because no significant energy from local events is expected in that range. The coherence is acceptable for the LOEV and WIED arrays but very low for the BELL array. This is also the reason why for later location analysis in chapter 6, only the center station of the BELL array is used.

Beamforming consists of a delay and sum approach where traces are stacked for each slowness point. The improvement this can yield is up to  $\sqrt{N}$  in SNR with  $N$  array elements. In case of cross-correlation, the search in slowness space can be reduced to the point of the slowness value which was already calculated for the template event because events will be located very closeby. A detection comparison with and without beamforming for a cross-correlation analysis is shown in Figure 4.29. The detection threshold is only improved slightly with beamforming but multiple false positives can be removed. The weak event (dashed cyan line) has a detection value above 0.3 only without beamforming.

Visualizing the results of beamforming over an apparent slowness range for a fixed back azimuth is done in the vespagram visualization. Seismograms are stacked for each apparent slowness value with the set back azimuth and plotted in consecutive rows. Figure 4.30 shows five seismogram stacks from all rings of the LOEV array over a apparent slowness range from 0 to  $10 \text{ s km}^{-1}$ . The matrix at the bottom shows the energy distribution of these stacks over time and apparent slowness in a finer resolution. The P-onset of the event shows a clear energy

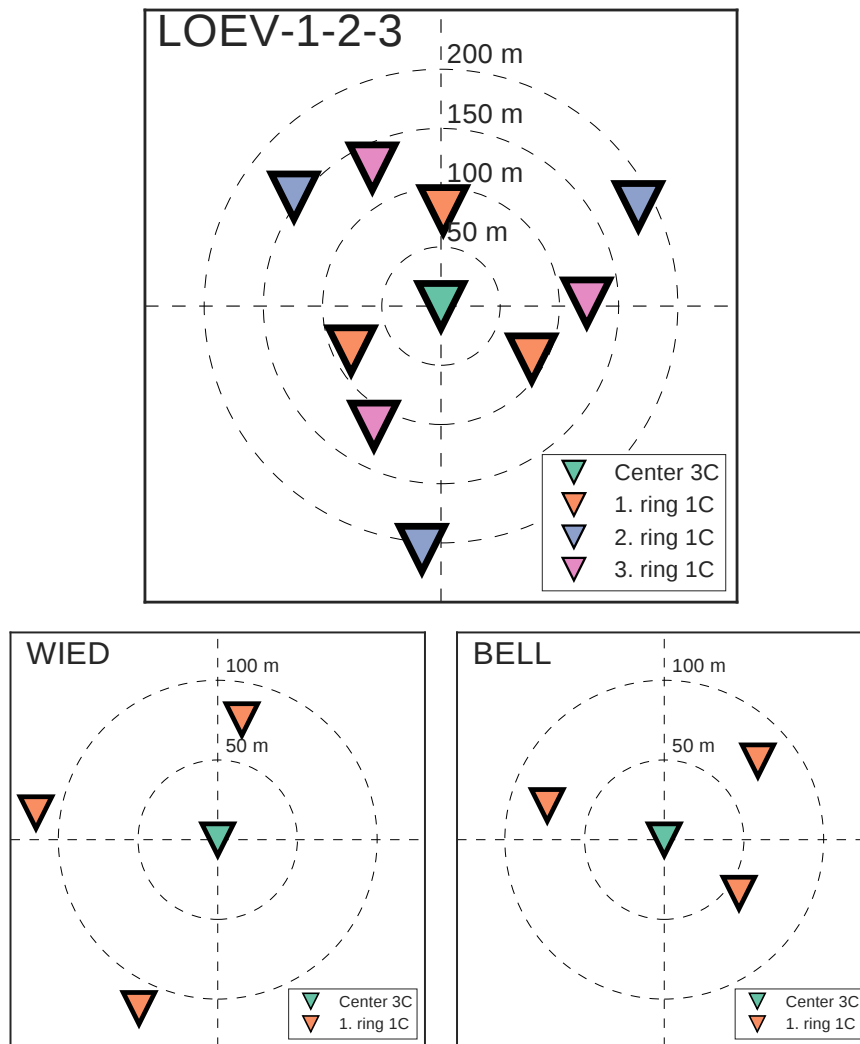


Figure 4.25: **DGMK** network array layouts. At the top the ten element LOEV array. The numbering of rings is chronological by installation time: 1. ring is the inner ring with an average distance of 85 m. 2. ring is the outer ring with an average distance of 274 m. 3. ring is the middle ring with an average distance of 131 m. The lower left shows the WIED mini-array and the lower right the BELL mini-array. For both of the mini-arrays it was not possible to build them optimally in a triangular aperture due to local constraints at the sites. Each of them contains an almost straight line of three sensors which decreases the accuracy of back azimuth and slowness determination.

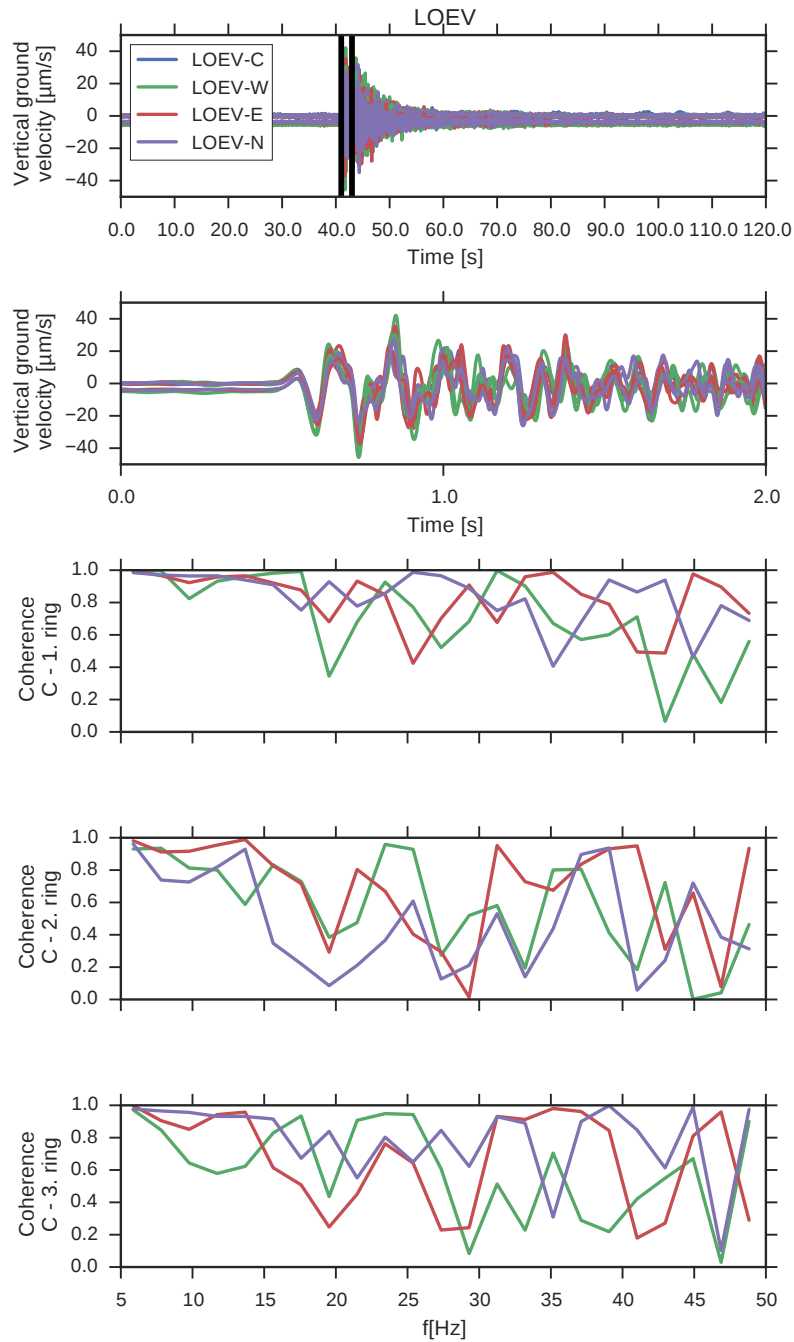


Figure 4.26: Coherence at LOEV array for Walsrode event from 2016/02/18. Coherence is shown for the time frame of the panel row (marked by black vertical lines in the first panel) between the central station (C) and the single stations of the respective array rings. The first ring of LOEV shows a constant high coherence between the frequencies of around 6 and 18 Hz.

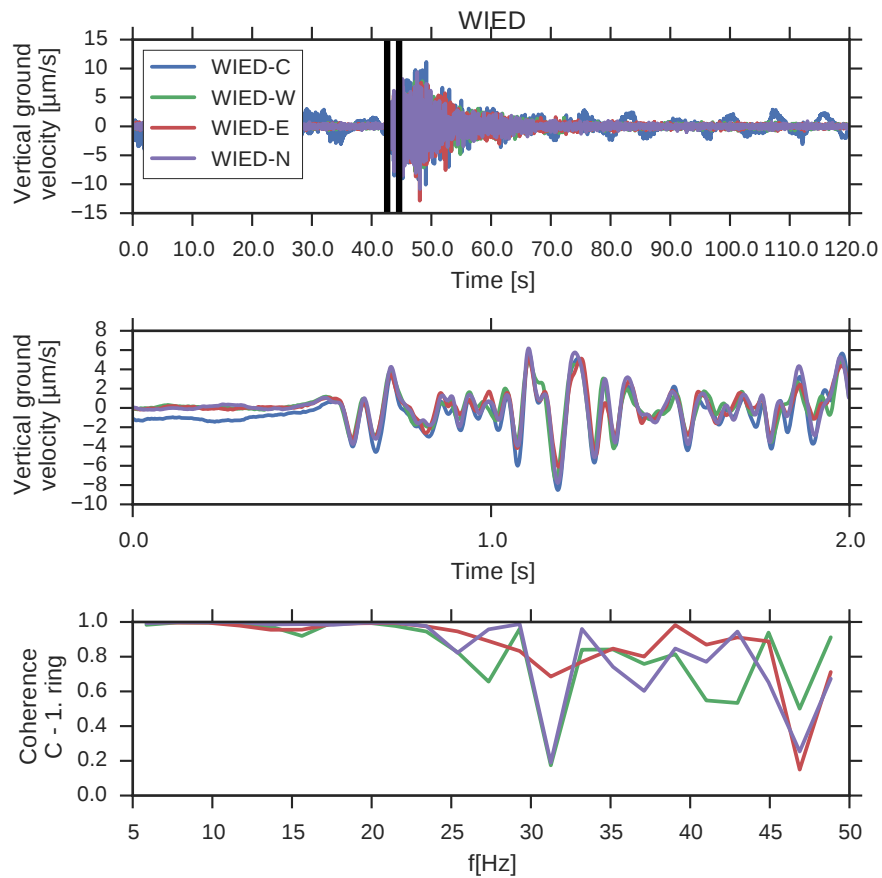


Figure 4.27: Coherence at WIED array for event from 2016/02/18, see Figure 4.26. WIED shows a constant high coherence between around 6 and 22 Hz.

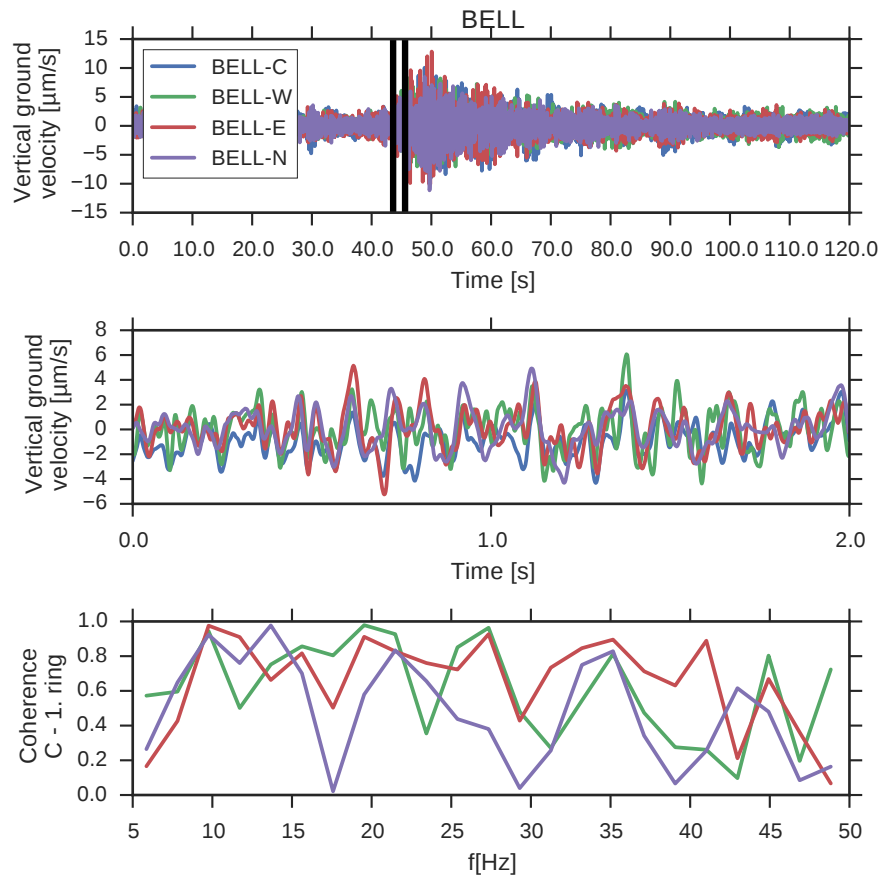


Figure 4.28: Coherence at BELL array for event from 2016/02/18, see Figure 4.26. The maximum amplitudes are similar to the station WIED. Both arrays have also a similar aperture. Nevertheless, BELL has much lower coherence values due to the lower SNR.

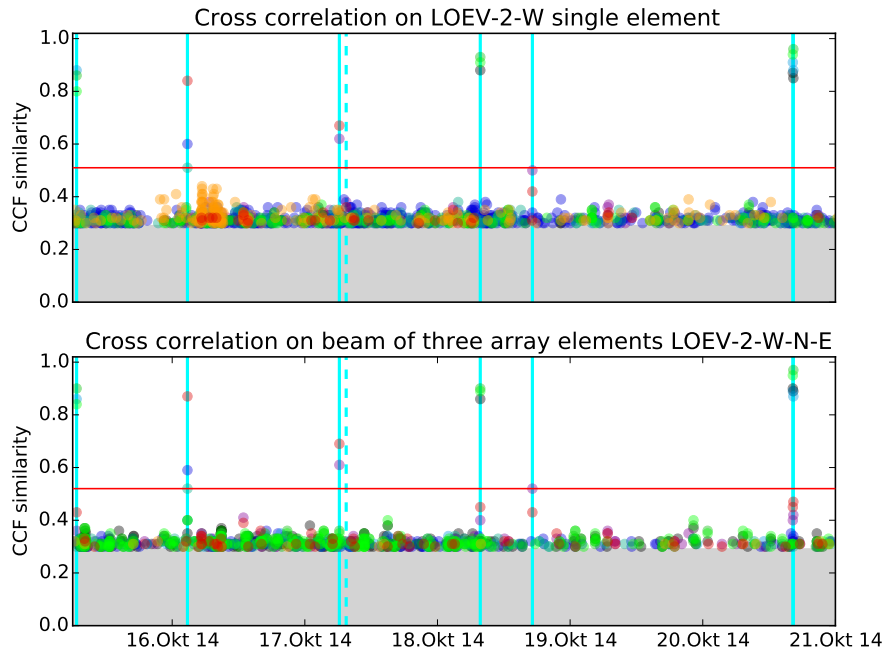


Figure 4.29: Cross-correlation on beam for Walsrode cluster similar to Figure 4.1. The top view shows results without using the array beam, the bottom view uses the beam (stack of the three available array components from LOEV-2, LOEV-1 was not available for most of the events). The beam is adjusted to point in the direction of the template events. Each dot represents the maximum cross-correlation value in a 60 s time window. The color of the dots represent the template (all seven events are used as a template). Comparisons of templates to itself were removed. The cross-correlation on the beam removes multiple false detections but does only improve the general detection threshold slightly. The weak event marked with the dashed cyan line is not detected with the beam cross-correlation.

contrast but no significant changes at the S-onset are visible even in the stacked view.

Another widely used array method is frequency wavenumber (FK) analysis (Capon, 1973; Harjes & Henger, 1973). FK transforms the wave-field of a time window into the frequency wavenumber domain. FK analysis then uses the absolute power as a measure of coherency. Usually the distribution of power is visualized in the frequency wavenumber plot to determine maxima. An example is given in Figure 4.32 where the maximum of each FK analysis per time step is taken.

A widely used technique in infrasound array monitoring for example for CTBT or volcano eruption warning which was originally developed for seismic event detection at seismic arrays is the so called Progressive Multi Channel Correlation (PMCC) method (Cansi, 1995). PMCC starts with a subset of array elements. Subsets are composed of triangular sub arrays where array responses optimally have one broad and symmetric main lobe. After an initial search with this sub array, additional elements are added progressively and all triangular combinations are tested (e.g. four combinations with four stations). Elements are added until an a priori threshold is met or all elements are added. The main CF of PMCC is called consistency and is based on the correlation between pairs from triangular subsets. These consistencies are calculated on a moving time frame and for different frequency bands. In a next step so called “families” in the time frequency matrix are searched for by comparing neighbouring consistency back azimuths and slownesses with each other. An event detection is declared if a family size exceeds a pre-set threshold. For details of the algorithm see (Bui Quang et al., 2015). The PMCC software is unfortunately closed-source and therefore the PMCC algorithm was redeveloped in Java for this study to be able to compare it to other array detection algorithms. Figure 4.32 shows the PMCC consistency values and family detections in one frequency band.

Motivated by a study from Caljé (2005) which compares the Fisher ratio to PMCC, the Fisher ratio was implemented as well for array detection. Calje came to the conclusions that the Fisher

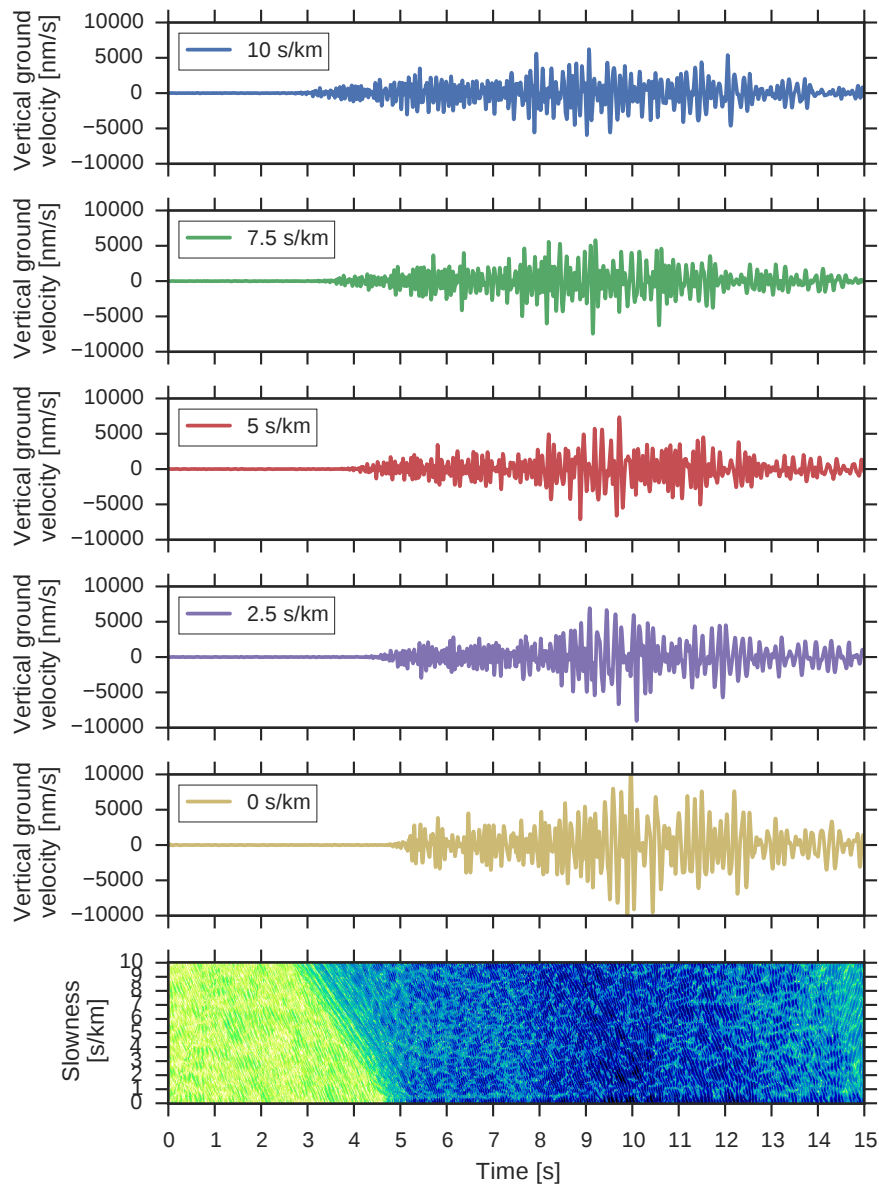


Figure 4.30: Vespagram at LOEV ten element array with local event from Bothel (start of plot 2016/05/28 21:13:40 UTC). Each row of seismograms shows a stack with a fixed back azimuth and varying apparent slowness value. The bottom view shows the energy distribution of these stacks over time and apparent slowness in  $0.05 \text{ s km}^{-1}$  steps. While the P-onset around 3 to 5 s shows a clear energy contrast, the S-onset which should be theoretically around 8 to 10 s can not be seen clearly.

ratio exceeds by far detections by [PMCC](#) for infrasound signals. Empirical tests in this thesis as also seen in [Figure 4.32](#) suggest that this is also true for local seismic events.

The Fisher ratio is the variance of a signal normalized by the variance of the noise at an array, see [equation 12](#) and [Figure 4.31](#). The variance of the signal ( $\sigma_s^2$ ) is calculated by the mean corrected stack of all traces over a short time window, see the nominator in [equation 12](#) and [equation 14](#) for the mean. The variance of the noise ( $\sigma_n^2$ ) on the other hand is the variance over all traces at each individual time step. It is calculated by the deviation of samples from the mean at the current time step, see the denominator in [equation 12](#) and [equation 13](#) for the mean.  $T$  is the length of the time window,  $N$  the total number of array elements and  $x$  is the filtered time-shifted seismogram.

$$F = \frac{\sigma_s^2}{\sigma_n^2} = \frac{\frac{1}{T-1} \sum_T \left( \frac{1}{N} \sum_N x_{nt} - \bar{x} \right)^2}{\frac{1}{T} \sum_T \left( \frac{1}{N-1} \sum_N (x_{nt} - \bar{x}_t)^2 \right)} \quad (12)$$

$$\bar{x}_t = \frac{1}{N} \sum_N x_{nt} \quad (13)$$

$$\bar{x} = \frac{1}{NT} \sum_T \sum_N x_{nt} \quad (14)$$

The algorithms in this study are based on an optimized calculation of the Fisher ratio for electric circuits and therefore also for digital processing by [Melton & Bailey \(1957\)](#), see [equation 15](#).

$$F = \frac{T(N-1) \sum_T (\sum_N x_{nt})^2 - \frac{1}{T} (\sum_T \sum_N x_{nt})^2}{N(T-1) \sum_T \sum_N x_{nt}^2 - \frac{1}{N} \sum_T (\sum_N x_{nt})^2} \quad (15)$$

[Figure 4.32](#) shows a comparison of the described array algorithms for a one hour time frame with a noise signal and a local seismic event in northern Germany. As a baseline algorithm a simple normalized correlation of all seismograms is shown there as well. The Fisher ratio exceeds by far all other algorithms. It is the only algorithm which has no significant detection apart from the actual event. [FK](#) analysis and the [STA/LTA](#) on the beam also show good results but have significant peaks at the noise signal.

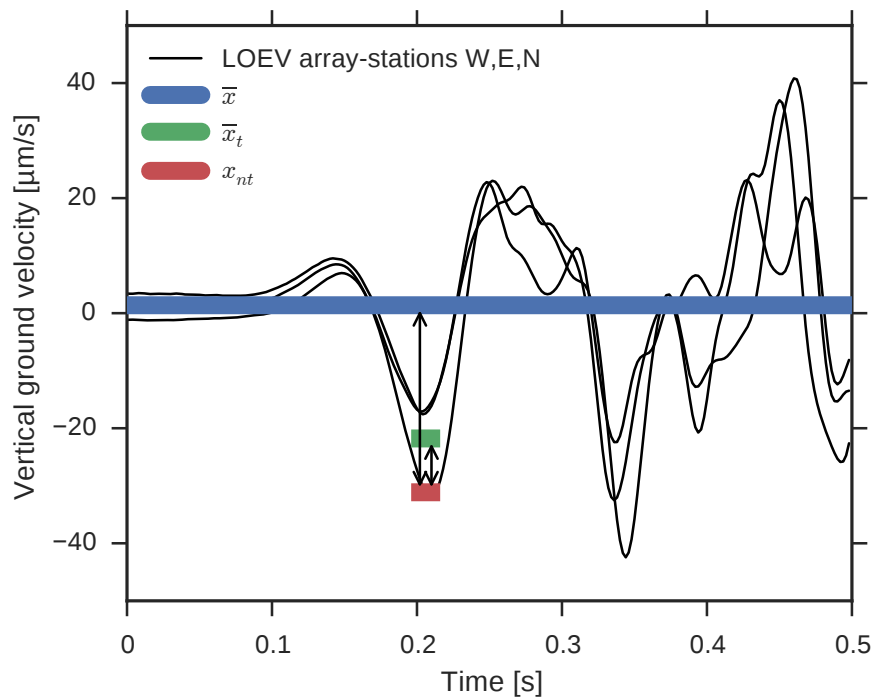


Figure 4.31: Simplified explanation of the Fisher ratio. The Fisher ratio is the ratio of two differences. The difference between sample values ( $x_{nt}$ ) and the mean of the whole time window ( $\bar{x}$ , see long double arrow) and the difference between sample values ( $x_{nt}$ ) and the current sample mean ( $\bar{x}_t$ , see short double arrow). The Fisher ratio thereby describes the ratio of the variance of the signal normalized by the variance of the noise.

The [PMCC](#) consistency shows false detections consistently but by using the [PMCC](#) families, only one false positive is detected.

Figure [4.33](#) and [4.34](#) show the Fisher ratio for different array setups and time frames. It shows that at least 5 elements are necessary to obtain reliable detection results in the case of the LOEV array. It also shows that the typical aperture for mini-arrays (LOEV-1) has advantages over the larger aperture from LOEV-2. The number of false positives with less elements than 5 elements is unacceptably high. For the first time frame the false positive number drops to 0 with 7 array elements. For the second time frame the false positive number is also the lowest with 7 elements but two events are missed (false negatives).

#### 4.3.2 *Combined array spectrograms*

Another approach to use coherent energy at multiple array elements for detection is the combination of multiple sonograms into so called super-sonograms as shown in Figure [4.35](#). These super-sonograms are well suitable for interactive visual inspection of seismic data but also for automatic detection with the SonoDet algorithm described in section [4.1.2](#). It allows to exclude noise sources at single array elements as for example footsteps near a station or ground coupled acoustic signals with slow wave propagation speeds.

#### 4.3.3 *Comparison of array algorithms at one mini-array*

The performance of different detectors at the Basel SNS2 mini-array with only one event type is shown in Figure [4.36](#): [STA/LTA](#), a cross-correlation on the beam, super-sonogram SonoDet, super-sonogram SegmentDet and Fisher ratio. As shown, the Fisher ratio performs worse than the coincidence [STA/LTA](#) and the array spectrogram pattern recognition algorithms which in both cases might be due to the low number of only four array elements. The best performance is obtained with the spectrogram pattern recognition algorithms (SonoDet and SegmentDet). When the

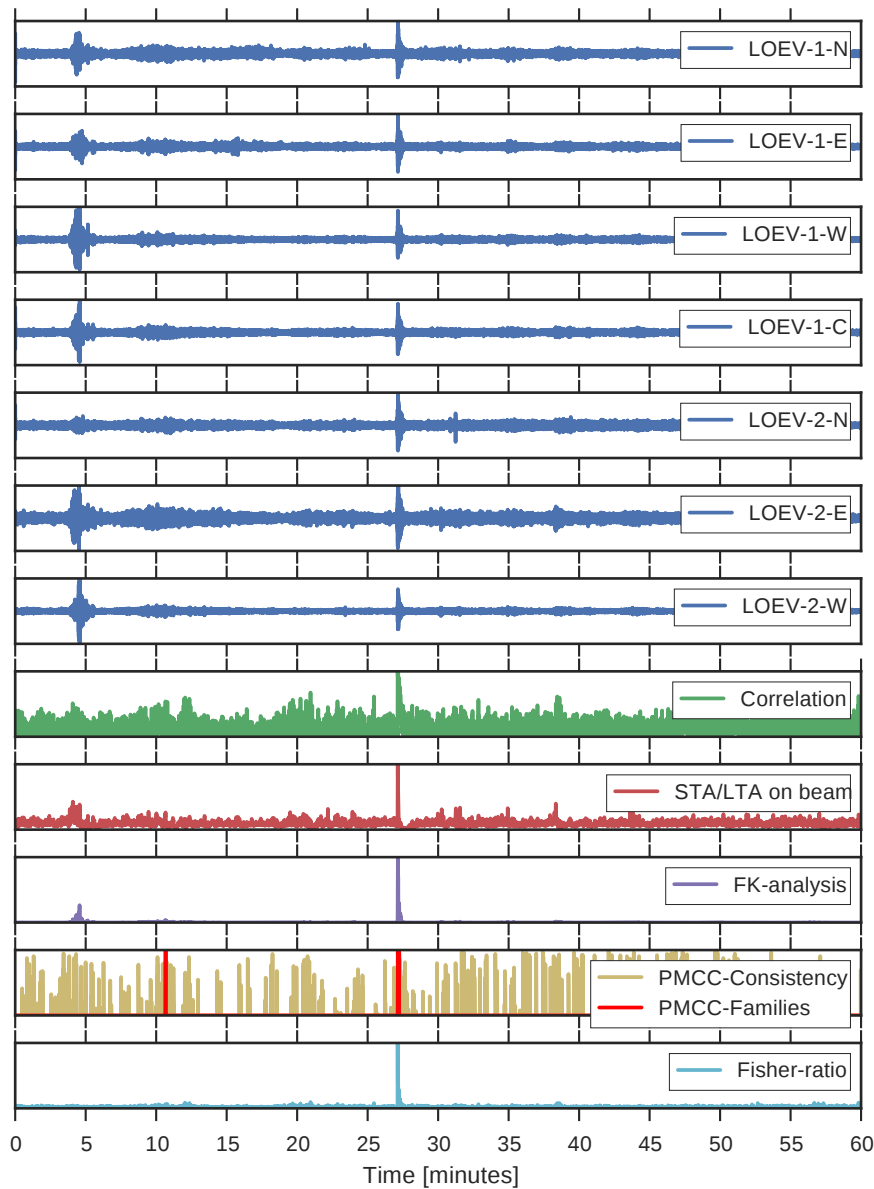


Figure 4.32: Comparison of array coherency detection algorithms at LOEV array with first and second ring active. The high amplitudes in the seismogram between minute 4 and 5 are from a local noise source while the actual event arrives around minute 27 (distance of 57 km,  $M_L = 2.1$ ). The detection statistic is calculated in a moving window with length 0.5 s and stepsize 0.1 s. All seismograms are bandpass filtered between 4 and 30 Hz. The Fisher ratio outperforms all other detection algorithms and is the only detector which has no significant peak apart from the seismic event.

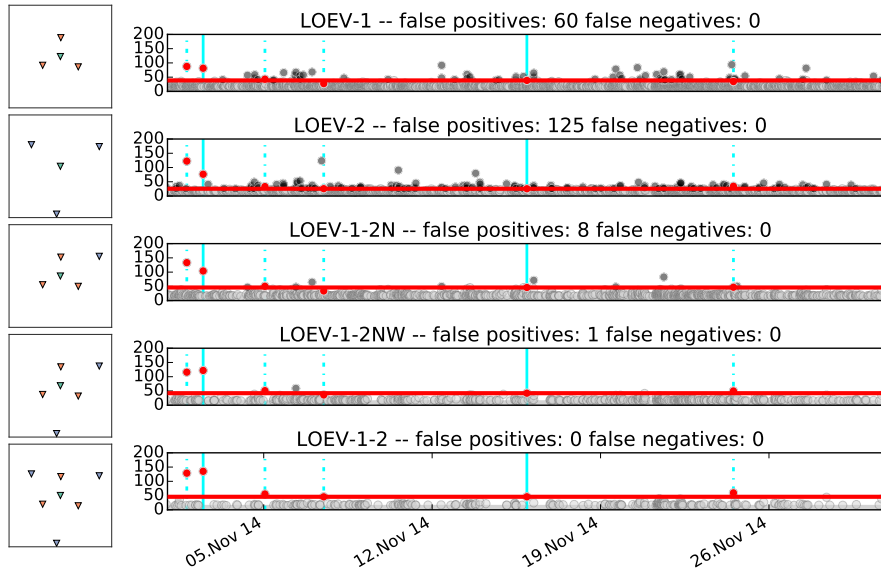


Figure 4.33: Fisher detection comparison with different array setups, first time frame. Each row shows a different subset of array stations at LOEV as indicated in the left column. Note how the number of false positives decreases as more array elements are used.

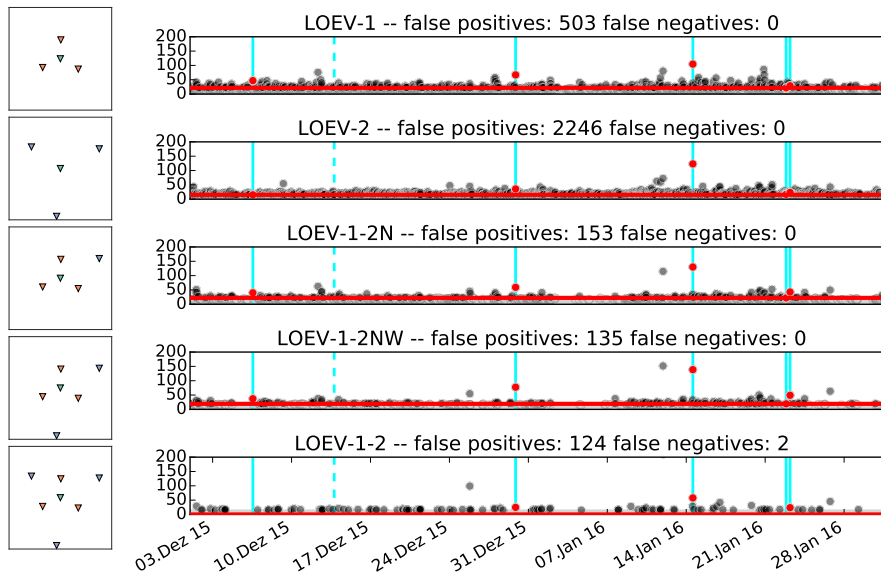


Figure 4.34: Fisher detection comparison with different array setups, second time frame. Each row shows a different subset of array stations at LOEV as indicated in the left column. The first and second last event can not be detected with the applied detection threshold and both rings active. The higher number of false positives compared to the previous timeframe can be explained by the lower SNR events.

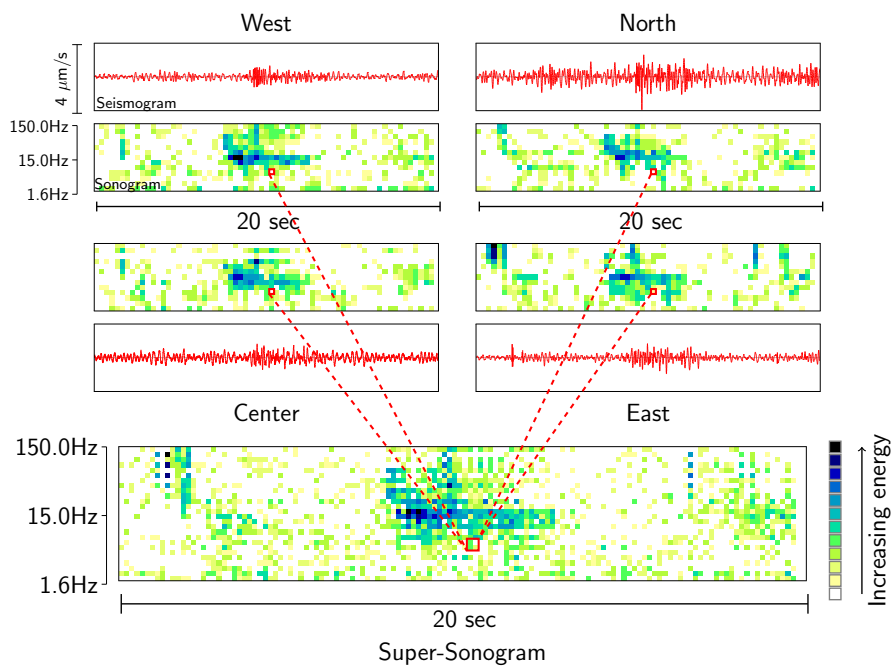


Figure 4.35: Compilation of super-sonogram from four sonograms of a mini-array (same event as in Figure 4.10). The pixels of each single sonogram create the “super-pixels” of the super-sonogram. The super-sonogram is an alternative method to make use of array waveform coherency for visual inspection but also for pattern recognition by SonoDet.

pattern number for SonoDet is increased, a precision of 1 can be kept up until a recall of around 0.85.

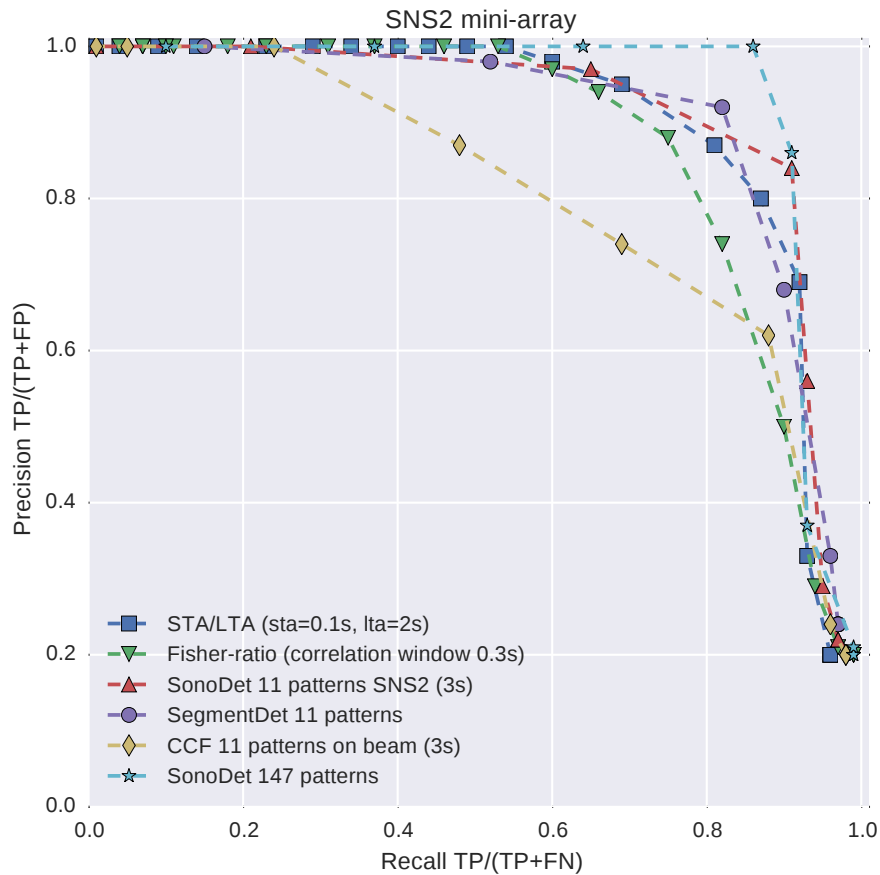


Figure 4.36: Precision recall plot for Basel monitoring similar to Figure 4.18 but with full mini-array processing instead of the single central trace. Inner-array coincidence STA/LTA, CCF on beam, super-sonogram SonoDet and SegmentDet and Fisher ratio. Most algorithms show a similar performance with the best being the spectral pattern recognitions (SonoDet and SegmentDet). The CCF on the beam shows worse results. The larger pattern base with 147 patterns is from the time between 19:50-21:50 instead of 19:50-20:00 for the 11 patterns.

---

## SEISMIC EVENT CLUSTERING BY UNSUPERVISED PATTERN RECOGNITION

---

The previous chapter gave an overview of detection and classification algorithms and showed the high potential of pattern recognition with sonograms. This chapter explores the potential of unsupervised learning algorithms for classification and prototype generation in a scenario where data is sparse (only one single vertical trace) and classified events are available, e.g. by a preceding or following dense network. Having only a vertical component eliminates the possibility to use a polarization analysis for back azimuth and incidence angle estimation.

The automatic pattern recognition approach is based on spectral features of the seismograms. Earlier studies on automatic classification derived characteristic features of seismic signals from, amongst others, times and amplitudes of phase arrivals and polarisation or spectral ratios (Tong & Kennett, 1996). Spectral features in particular have been found to be both accurate and robust in distinguishing different event types (Joswig, 1990; Dowla et al., 1990; Gendron, 2000; Ohrnberger, 2001; Köhler et al., 2009; Hammer et al., 2012a). In most cases the feature vectors of the events are not intuitively interpretable and the internal mechanics of the classifier is hidden from the analyst. A key element of the approach shown here is to keep the result of the feature extraction in a human readable manner. This allows an analyst to understand the decisions taken by the algorithm and to get a qualitative description of different event types.

Often, feature selection procedures act like black boxes and informative or interesting features remain unnoticed. In addition, some parameters, such as the correct picking of uncertain

S-phases, need further manual intervention. An adapted variant of spectrograms, the so-called sonograms are used here, which have proven to be effective for classification as well as for continuous data visualization (Joswig 1995 and section 4.1.2). Distinct features of sonograms are the frequency-dependent noise adaptation for robustness and an intuitive visualization, optimised for human readability. For the human observer, patterns in sonograms are apparent even for small ( $M_L < -2.0$ ) and short ( $< 3s$ ) events when viewing large datasets (Sick et al., 2012, 2013).

Here, the sonogram transformation serves as a feature selection step for the unsupervised analysis based on principal component analysis (PCA) (Jolliffe, 1986) and self-organizing maps (SOMs) (Kohonen, 2001). PCA is used to transform the sonograms so that their components are aligned according to their descending variance, which enables us to extract the most informative features. SOMs are a powerful tool to project high-dimensional data to a lower-dimensional space (typically 2- or 3-dimensional), the so-called grid, to make it accessible for visual inspection. Each node of the grid ideally represents a prototypical event of the given dataset and the continuous sonogram representation of the feature vectors makes it possible to analyze these prototypes visually. Here, the SOMs are used to generate prototypes of event classes and visualize them. New unknown events are compared for similarity to these prototypes and thereby classified as belonging to a certain event type or geographic region.

The ground-truth for this study consists of the locations acquired with all 32 seismic sensors of the PISCO '94 campaign. The analysis in this study is restricted to the recordings of the vertical trace of one station of the network (station A04) and compares the location results based on pattern recognition to the ground truth (station A07 is used additionally to examine station dependant differences). Five classes based on a statistical separation with respect to depths, source processes and recurrence were defined. For some of these classes sub-clusters were defined, in order to further explore the capabilities of the

Table 3: Number of events per class.

<b>Class</b>	<b>Sub-class</b>	<b>Number of events</b>
<i>CRUST</i>	<i>CRUST</i>	13
<i>CENTER</i>	<i>CENTER</i>	136
	<i>CENTER_N</i>	47
	<i>CENTER_E</i>	36
	<i>CENTER_S</i>	13
<i>NORTH</i>	<i>NORTH</i>	11
	<i>NORTH_E</i>	12
<i>DEEP</i>	<i>DEEP</i>	76
	<i>DEEP_N</i>	17
<i>QUARRY</i>	<i>QUARRY</i>	16

algorithms. All events of the *CENTER* classes are located in the center of the active area and have events of medium depth ( $\approx 85 - 135$  km). The *DEEP* classes cover events with large depth ( $\approx 170 - 230$  km, which are located to the east along the submerging plate. The *CRUST* cluster has crustal events of a low depth ( $< 50$  km). The *QUARRY* cluster has very shallow events induced by mine blasts from one of the largest copper mines in the world (Chuquicamata mine) and its events are therefore confined to a small geographic region. The *NORTH* clusters consist of events which are similar in depth but north of the *CENTER* events. Therefore the dataset includes clusters which vary greatly in depth and distance to the recording station (*DEEP* vs. the rest) which enables us to test for geographic clustering but also clusters with similar depth but different epicenter distance (*CENTER* vs. *NORTH*) or different depth and similar epicenter distance (*CRUST* vs. *CENTER*). Additionally there are events with a similar epicenter distance but a different source mechanism (*QUARRY* vs. *CENTER*). The number of events in each class is shown in Table 3.

A unique property of the dataset is the excellent **SNR**, owing to a sparse population in this area, dry climate and meager vegetation. A histogram of **SNRs** based on the ratio of maximum amplitudes in a ten second window before and after the P-onset time of all studied events at station A04 is shown in Figure 5.1.

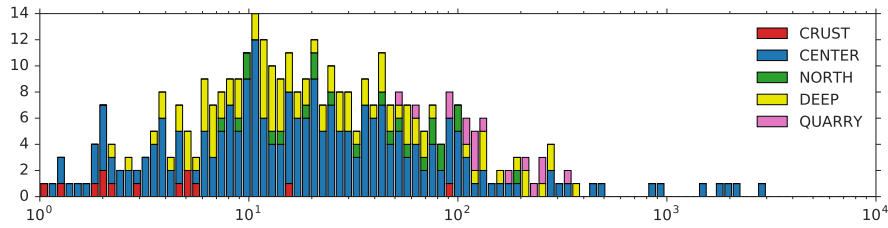


Figure 5.1: PISCO events SNR histogram at station A04 colored by event class. The high SNRs of QUARRY events can be explained by the close proximity of the quarry to the recording station. Median SNR is 19.1. The minimum SNR of 0.02 due to a digitizer calibration signal just before one event is excluded in the figure.

### 5.1 FEATURE EXTRACTION BY TRANSFORMATION TO SONOGRAMS

In the feature extraction procedure each event is transformed into a special spectral representation, the sonogram (section 4.1.2, Joswig 1993b). A main advantage of the sonograms is that stationary background noise is filtered (Joswig, 1995), which allows a reliable classification even under challenging noise conditions.

Figure 5.2 gives an example of a typical event of the CENTER class in both the seismogram and the sonogram representation.

The event bulletin available for the PISCO dataset contains the P-onset times of recorded seismic events. The focus here lies only on the classification of already detected events. The extracted sonogram of each event comprises a fixed 45 seconds window starting one second before the P-onset time. This window size turned out to be the best trade-off between visual interpretability and usability for the cluster algorithms. The usability evaluation was done with the Silhouette coefficient (Rousseeuw, 1987). This metric calculates the ratio of the difference of the mean distance of elements to their own cluster and the mean distance to elements of the neighbouring cluster, thus combining cluster cohesion and separation.

Often, two similar events with related source processes have very different amplitudes but general patterns are similar up to a difference of the order of two magnitudes. In this study it is

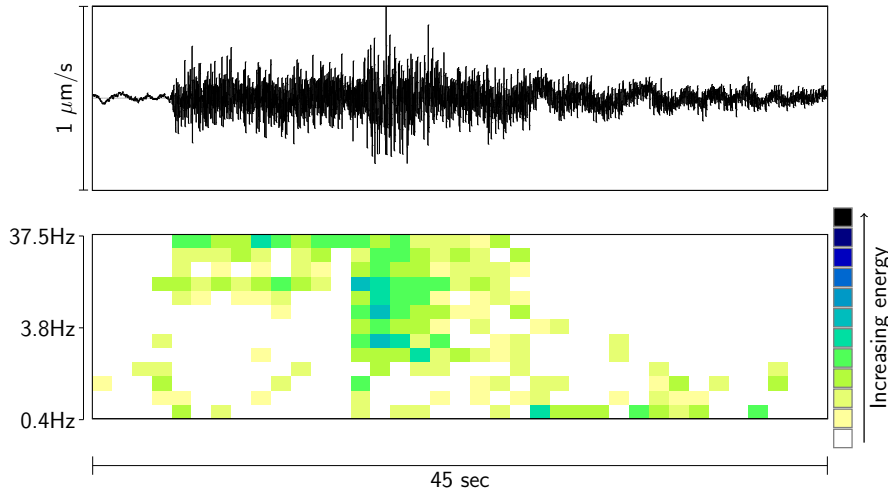


Figure 5.2: Example of a *CENTER* event from the catalog, unfiltered seismogram on the top and sonogram representation below. The sonogram allows to distinguish changes in frequency content easily.

not desirable that these events end up in two different clusters. Therefore the amplitude of the sonograms is normalized based on the difference of the global mean of all events in the dataset to the individual mean of the event. Figure 5.3 shows five exemplary events of each class in sonogram space.

### 5.1.1 Interpretation

The visualization in sonogram space allows for a qualitative description of different event types (Figure 5.3). A characteristic feature of the earthquakes from the *CENTER* classes is a small time difference between P- and S-onset ( $t_S - t_P$ ) of around 15 s. By contrast, *DEEP* events have longer  $t_S - t_P$  time differences (around 30 s) and are further characterized by high energies at lower frequencies due to their greater distance to the recording station. *CENTER* and *NORTH* earthquakes have a very similar hypocenter depth and associated source processes. Class assignment is solely based on geographic information. Earthquakes north of  $21.65^\circ$  South are classified as *NORTH* events and the remaining earthquakes as *CENTER* events. *QUARRY* events represent mine explosions and are clearly distinguishable through

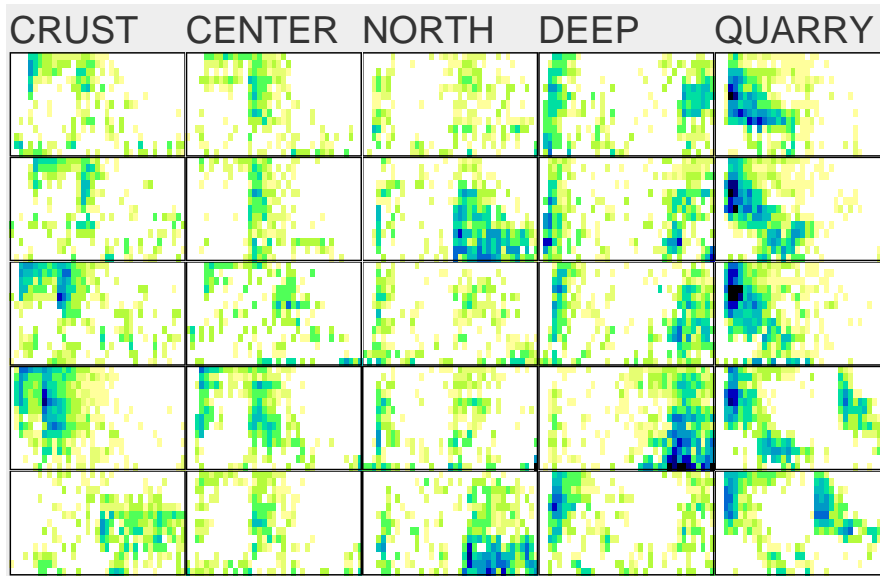


Figure 5.3: Five exemplary events of each of the five classes, dimensions of each event are as in Figure 5.2. The left column shows the big differences in *CRUST* events between each other. The bottom two events in the right column are two explosions followed very closely to each other.

their less clear S-phase and relatively low energies at high frequencies. Each of the sonograms of the *QUARRY* class shows a diagonal transition of energy from high frequency energy in the P-coda to low frequency energy around 20 s later. Four of the *QUARRY* events are double explosions with two explosions shortly after each other, a fact that complicates the clustering considerably.

Although only few events in the bulletin were crustal earthquakes, they are characterized by low energies at minor frequencies. For more information about the *CRUST* events see [Belmonte-Pool \(2002\)](#).

The dominant visual discrimination criterion for all classes is the time difference between the P- and S-wave and therefore the distance. Figure 5.4 shows the P-wave velocity model of the area according to [Graeber \(1997\)](#). As a basis from this model, a P-wave velocity of  $v_p \approx 7.5$  km/s and a S-wave velocity of  $v_s \approx v_p/\sqrt{3} \approx 4.3$  km/s is assumed for a rough  $t_s - t_p$  time difference calculation. Thus the  $t_s - t_p$  time difference of arrival is

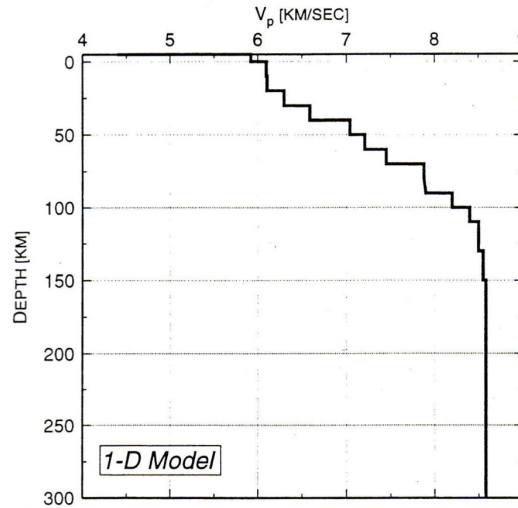


Figure 5.4: 1-D velocity model for P-waves in the measurement area (Graeber, 1997).

$\approx 10$  seconds for 100 km hypocenter distance. Hypocenter distances vary between 20 and 400 km, resulting in large variations of  $t_s - t_p$  time differences. Because the focus of this analysis is on data with only one vertical seismic trace, no azimuth can be calculated and the classification of events with the same distance from different classes is entirely based on pattern differences of the sonograms.

## 5.2 APPLICATION OF CLUSTERING ALGORITHMS

In sonogram space, each of the 377 events of 45 seconds duration consists of a 37 (number of pixels in the time domain with 100 Hz sample rate) by 13 (number of frequency bands) time-frequency matrix of discretized values between 0 and 12 (corresponding to the color palette of the sonograms). Subsequently the time-frequency matrices are converted to a one-dimensional vector of length 481 by concatenating the rows of the matrix. This concatenation unfortunately removes the two-dimensional neighborhoods. PCA is applied to each vector for feature reduction and for the purpose of providing an overview of the clustering (section 5.3). Finally, SOMs are used for further inspection, visualization and classification with event prototypes (section 5.4).

### 5.3 PRINCIPAL COMPONENT ANALYSIS (PCA)

**PCA** is a multivariate statistical method, which can be used to structure, reduce and visualize multidimensional data. It performs an orthogonal linear transformation into a new coordinate system spanned by the so-called principal components - linear combinations of dimensions that are ordered by the amount of explained variance in the data (Jolliffe, 1986). The first principal component corresponds to the direction of largest variance in the data and each succeeding component accounts for maximum variance under the constraint of being uncorrelated to the preceding components.

#### 5.3.1 Cluster analysis with PCA

In an initial step, **PCA** was used to provide an overview of the cluster structure of the data. The input data comprised 377 vectors (corresponding to the number of events) of length 481 (corresponding to the length of sonogram vectors), which can be thought of as 377 samples in a 481-dimensional space. These samples can be fully described by a 377-dimensional orthogonal vector system. It is calculated with **PCA** by solving the eigenvalue-problem of the covariance matrix of the mean corrected input vectors. The output of the **PCA** consists of 377 orthogonal eigenvectors with corresponding eigenvalues, which describe the variance along each respective principal component.

**PCA** revealed that more than 50% of the variance is explained by the first 80 principal components. However, already the data of the first two principal components (6.6% variance) show a clear cluster structure according to event type, as evident from Figure 5.5 for station A04 and Figure 5.8 for station A07. The amplitude normalization successfully prevents a clustering mainly thereof. For station A04, events belonging to the *DEEP* class are clearly separated from other events along the first principal component, whereas *QUARRY* events show a good separation along the second principal component. Interestingly, even the

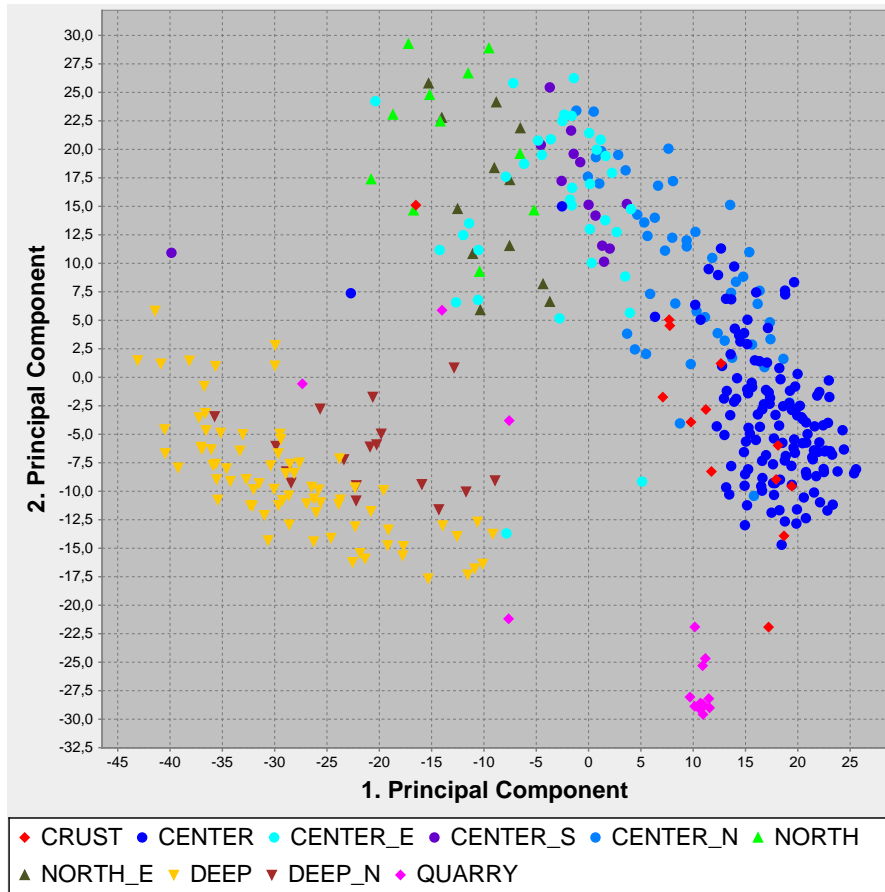


Figure 5.5: Station A04 input data along first two principal components clustered by regional classes. Good separation of *DEEP* and *QUARRY* events.

*CENTER* and the *NORTH* classes tend to populate separate clusters despite their similarity in hypocenter depth (Figure 5.7). As expected, there is an overlap between the *NORTH* class and the *CENTER\_E* sub-class, likely due to their similarity in terms of distance to the measurement station. Statements about the *CRUST* class are difficult, given the low number of events, although there seems to be a tendency for considerable overlap with the *CENTER* class along the first two principal components. See also Figure 5.6, 5.9 and 5.10.

### 5.3.2 Feature reduction

Although the sonogram transformation already leads to a considerable feature reduction, the number of features (481) still

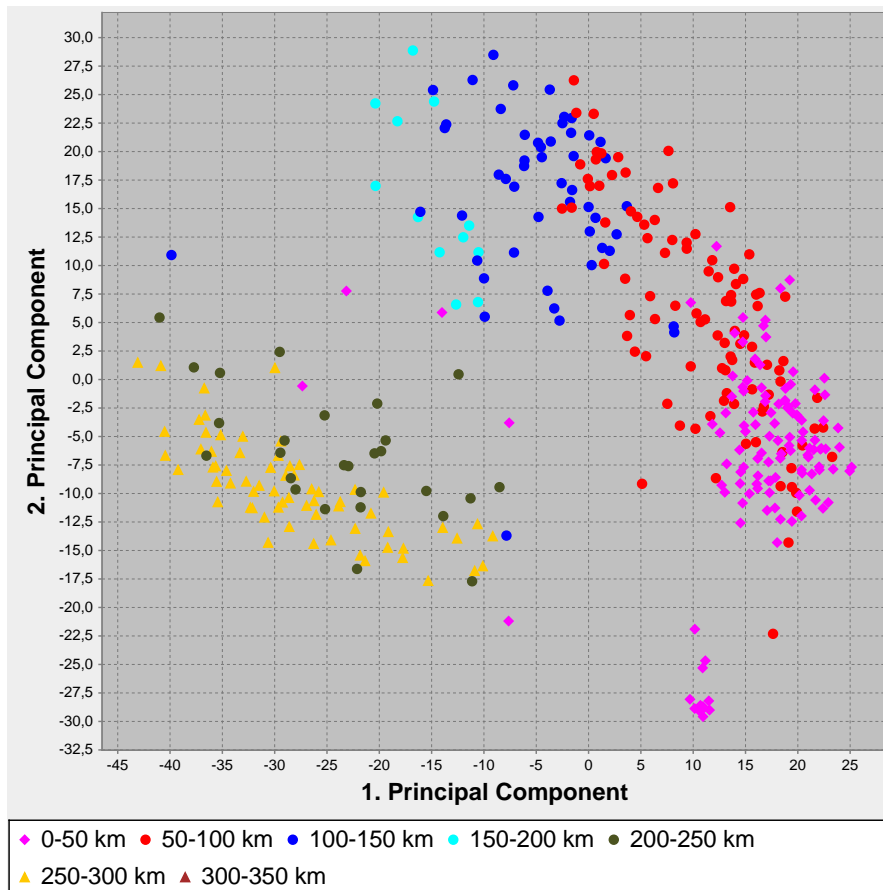


Figure 5.6: Station A04 input data along first two principal components clustered by epicentral distance. *QUARRY* events with similar epicentral distance to *CENTER* events are well separated.

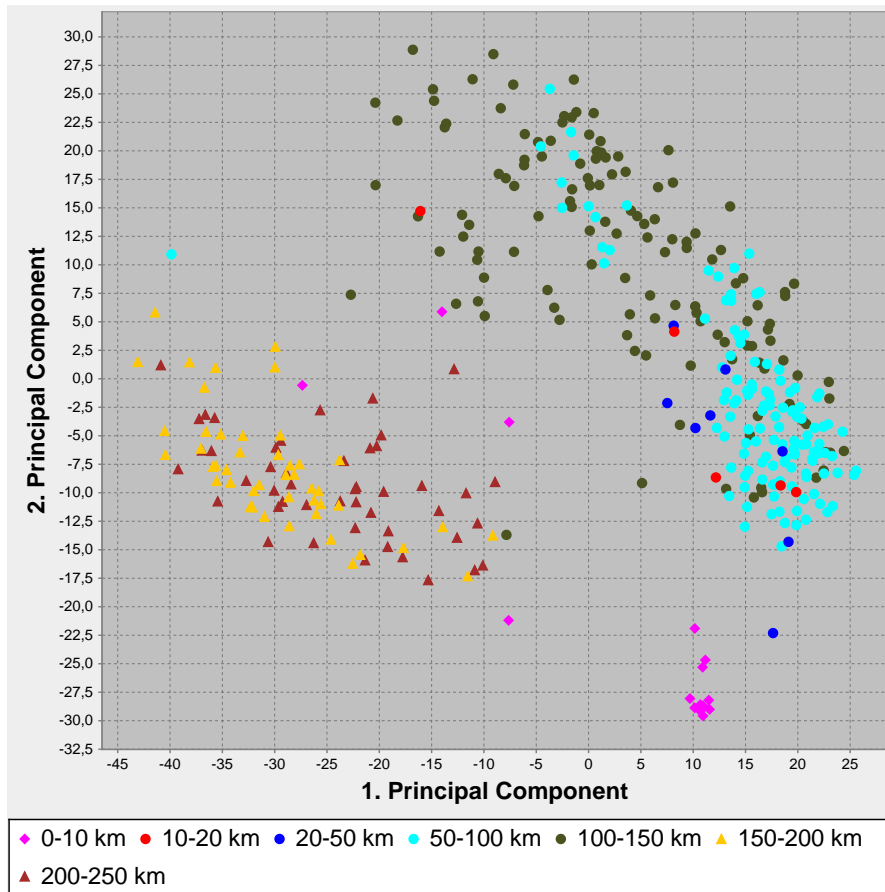


Figure 5.7: Station A04 input data along first two principal components clustered by depth. Sub-clusters of *CENTER* and *DEEP* are not well separable by depth.

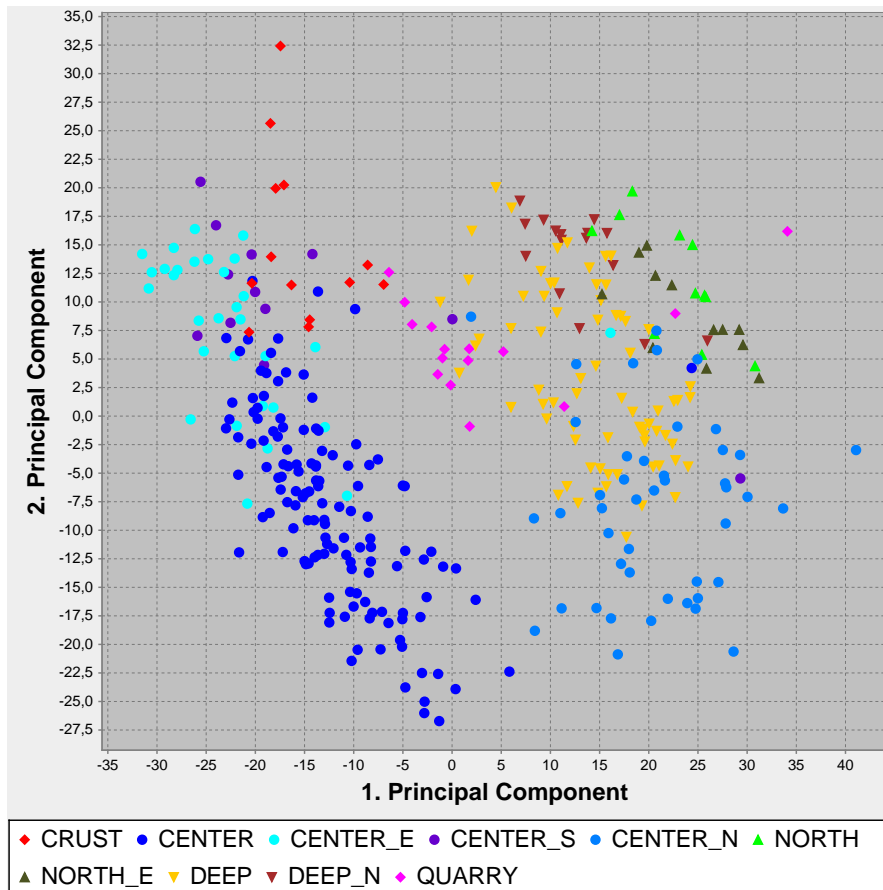


Figure 5.8: Station A07 input data along first two principal components clustered by regional classes. Worse separation of classes. *DEEP* events overlap with *CENTER\_N* events with similar epicentral distance.

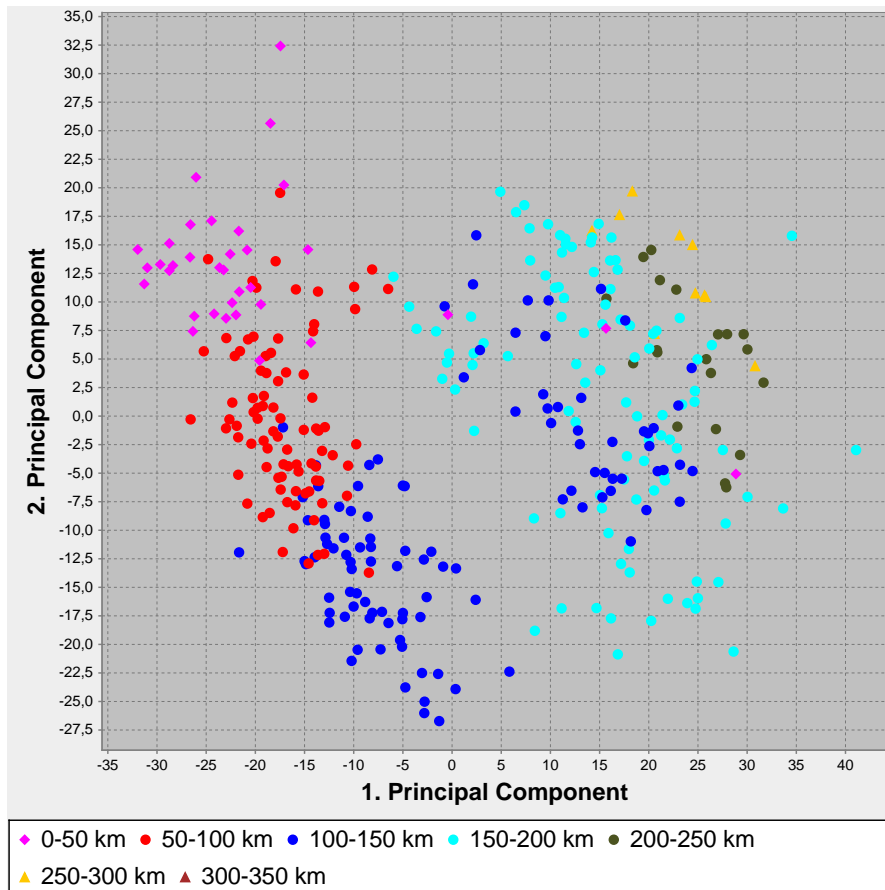


Figure 5.9: Station A07 input data along first two principal components clustered by epicentral distance. Worse separation of classes. *DEEP* events overlap with *CENTER\_N* events with similar epicentral distance.

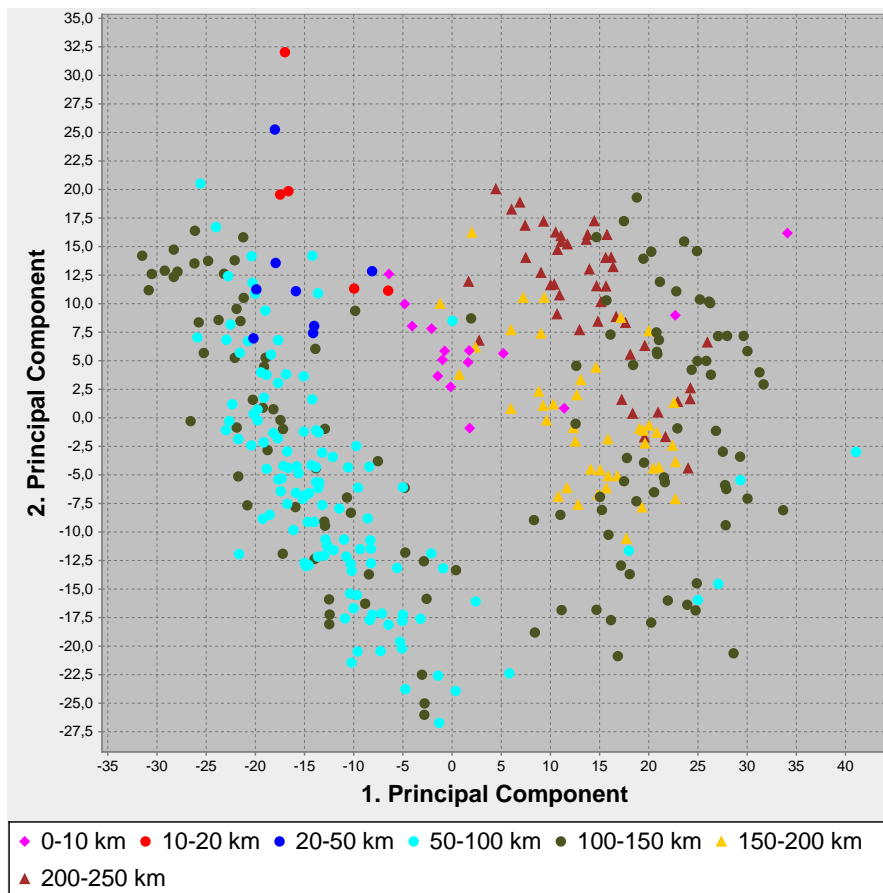


Figure 5.10: Station A07 input data along first two principal components clustered by depth. Worse separation of classes. *DEEP* events overlap with *CENTER\_N* events with similar epicentral distance. Depth does not provide a strong cluster separation.

exceeds the number of samples (377), bearing the danger of the curse of dimensionality (see e.g. Bishop (2006)). Therefore PCA is applied to further reduce the number of features using the Silhouette coefficient (Rousseeuw, 1987) to estimate the optimal number of principal components. The Silhouette analysis revealed the first 80 principal components as the optimal number of components, which together account for around 50% of the variance. All subsequent analyses are therefore based on these 80 first principal components. A reference example of a similar feature reduction technique can be found e.g. in the “Eigenfaces” face recognition algorithm (Turk & Pentland, 1991).

### 5.3.3 Visualization by back-transformation

Inverse transformation can be used to visualize the 80 principal components of each event in sonogram space. Given that some of the variance is lost in the 297 unused principal components, the inverse transformation yields a blurred version of the original sonograms. Figure 5.11 shows a back-transformed event of the *CENTER* class, which still contains most of the coarse characteristic features of this class (like e.g. frequency content and  $t_s - t_p$  time difference), whereas small details are smoothed due to implicit low-pass filtering. This reduction in complexity allows to use it as a visual inspection tool for the operating analyst. Figure 5.12 shows the back-transformation after PCA for the five exemplary events of each class from Figure 5.3.

### 5.3.4 Variations along principal components

To visualize the variation in the sonograms along a given principal component, the eigenvectors of all other components are set to zero. The current eigenvector is sampled in discretized steps from the lowest to the highest value (according to the variance). The back-transformed sonograms of 5 sampling steps along each of the first three principal components are depicted in Figure 5.13. Here, the linear variation of the eigenvector results in com-

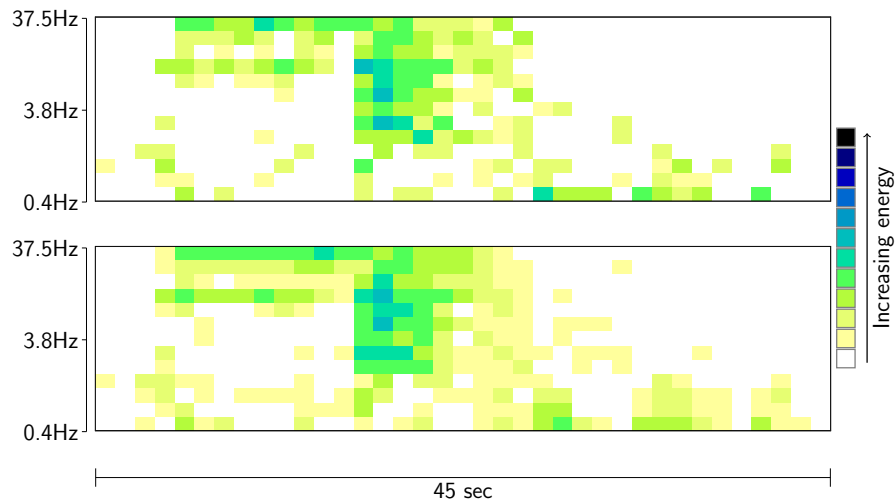


Figure 5.11: Original sonogram of *CENTER* event on the top, *PCA* forward and back transformed sonogram with 80 principal components. The *PCA* transformed sonogram has less sharp changes in frequency and time.

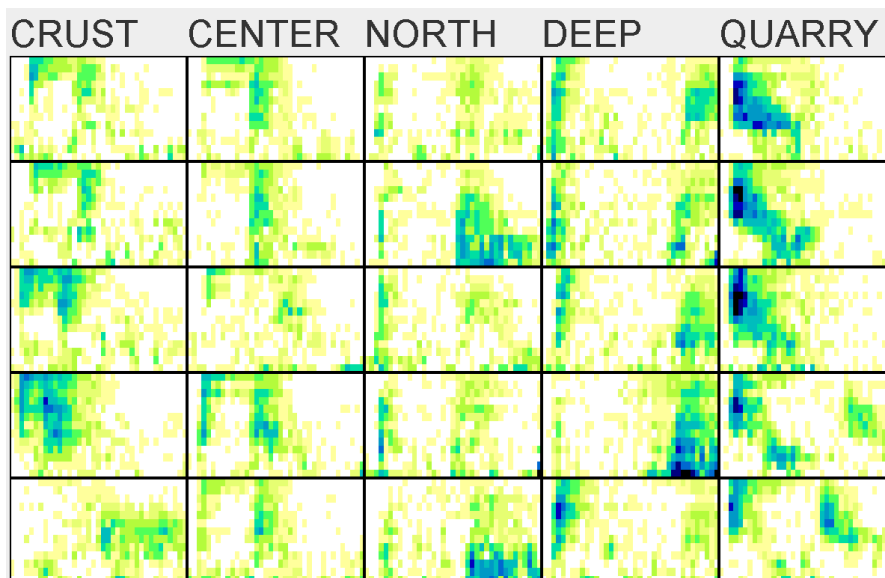


Figure 5.12: Five exemplary events of each of the five classes back transformed with 80 principal components.

plex variations of the back-transformed sonograms. These quite complex variations of a feature vector are conveniently visualized in sonogram space. The first principal component, which contains 4.0% of the total variance, clearly affects the energy of the events and the  $t_S - t_P$ -onset time difference. This characteristic likely explains the strong separation of *DEEP* events along the first principal component. The second and third principal component (2.6 and 1.9% variance) affect mostly the relocation of energies from small delays after the P-onset to larger ones. This behavior likely explains the separation of *QUARRY* events from other events, due to their diagonal energy “tail” in the P-coda. Succeeding principal components contain less than 1.5% of the total variance per component and are based on a mix of multiple features, preventing a simple description. Note that a single principal component contains two-dimensional properties of the sonograms. For instance in Figure 5.13, the first principal component comprises the feature associated with the  $t_S - t_P$ -onset time difference (horizontal sonogram feature) and the feature associated with a energy shift along the frequencies (vertical sonogram feature). The Euclidean distance on the values of the principal components can therefore be seen as a two-dimensional distance measure in sonogram space.

#### 5.4 SELF-ORGANIZING MAPS (SOMS)

**PCA** provides a first overview of the cluster structure within the data and is useful for feature reduction. In a next step, self-organizing maps (**SOMs**) (Kohonen, 2001, 1982) are used to generate a low-dimensional topological map of the data space. The resultant map consists of a pre-specified number of nodes, each of which may represent a certain class of events (“prototypes”). **SOMs** were first used for the analysis of seismic data by Maurer (1992) and some studies have followed since (Musil & Plesinger (1996); Essenreiter et al. (2001); Tarvainen (1999); Masiello et al. (2005); Klose (2006); De Matos et al. (2007); Esposito et al. (2008); Langer et al. (2009); Köhler et al. (2010)). These previous studies have used the **SOM** algorithm for the

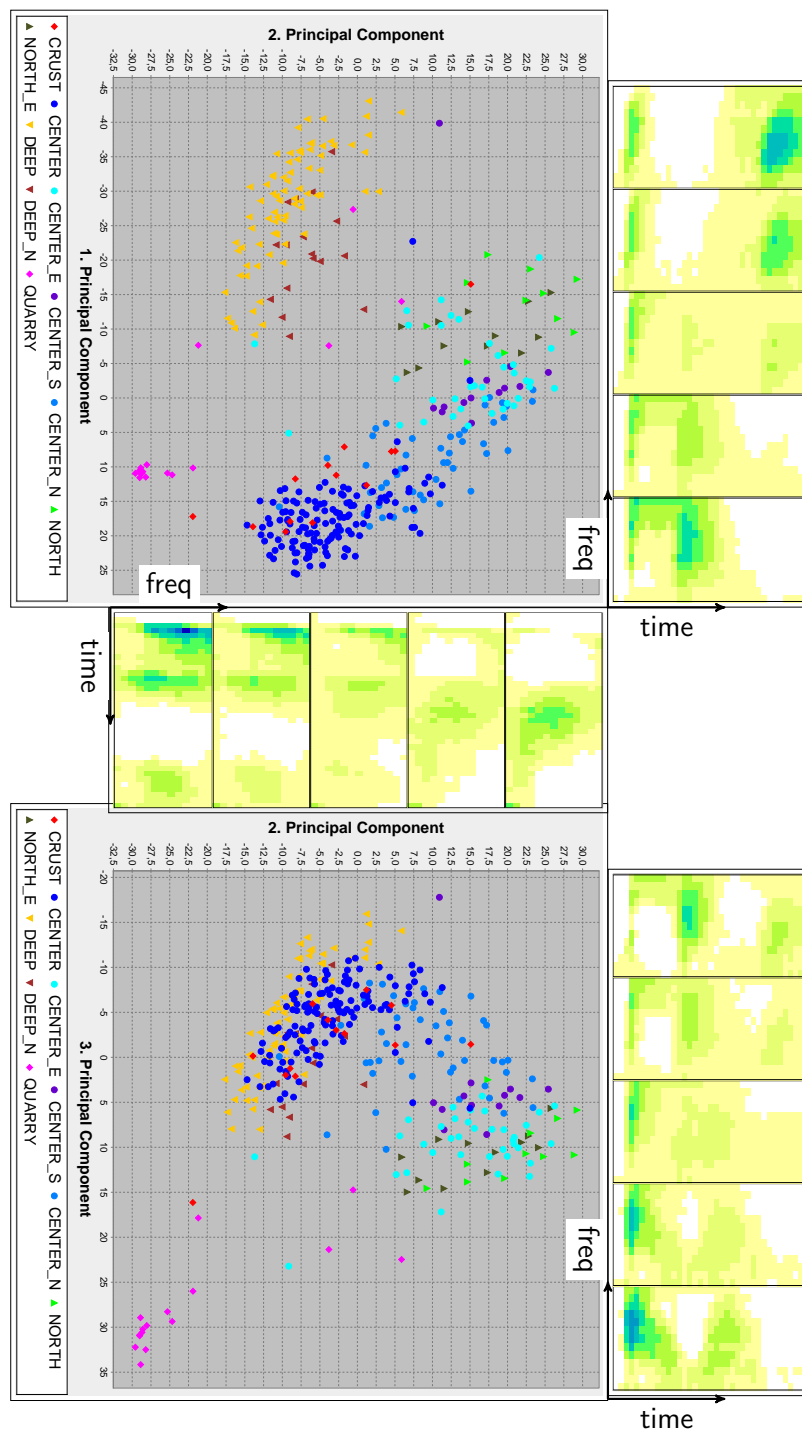


Figure 5.13: Visualization of events in the two-dimensional space spanned by the first and the second principal component (left panel) and by the second and the third principal component (right panel). Sonograms depict the variation along each principal component.

extraction of prototypical event clusters, but apart from Köhler et al. (2010), not for classification. Furthermore these studies lack the convenient visualization ability provided by the sonogram data format. The SOM consists of  $m = 50$  nodes, which are placed on fixed positions on a two-dimensional grid (5 rows, 10 columns). The number of rows and columns was chosen empirically. Each node has an associated weight vector, which is located in the input space. For the visualization of the SOM algorithm the two-dimensional representation of the events from Figure 5.5 are used hereafter. Note, that the actual input space is 80-dimensional, whereas the SOM grid itself is two-dimensional. A similar algorithm from unsupervised learning is the k-means clustering (Forgy, 1965). However k-means does not provide the 2-dimensional topologic projection introduced by the neighbourhood function of SOMs and thereby is less suitable for visual inspection.

The SOM is trained in an iteration loop over so-called epochs (denoted by  $t$ ):

1. Before the start of the first training epoch, the weight vectors of the SOM nodes are initialized along an equally spaced grid of the first two principal components (Kohonen & Somervuo (2002)) of the input data (Figure 5.14 (a)). The remaining principal components are set to zero. The weight vectors therefore span an orthogonal grid in the first two input space dimensions upon initialization, similar to the representation in section 5.3.4 (random initialization of the weight vectors is another common technique, but typically increases training time).
2. During training, data samples (PCA-reduced sonograms of events) are sequentially passed to the SOM. For each training sample  $x_i$ , a winning node is determined based on the shortest Euclidean distance between the weight vectors associated with each node and the data vector. Subsequently, all nodes  $w_j$  are adapted according to Equation 16, where  $\alpha(t)$  is the learning function (Equation 17) and  $h(r, t)$  is the neighbourhood function (Equation 18). Within each

epoch, all samples of the training set are presented to the **SOM**. The learning function  $\alpha(t)$  monotonically decreases as a function of  $t$  to ensure a smooth unfolding of the map. The neighbourhood function is a two-dimensional symmetric Gaussian function  $\mathcal{N}(0, 1)$  in the map space with its maximum at the winning node, thereby introducing a distance dependency for the update of the weight vectors. The closer a node to the winning node, the more its associated weight vector will be pulled towards the current input data vector. Note that the neighbourhood function operates in map space and not input space.

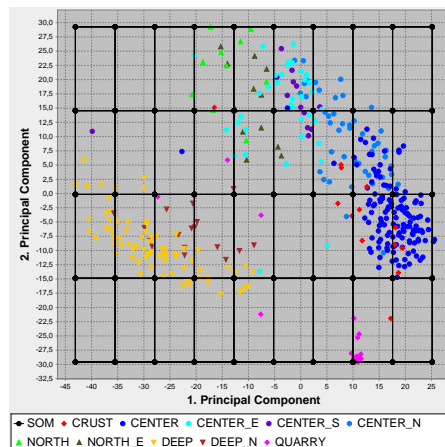
3. The training cycle is repeated for a predefined number of  $T_{\text{Max}} = 2000$  epochs. The result of a trained map in the input space is shown in Figure 5.15 (a).

$$w_j(t+1) = w_j(t) + \alpha(t) h(r, t) (x(t) - w_j(t)) \quad (16)$$

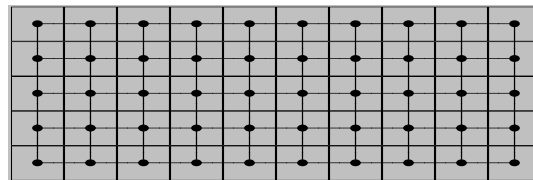
$$\alpha(t) = 1 - \frac{t}{T_{\text{Max}}} \quad (17)$$

$$h(r, t) = e^{\left(-\frac{r^2}{2 \cdot \sigma^2(t)}\right)} \quad (18)$$

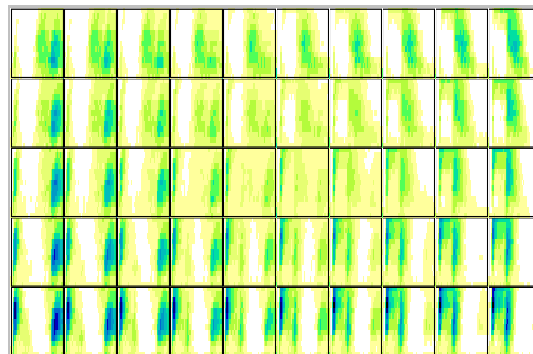
Figure 5.15 (b) shows a converged **SOM** after training on the training dataset. Colored rectangles depict the class labels corresponding to the event class for which the node was the winning node in the last training epoch. For instance, the upper left node selectively represents *NORTH* events (green rectangles). The right half of the map is generally dominated by *CENTER* events, while the bottom left is dominated by *DEEP* events. The thickness of the borders between node cells depicts the Euclidian distance between nodes and shows that the *DEEP* cluster (orange) is clearly separated from the rest of the data, which was to be expected given the considerable separation already along the first two principal components (Figure 5.15 (a)).



(a) Initialization of SOM weight vectors in PCA space.

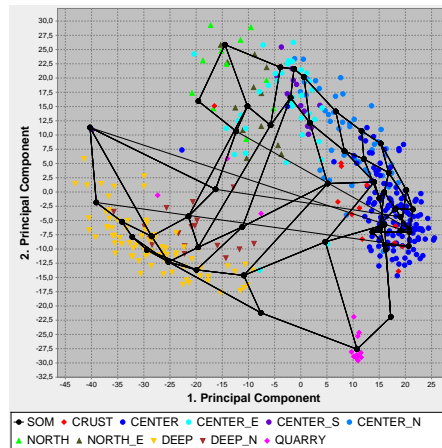


(b) SOM grid before learning. The nodes have no input data attached yet.

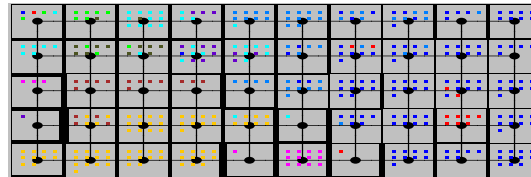


(c) SOM nodes visualized by back-transformed sonograms before learning.

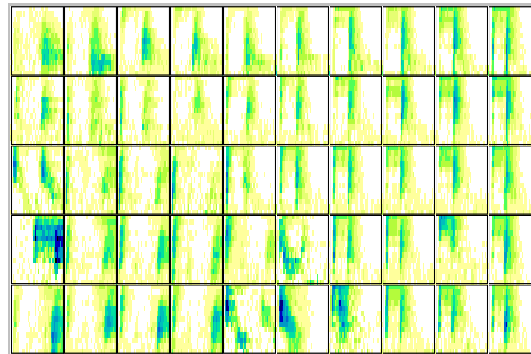
Figure 5.14: Initialization of the SOM. Individual clusters are shown as different colors. Connections between map nodes in the input space indicate neighbouring nodes in the map space. (a) A weight vector located in input space is assigned to each node (black dots) of the map. (b) The fixed nodes in the map space. (c) The weight vectors of the nodes in the map space visualized as sonograms. These sonograms are a sampling of the PCA space at initialization and show the changes along individual components.



(a) Learned SOM weight vectors in PCA space.



(b) SOM grid after learning with labels of corresponding input data.



(c) SOM nodes visualized by back-transformed sonograms after learning.

Figure 5.15: A trained SOM. The proximity of nodes on the map reflects the similarity of the weight-vectors. The input space is now projected in a topology-preserving manner onto the map space such that the proximity of nodes on the map reflects the similarity of the weight vectors. (b) Black borders between SOM nodes indicate similarity of the corresponding nodes (thicker borders correspond to a lower similarity). (c) The SOM sonograms now represent individual event clusters.

#### 5.4.1 Visualization of SOM nodes

Another major advantage to use sonograms as features is their visual interpretability and, in the context of the SOM algorithm, the ability to transparently visualize the trained SOM. A trained SOM allows the analyst to quickly identify different prototype events represented by the nodes of the SOM. Figures 5.14 (c) and 5.15 (c) show the SOM in sonogram space before and after training. Ideally, the nodes capture all distinct and common event types within the entire dataset. Another feature of the SOM is that the underlying algorithm preserves the topology of the input data, that is, similar event classes are grouped together, whereas highly dissimilar event classes are further apart in the two-dimensional SOM space. A dominant factor for the topological alignment is the  $t_s - t_p$ -onset time, as evident from the energy onsets in Figure 5.15 (c) where long  $t_s - t_p$ -onset times can be seen on the left side of the SOM, whereas short ones on the right side.

#### 5.4.2 Event locations of SOM nodes

Since the hypocenters of all events are known, the cluster structure of the trained SOM can be further investigated based on hypocenter location. A convenient way to visualize hypocenter clustering is to overlay the measurement area on top of each node cell and to depict the location of all those events, for which the corresponding node was the winning node (Figure 5.16). The display additionally visualizes distance to the recording station (on the top of each node) and depth (on the right-hand side). The latter visualization reveals that the clustering is mainly based on distance and depth, rather than location, and most nodes seem to represent a narrow range with respect to hypocenter distance and depth. A prominent exception is the top left node, where a *CRUST* event with a small depth is grouped together with events from the *CENTER* and *NORTH* cluster with larger depths.

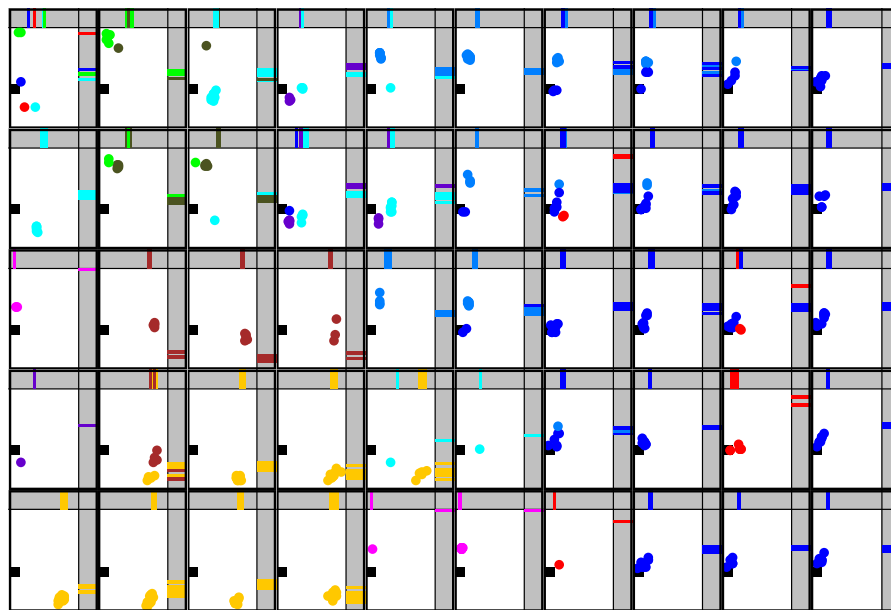
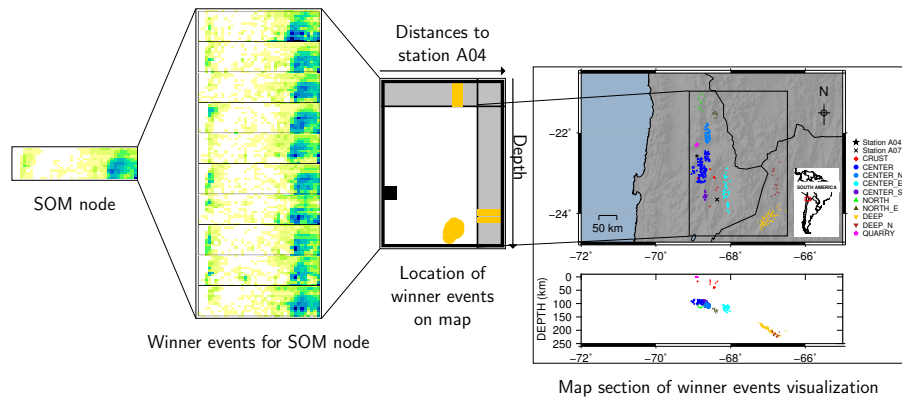


Figure 5.16: Locations of events for SOM nodes. Each node represents the rectangular geographic region depicted above and each dot corresponds to a location of an event in that region. The location of the station A04 is depicted in black. On the top of each node the events are visualized along a hypocentral-distance axis with the width of the node corresponding to the maximum distance from station A04. Events lying more to the right of that axis are further away from the recording station. The axis on the right-hand side of each node displays the depth of each event, increasing to the bottom. A prominent feature of the map is a general clustering of events according to depth and hypocenter distance.

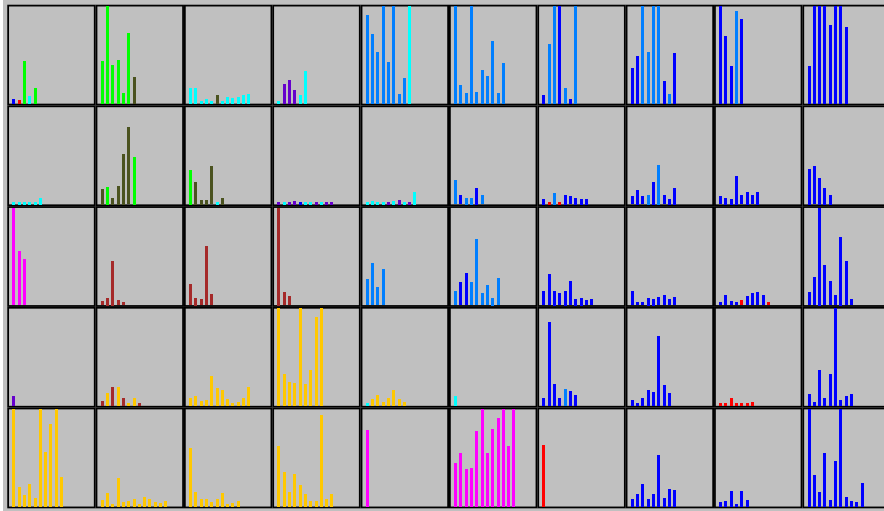


Figure 5.17: Vertical bars show the amplitudes of events for SOM nodes. Although some nodes show only events with similar amplitudes, a general (unwanted) clustering according to amplitude is not existent. Note that the bars are cut-off at 10,000 nm/s to visualize the dynamic range of smaller amplitudes.

### 5.4.3 Amplitude invariance

An important goal of the analysis is to extract clusters of events according to source process and geographic location, but independent of the overall magnitude of events. To this purpose the amplitudes of all sonograms are normalized (see section 5.1). To test whether this normalization procedure successfully eliminated the influence of amplitude, the SOM is visualized in terms of the individual maximal amplitudes (corresponding to the maximal amplitude of the underlying unfiltered seismograms) of the events (Figure 5.17). Although a few nodes comprise predominantly weak events, there is clearly no consistent topological ordering with respect to amplitude across the SOM. Most nodes capture a large range of different amplitudes, demonstrating the effectiveness of the amplitude normalization.

#### 5.4.4 Supervised classification with SOM

The trained SOM allows to classify new events based on a nearest-neighbour comparison. To guarantee the independence of training and test data, a two-fold cross-validation procedure is applied, in which the dataset is split multiple times randomly into a training and a testing dataset under the constraint that each class is represented evenly. Note, that in the previous Figures all of the events were shown.

1. PCA is performed on the training dataset and the sonograms of the training events are transformed in the space of the first 80 principal components. Subsequently the SOM is trained on the PCA-reduced sonograms of the training dataset.
2. Each node of the trained SOM is given a class name label based on the maximum number of events for which the node was the winning node (assigned events). E.g. if the majority of assigned events were from the *CENTER\_E* class, the SOM node label will also be *CENTER\_E*. If there is no clear assigned events class because at least two event classes are represented more than once, the node is discarded. E.g. if the assigned events contain at least two events from the *CENTER\_E* and at least two events from the *QUARRY* class. After SOM nodes are given a label, all assigned events are given this same label for later classification. For discarded SOM nodes, the events retain their original label.
3. PCA is performed on the test dataset and the sonograms of the test events are transformed in the space of the first 80 principal components.
4. In the classification step, each test event is assigned the class label pertaining to the SOM node with the smallest Euclidean distance in input space (one-nearest neighbour classification). To quantify the classification accuracy, the

assigned class labels are compared with ground truth labels.

5. Training dataset and test dataset are switched and the previous four steps are repeated.

The random division in training and test dataset and the classification is repeated 100 times to avoid any bias. The final classification for each event is based on the average of all cross-validation runs. Figure 5.18 shows the confusion matrix for all sub-classes for stations A04 and A07 (the sum of events might deviate from the total number of events due to rounding errors). As evident from the confusion matrix, all meta-classes (*CENTER*, *NORTH*, *QUARRY*, *CRUST* and *DEEP*) are almost perfectly classified and mis-classifications mainly affect sub-classes of the same meta-class. Remarkably, the correct classification of *QUARRY* events also includes most events with a double-explosion. The fact that the *CRUST* class is classified below average is likely explained by the similarity to the *CENTER* classes. The overall classification accuracy is 95.1% for the five meta-classes. If the sub-classes are taken into account as well, an overall correct classification rate of 80.5% is achieved for station A04 and 86.3% for station A07, respectively. Although the separation of classes for station A07 on the first two principal components as shown in Figure 5.8 was significantly worse than for station A04 (Figure 5.5), the total classification accuracy is better. This shows that either more significant cluster separations for station A07 lie in lower dimensions or that the improved rate stems from the better separation of the clusters *CENTER* and *CENTER\_N* in the first two components which include both a large amount of events. Confusion matrices are also plotted for the epicentral distance and depth classes which show a good clustering for both stations. Most mis-classifications are at the neighbouring classes which can be explained by events close to cluster borders.

As an additional control analysis the sonogram feature extraction is replaced by a seismogram-based feature extraction, in which features corresponded to the seismograms filtered at

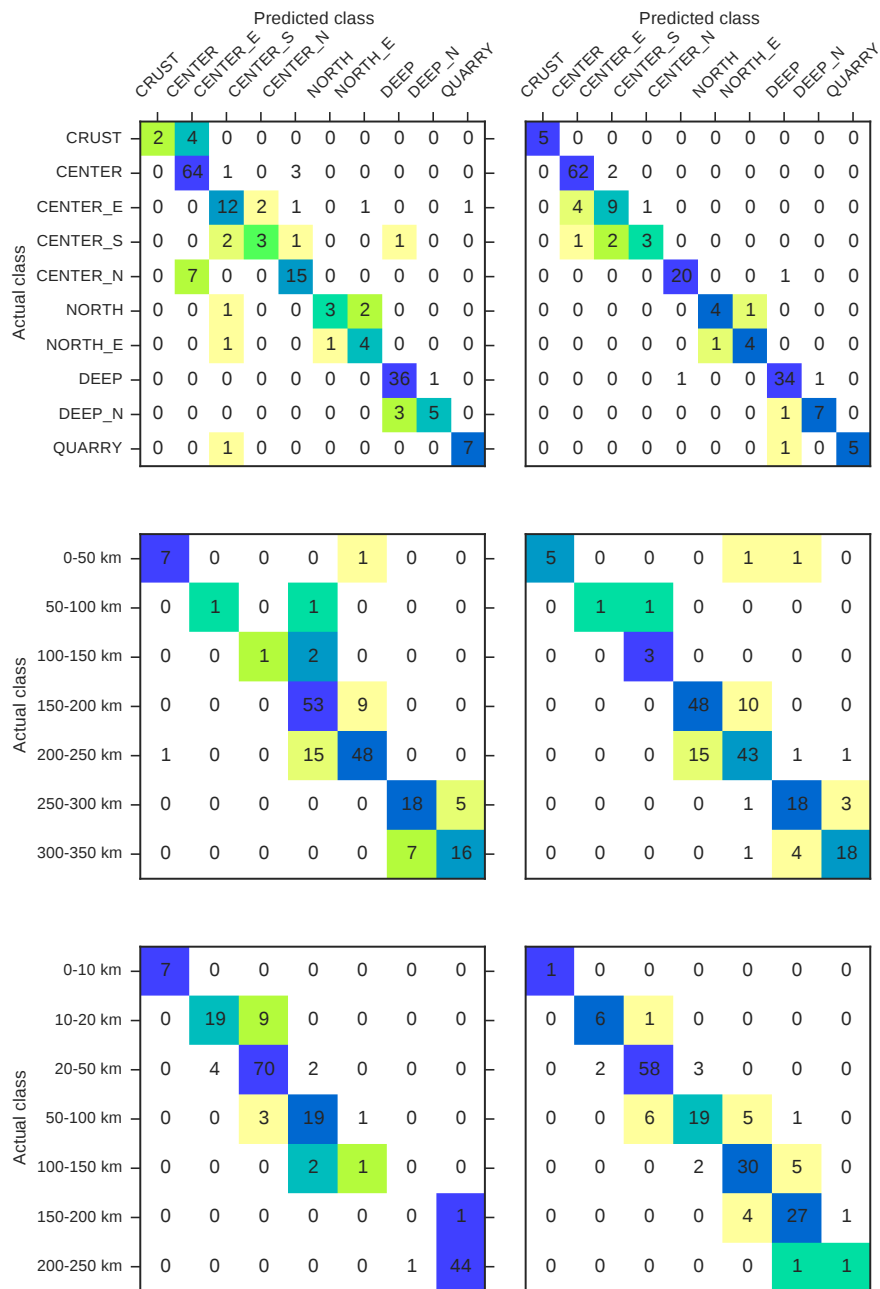


Figure 5.18: Confusion matrices for stations A04 and A07 of the classification with SOM for the regional, epicentral distance and depth classes. CRUST events have as expected the worst accuracy due to their strong similarity to CENTER events and few available events for training.

different bandpass frequencies. This procedure was inferior to the sonogram-based approach with classification accuracies ranging between 50-70% for the five meta-classes.

To test how the classification accuracy deteriorates if the SNR of the events is lower, artificial Gaussian noise was added to the seismograms before sonogram generation and further processing. Figure 5.20 shows the confusion matrix of the previously described classification scheme, where Gaussian noise with a variance corresponding to 25% of the median maximum value of all unfiltered event seismograms was added. Despite the addition of noise, the classification accuracy showed only a moderate drop to 75.6%, demonstrating the robustness of our approach even under noisy conditions.

#### *Exploratory analysis with additional machine learning algorithms*

Exploratory analyses with a random forest classifier (Tin Kam Ho, 1995) and a naïve Bayes classifier (e.g. Zhang 2004) (replacing the one-nearest neighbour classifier) did only yield small improvements in the case of the naïve Bayes classifier (random forest: 74.9% classification accuracy; Naïve Bayes: 81.9%). A comparison of the confusion matrices of both classifiers is presented in Figure 5.20 in the left column. These algorithms in contrast to all others were not re-developed but the scikit-learn Python library was used (Pedregosa et al., 2011).

The training with the random forest also allows a visualization of the sonogram pixels which turn out to have the strongest discriminative power for the algorithm, see Figure 5.19. Especially high frequency pixels in the second quarter of the sonogram are of importance. High energy in this area is only present in the *CRUST* and *CENTER* classes.

#### *Exploratory analysis with deep neural networks*

SOMs are a special kind of neural network with one layer and an alternative learning function compared to the commonly used back propagation algorithm. Recent breakthroughs in speech and image recognition with deep neural networks (deep learn-

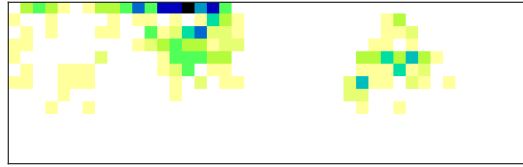


Figure 5.19: Random forest feature importance. The energy of each pixel represents the discriminative power of it for the algorithm. Notice the highest importances are in the high upper frequencies of the second quarter most prominent in the *CRUST* and *CENTER* classes.

ing) which make use of many neural network layers motivated a further test of these techniques on the [PISCO](#) data. The study here is only of exploratory nature and individual techniques are not explained in detail. This section only shows the general possibility of using deep learning in seismology. Although typical training datasets in deep learning are in the range of hundreds of thousands or millions, promising results could be obtained already without expanding the [PISCO](#) training set artificially. Overfitting can be a problem with such a small dataset. Three deep neural network architectures were tested: a conventional neural network ([NN](#)), a recurrent neural network ([RNN](#)) with long short term memory ([LSTM](#), [Hochreiter & Schmidhuber 1997](#)) and a convolutional neural network ([CNN](#)), [Homma et al. \(1988\)](#).

[RNN](#) weight learning is dependent on previous network states which fits to the usage for time dependent seismic signals. First tests in seismology with [RNNs](#) were done by [Wiszniowski et al. \(2014\)](#); [Doubrovová et al. \(2016\)](#) but only with single layer architectures. Their feature engineering is similar to the sonogram feature extraction as they use a filter bank of [STA/LTA](#) ratios as input to the network.

The [CNN](#) approach is new in seismology and is motivated by the two-dimensional representation in sonograms. [CNNs](#) are primarily used in image recognition tasks as they learn image processing filters as network weights. Since 2012 they have beaten most image processing benchmarks ([Ciresan et al., 2012](#)). These filters can contain special edge or blob detections which

can be useful to classify seismic events in sonograms which display certain two dimensional patterns.

Since 2005 Graphical Processing Units (GPUs) are used in machine learning to train neural networks more efficiently (Steinkraus et al., 2005) which allows deeper networks. In this study a computer with an Intel Core i5 4-core and 3.1 GHz in combination with a Nvidia GeForce GT 640 GPU is used for training and prediction. The Python neural network library Keras (Chollet, 2015) was used to create and train the neural networks. Keras in turn uses the Theano (Theano Development Team, 2016) library to do necessary tensor calculations on the GPU.

The following neural network layouts were used (inspired from the Keras documentation):

- The conventional neural network layers:
  1. Fully connected input layer
  2. Dropout layer (dropout fraction 0.5)
  3. Fully connected layer
  4. Dropout layer (dropout fraction 0.5)
  5. Fully connected output layer
- The recurrent neural network layers:
  1. LSTM layer
  2. Dropout layer (dropout fraction 0.25)
  3. LSTM layer
  4. Dropout layer (dropout fraction 0.5)
  5. Fully connected output layer
- The convolutional neural network layers:
  1. Convolutional layer (3x3 convolutional filter)
  2. Convolutional layer (3x3 convolutional filter)
  3. Max-pooling layer (downscale the sonogram images by a factor of two in both dimensions)
  4. Dropout layer (fraction 0.25)

5. Flatten layer (convert the two-dimensional input into one-dimensional arrays)
6. Fully connected layer
7. Dropout layer (fraction 0.5)
8. Fully connected output layer

For a detailed description of each layer, please consult the Keras documentation. Results of all three neural network architectures can be seen in the confusion matrices in Figure 5.20 in the right column. By using CNNs the highest classification rate of 82.9% could be obtained. NNs scored 81.8% and RNNs 78.8% (all with station A04 and the fine grained clusters).

#### *Comparison to polarization analysis*

A well-established method to roughly locate seismological events detected only at a single station is a polarization analysis, in which the back azimuth and incidence angle of events are estimated from the particle motion at a three-component station by PCA (section 4.1.1, Jurkevics 1988). Here a polarization analysis to compare the ensuing results to our SOM-based classification approach is performed. The polarization analysis resulted in a mean back azimuth error of  $44.0^\circ$  for the 377 events. A comparison to the pattern recognition approach can be done by comparing true event back azimuths to the ones of their nearest neighbour from the SOM based classification, as described above. This latter approach results in a mean error of only  $19.8^\circ$ . However, the comparison is limited, as the position of station A04 relative to the studied events limits back azimuths between  $197^\circ$  and  $359^\circ$ . Of note, the SOM-based pattern recognition approach, as opposed to the polarization analysis, works on single-component records.

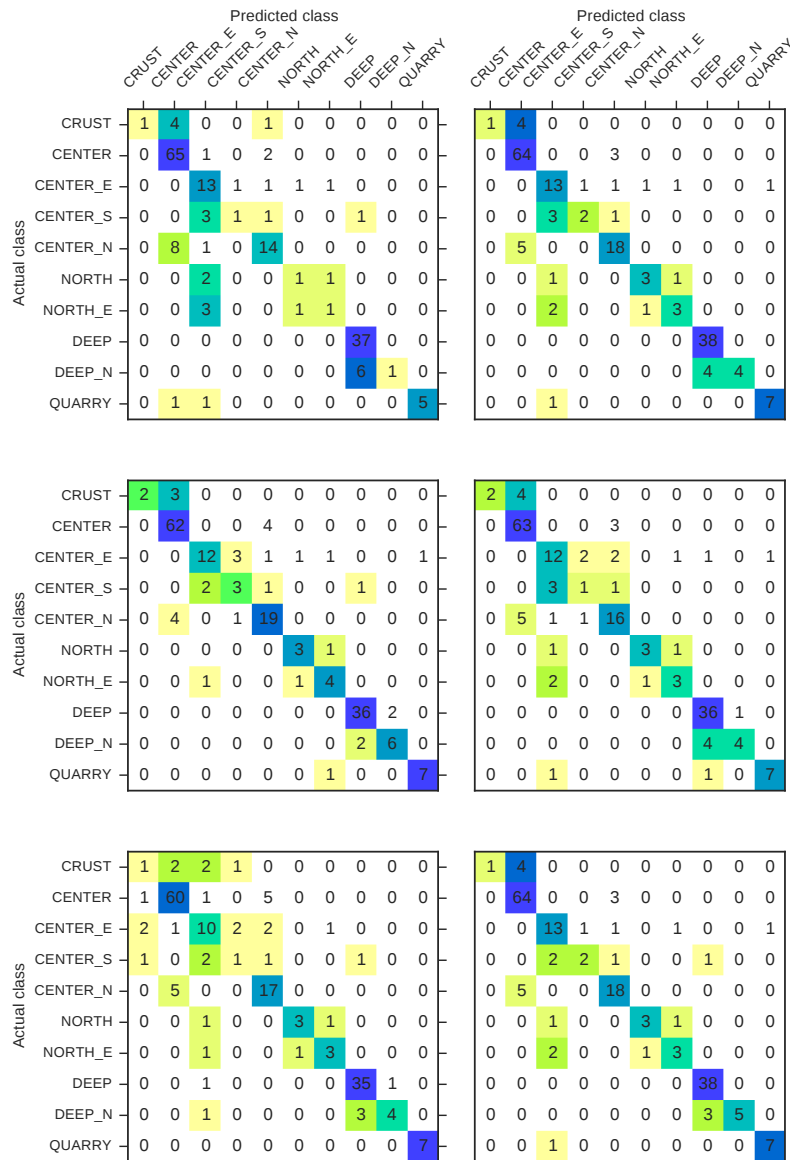


Figure 5.20: Confusion matrices of the classification with SOM and exploratory analyses with the following classifiers: random forest (top left), naïve Bayes (center left), neural network (top right), recurrent neural network (center right) and convolutional neural network (lower right). Furthermore the confusion matrix of the classification with SOM with an artificially increased noise floor by adding Gaussian noise with a variance corresponding to 25% of the median maximum value of all unfiltered event seismograms (lower left).



---

## COMBINATION OF NETWORK AND ARRAY WAVEFORM-COHERENCE FOR SEISMIC EVENT LOCATION

---

While the previous chapter 5 showed the capabilities of single station event clustering, this chapter introduces a new method to locate seismic events in small networks by source scanning.

Seismic monitoring in most cases includes seismic event location to characterize events. The location in conjunction with the observed amplitudes allows to calculate the event's magnitude which provides a way to estimate the released energy of an event. The released energy allows reasoning about fracture sizes. Event location furthermore provides a way to relate events to each other and to possibly existing fracture zones. In induced seismicity monitoring the estimation of epicenter location and especially hypocenter depth plays a significant role to draw conclusions if an event was in fact induced. Induced origins are more probable if an event lies in the region of carbon extraction fields. Otherwise it might have come from natural stress releases. This chapter shows two main approaches to seismic event location: the conventional way by phase picking and the minimization of residuals, and source scanning on predefined location grids without phase picking. Another approach to the location of seismic events is the relative location. Relative location can be done by pattern recognition as shown in section 4.1.2 and chapter 5. If earthquake clusters exist, the master event or double-difference minimization as done by the software HypoDD [Waldhauser \(2000\)](#) can also lead to improved results as shown by [Schaff et al. \(2004\)](#). However all relative loca-

tion techniques introduce restrictions by the need of previously registered events and will not be discussed in this chapter.

### 6.1 PROBLEMS OF CONVENTIONAL RESIDUAL MINIMIZATION

Conventional seismic event location is done by the minimization of residuals between theoretical and observed onset times (both travel time and origin time is unknown). The Geiger inversion scheme (Geiger 1912, original Geiger 1910 in German) is used mostly to find the minimum residual. Alternatively a grid search can be used as is done for example by the widely used location software NonLinLoc (Lomax et al., 2009). NonLinLoc uses a 3D travel time calculation library by Podvin & Lecomte (1991) and iterates over a 3D location grid. For each grid point the theoretical travel time to each station is compared to the observed wave onset determined by a phase pick. Grid sizes are then refined around local minima to allow the reliable discovery of global minima in the solution space.

The problem of these approaches with uncertain phase onsets is the strict separation between single station phase picking and location procedure (for well defined phase onsets the separation can be an optimization advantage). No feedback exists between these steps which would allow for pick correction based on the results from the location procedure. A phase pick is only regarded as a single instant in time assigned with an uncertainty based on SNR mostly. Problems of wrongly associated picks can occur in manual and automated analysis and wrongly associated phases result only in an overall higher global residual. In automatic processing, wrongly assigned phases can only be identified by adding multiple manually defined rules to the location process or by a possible jack-knifing procedure where single phase picks are removed and strong differences of the residual are checked. Figure 6.1 shows an event example with conventional automatic phase picking. The seismograms were pre-filtered with a four pole Butterworth bandpass filter with corner frequencies of 5 and 40 Hz. The automatic picking algorithm FilterPicker (Lomax et al., 2012) was applied to pick

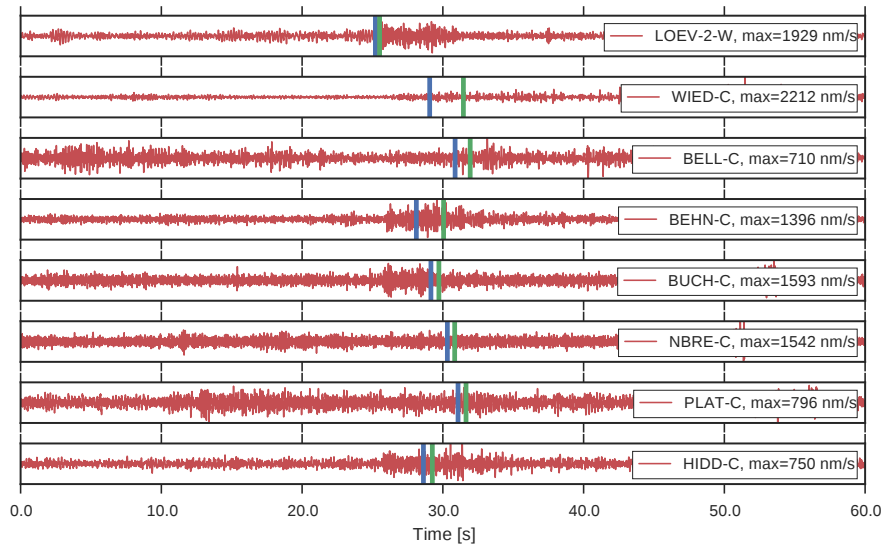


Figure 6.1: Automatic phase picking with low SNR event is not reliable. All seismograms were pre-filtered with a bandpass of 5 to 40 Hz. P-phases (blue) were picked on shown vertical traces, S-phases (green) on not shown horizontal traces with FilterPicker algorithm (Lomax et al., 2012). The only correctly picked phase is the P-phase of station LOEV. Multiple frequency bands, picking parameters and time windows were tested without significant improvements to the results.

P-phases on the vertical components and S-phases on the horizontal components (horizontal components are not shown in the Figure). Trigger thresholds for each trace were continuously decreased until a pick was found. Only one correct phase association could be determined for this event with this picker. Thereby the results are not usable for event location in that case. The same event will be successfully located automatically with source scanning in section 6.3.2 with an epicentral error of 2.2 km without array methods and 1.4 km with array methods.

The interactive graphical event location scheme which is primarily used in Nanoseismic Monitoring campaigns tries to establish a feedback between event location and picks. It is described in Joswig (2008) and uses tP-tP hyperbolae, tS-tP ellipsoids and array beams as event constraints in a graphical display. An analyst can examine each location constraint and connect it to the provided picks by the responsible stations. This allows the

re-evaluation of outliers and can improve low SNR event location tremendously. However the transfer of this technique into automatic processing would result in an extremely complex rule based system.

The next section will therefore examine the alternative approach of source scanning which allows a more reliable low SNR event location by connecting the location and arrival time determination without the need of large amounts of manually introduced rules.

## 6.2 SOURCE SCANNING AND THE INTEGRATION OF ARRAY METHODS

Source scanning allows to remove the single station detection decision by integrating all CFs from detection or phase picking algorithms into the location procedure. Location by source scanning is done on a predefined three dimensional geographic grid. Grid cell size and grid extensions are varied according to sought after events and the recording network setup. The P and S travel times between each grid cell and each seismic station and the CF at each seismic station are calculated a priori. Hypothetical seismic events over a range of source times are assumed at each grid node. For each of these events, the CFs of all stations are shifted by their theoretical travel times (of P and S waves respectively) and stacked (Figure 6.2). The theoretical travel time calculation requires a local velocity model and is therefore subject to error (which will be discussed later in the paper). These travel time errors and the onset uncertainty can be included by stacking a small region weighted by a Gaussian distribution around the theoretical onset. Maxima in the resulting stack at specific times and grid locations indicate events. The new method proposed in this study extends the conventional source scanning work-flow by using additionally array processing methods to calculate specific CFs for each grid cell and array station.

Source scanning is being developed since the beginning in 1994 (Shearer, 1994) from a method for teleseismic monitoring to

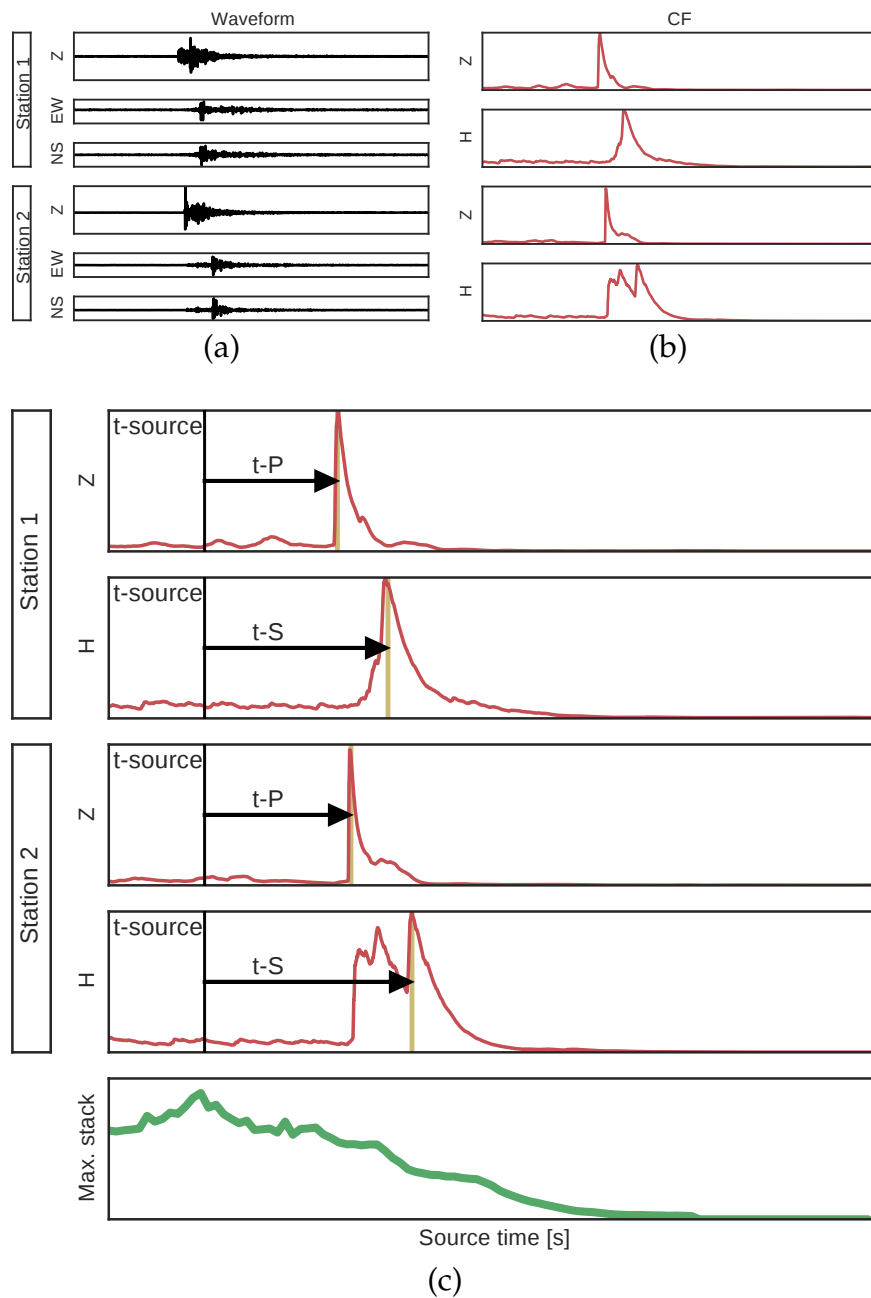


Figure 6.2: Overview of source scanning steps. (a) Data retrieval: loading of input data with bandpass filtered vertical and horizontal seismograms. (b) Data processing: calculation of a characteristic function (CF) to highlight seismic onsets. (c) Migration: loop over source time and hypocenter grid-cells with stacking of CFs at theoretical travel time onsets. The grid-cell for which the stack has its maximum is stored for each time step which allows to detect and locate events.

regional monitoring and lately to local microseismic monitoring. Depending on the monitoring challenges, different CFs are used and multiple improvements were integrated into the original algorithm. The term source scanning has been used first by [Kao & Shan \(2004\)](#) and refers to the “scanning” over source time and multiple potential source grid cells to test if an event hypothesis fits. Sometimes the term “(reverse time) migration” is used but originally refers to a method used in exploration seismics ([Gajewski & Tessmer, 2005](#)). Another similar method is the Kirchhoff location procedure ([Baker et al., 2005](#)).

[Shearer \(1994\)](#) was the first who used matched filters to detect expected profiles with long period seismic records in a teleseismic setting with *STA/LTA* as the CF. [Young et al. \(1996\)](#) further developed this method for the CTBT. [Ekstrom \(2006\)](#) used surface waves and developed a nested grid search.

The use of source scanning in regional and local monitoring was started by [Withers et al. \(1999\)](#) who correlated theoretical travel time envelopes with *STA/LTA*, similar to [Young et al. \(1996\)](#) but in a regional/local setting instead of a teleseismic one. [Kao & Shan \(2004\)](#) stacked normalized absolute values of seismograms. They introduced a small uncertainty window based on theoretical travel time errors for stacking. [Drew et al. \(2005\)](#) introduced the combination of P- and S-onsets by multiplication of the respective CFs. [Kao & Shan \(2007\)](#) extended their previous method by using seismic envelopes. [Gharti et al. \(2010\)](#) rotated seismograms into the LVQ system before stacking to improve S-onsets. [Liao et al. \(2012\)](#) made further improvements to the method of Kao by using a three-component analysis for P- and S-phase onsets and made the travel time uncertainty dependent on the grid cell sizes. [Grigoli et al. \(2013, 2014\)](#) picked up the original *STA/LTA* CF from [Shearer \(1994\)](#) to locate induced events from mining in Germany and crustal earthquakes in southern Italy. [Langet et al. \(2014\)](#) introduced the Kurtosis as a CF and located events related to volcano activities with source scanning. [Cesca & Grigoli \(2015\)](#) compared different CFs and showed that *STA/LTA* outperforms the energy, Kurtosis and envelope for mining induced events. [Zhang & Wen \(2015b,a\)](#) in-

roduced the match and locate method where, similar to [Young et al. \(1996\)](#), correlation was used to find a potential additional underground nuclear explosions test by the Democratic Republic of North Korea (discussions about the true nature of the detected event can be found in [Ford & Walter 2015](#)).

All mentioned studies about source scanning used networks of single seismic stations for the location. This thesis chapter however was motivated by the results of manual microseismic monitoring analysis with surface mini-arrays. The monitoring method is called Nanoseismic Monitoring ([Joswig, 2008](#)) and can increase detection and location capabilities with a small effort in comparison to single station networks ([Wust-Bloch & Joswig, 2006](#); [Häge et al., 2012](#); [Sick et al., 2012](#); [Walter et al., 2012](#); [Sick et al., 2013](#); [Blascheck et al., 2015](#); [Vouillamoz et al., 2016](#)). Small tripartite surface arrays with one three-component central station, three vertical-component satellite elements and an aperture of around 100 meters are used. The challenge was to transfer the manual analysis which combines network and array methods to an automatic processing.

The [CTBTO](#) uses the Global Association algorithm ([Bras et al., 1994](#)) with array- and single-station information. The algorithm uses a combination of the Intelligent Monitoring System ([Bache et al., 1993](#)) and Generalized Beamforming ([Ringdal & Kväerna, 1989](#)). Travel times, back azimuths, slownesses and a general probability for an event detection over a global grid for each station are pre-calculated. A least squares inversion is then used to find the most likely hypocenter. However slowness and back azimuth information (from three-component stations and arrays) is only used if less than seven “defining arrival times” are available ([Bormann, 2002](#)).

Motivated by the Global Association algorithm, first tests were made for this thesis with extensive rule based systems which combine conventional phase picking algorithms as e.g. from [Baer & Kradolfer \(1987\)](#); [Lomax et al. \(2012\)](#); [Küperkoch et al. \(2010\)](#) with a weighting from beamforming array analysis. However because the phase picking algorithms turned out to

be too error-prone with low SNR events, this approach did not yield the necessary accuracy.

To overcome the phase picking, a new combination of the robust location with source scanning and array processing techniques was developed. It turned out to work reliably even with few recording stations and low SNRs. After development of the method, a previous study, which combined source scanning and array methods was found. Kito et al. (2007) implemented a slowness and back azimuth weighted migration and applied it to teleseismic data. It uses a conventional migration and afterwards weights each solution by deviations from slowness and back azimuth. It is thereby different from the method developed in this thesis where the slowness and back azimuth information is integrated directly into the CF and thereby into the source scanning stacking. Furthermore the application of the approach from this thesis is developed for local seismology monitoring with small arrays.

A typical application of this method is the real-time monitoring of seismicity. Traffic light systems are a common procedure in this field which rely on certain thresholds of event numbers and magnitudes to decide if for example a hydraulic fracture process has to be stopped. The reliable real-time location of events is mandatory to estimate magnitudes of events and to rule out possible natural events outside of the monitoring region. Seismic monitoring networks are restricted to few available locations with often poor noise conditions due to the industrial setting. Ongoing work at borehole sites might result in strong noise spikes at the whole monitoring network. The number of seismic stations is furthermore restricted by available budget.

The general method of the source scanning algorithm with array extensions is explained in the following sections. It is followed by examples from two local seismic monitoring campaigns and one CTBTO OSI training exercise in section 6.3. The location capabilities of the source scanning method without and with the array extensions are compared with each other for each dataset. Figure 6.3 gives a flowchart of the general work flow of the developed method including the array methods.

An application of a simplified source scanning to remove noise from acoustic sources at monitoring networks is given in the appendix B. The property of source scanning which allows to restrict events to only certain regions is used there.

### 6.2.1 *Characteristic function (CF)*

The CF optimally highlights P- and S-onset phases respectively and is robust against noise bursts. The narrower and larger the CF gets at the time of the actual phase onsets, the better. By shifting traces according to their P- or S-phase travel times, a similar effect to dynamic time warping or dynamic waveform matching (Schulte-Theis & Joswig, 1990) is achieved.

The first step in calculating the CF is bandpass filtering all vertical and horizontal component seismograms with respective corner frequencies depending on known characteristics of expected events and SNR, i.e. noise. In this study, vertical traces are filtered with a four pole Butterworth filter with corner frequencies of 5 and 40 Hz. The horizontal traces are filtered with the same filter but with corner frequencies of 5 and 20 Hz. The corner frequencies are chosen empirically from the experience of the manual processing of the shown datasets and similar datasets from local monitoring campaigns.

As a second step, the rotated horizontal components for each back azimuth from a back azimuth slowness grid are created. A mapping for each geographic grid cell to a back azimuth slowness value by using the ray parameter is done later during the stacking (Figure 6.4). The ray parameter for the horizontal slowness estimation of a ray between a source grid point and a sensor has the advantage that for refracted rays it is only dependent on the seismic velocities of the refracted layers. Thereby often less well known near surface seismic velocities do not influence the horizontal slowness. Rays will be mostly refracted at lower layers even at small distances due to the large increase of seismic velocity at larger depths in the test datasets (except deep events with small epicentral distance to stations). Tests with a three-dimensional rotation of all three components based

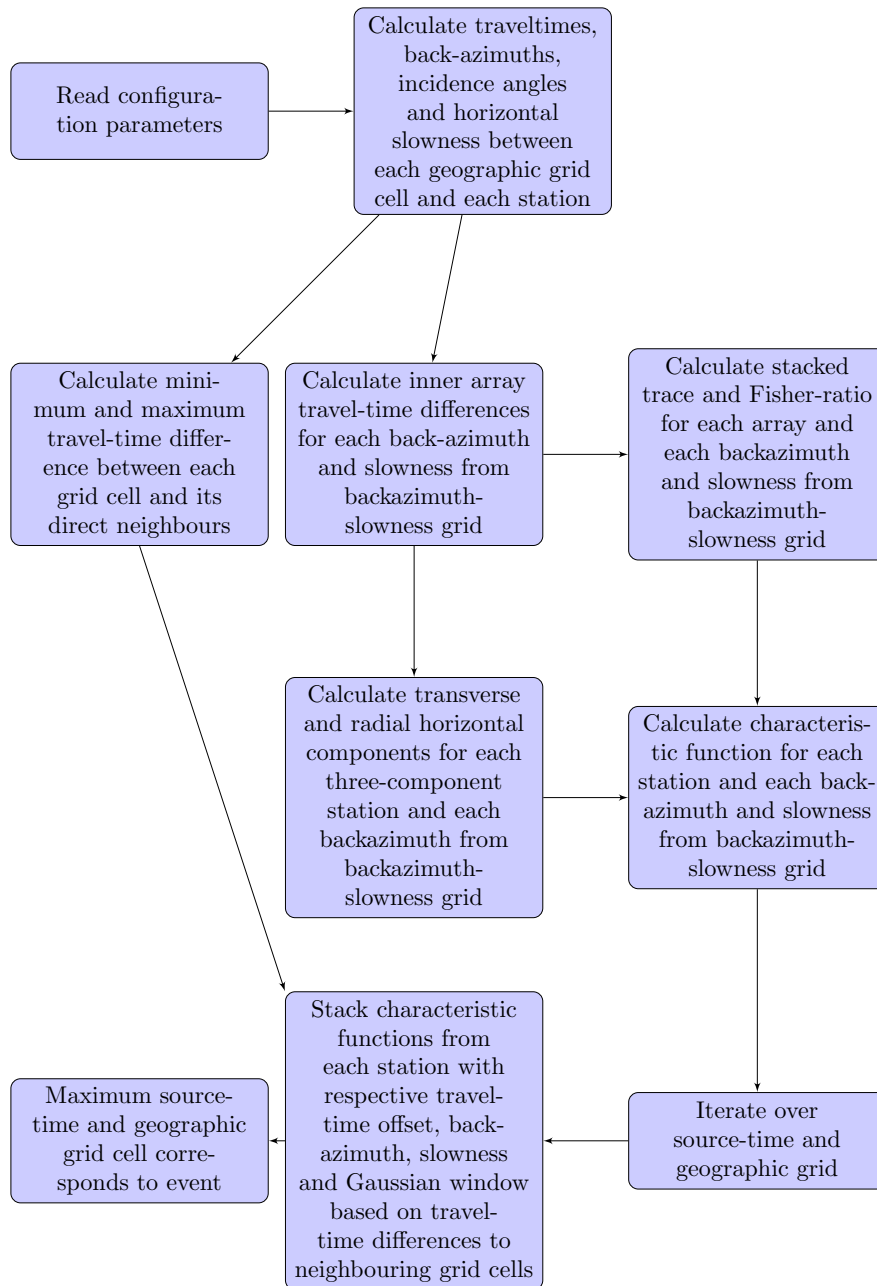


Figure 6.3: Flowchart of source scanning location steps with inclusion of array methods.

on the theoretical incidence angle at sensors did not result in better results. This might be due to local heterogeneities and overlays of arriving and reflected waves at the surface. Therefore the polarization of the particle motion is not in the direction of the incident ray and an incidence angle of zero degree (vertical direction) is assumed for single stations.

For array stations with at least three available elements, the raw filtered seismograms are stacked with time delays based on the back azimuth slowness grid (Figure 6.4). Back azimuth steps in this study are  $10^\circ$  and four slowness steps are used with a step size of  $0.05 \text{ s km}^{-1}$  starting at  $0.05 \text{ s km}^{-1}$ . Stacking is done according to the description from the beamforming section 4.3.1. Uneven topography array apertures are furthermore height corrected as also explained in that section. This applied to the mini-array SNS2 at a slope near Basel.

For each element of the back azimuth slowness grid the S-phase  $CF_R$  (radial) and  $CF_T$  (transverse) for the horizontal east-west and north-south component are calculated. This is done in the same way for single and array stations. For array stations the central array element horizontal traces are used (all used arrays in this study have a three-component station only for the central element). The P-phase  $CF_P$  is calculated from the vertical component for single-stations or accordingly from the stacked seismogram for array stations. The S-phase CF of arrays is not calculated on the vertical stacked trace because the horizontal traces provided more reliable results. Each CF consists of the STA/LTA. See equation 1 for a recursive implementation where  $N_{STA}$  and  $N_{LTA}$  are the lengths of the short and long term window respectively and  $x$  is the seismogram (stacked seismogram  $z$  for array stations). In this study the window lengths are  $N_{STA} = 0.5 \text{ s}$  and  $N_{LTA} = 10 \text{ s}$ .

The mapping from geographic grid cells to the back azimuth slowness grid has the advantage that far fewer CFs need to be calculated and therefore results in a huge performance increase (e.g. a geographic grid with 60 cells in  $x$ ,  $y$  and  $z$  corresponds to 216.000 grid cells whereas the back azimuth slowness grid with 36 ten-degree and four  $0.05 \text{ s km}^{-1}$  steps only contains 144

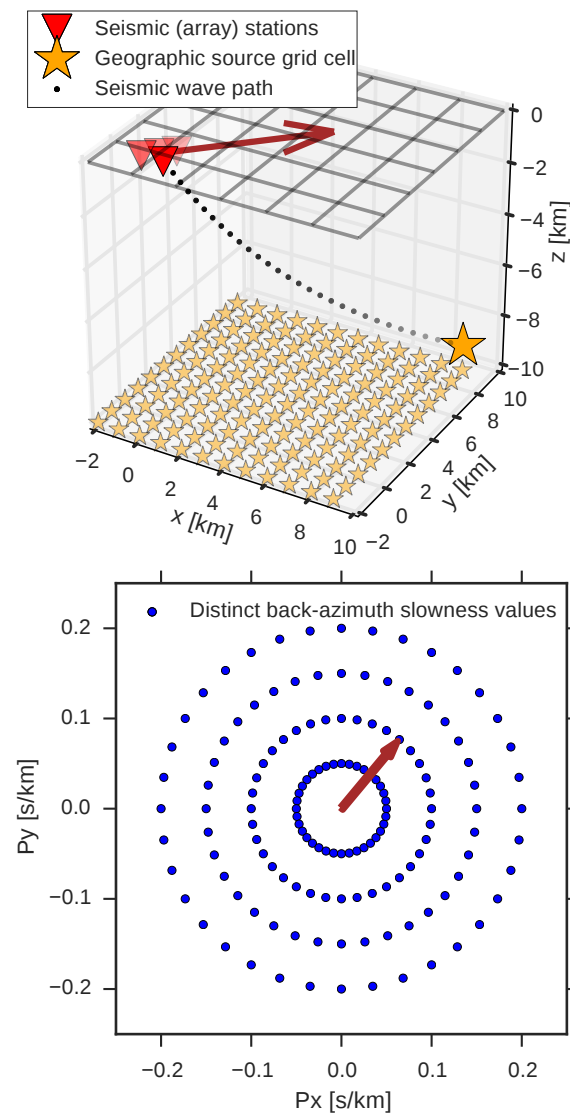


Figure 6.4: The travel time, back azimuth and incidence angle are calculated for each station for all geographic grid cells based on the theoretical seismic velocity model (top). The horizontal slowness is derived from the ray parameter and the closest back azimuth slowness grid point is assigned from a fixed grid (bottom). As the back azimuth and incidence/slowness affect the seismograms of the transverse, radial, stacked seismogram and Fisher ratio, an individual CF is calculated for each station and each back azimuth slowness grid point.

elements). The algorithms are written in a modular way so that alternative functions can be used easily and the following CFs were additionally implemented: Envelope (Kao & Shan, 2007), Kurtosis (Langet et al., 2014), super-sonogram (Sick et al., 2015), FilterPicker (Lomax et al., 2012) and cross-correlation (Zhang & Wen, 2015b).

The CFs of the two horizontal traces are combined by vector addition to the final  $CF_S = \sqrt{CF_R^2 + CF_T^2}$ .

### 6.2.2 Weighting with Fisher ratio

As shown in section 4.3.1, the Fisher ratio (Fisher R.A., 1948) is an excellent detector. It results in very few false positive detections even in areas with high background noise while still maintaining detection capabilities for low SNR microseismicity. It highlights coherent P-phases depending on back azimuth and slowness at an array with a narrow peak making it an ideal candidate for a CF for source scanning.

Using the Fisher ratio as well for S-phase picking on arrays did not lead to improved results in comparison to using the STA/LTA CF of the horizontal components of the central array element. One would expect a local maximum in the Fisher ratio at the time of the S-phase onset with a slowness of the P-phase slowness multiplied by the  $v_P/v_S$  ratio. However no clear maxima could be found on a wide range of slownesses (0.05 to 2 s km<sup>-1</sup>) and lengths of Fisher ratio correlations (0.5 to 2 s).

The Fisher ratio is calculated for each array station and each point of the back azimuth slowness grid from Figure 6.4 in small overlapping time intervals. To eliminate undesired secondary peaks after the initial P-onset and to smooth the Fisher ratio, the STA/LTA ratio is furthermore applied. Tests showed that for most events the STA/LTA of the Fisher ratio provides a superior CF than the direct STA/LTA on the stacked seismograms. However few cases exist in which the maximum of the Fisher ratio is after the initial P-onset. Therefore the STA/LTA of the Fisher

ratio is combined by multiplication with the direct *STA/LTA* from the stacked seismogram as shown in equation 19. This combination proved to eliminate maxima before or after the P-onset in either of the two functions, see also Figure 6.5 and 6.6. The Figures show how the *STA/LTA CF* can not highlight phase onsets significantly even on the stacked traces. Including the Fisher ratio however improves the *CFs* tremendously. The Fisher ratio in this study is calculated with a window length of 0.5 s with a time step size of 1 sample. *STA/LTA* window lengths for the Fisher ratio are  $N_{STA} = 0.1$  s and  $N_{LTA} = 10$  s.

$$CF_P = CF_{\text{stacked-seismogram}} \cdot CF_{\text{Fisher}} \quad (19)$$

### 6.2.3 Normalization of characteristic functions

To prevent that single noise bursts or *CFs* from stations very close to events influence the final stack disproportionately high, a normalization is necessary (Kao & Shan, 2004). Normalization is done here depending on the ratio of the maximum and the 70%-Quantil ( $Q_{0.7}$ ) of the *CF*, equation 20. This has the advantage that it also reduces the weighting of *CFs* with multiple peaks instead of one narrow peak which is usually an indication of uncertain onsets. The values of this normalization are based on empirical tests on the datasets of this study. A further normalization based on the maximum at the current time step for all back azimuth slowness values is applied and *CFs* from array stations are weighted by a factor of 1.5 due to their additionally available information of back azimuth and slowness. Note that

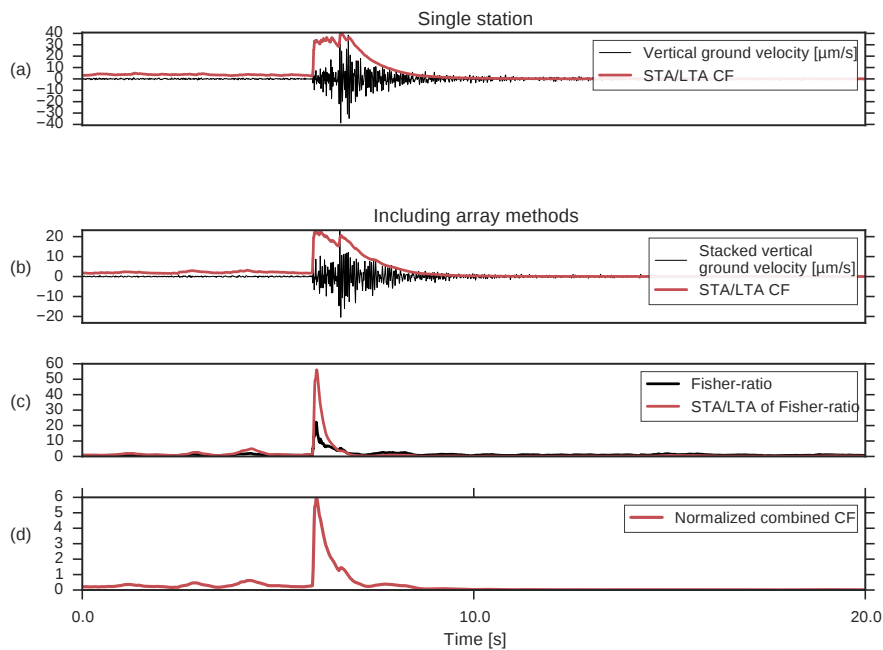


Figure 6.5: Calculation of the CF at mini-array SNS<sub>1</sub> (see Figure 3.1) of Basel monitoring network for a high SNR event (2006/12/06 19:22:35 UTC  $M_L = 1.4$ ). (a) Using only the single central-station seismogram results in a maximum of the vertical component CF at the S-onset instead of the P-onset. (b) The P-onset in the CF is improved in the stacked seismogram but a second peak is still present. (c) The Fisher ratio and especially the STA/LTA function of it show a clear narrow peak at the P-onset. (d) Combining the STA/LTA of the stacked seismogram and the STA/LTA of the Fisher ratio by multiplication results in a robust CF. This combined CF eliminates unwanted peaks which are only present in one CF.

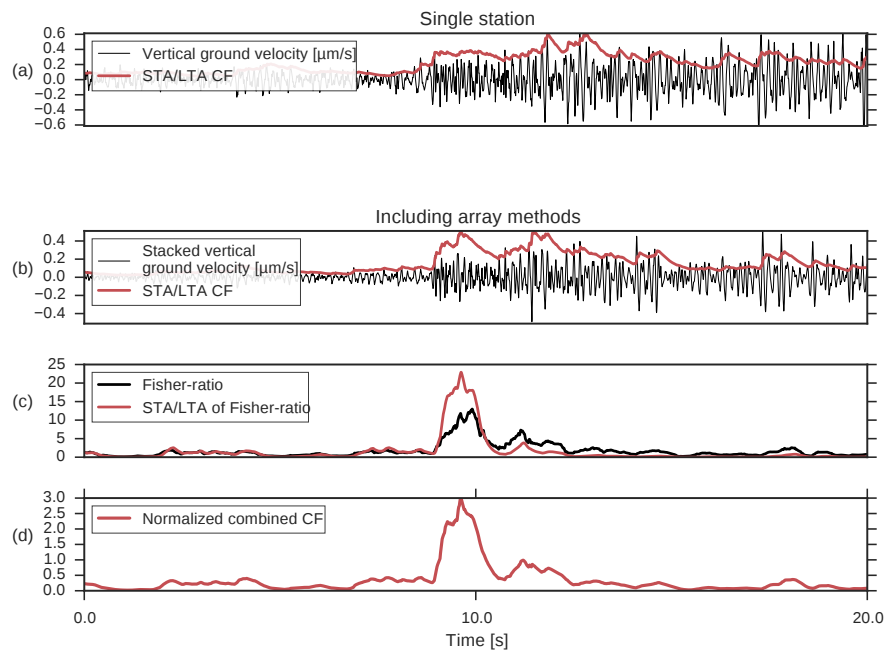


Figure 6.6: Calculation of the **CF** at mini-array WIED (see Figure 6.11) for an event from the Walsrode cluster with a low **SNR** (2010/10/15 06:41:57 UTC  $M_L = 1.0$ ). (a) Using only the single central-station seismogram results in two maxima of the **CF** between the P- and S-onset at around 5 s after the actual P-onset. (b) The P-onset in the **CF** is improved in the stacked seismogram but a second peak at around 4 s after the actual P-onset is still present. (c) The Fisher ratio and especially the **STA/LTA** function of it improve the peak at the P-onset considerably. The maximum is now less than 1 s after the actual P-onset. (d) Combining the **STA/LTA** of the stacked seismogram and the **STA/LTA** of the Fisher ratio by multiplication improves the maximum at the actual P-onset.

for the northern Germany dataset, the last normalization step for  $\text{SNR}$  values larger 8 is omitted.

$$\text{SNR} = \frac{\text{CF}_{\max}}{\text{CF}_{Q_{0.7}}}$$

$$\text{CF} = \begin{cases} \frac{\text{CF}}{\text{CF}_{\max}} \cdot 1 & \text{if } \text{SNR} > 1 \\ \frac{\text{CF}}{\text{CF}_{\max}} \cdot 2 & \text{if } \text{SNR} > 2 \\ \frac{\text{CF}}{\text{CF}_{\max}} \cdot 3 & \text{if } \text{SNR} > 5 \\ \frac{\text{CF}}{\text{CF}_{\max}} \cdot 4 & \text{if } \text{SNR} > 8 \end{cases} \quad (20)$$

A normalization based on the distance of stations to geographic grid cells was also analysed. The idea behind this is, that closer stations should have more reliable phase onsets due to higher  $\text{SNR}$ . A linear and an exponential decay over epicentral distance was implemented but did not yield better results. This is most probably because for both datasets (Basel and DGMK), station noise conditions vary too much between each other. This can lead to higher  $\text{SNRs}$  at more distant stations, see for example the more distant mini-array SNS2 with a higher  $\text{SNR}$  compared to SNS1 at the Basel monitoring (Figure 6.7).

#### 6.2.4 Final stacking of travel time corrected characteristic functions

To stack the  $\text{CFs}$  for cells of the geographic grid, the theoretical travel times  $tt$ , back azimuths  $\alpha$  and incidence angles for each grid cell are calculated at each station. The slowness  $s$  of incoming waves from a grid cell is derived from the incidence angle and the local near-surface seismic velocity at stations.

Travel times are either calculated with a fast ray-tracer for horizontally layered velocity models (Joswig 2008, DGMK dataset) or with the Time3D eikonal wavefront solver (Podvin & Lecomte 1991, Basel dataset with included topography) for three-dimensional velocity models.

The algorithm implementation allows to include local topography derived from the Shuttle Radar Topography Mission (SRTM,

USGS 2006) in the 3D model. This enables the exclusion of physically impossible ray paths for near-surface local events and can therefore further constrain epicenters, see section 6.3.3.

To account for errors in the velocity model and to include phase onset uncertainties, a Gaussian window around the theoretical travel time onset of each CF is used for stacking instead of only using one sample value at the theoretical travel time onset. The window length  $K_n$  of the stack length for station  $n$  is based on the source time increment  $\delta t$  and grid time differences as given in equation 21. This means that for example for larger geographic grid cells, the stacking length increases. A larger stacking length in turn allows values of the CF which are further before or after the theoretical travel time onset to be included in the final stack. Therefore a higher  $K_n$  introduces a larger uncertainty for the location. Liao et al. (2012) used travel time errors based on the time a wave would need to travel along half a grid cell around the current hypocenter. In this thesis the time to travel along a full grid cell is used for the uncertainty window  $K$ . Therefore the uncertainty window length varies for each hypocenter location.

$$K_n = \max\{|\text{tt}_{x\pm 1, y\pm 1, z\pm 1} - \text{tt}_{x, y, z}|\} + \delta t \quad (21)$$

The resulting stack for a specific source time step  $t$  and geographic grid cell  $x, y, z$  is calculated by addition of the time shifted  $\text{CF}_P$  and  $\text{CF}_S$  as shown in equation 22 where the back azimuth  $\alpha$  and the slowness  $s$  both depend on  $x, y, z$ . Depending on  $\alpha$  and  $s$  the closest point from the back azimuth slowness grid is used for the choice of the respective CF. For the DGMK dataset we included furthermore an uncertainty for the back azimuth due to larger uncertainties in the calculations. Therefore we compare the CF values for the calculated back azimuth and the two neighbouring back azimuths from the back azimuth slowness grid. We then use the back azimuth with the maximum CF value.

Table 4: Overview of source scanning steps for single and array stations.

	Vertical components	Horizontal components
Pre-processing (all)	Filter between 5 and 40 Hz	Filter between 5 and 20 Hz
Single stations	STA/LTA	Rotate to back azimuth grid, apply STA/LTA, combine the two components
Array stations	Shift and stack using values from the back azimuth slowness grid, apply STA/LTA and weight by Fisher ratio	As for single stations but only on array central station
Post-processing (all)	Apply SNR normalizations and up-weight array CFs	Apply SNR normalizations

$\mathcal{N}$  is a normalized Gaussian distribution with the variance  $\sigma^2 = K$  and an area of 1.  $N$  is the number of stations and  $w_n$  are the station specific weights. Individual weights can be set for each station depending on previous station performance (e.g. based on background noise). The time step size of source times is 0.1 s. [Drew et al. \(2005\)](#) used multiplication of the squared CF from P- and S-onset times. This did not yield satisfying results with the unclear S-onsets of the analysed low SNR events in this thesis. Table 4 furthermore gives an overview for single and array stations of all the involved steps.

$$CF_{t,x,y,z} = \sum_{n=1}^N \left\{ w_n \sum_{k=-\frac{K_n}{2}}^{\frac{K_n}{2}} \mathcal{N}(k) \sqrt{CF_{P_{n,\alpha,s}}(t + tt + k)^2 + CF_{S_{n,\alpha,s}}(t + tt + k)^2} \right\} \quad (22)$$

### 6.3 APPLICATION

The method is applied to data from two local seismicity monitoring networks and one [CTBTO OSI](#) training exercise where a mix of single and array stations was available (Basel, [DGMK](#) and [IFE14](#)). For each dataset, location results are compared for source scanning without and with the array processing methods. For the application without array methods, each array is converted to a single station by only using its central three-component element. Synthetic waveforms were used to get insight into the differences between the two methods and to get first estimates of parameters.

Although both induced seismicity datasets include events which could benefit from a relative location technique as for example master event or double-difference ([Waldhauser, 2000](#)), it is not applied here. The reason is that this study is meant to show a technique which can be applied without the restriction of having a set of previously located master events. It can therefore be used in real-time monitoring where it is mandatory to detect and locate a priori unknown events.

The two datasets from seismicity monitoring show the application of the new source scanning method with two different challenges. The events from Basel have higher [SNRs](#) and the ground truth is of high quality. The challenge here is to locate events with well known phase picks but with high residuals because of the heterogeneous (unknown) velocity structure. On the other hand the [DGMK](#) events have very low [SNR](#) and the ground truth is not well known. The [IFE14](#) dataset has few events with low [SNR](#) in an area with strong topography.

#### 6.3.1 *Basel Deep Heat Mining project monitoring*

The first dataset is from an additional monitoring with stations deployed on the surface of the Basel hydraulic stimulation Deep Heat Mining Project ([Häge et al., 2012](#)), see section [3.1](#). The project was well monitored by an extensive network of borehole seismometers from Geothermal Explorers. To test and

compare the capabilities of surface monitoring, two mini-arrays (SNS<sub>1</sub> and SNS<sub>2</sub>) were temporarily deployed on the surface at a distance of 2.1 and 4.8 km to the well head for two days by the Institute for Geophysics, University of Stuttgart (Häge et al., 2012). This data is combined here with data from three three-component borehole stations of the Swiss Seismological Service (SED) which are publicly available (JOHAN, MATTE and OTER<sub>1</sub>). The locations of all stations can be seen in Figure 6.8. The weights for all stations are initialized to 1.

The ECOS-09 bulletin of the SED is used as ground truth information which contains 57 events with magnitudes between  $M_L = 0.8$  and  $M_L = 2.6$  (Fäh et al., 2011) during the time when the mini-arrays were deployed. The casing shoe of the borehole was at 4629 m and Deichmann & Giardini (2009) located events at +/- 600 m of the casing shoe. Data from station "MATTE" could be downloaded only until 2006/12/07 00:38:29 UTC and data from station "JOHAN" until 2006/12/07 00:18:43 UTC. These stations were therefore only available for the location of the first eight events. Figure 6.7 shows the seismograms and overlaid CFs of an example event. It also shows the regions of stacking where the overall stack had its maximum. As can be seen, the stacking region is not necessary at single station CF maxima.

The velocity model which is used by the SED did result in large residuals when locating events manually with the local stations. The SED usually locates events in a regional setting with this velocity model. Deichmann & Giardini (2009) used a 3D velocity model and they mention that the Basel area contains strong heterogeneities. As the 3D model was not available, it was tried to add thin low velocity layers to the original model. This only reduced residuals slightly and a simple halfspace model with  $v_p = 3.5 \text{ km s}^{-1}$  and a  $v_p/v_s$  ratio of 1.75 as used by (Häge et al., 2012) did give the best results and was used.

All events are located twice with source scanning. One time without the array processing techniques (i.e. stacking and Fisher ratio) and one time with these techniques. The locations of both techniques can be seen in comparison to the SED locations in

Figure 6.8. A grid cell size of 500 m was used for the source scanning. 20 km in x and y direction and 10 km in depth was the extension of the grid. The location errors from ECOS-09 are mostly given as  $< 10$  km and many times  $< 5$  km in east-west, north-south and depth.

The comparison clearly shows the advantages from the inclusion of array methods into the location procedure. The general hypocenter location error in comparison to the SED locations is reduced from 3.8 km to 1.3 km. Epicentral location as well as depth are restrained far better. Manual locations are at a depth of either 4 or 5 km. The source scanning without array methods regularly locates events in a more shallow region and further to the west. With array methods, the epicenter gets very well constrained and events are located deeper.

To investigate the algorithms in more detail, it is possible to visualize the maximum energy of the source scanning over the geographic grid cells at the source time of the overall maximum (Figure 6.9). This shows that the maximum of the stack amplitude is less prominent and as expected further away from the ground truth epicenter when the array procedures are not used. Multiple local maxima are visible while for the improved procedure only one well defined maximum in the vicinity to the ground truth location is visible.

### 6.3.2 *Gas field monitoring in northern Germany*

The second example is from a two and a half year monitoring research network in northern Germany funded by Deutsche Wissenschaftliche Gesellschaft für Erdöl, Erdgas und Kohle e.V. (DGMK) and deployed by the Institute for Geophysics, University of Stuttgart (IfG), see 3.2. It combines five single three-component sensors, two four-element mini-arrays and one ten-element array (Figure 6.11). Natural and potentially induced seismicity in the region is infrequent. Detection and location of seismic events is difficult due to several man made noise sources (e.g. army artillery practice) in combination with soft sedimentary surface layers in which noise gets amplified.

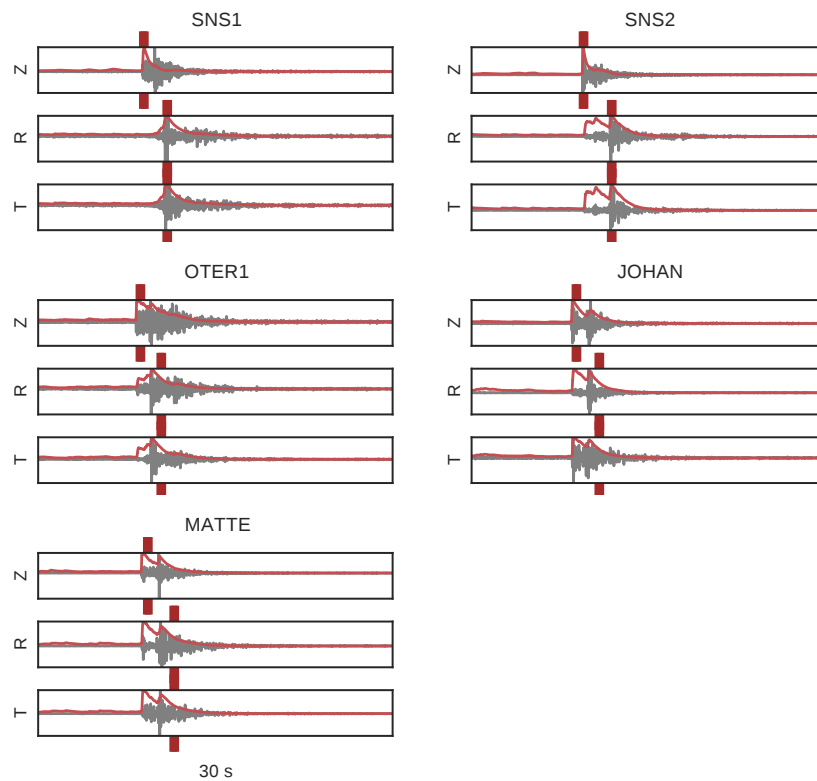


Figure 6.7: After stacking of the travel time aligned CFs for each geographic grid cell and over a range of source times, the maximum stack is used for the event location and time. This Figure shows the filtered seismograms (black) of the vertical (Z), radial (R) and transverse (T) components, the CFs (red) and the theoretical onset times (red markers) of the calculated maximum grid cell and source time of an event from the Basel monitoring (2006/12/06 19:22:35 UTC,  $M_L = 1.4$ ). S onset times of the borehole stations have large errors due to the discrepancies between  $v_P/v_S$  ratio. The thickness of the theoretical onset markers indicates the used uncertainty. CFs are normalized to a range between 1 and 6 depending on SNR.

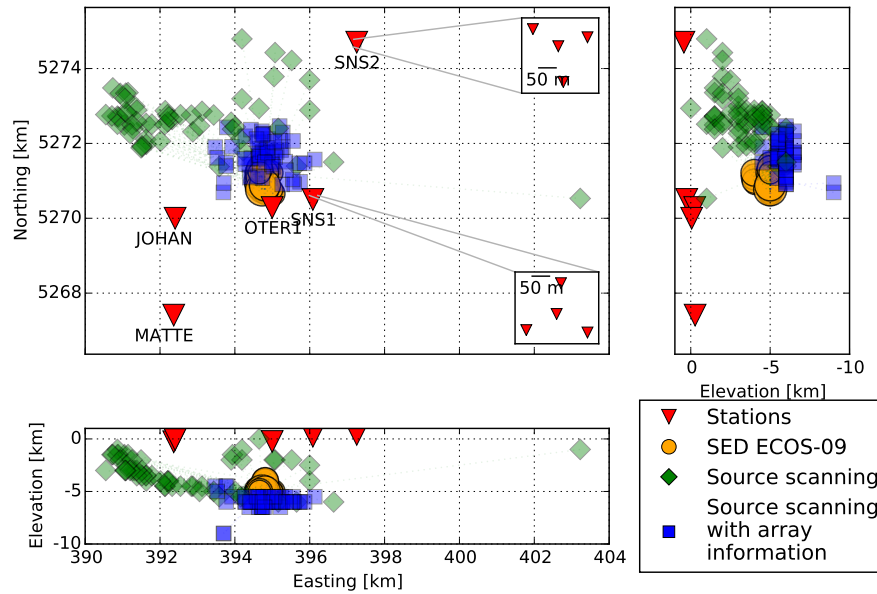


Figure 6.8: Comparison of automatic locations with source scanning for Basel monitoring without and with array methods to ground truth from SED. For each event of the SED bulletin during the time when the two mini-arrays were deployed, the source scanning was done in a time window 12 s before the P-onset for 30 s. The overall maximum per event was stored and is visualized here. Using the array methods improves the location considerably from an average error of 3.8 km to 1.3 km.

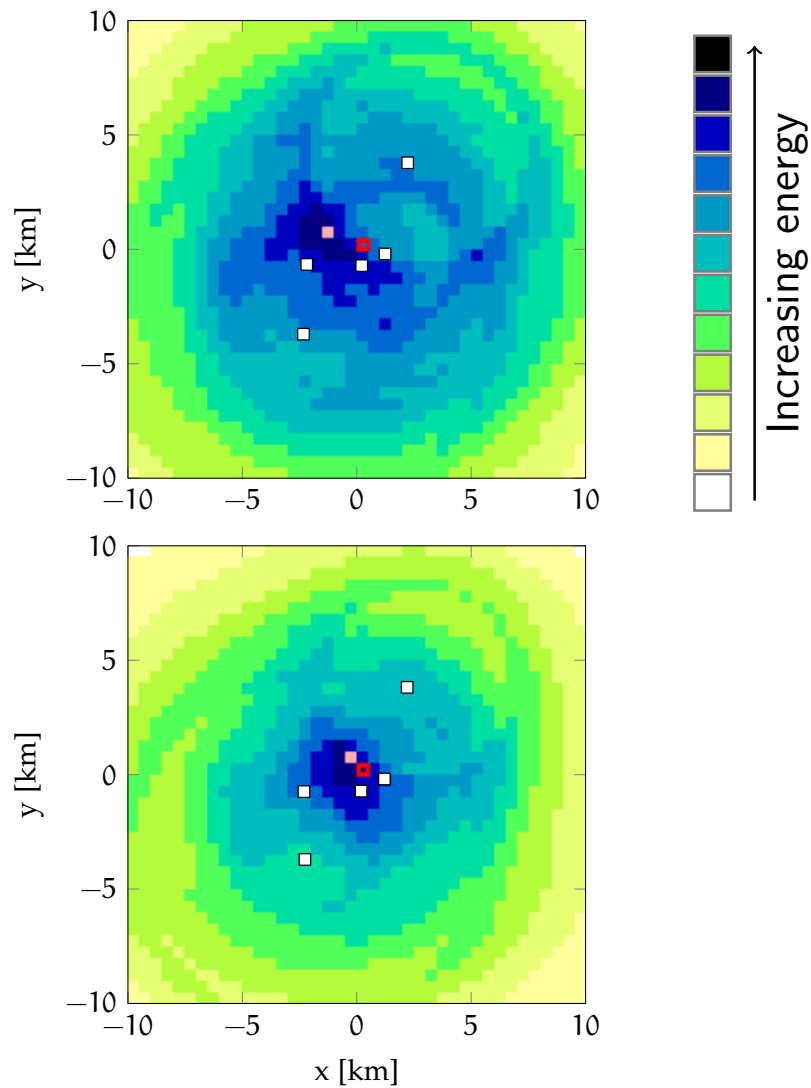


Figure 6.9: XY-grid showing the stack energy at the time and depth of the overall maximum for Basel event from Figure 6.7. Top: without array processing at a depth of 5.5 km. Bottom: with array processing at a depth of 6.0 km. The red square marks the SED location (depth 5 km), the pink square marks the point of the maximum source scanning energy and the white squares mark the station locations. The grid resolution is 500 m. The use of array methods improves the location of the final maximum and also reduces the uncertainty as can be seen from the fast decay of energy around the maximum. The uncertainty without array methods includes a larger area in comparison to the integration of array methods.

Between November 2013 and February 2016 only nine significant seismic events in a radius of 30 km around the network could be registered. Additional events were found by cross-correlation but these events are too weak to be located reliably without relative location techniques: they are mostly only detected at one station and are often not visible by manual inspection of the waveforms. The weights for the two used array stations LOEV and WIED are initialized to 1 and all other weights to 0.3 to allow a stronger influence of the array methods.

Six of the events belong to a temporal (15 October - 15 November 2014) and spatial cluster in the vicinity of the city of Walsrode. One of these events falls temporarily in the same time frame but has a location far deeper and around 5 km to the south-east of the main cluster (see also section 4.1.2 where additionally weaker events are considered). The seventh event occurred on 14 August 2014 near the city of Bothel. An additional event was recorded in February 2016, one again near Walsrode and one in the vicinity of the LOEV array site. All event times, locations, magnitudes and traces which are missing at the event time are listed in table 5. The BELL mini-array was only used as a single station because of consistent large discrepancies between array beams and event epicenters most likely due to strong geologic heterogeneities below individual array elements.

Manual location was done by experienced seismologists of the Institute for Geophysics, University of Stuttgart with the NanoseismicSuite screening and location software (Sick et al. (2012)). The stations from the DGMK network and (if available) four additional stations from the BGR, namely stations GOLD, BKSB, DEEL and RETHO were used. A simplified version of the sediment layer model (sed) of Dahm et al. (2007) served for the manual and source scanning locations. Most of the locations could furthermore be compared to hypocenter locations from BGR.

Figure 6.10 shows the seismograms and overlaid CFs of the same event as from Figure 6.5. Note that for this event the phase picking algorithm “FilterPicker” by Lomax et al. (2012) only

Table 5: Event bulletin from monitoring in northern Germany. LOEV-1 is the center station plus the inner ring at the LOEV array, marked as transparent red in the map of Figure 6.11. LOEV-2 is the outer ring at the array, marked in solid red. LOEV-3 are the three stations in transparent black in the map which were deployed in October 2015 and therefore only available for the last event. Abbreviations -E, -W, -N stand for array elements east, west and north respectively.

Date Time	Lat- idute	Long- itude	Depth [km]	$M_L$	Missing traces
15/10/14 06:42:10	52.87335	9.50697	5.2	1.2	LOEV-1 LOEV-3
16/10/14 02:45:30	52.86360	9.52793	3.5	1.2	LOEV-1 LOEV-3
20/10/14 16:17:55	52.85818	9.50956	3.7	1.1	LOEV-1 LOEV-3
20/10/14 16:23:18	52.86985	9.52914	2.8	1.8	LOEV-1 LOEV-3
02/11/14 11:34:47	52.79328	9.54796	25.5	1.8	LOEV-3
15/11/14 22:30:54	52.86268	9.53497	2.5	0.9	PLAT, LOEV-3
14/08/15 06:21:05	53.10010	9.50220	5.7	2.5	PLAT, BUCH LOEV-3 WIED-E/W/N
18/02/16 14:56:51	52.89000	9.52000	4.0	2.2	PLAT

determined one single correct P-phase on the LOEV station, see Figure 6.1. While a location with conventional picking routines was impossible, the source scanning approach yields good results. Most of the stacking regions correspond to actual phase onset times. Figure 6.11 shows, similar to the previous map from Basel (Figure 6.8), the comparison of the manual locations to source scanning locations without and with the array processing techniques. Here a grid cell size of 1 km was used due to the larger area and larger uncertainties in ground truth hypocenter locations compared to Basel. The extension of the grid was 30 km in depth and 40 km in x and y direction. The differences between the two location techniques are less prominent here. An explanation is that for most of the events, the LOEV array contained only three available traces and for the event north-west of the network, the WIED array consisted only of the central station. Therefore single stations dominate the network. Nevertheless, the array processing techniques can reduce the distance in hypocenter location to manual locations from 4.0 km to 2.9 km in average.

Again as for the Basel dataset, algorithms can be investigated in more detail by visualizing the maximum energy of the source scanning over the geographic grid cells at the source time of the overall maximum (Figure 6.12). This shows again that the maximum of the stack amplitude is less prominent and as expected further away from the ground truth epicenter when the array procedures are not used.

Figure 6.13 allows to analyse the changes of the source scanning energy distribution over time and depth for both methods. Similar results as from Figure 6.12 can be seen over multiple time steps and depths. Using the array methods leads to considerably decreased uncertainties.

### 6.3.3 CTBTO on-site inspection Integrated Field Exercise 2014

The improvement that can be achieved by integrating array processing methods into source scanning was shown with the help of the previous two datasets. This section will show how

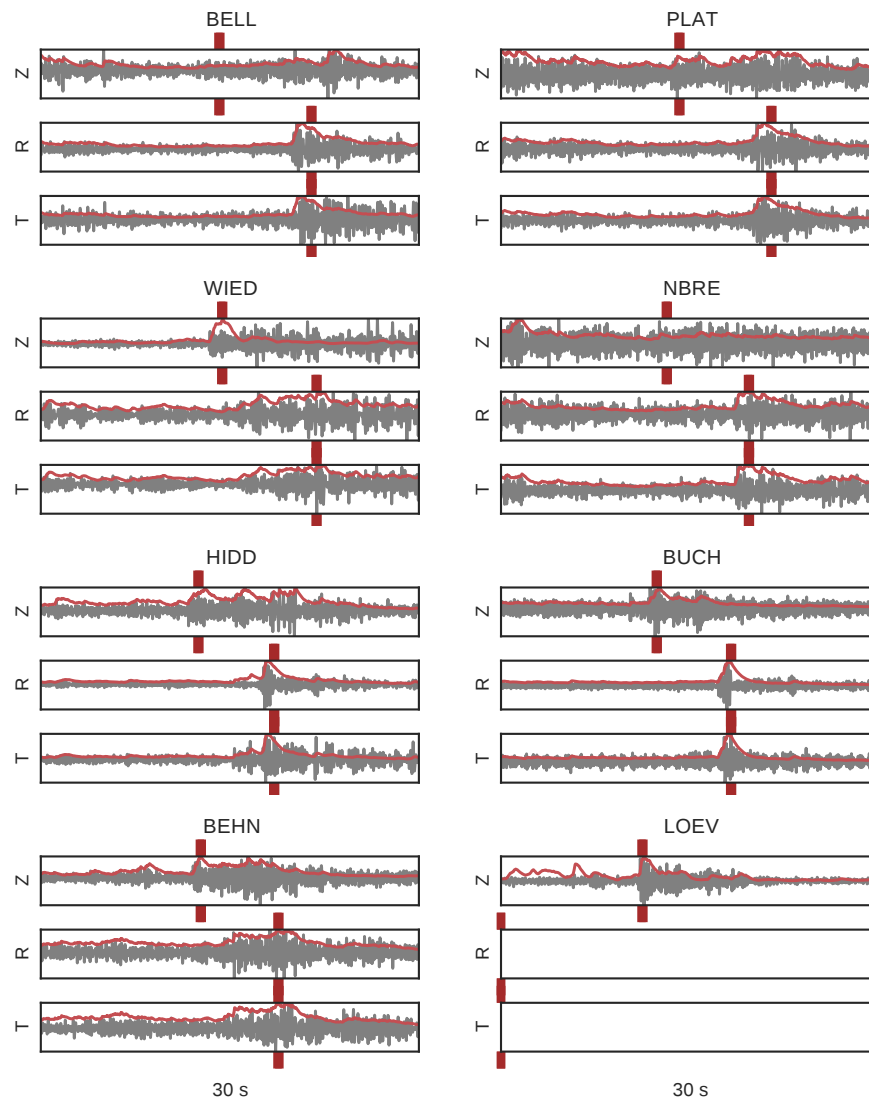


Figure 6.10: Similar to Figure 6.7 but with a low SNR event from the northern Germany monitoring (2014/10/15 06:42:14 UTC,  $M_L = 1.0$ ). Although the event is located outside of the seismic network and the signal-to-noise ratio is below 1 for multiple stations, the epicenter is in a distance of 1.4 km of the manually located event (2.2 km without array methods). The offsets in S-picks can be explained with a wrong S-wave velocity or wrong depth assumptions.

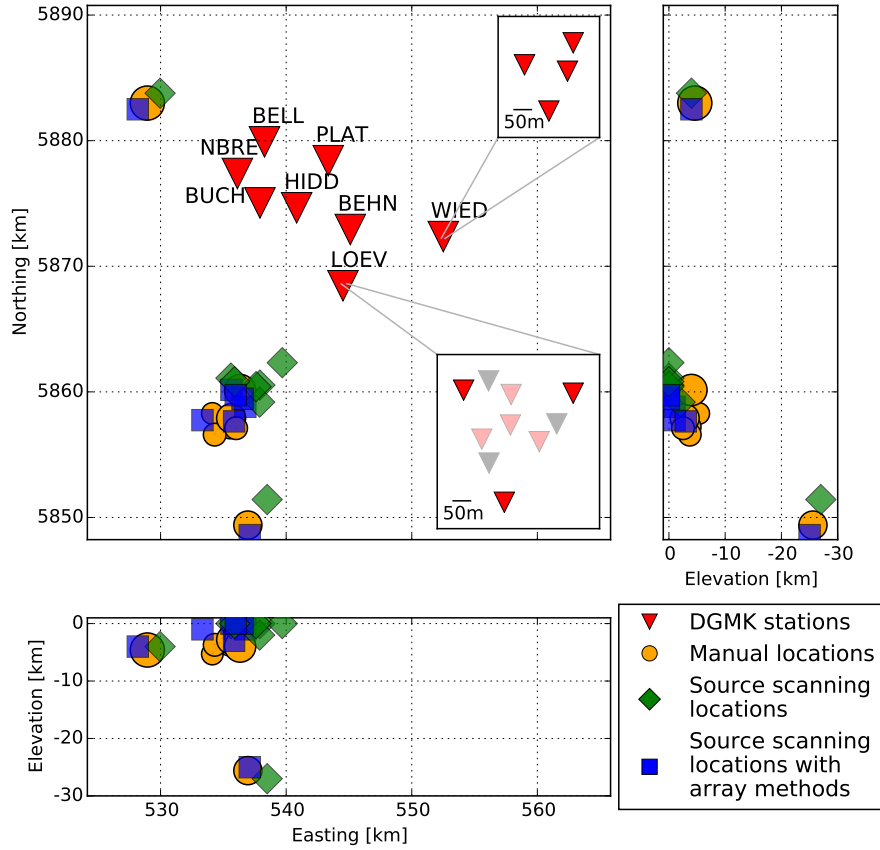


Figure 6.11: Comparison of automatic locations for northern Germany monitoring without and with array methods similar to Figure 6.8. Overall hypocenter errors are reduced from 4.0 km to 2.9 km with array methods. The improvement is considerable even though for four of the eight events, the LOEV array consisted only of the outer three elements. For three other events, it consisted of the seven elements shown in red. The full LOEV array with ten elements was only available for one event. For the event in the north, WIED consisted only of the central station. Therefore, the overall effect of the array processing methods was limited.

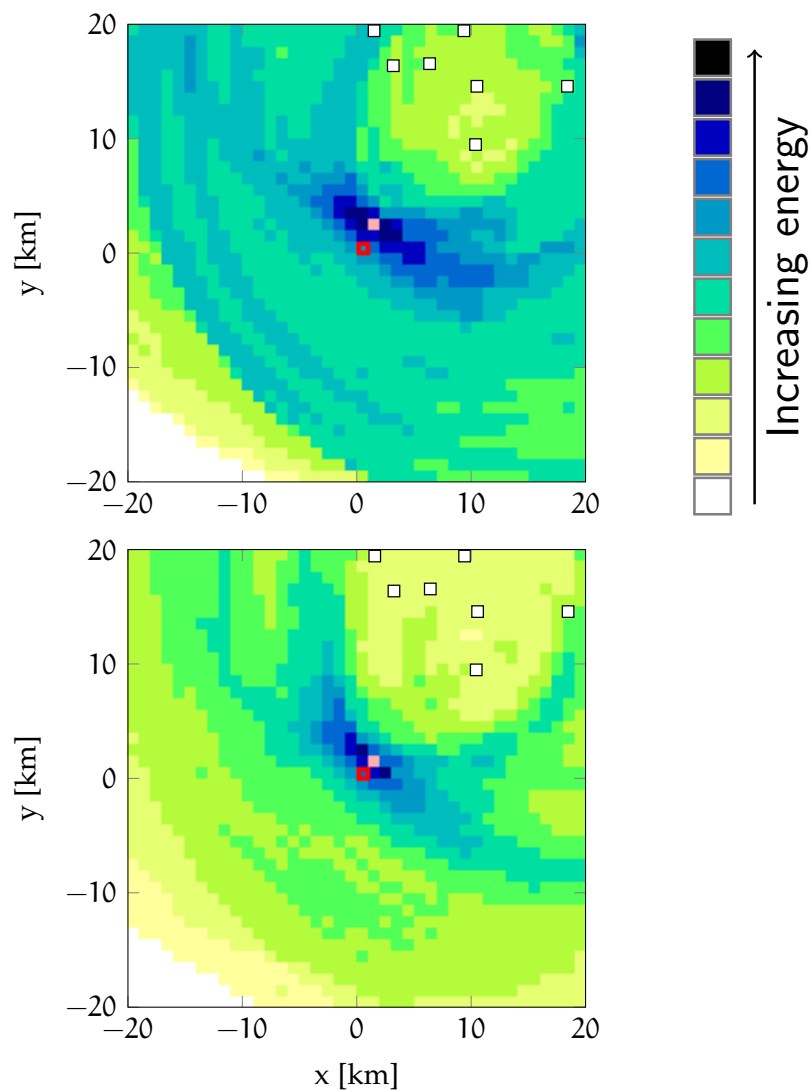


Figure 6.12: XY-grid showing the stack energy at the time and depth of the overall maximum for northern Germany event from Figure 6.10. Top: without array processing at a depth of 0 km. Bottom: with array processing at a depth of 0 km. The red square marks the manual location (depth 5.3 km), the pink square marks the point of the maximum source scanning energy and the white squares mark the station locations. The grid resolution is 1 km. The use of array methods improves the location of the final maximum and also reduces the uncertainty as can be seen from the fast decay of energy around the maximum. The uncertainty without array methods includes a larger area in comparison to the integration of array methods.

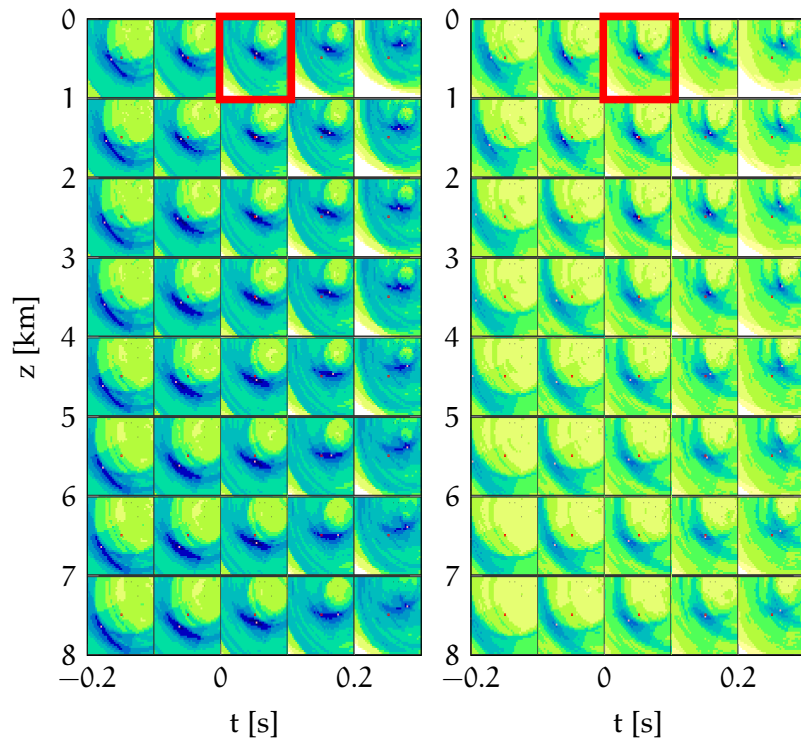


Figure 6.13: Iteration of x-y grids of source scanning energy over source times (horizontal axis) and depths (vertical axis) for DGMK event from Figure 6.10. The left frame shows the iteration without array methods, the right frame with array methods. The red rectangle marks the grid with the overall maximum energy ( $t = 0$ ) as shown and explained in Figure 6.12. The maxima change over time and depth. The array methods have consistently less uncertainties over time and depth.

including additionally the topography of the monitoring region can further constrain epicenter locations for near-surface events. The used dataset is from the Integrated Field Exercise 2014 (IFE14), see section 3.3 for the dataset overview. During the exercise, three explosions were triggered in boreholes of around five meters depth with yields of 10, 5 and 3 kg TNT. The explosions were used as a test for the seismic aftershock monitoring system (SAMS) to determine detection thresholds and location capabilities. Due to high background noise, the explosions were only visible at a few stations. Additionally multiple mini-arrays had broken cables from possible animal bites which reduced them to single stations. Therefore detection and location of the explosions was difficult. The map in Figure 6.14 shows a zoomed in view into the northern part of the inspection area where the explosions took place. Similar to the previous location maps, it compares the location without and with array methods to the ground truth. Here an improvement of average hypocenter error from 3.3 km to 1.6 km compared to the ground truth explosion locations could be achieved. The map also includes the manual locations of SAMS analysts which have an average error of 1.2 km.

The extreme topography in the region can be seen in the map from Figure 6.14. The inclusion of topography in array beamforming and for travel path calculation was studied. A detailed comparison of the source scanning energy distribution for the strongest of the three events can be seen in Figure 6.15 which compares the influence of including array methods and local topography into the velocity model. Adding topography removes nearly one third of the solution space and thereby constrains possible event locations considerably. It is only possible to get a reasonable event location by adding the array methods. The epicentral error to the manual location is removed completely.

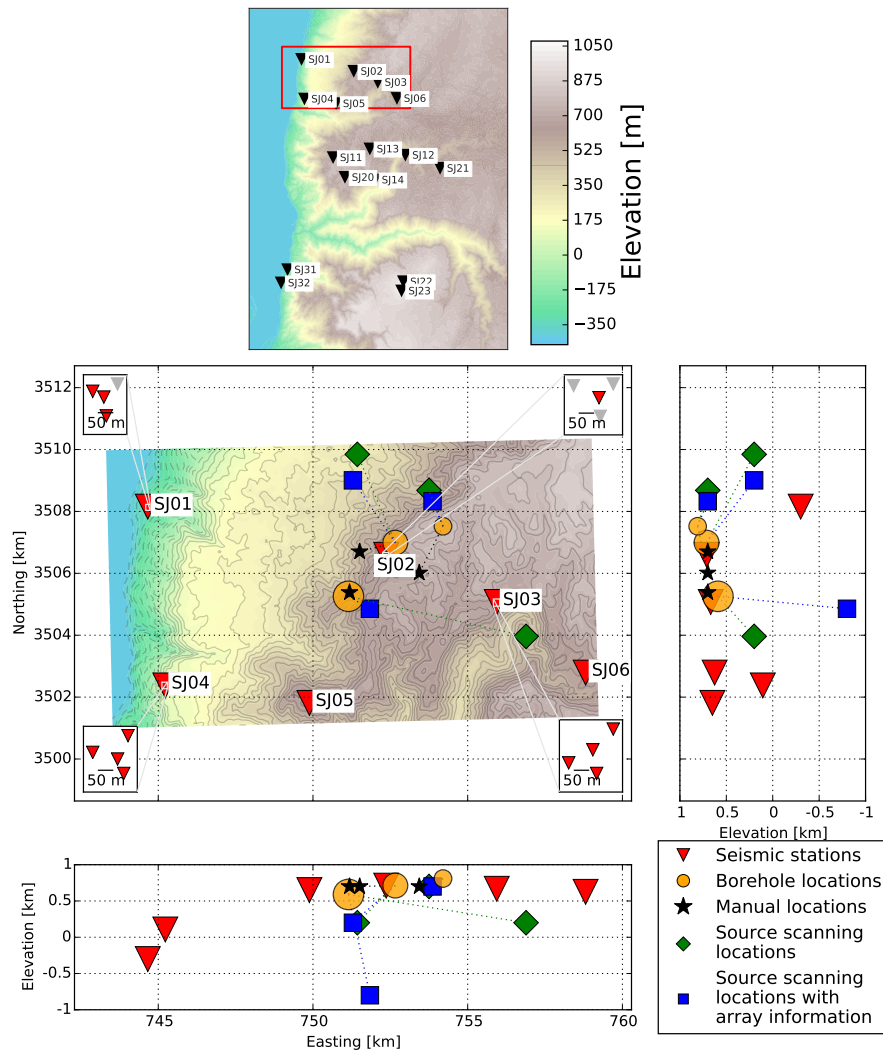


Figure 6.14: Comparison of automatic locations for [IFE14](#) monitoring without and with array methods. Including the array methods improves the epicenter of the strongest event considerably (however depth determination is worse). Also the two weaker locations are closer to the actual boreholes. The average error is reduced from 3.3 km to 1.6 km. Manual locations by the [SAMS](#) inspectors have an average error of 1.2 km. Stations marked in grey in the mini-array zooms were only available for the first strongest explosion which explains the small deviations for locations without and with array methods for the other two events.

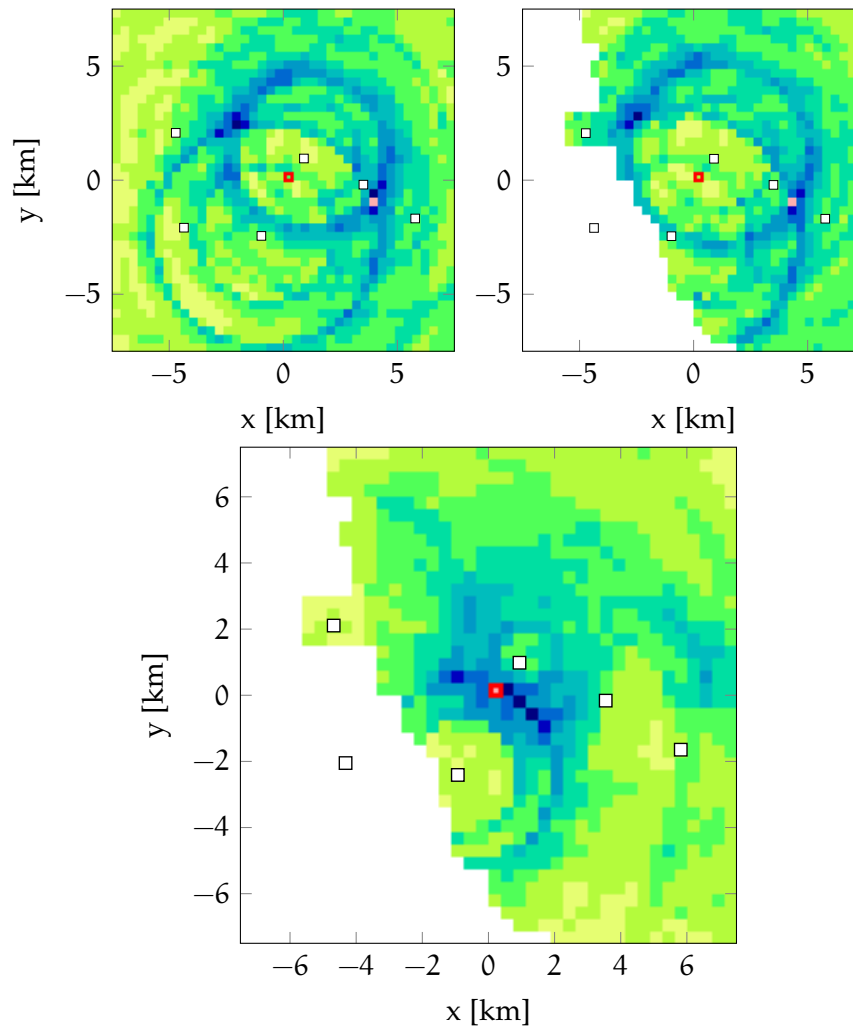


Figure 6.15: Influence from topography and array methods on source scanning energy distribution. Depth for all panels is 0. Top left without topographic and array constraints. Top right with topographic but without array constraints. Bottom with both topographic and array constraints. Red rectangle is ground truth location, pink rectangle is maximum stack energy and white squares are stations. The topographic information eliminates around a third of the rectangular region in the east as possible epicenters. Only by adding array information the location can be pinpointed to the actual ground truth borehole location.



---

## CONCLUSIONS AND OUTLOOK

---

This thesis showed that the detection and location of seismic events which have either low signal-to-noise ratios (SNRs) or are recorded by only few stations is possible when appropriate tools are used. A new approach for single station event classification by spectral pattern recognition and a new way to locate events by source scanning with an integration of mini-arrays was presented.

The thesis first gave an extensive explanation and comparison of multiple state-of-the-art algorithms. This comparison showed that the approach to detect seismic events must be based on the problem setting. If no information about sought after events and no previous recordings are available, detectors with only few a priori conditions must be used. The short term average / long term average (STA/LTA) algorithm provided good results for single stations on various datasets. Only little knowledge and few training is necessary for this algorithm. More complex algorithms were tested but have to be tuned on specific datasets which makes them less versatile.

Pattern recognition can be used if previous event knowledge is available to improve detection statistics. The cross-correlation waveform pattern recognition and the SonoDet spectrogram pattern recognition were analysed in detail on multiple datasets. Cross-correlation allowed to detect similar events with extremely low SNR which were not found by manual analysis. SonoDet allowed to detect less similar events, for example explosion events at different locations with patterns from a different campaign. SonoDet could thereby reduce false positive detections

(false alarms) considerably without the need to have previously detected patterns from the same dataset.

The coincidence analysis of the discussed single station algorithms showed how the combination of multiple single stations in a seismic network can further lower false positives. However this can also result in an increased number of false negatives (missed events) if events are only detected at one or two stations.

The usage of small aperture arrays for event detection can resolve the predicament that single station detections result in too many false positives from local noise bursts while coincidence detections result in too many false negatives because events are detected at too few stations. Multiple array algorithms which use the coherence of single waveforms from seismic arrays were analysed and compared. Especially the Fisher ratio provided robustness and high sensitivity with small aperture arrays with at least five stations without the need for previously detected events.

Chapter 5 showed how an unsupervised learning approach based on self-organizing maps (SOMs) and principal component analysis (PCA) can be applied to a high-quality dataset in the Atacama desert (PISCO). Specially transformed spectrograms (sonograms) served as input to the unsupervised algorithms, providing an informative, robust and visually interpretable feature format. PCA as a processing step on top of the sonograms reduced the number of features from 481 to 80 and enabled a visualization of the data either along the first two principal components, or along individual components chosen by the analyst. The SOM as a clustering algorithm with topological projection and prototype generation is ideally suited to provide an overview over common event types in a large dataset. It allows the analyst to examine how common event types differ in terms of location, distance, depth and amplitudes. The SOM showed how a geographic clustering with only one station is possible.

Furthermore, the trained SOM can be used to classify unknown events with high accuracy based on a nearest-neighbour comparison to the SOM prototypes. In the case of the PISCO

dataset, classification was possible for event type (*QUARRY* vs. rest) and coarse location/depth (*DEEP* vs. rest). Even subtle pattern differences in cases where the underlying source processes (e.g. depth) are similar, can be detected (e.g., see the comparison of *NORTH* and *CENTER* events). However, the classification accuracy was lower, when events differed only in depth, but not in epicenter distance and azimuth to the recording station (e.g., see the comparison of *CENTER* and *CRUST* events). Although our dataset additionally suffered from a lower number of training events in these cases. The one-nearest neighbour classification was done with a two-fold cross-validation and achieved an overall classification accuracy of 95.1% for the five classes. If more detailed sub-classes are taken into account as well, an overall correct classification rate of 80.5% is achieved for station A04 at the western side of the network and 86.3% for station A07 which is in a more central location. In an exploratory analysis multiple additional machine learning classifiers were tested on the same cross-validation: random forest, naïve Bayes, neural network (**NN**), recurrent neural network (**RNN**) and convolutional neural network (**CNN**). The best results were achieved with the **CNN** with a classification rate of 82.9% for the detailed classes at station A04.

Chapter 6 showed how the automatic location for microseismic monitoring in small local seismic networks can benefit by integrating the information of small aperture arrays into the source scanning technique. Multiple steps from literature are combined with the new approach of using the **STA/LTA** of the Fisher ratio in combination with the **STA/LTA** on the stacked seismograms as the characteristic function (**CF**) for source scanning. Separate stacks for P- and S-onsets with individual velocity models are combined. Horizontal traces are rotated depending on back azimuth and all **CFs** are normalized. A Gaussian uncertainty window around theoretical onset times is used for stacking with a window size depending on source grid cell location. 3D velocity models are supported and easy integration of surface topography in the models is provided. Considering all steps, the **CF** becomes strongly dependent on the source

location grid cell. Source locations with for example wrong back azimuths to stations are thereby ruled out immediately. The Fisher ratio allows to highlight P-onsets sharper and more reliable against the noise floor in the CF. The location becomes more accurate due to fewer and less pronounced peaks in the CF at noise disturbances.

It was shown how conventional phase picking algorithms can not provide reliable results for low SNR events. As an alternative, conventional source scanning was compared to the newly developed method which integrates array processing methods for two datasets from microseismic monitoring of induced seismicity.

One dataset (Basel) contains events with high SNRs but only few recording stations and a velocity model with large uncertainties. The used recording network consists of three borehole stations from the Swiss Seismological Service (SED) and two mini-arrays on the surface with four elements each. Data from two of the borehole stations was only available for a fraction of the analysed events. For this dataset, the average error in hypocenter distance by using the new method could be reduced from 3.8 km to 1.3 km in comparison to the ground truth from the SED with additional stations. Integrating array processing techniques into source scanning can thereby improve the automatic location considerably when SNRs are high but many unknown heterogeneities exist in the underground as with the Basel dataset.

The other dataset contains events with extremely low SNRs (DGMK). A recording network of six single stations on the surface and two arrays on the surface was used. One of the arrays is a mini-array with four elements. The other array was consecutively extended during the recording time. It has only three available elements for four events, seven elements for three events and ten elements for one event. The average hypocenter error by using the new method could be reduced from 4.0 km to 2.9 km compared to the ground truth. The ground truth was obtained by a manual location and by using additional stations from the monitoring network of the BGR and the WEG networks.

The comparison of the conventional and new source scanning method with events from the [DGMK](#) dataset shows how the new method can locate events with a good precision even when [SNRs](#) are too small to use automatic phase pickers and/or too few stations record the events to reliably use conventional source scanning. The new method is thereby well suitable to improve the automatic detection and location for real time monitoring of seismicity.

Deployment sites for seismic stations must transmit data in real time to allow the use of traffic light warning systems. Site locations are therefore often limited by road access for maintenance and the availability of permanent electricity and mobile network coverage. Those locations in turn often provide only sub-optimal [SNR](#) conditions as they are close to noise sources from anthropogenic activities for example. As shown, using small aperture arrays at these sites can considerably improve the detection and location capabilities. The number of deployment sites and data management infrastructure can be reduced. Array methods based on beamforming are independent of the surrounding velocity model as long as the geology inside the array aperture is consistent. Well constrained 3D underground velocity models might be only available in the direct vicinity of boreholes. Location of events as for example from the Basel dataset included high residuals because the underground velocity model was imprecise. The array methods provided a stabilization and correction of locations in this case.

## 7.1 OUTLOOK

Not having enough training data is a common problem in seismology, especially at microseismic monitoring. While this thesis showed approaches for automatic event detection with only few or no training data, more research needs to be done in this field to match or exceed manual performance in some cases. An approach from data mining would be to combine the knowledge of various microseismic monitoring campaigns for algorithm training. This thesis showed for example how the explosion

patterns from a campaign in Hungary could be used to detect similar explosions in a completely different geographic area in Jordan.

Studies in speech and image recognition artificially increase available training data by deforming training images according to certain rules. One approach to extend training data in seismology could be to use the SonoDet amplitude adaptation rules to create multiple patterns from single events. Thereby the results from feature engineering can be used for training of machine learning models. The PISCO analysis showed how the PCA space contains infinite variations of the provided patterns. Points in this space between certain events can be seen as interpolations between them. The visual analysis already confirmed that these interpolations look like physically possible seismic event signatures. Therefore it should be analysed how this interpolations could be used to furthermore increase training datasets for machine learning algorithms.

Another approach when expected events are rare can come from outlier detection. By using only the background noise over long time intervals, good models can be built of typical noise sources. An algorithm can then detect deviations from the learnt models to query analysts if these outliers correspond to events.

The convolutional neural networks (CNNs) used in the exploratory analysis of the PISCO dataset provided the best classification results. More research should be done to show how the use of these neural networks which come from image recognition can be used for pattern recognition in two-dimensional spectrograms of seismic events. It should be analysed in which ways the combination of multiple sensors similar to source scanning could be used with neural networks.

The source scanning in this study only benefited from array methods for the P-phase detection. For S-phases, the single station horizontal components provided better results. If arrays are deployed with three-component sensors at all elements instead of only the central element, the S-phase detection could be improved significantly. As for P-phases, stacking and the Fisher ratio could be used on the horizontal components. Addi-

tional tests with arrays where all elements are three-component sensors could show possible benefits.

The source scanning result can provide a four-dimensional uncertainty distribution over time and space. Based on statistics of this distribution, the certainty of event locations can be estimated. Clear global maxima in the CF stack over time in combination with clear global maxima in space indicate well constrained hypocenters. Similar to error ellipses from conventional processing using a 95% confidence region, this could provide an uncertainty estimation which is easy to understand for analysts.

Additional CFs for source scanning were tested for this thesis but further analyses are necessary. The robustness and inclusion of multiple frequency bands with sonograms for the CF was promising but could only be tested shortly during this study.

More research should also be done in parameter optimizations for available algorithms. Even the results of the simple STA/LTA detector are highly dependent on a priori applied bandpass filters, the short and long term window lengths and the used thresholds. The application of automatic algorithms on new datasets can not always be done by experts of these algorithms. Therefore routines for automatic parameter configurations are necessary to gain optimal results. A grid search or a Monte Carlo simulation over the whole parameter space of algorithms is necessary in combination with long data time frames. This also applies to coincidence detectors which are highly dependent on the monitoring network layout. Based on the layout of the network and locations of expected events, the automatic configuration of these parameters is possible.

Furthermore combinations of different detectors and classifiers with intelligent voting techniques can provide improved results. Different algorithms can be benchmarked automatically if enough training data is available. Based on the results, an automatic voting can be proposed.

The lack of available benchmarking datasets for automatic processing as described in chapter 2 should also be addressed. Multiple open datasets for different problem settings need to be

available with accompanying automatic detector and location statistics. New algorithms can then be easily checked against state-of-the-art procedures without the need to re-implement them as had to be done in this thesis. In combination with these datasets, catalogs with optimal parameter settings for each algorithm and problem setting should be provided.

## 7.2 ALGORITHM IMPLEMENTATIONS

Almost all algorithms were implemented from scratch by the author of this thesis in Java and Python. Almost all Figures in this thesis are solely based on scripts and created without a computer mouse. The algorithm source codes and the compiled programs can be provided upon request to interested readers.

---

## REFERENCES

---

- Akaike, H., 1971. Autoregressive model fitting for control, *Ann. Inst. Statist. Math.*, **23**, 163–180.
- Akaike, H., 1974. Markovian representation of stochastic processes and its application to the analyses of autoregressive moving average processes, *Ann. Inst. Statist. Math.*, **26**, 363–387.
- Aldersons, F., 2004. *Toward a Three-Dimensional Crustal Structure of the Dead Sea region from Local Earthquake Tomography*, Dissertation, Tel-Aviv University.
- Allen, R. V., 1978. Automatic earthquake recognition and timing from single traces, *Bull. seism. Soc. Am.*, **68**(5), 1521–1532.
- Allen, R. V., 1982. Automatic phase pickers: their present use and future prospects, *Bull. seism. Soc. Am.*, **72**(6), 225–242.
- Anstey, N., 1964. Correlation Techniques—a Review, *Geophysical Prospecting*, **12**(4), 355–382.
- Arora, N. S., Russell, S., & Sudderth, E., 2013. NET-VISA: Network Processing Vertically Integrated Seismic Analysis, *Bulletin of the Seismological Society of America*, **103**(2A), 709–729.
- Bache, T. C., Bratt, S. R., Swanger, H. J., Beall, G. W., & Dashiell, F. K., 1993. Knowledge-based interpretation of seismic data in the Intelligent Monitoring System, *Bulletin of the Seismological Society of America*, **83**(5), 1507–1526.
- Baer, M. & Kradolfer, U., 1987. An automatic phase picker for local and teleseismic events, *Bull. seism. Soc. Am.*, **77**(4), 1437–1445.

- Baker, T., Granat, R., & Clayton, R. W., 2005. Real-time earthquake location using Kirchhoff reconstruction, *Bull. seism. Soc. Am.*, **95**(2), 699–707.
- Bay, H., Tuytelaars, T., & Van Gool, L., 2006. SURF: Speeded Up Robust Features, in *Computer Vision – ECCV 2006: 9th European Conference on Computer Vision, Graz, Austria, May 7-13, 2006. Proceedings, Part I*, pp. 404–417, Springer Berlin Heidelberg.
- Belmonte-Pool, A., 2002. Crustal seismicity, structure and rheology of the upper plate between the pre-cordillere and the volcanic arc in northern Chile (22°S-24°S), *PhD thesis, FU Berlin*.
- Beyreuther, M., Hammer, C., Wassermann, J., Ohrnberger, M., & Megies, T., 2012. Constructing a Hidden Markov Model based earthquake detector: application to induced seismicity, *Geophysical Journal International*, pp. no–no.
- Bishop, C. M., 2006. *Pattern Recognition and Machine Learning*, Springer.
- Blascheck, P., Nussbaum, C., & Joswig, M., 2015. Mont Terri research rock laboratory (Switzerland): Pilot project for assessing the seismic impact on a deep geological disposal for radioactive wastes, in *Proceedings of the ISRM Regional Symposium EUROCK 2015 & 64th Geomechanics Colloquium, Salzburg, Austria*, pp. 353–358.
- ed. Bormann, P., 2002. *New Manual of Seismological Observatory Practice (NMSOP-2)*, IASPEI, GFZ German Research Centre for Geosciences, Potsdam.
- Bras, R. L., Swanger, H., Sereno, T., Beall, G., Jenkins, R., & Nagy, W., 1994. Global Association Design Document and User's Manual, Tech. rep., Science Applications International Corporation.
- Bui Quang, P., Gaillard, P., Cano, Y., & Ulzibat, M., 2015. Detection and classification of seismic events with progressive

- multi-channel correlation and hidden Markov models, *Computers & Geosciences*, **83**, 110–119.
- Caljé, L., 2005. *Exploring boundaries of the Fisher and PMCC signal-detectors using infrasound signals*, Master's thesis, University of Utrecht.
- Cansi, Y., 1995. An automatic seismic event processing for detection and location: the PMCC method, *Geophysical Research Letters*, **22**, 1021–1024.
- Capon, J., 1973. Signal processing and frequency wavenumber spectrum analysis for a large aperture seismic array, *Methods Comput. Phys.*, **13**, 1–59.
- Cesca, S. & Grigoli, F., 2015. Full Waveform Seismological Advances for Microseismic Monitoring, in *Advances in Geophysics*, vol. 56, pp. 169–228, Elsevier Ltd.
- Chiu, J. M., Steiner, G., Smalley Jr., R., & Johnston, A. C., 1991. PANDA: A simple, portable seismic array for local- to regional-scale seismic experiments, *Bull. seism. Soc. Am.*, **81**, 1000–1014.
- Chollet, F., 2015. Keras.
- Cichowicz, B. Y. A., 1993. An Automatic S-Phase Picker, *Bull. seism. Soc. Am.*, **83**(1), 180–189.
- Ciresan, D., Meier, U., & Schmidhuber, J., 2012. Multi-column Deep Neural Networks for Image Classification, *arXiv*.
- Dahm, T., Kruger, F., Stammer, K., Klinge, K., Kind, R., Wylegalla, K., & Grasso, J.-R., 2007. The 2004 Mw 4.4 Rotenburg, Northern Germany, Earthquake and Its Possible Relationship with Gas Recovery, *Bull. seism. Soc. Am.*, **97**(3), 691–704.
- Dai, H. & MacBeth, C., 1995. Automatic picking of seismic arrivals in local earthquake data using an artificial neural network.pdf, *Geophys. J. Int.*, **120**.
- D'Alessandro, a., Mangano, G., D'Anna, G., & Luzio, D., 2013. Waveforms clustering and single-station location of

- microearthquake multiplets recorded in the northern Sicilian offshore region, *Geophysical Journal International*, **194**(3), 1789–1809.
- De Matos, M. C., Osorio, P. L. M., & Johann, P. R. S., 2007. Unsupervised seismic facies analysis using wavelet transform and self-organizing maps, *Geophysics*, **72**(1), 9–21.
- Deichmann, N. & Giardini, D., 2009. Earthquakes Induced by the Stimulation of an Enhanced Geothermal System below Basel (Switzerland), *Seismological Research Letters*, **80**(5), 784–798.
- Doubravová, J., Wiszniowski, J., & Horálek, J., 2016. Single Layer Recurrent Neural Network for detection of swarm-like earthquakes in W-Bohemia/Vogtland—the method, *Computers & Geosciences*, **93**, 138–149.
- Douglas, A., 2007. Forensic seismology revisited, *Surveys in Geophysics*, **28**(1), 1–31.
- Dowla, F. U., Taylor, S. R., & Anderson, R. W., 1990. Seismic discrimination with artificial neural networks: preliminary results with regional spectral data, *Bull. seism. Soc. Am.*, **80**(5), 1346–1373.
- Drew, J., Leslie, D., Armstrong, P., & Michaud, G., 2005. Automated microseismic event detection and location by continuous spatial mapping, in *SPE Annual Technical Conference and Exhibition*, p. Paper 95513.
- Dysart, B. Y. P. S. & Pulli, J. A. Y. J., 1990. Regional seismic event classification at the noress array: seismological measurements and the use of trained neuralnetworks, *Bull. seism. Soc. Am.*, **80**(6), 1910–1933.
- Ekstrom, G., 2006. Global Detection and Location of Seismic Sources by Using Surface Waves, *Bulletin of the Seismological Society of America*, **96**(4A), 1201–1212.
- Esposito, A., Giudicepietro, F., Marinaro, M., Martini, M., & Scarpetta, S., 2003. Discrimination of Earthquakes and Un-

- derwater Explosions Using Neural Networks, *Bull. seism. Soc. Am.*, **93**(1), 215–223.
- Esposito, A., Giudicepietro, F., Scarpetta, S., D'Auria, L., Marinaro, M., & Martini, M., 2006. Automatic Discrimination among Landslide, Explosion-Quake, and Microtremor Seismic Signals at Stromboli Volcano Using Neural Networks, *Bulletin of the Seismological Society of America*, **96**(4A), 1230–1240.
- Esposito, A. M., Giudicepietro, F., Scarpetta, S., Martini, M. G., Coltelli, M., & Marinaro, M., 2008. Unsupervised neural analysis of very-long-period events at Stromboli volcano using the self-organizing maps, *Bull. seism. Soc. Am.*, **98**(5), 2449–2459.
- Esposito, A. M., D'Auria, L., Giudicepietro, F., Peluso, R., & Martini, M., 2012. Automatic Recognition of Landslides Based on Neural Network Analysis of Seismic Signals: An Application to the Monitoring of Stromboli Volcano (Southern Italy), *Pure and Applied Geophysics*, **170**(11), 1821–1832.
- Essenreiter, R., Karrenbach, M., & Treitel, S., 2001. Identification and classification of multiple reflections with self-organizing maps, *Geophys. Prospect.*, **49**(3), 341–352.
- Fäh, D., Giardini, D., Kästli, P., Deichmann, N., Gisler, M., Schwarz-Zanetti, G., Alvarez-Rubio, S., Sellami, S., Edwards, B., Allmann, B., Bethmann, F., Woessner, J., Gassner-Stamm, G., Fritsche, S., & Eberhard, D., 2011. ECOS-09 Earthquake Catalogue of Switzerland Release 2011. Report and Database., *Sed/Ecos/R/001/20110417*, pp. 1–42.
- Fisher R.A., 1948. Statistical methods for research workers, *London, Oliver and Boyd*.
- Ford, S. R. & Walter, W. R., 2015. International Monitoring System Correlation Detection at the North Korean Nuclear Test Site at Punggye-ri with Insights from the Source Physics Experiment, *Seismol. Res. Lett.*, **86**(4), 1–11.

- Forgy, E., 1965. Cluster analysis of multivariate data: efficiency versus interpretability of classifications, *Biometrics*, **21**, 768–769.
- Freiberger, W. F., 1963. An approximate method in signal detection, *Quarterly Appl. Math.*, **20**(4), 373–378.
- Fulkerson, B., Vedaldi, A., & Soatto, S., 2009. Class segmentation and object localization with superpixel neighborhoods, in *2009 IEEE 12th International Conference on Computer Vision*, pp. 670–677, IEEE.
- Gajewski, D. & Tessmer, E., 2005. Reverse modelling for seismic event characterization, *Geophysical Journal International*, **163**(1), 276–284.
- Garofolo, J., Lamel, L., Fisher, W., Fiscus, J., Pallett, D., Dahlgren, N., & Zue, V., 1993. TIMIT Acoustic-Phonetic Continuous Speech Corpus LDC93S1.
- Geiger, L., 1910. Herdbestimmung bei Erdbeben aus den Ankunftszeiten, *Nachrichten von der Gesellschaft der Wissenschaften zu Göttingen*, pp. 331–349.
- Geiger, L., 1912. Probability method for the determination of earthquake epicenters from the arrival time only (translated from Geiger's 1910 German article), *Bull. St Louis Univ.*, **8**, 56–71.
- Geller, R. J. & Mueller, C. S., 1980. Four similar earthquakes in central California, *Geophys. Res. Lett.*, **7**, 821–824.
- Gendron, P., 2000. Rapid Joint Detection and Classification with Wavelet Bases via Bayes Theorem, *Bulletin of the Seismological Society of America*, **90**(3), 764–774.
- Gentili, S. & Michelini, A., 2006. Automatic picking of P and S phases using a neural tree, *Journal of Seismology*, **10**, 39–64.
- GEOFON, 2010. Geofon Projekt.

- Gharti, H. N., Oye, V., Roth, M., & Kühn, D., 2010. Automated microearthquake location using envelope stacking and robust global optimization, *Geophysics*, **75**(4), MA27–MA46.
- Giudicepietro, F., Ezin, E. C., Petrosino, S., Pezzo, E. D., Martini, M., & Marinaro, M., 2005. Automatic Classification of Seismic Signals at Mt. Vesuvius Volcano, Italy, Using Neural Networks, *Bull. seism. Soc. Am.*, **95**(1), 185–196.
- Goforth, T. & Herrin, E., 1981. An automatic seismic signal detection algorithm based on the walsh transform, *Bull. seism. Soc. Am.*, **71**(4), 1351–1360.
- Graeber, F., 1997. *Seismische Geschwindigkeiten und Hypozentren in den südlichen zentralen Anden aus der simultanen Inversion von Laufzeitdaten des seismologischen Experiments PISCO'94 in Nordchile*, Dissertation, Freie Universität Berlin.
- Grigoli, F., Cesca, S., Dahm, T., & Krieger, L., 2012. A complex linear least-squares method to derive relative and absolute orientations of seismic sensors, *Geophysical Journal International*, **188**(3), 1243–1254.
- Grigoli, F., Cesca, S., Vassallo, M., & Dahm, T., 2013. Automated Seismic Event Location by Travel-Time Stacking: An Application to Mining Induced Seismicity, *Seismological Research Letters*, **84**(4), 666–677.
- Grigoli, F., Cesca, S., Amoroso, O., Emolo, A., Zollo, A., & Dahm, T., 2014. Automated seismic event location by waveform coherence analysis, *Geophysical Journal International*, **196**(3), 1742–1753.
- Gutenberg, B. & Richter, C., 1954. *Seismicity of the Earth and Associated Phenomena*, Princeton, N.J.: Princeton University Press, 2nd edn.
- Häge, M. & Joswig, M., 2009. Spatiotemporal characterization of interswarm period seismicity in the focal area Nový Kostel (West Bohemia/Vogtland) by a short-term microseismic study, *Geophys. J. Int.*, **179**, 1071–1079.

- Häge, M., Blascheck, P., & Joswig, M., 2012. EGS hydraulic stimulation monitoring by surface arrays - location accuracy and completeness magnitude: the Basel Deep Heat Mining Project case study, *Journal of Seismology*.
- Hammer, C., Beyreuther, M., & Ohrnberger, M., 2012a. A Seismic-Event Spotting System for Volcano Fast-Response Systems, *Bulletin of the Seismological Society of America*, **102**(3), 948–960.
- Hammer, C., Ohrnberger, M., & Fah, D., 2012b. Classifying seismic waveforms from scratch: a case study in the alpine environment, *Geophysical Journal International*, **192**(1), 425–439.
- Harjes, H.-P., 1990. Design and siting of a new regional array in Central Europe, *Bull. seism. Soc. Am.*, **80**, 1801–1817.
- Harjes, H.-P. & Henger, M., 1973. Array-Seismologie, *Zeitschrift für Geophysik*, **39**, 865–905.
- Haubrich, R. A., 1968. Array design, *Bull. seism. Soc. Am.*, **58**, 977–991.
- Hochreiter, S. & Schmidhuber, J., 1997. Long short-term memory, *Neural computation*, **9**(8), 1735–80.
- Homma, T., Atlas, L., & II, R. M., 1988. An Artificial Neural Network for Spatio-Temporal Bipolar Patterns: Application to Phoneme Classification, *Advances in Neural Information Processing Systems 1*, pp. 31 – 40.
- Hsu, R. C. & Alexander, S. S., 1993. Recognition of earthquakes and explosions using a data compression neural network, *IEEE*.
- Johnson, C., Bittenbinder, A., Bogaert, B., Dietz, L., & Kohler, W., 1995. Earthworm: A flexible approach to seismic network processing, *Incorporated Research Institutions for Seismology Newsletter*, **14**(2), 1–4.
- Jolliffe, I., 1986. Principal component analysis, *New York: Springer*.

- Joswig, M., 1987. *Methoden zur automatischen Erfassung und Auswertung von Erdbeben in seismischen Netzen und ihre Realisierung beim Aufbau des lokalen 'Bochum University Germany' - Netzes*, Dissertation, Ruhr-Univ. Bochum.
- Joswig, M., 1990. Pattern recognition for earthquake detection, *Bull. seism. Soc. Am.*, **80**(1), 170–186.
- Joswig, M., 1993a. Automated Seismogram Analysis for the Tripartite Bug Array: An Introduction, *Computers & Geosciences*, **19**(2), 203–206.
- Joswig, M., 1993b. Single-trace detection and array-wide coincidence association of local earthquakes and explosions, *Computers & Geosciences*, **19**(2), 207–221.
- Joswig, M., 1995. Automated classification of local earthquake data in the BUG small array, *Geophys. J. Int.*, **120**, 262–286.
- Joswig, M., 2008. Nanoseismic monitoring fills the gap between microseismic networks and passive seismic, *First Break*, **26**, 117–124.
- Jurkevics, A., 1988. Polarization analysis of three-component array data, *Bull. seism. Soc. Am.*, **78**(5), 1725–1743.
- Kao, H. & Shan, S.-J., 2004. The Source-Scanning Algorithm: mapping the distribution of seismic sources in time and space, *Geophysical Journal International*, **157**(2), 589–594.
- Kao, H. & Shan, S. J., 2007. Rapid identification of earthquake rupture plane using Source-Scanning Algorithm, *Geophysical Journal International*, **168**(3), 1011–1020.
- Kennett, B. L. N., Brown, D. J., Sambridge, M., & C., T., 2003. Signal Parameter Estimation for Sparse Arrays, *Bull. seism. Soc. Am.*, **93**, 1765–1772.
- Kito, T., Rietbrock, A., & Thomas, C., 2007. Slowness-backazimuth weighted migration: A new array approach to a high-resolution image, *Geophysical Journal International*, **169**(3), 1201–1209.

- Klose, C. D., 2006. Self-organizing maps for geoscientific data analysis: geological interpretation of multidimensional geophysical data, *Comput. Geosci.*, **10**(3), 265–277.
- Köhler, A., Ohrnberger, M., & Scherbaum, F., 2009. Unsupervised feature selection and general pattern discovery using Self-Organizing Maps for gaining insights into the nature of seismic wavefields, *Computers & Geosciences*, **35**(9), 1757–1767.
- Köhler, A., Ohrnberger, M., & Scherbaum, F., 2010. Unsupervised pattern recognition in continuous seismic wavefield records using self-organizing maps, *Geophys. J. Int.*, **182**, 1619–1630.
- Kohonen, T., 1982. Self-organized formation of topologically correct feature maps, *Biological Cybernetics*, **43**(1), 59–69.
- Kohonen, T., 2001. Self-organizing maps, *Springer Ser. Inf. Sci.*, **30**, 501 pp.
- Kohonen, T. & Somervuo, P., 2002. How to make large self-organizing maps for non-vectorial data, *Neural Networks*, **15**(114), 945–952.
- Küperkoch, L., 2010. *Automated Recognition, Phase Arrival Time Estimation, and Location of Local and Regional Earthquakes*, Ph.D. thesis, Ruhr-Universität Bochum.
- Küperkoch, L., Meier, T., Lee, J., Friederich, W., & Working Group, E., 2010. Automated determination of P -phase arrival times at regional and local distances using higher order statistics, *Geophys. J. Int.*, pp. 1159–1170.
- Kvaerna, T. & Ringdal, F., 1992. Integrated array and three-component processing using a seismic microarray, *Bull. seism. Soc. Am.*, **82**(2), 870–882.
- Langer, H., Falsaperla, S., Masotti, M., Campanini, R., Spampinato, S., & Messina, a., 2009. Synopsis of supervised and unsupervised pattern classification techniques applied to volcanic tremor data at Mt Etna, Italy, *Geophysical Journal International*, **178**(2), 1132–1144.

- Langet, N., Maggi, A., Michelini, A., & Brenguier, F., 2014. Continuous Kurtosis-Based Migration for Seismic Event Detection and Location, with Application to Piton de la Fournaise Volcano, La Réunion, *Bull. seism. Soc. Am.*, **104**(1), 229–246.
- Lay, T. & Wallace, T. C., 1995. *Modern Global Seismology*, Academic Press.
- Lee, W. & Stewart, S., 1981. *Principles and Applications of Microearthquake Networks*, vol. 31, Academic Press.
- Leonard, G., Villagran, M., Joswig, M., Bartal, Y., Rabinowitz, N., & Saya, A., 1999. Seismic Source Classification in Israel by Signal Imaging and Rule-Based Coincidence Evaluation, *Bull. seism. Soc. Am.*, **89**(4), 960–969.
- Leonard, M., 2000. Comparison of Manual and Automatic Onset Time Picking, *Bulletin of the Seismological Society of America*, **90**(6), 1384–1390.
- Liao, Y. C., Kao, H., Rosenberger, A., Hsu, S. K., & Huang, B. S., 2012. Delineating complex spatiotemporal distribution of earthquake aftershocks: An improved Source-Scanning Algorithm, *Geophysical Journal International*, **189**(3), 1753–1770.
- Lomax, A., Michelini, A., & Curtis, A., 2009. Earthquake location, direct, global-search methods, *Encyclopedia of Complexity and System Science*, pp. 2449–2473.
- Lomax, A., Satriano, C., & Vassallo, M., 2012. Automatic Picker Developments and Optimization: FilterPicker—a Robust, Broadband Picker for Real-Time Seismic Monitoring and Earthquake Early Warning, *Seismological Research Letters*, **83**(3), 531–540.
- Magana-Zook, S., Gaylord, J., Knapp, D., Dodge, D., & Ruppert, S., 2016. Large-scale seismic waveform quality metric calculation using Hadoop, *Computers & Geosciences*, **94**, 18–30.
- Masiello, S., Esposito, A. M., Scarpetta, S., Giudicepietro, F., Esposito, A., & Marinaro, M., 2005. Application of self organized

- maps and curvilinear component analysis to the discrimination of the Vesuvius seismic signals, in *Proc. of the Int. Workshop on Self Organizing Maps WSOM2005*, pp. 387–396.
- Maurer, W. J., 1992. Seismic event interpretation using self-organizing neural networks, *Proc. of SPIE*, **1709**, 950–958.
- Megies, T., Beyreuther, M., Barsch, R., Krischer, L., & Wassermann, J., 2011. ObsPy – What can it do for data centers and observatories?, *Annals of Geophysics*, **54**(1).
- Melton, B. S. & Bailey, L. F., 1957. Multiple Signal Correlators, *Geophysics*, **22**(3), 565.
- Mermelstein, P., 1976. Distance measures for speech recognition, psychological and instrumental, in *Pattern Recognition and Artificial Intelligence*, pp. 374–388, ed. Chen, C. H., Academic Press, New York.
- Morita, Y. & Hamaguchi, H., 1984. Automatic detection of onset time of seismic waves and its confidence interval using the autoregressive model fitting, *Zisin*, **37**, 281–293.
- Murat, M. E. & Rudman, A. J., 1992. Automated First Arrival Picking: A Neural Network Approach, *Geophysical Prospecting*, **40**(February), 587–604.
- Musil, M. & Plesinger, A., 1996. Discrimination between local microearthquakes and quarry blasts by multi-layer perceptrons and Kohonen maps, *Bull. seism. Soc. Am.*, **86**(4), 1077–1090.
- Mykkeltveit, S., Åstebøl, K., Doornbos, D. J., & Husebye, E., 1983. Seismic array configuration optimization, *Bull. seism. Soc. Am.*, **73**, 173–186.
- N. Dalal, B. T., 2005. Histograms of Oriented Gradients for Human Detection., *IEEE Conference on Computer Vision and Pattern Recognition (CVPR)*.
- Ohrnberger, M., 2001. *Continuous Automatic Classification of Seismic Signals of Volcanic Origin at Mt. Merapi, Java, Indonesia*, Ph.D. thesis, Universität Potsdam.

- Pearson, K., 1895. Notes on regression and inheritance in the case of two parents, *Proceedings of the Royal Society of London*, **58**, 240–242.
- Pedregosa, F., Varoquaux, G., Gramfort, A., Michel, V., Thirion, B., Grisel, O., Blondel, M., Prettenhofer, P., Weiss, R., Dubourg, V., Vanderplas, J., Passos, A., Cournapeau, D., Brucher, M., Perrot, M., & Duchesnay, E., 2011. Scikit-learn: Machine Learning in Python, *Journal of Machine Learning Research*, **12**, 2825—2830.
- Podvin, P. & Lecomte, I., 1991. Finite difference computation of traveltimes in very contrasted velocity models: a massively parallel approach and its associated tools, *Geophys. J. Int.*, **105**, 271–284.
- Richter, C., 1956. *Elementary seismology*, W.H. Freeman and Company, San Francisco.
- Ringdal, F., 1990. Introduction to the special issue on regional seismic arrays and nuclear test ban verification, *Bull. seism. Soc. Am.*, **80**, 1775–1776.
- Ringdal, F. & Husebye, E. S., 1982. Application of arrays in the detection, location, and identification of seismic events, *Bull. seism. Soc. Am.*, **72**, 201–224.
- Ringdal, F. & Kväerna, T., 1989. A multi-channel processing approach to real time network detection, phase association, and threshold monitoring, *Bull. seism. Soc. Am.*, **79**(6), 1927–1940.
- Romeo, G., Mele, F., & Morelli, A., 1995. Neural networks and discrimination of seismic signals, *Comput. Geosci.*, **21**(2).
- Rousseeuw, P. J., 1987. Silhouettes: A graphical aid to the interpretation and validation of cluster analysis, *Journal of Computational and Applied Mathematics*, **20**, 53–65.
- Saragiotis, C. D., Hadjileontiadis, L. J., & Panas, S. M., 2002. PAI-S/K: A robust automatic seismic P phase arrival identification

- scheme, *IEEE Transactions on Geoscience and Remote Sensing*, **40**(6), 1395–1404.
- Schaff, D. P. & Waldhauser, F., 2010. One magnitude unit reduction in detection threshold by cross correlation applied to parkfield (California) and China seismicity, *Bulletin of the Seismological Society of America*, **100**(6), 3224–3238.
- Schaff, D. P., Bokelmann, G. H. R., Ellsworth, W. L., Zankerka, E., Waldhauser, F., & Beroza, G. C., 2004. Optimizing correlation techniques for improved earthquake location, *Bulletin of the Seismological Society of America*, **94**(2), 705–721.
- Scherbaum, F. & Johnson, J., 1992. Programmable Interactive Toolbox for Seismological Analysis (PITSA), in *IASPEI Software Library*, vol. 5, Seismological Society of America, El Cerrito.
- Schulte-Theis, H. & Joswig, M., 1990. Clustering and location of mining induced seismicity in the ruhr basin by automated master event comparison based on dynamic waveform matching (DWM), *Computers & Geosciences*, **V**(19), 233–241.
- Shearer, P. M., 1994. Global seismic event detection using a matched filter on long-period seismograms, *Journal of Geophysical Research*, **99**.
- Shearer, P. M., 1999. *Introduction to seismology*, vol. 6, Cambridge University Press.
- Sick, B., Walter, M., & Joswig, M., 2012. Visual Event Screening of Continuous Seismic Data by Supersonograms, *Pure and Applied Geophysics*, **171**(3-5), 549–559.
- Sick, B., Walter, M., & Joswig, M., 2013. Near-surface fracture and impact discovery from landslides and sinkholes by sonogram screening, *First Break*, **31**, 95–101.
- Sick, B., Guggenmos, M., & Joswig, M., 2015. Chances and limits of single-station seismic event clustering by unsupervised pattern recognition, *Geophys. J. Int.*, **201**(3), 1801–1813.

- Sleeman, R. & van Eck, T., 1999. Robust automatic P-phase picking: an on-line implementation in the analysis of broadband seismogram recordings, *Physics of the Earth and Planetary Interiors*, **113**(1-4), 265–275.
- Sokolowski, T. J. & Miller, G. R., 1967. Automated epicenter locations from a quadripartite array, *Bull. seism. Soc. Am.*, **57**, 269—275.
- Steinkraus, D., Buck, I., & Simard, P., 2005. Using GPUs for machine learning algorithms, in *Eighth International Conference on Document Analysis and Recognition (ICDAR'05)*, pp. 1115–1120 Vol. 2, IEEE.
- Suyehiro, S., 1967. A search for small, deep earthquakes using quadripartite stations in the Andes, *Bull. seism. Soc. Am.*, **57**, 447–461.
- Takanami, T. & Kitagawa, G., 1988. A new efficient procedure for the estimation of onset times of seismic waves, *J. Phys. Earth.*, **36**, 267–290.
- Tarvainen, M., 1999. Recognizing explosion sites with a self-organizing network for unsupervised learning, *Phys. Earth Planet. Inter.*, **113**(1-4), 143–154.
- Theano Development Team, 2016. Theano: A {Python} framework for fast computation of mathematical expressions, *arXiv e-prints*, **abs/1605.0**.
- Tin Kam Ho, 1995. Random decision forests, *Proceedings of 3rd International Conference on Document Analysis and Recognition*, **1**, 278–282.
- Tong, C. & Kennett, B. L. N., 1996. Automatic Seismic Event Recognition and Later Phase Identification for Broadband Seismograms, *Bull. seism. Soc. Am.*, **86**(6), 1896–1909.
- Turk, M. A. & Pentland, A. P., 1991. Eigenfaces for recognition, *J. Cognitive Neurosci.*, **3**(1).

- USGS, 2006. Shuttle Radar Topography Mission (SRTM), Tech. rep., United States Geological Survey.
- van Trees, H., 1968. *Detection, Estimation and Modulation Theory*, John Wiley and Sons, Inc., New York.
- Vidale, J. E., 1986. Complex polarization analysis of particle motion, *Bssa*, **76**(5), 1393–1405.
- Vouillamoz, N., Wust-Bloch, G. H., Abednego, M., & Mosar, J., 2016. Optimizing Event Detection and Location in Low-Seismicity Zones: Case Study from Western Switzerland, *Bull. seism. Soc. Am.*, **106**(5), 2023–2036.
- Waldhauser, F., 2000. A Double-Difference Earthquake Location Algorithm: Method and Application to the Northern Hayward Fault, California, *Bulletin of the Seismological Society of America*, **90**(6), 1353–1368.
- Walter, M. & Joswig, M., 2009. Seismic characterization of slope dynamics caused by softrock-landslides: The Super-Sauze case study, in *Malet, J.-P., Remaître, A., Boogard, T. (Eds), Proceedings of the International Conference on Landslide Processes: from geomorphologic mapping to dynamic modelling, Strasbourg, CERG Editions.*
- Walter, M., Niethammer, U., Rothmund, S., & Joswig, M., 2009. Joint analysis of the Super-Sauze (French Alps) mudslide by nanoseismic monitoring and UAV-based remote sensing, *First Break*, **27**(8), 75–82.
- Walter, M., Arnhardt, C., & Joswig, M., 2011a. Seismic monitoring of rockfalls, slide quakes, and fissure development at the Super-Sauze mudslide, French Alps, *Engineering Geology*, **128**, 12–22.
- Walter, M., Walser, M., & Joswig, M., 2011b. Mapping rainfall-triggered fracture processes, and seismic determination of landslide volume at the creeping Heumoes slope, *Vadose Zone Journal*, **10**(2), 487–495.

- Walter, M., Schwaderer, U., & Joswig, M., 2012. Seismic monitoring of precursory fracture signals from a destructive rockfall in the Vorarlberg Alps, Austria, *Natural Hazards and Earth System Science*, **12**(11), 3545–3555.
- Wang, J. & Teng, T.-l., 1995. Artificial Neural Network-Based Seismic Detector, *Bull. seism. Soc. Am.*, **85**(1), 308–319.
- Ward, P. L. & Gregersen, S., 1973. Comparison of earthquake locations determined with data from a network of stations and small tripartite arrays on Kilauea Volcano, Hawaii, *Bull. seism. Soc. Am.*, **63**, 679–711.
- Wessel, P. & Smith, W. H. F., 1998. New improved version of generic mapping tools released, *Eos Trans. AGU*, **79**(47), 579.
- Wiszniowski, J., Plesiewicz, B. M., & Trojanowski, J., 2014. Application of Real Time Recurrent Neural Network for Detection of Small Natural Earthquakes in Poland, *Acta Geophysica*, **62**(3), 469–485.
- Withers, M., Aster, R., Young, C., Beiriger, J., Harris, M., Moore, S., & Trujillo, J., 1998. A Comparison of Select Trigger Algorithms for Automated Global Seismic Phase and Event Detection, *Bull. seism. Soc. Am.*, **88**(1), 95–106.
- Withers, M., Aster, R., & Young, C., 1999. An Automated Local and Regional Seismic Event Detection and Location System Using Waveform Correlation, *Bull. seism. Soc. Am.*, **89**(3), 657–669.
- Wust-Bloch, G. H. & Joswig, M., 2006. Pre-collapse identification of sinkholes in unconsolidated media at Dead Sea area by 'nanoseismic monitoring' (graphical jackknife location of weak sources by few, low-SNR records), *Geophys. J. Int.*, **167**, 1220–1232.
- Young, C., Harris, M., Beiriger, J., Moore, S., Trujillo, J., Withers, M., & Aster, R., 1996. The Waveform Correlation Event Detection System Project , Phase 1 : Issues in Prototype Development and Testing, *Sandia Report*.

- Zhang, H., 2004. The Optimality of Naive Bayes, *Proceedings of the Seventeenth International Florida Artificial Intelligence Research Society Conference FLAIRS 2004*, **1**(2), 1 – 6.
- Zhang, M. & Wen, L., 2015a. An effective method for small event detection: match and locate (M&L), *Geophysical Journal International*, **200**(3), 1523–1537.
- Zhang, M. & Wen, L., 2015b. Seismological Evidence for a Low-Yield Nuclear Test on 12 May 2010 in North Korea, *Seismological Research Letters*, **86**(1), 138–145.
- Zhao, Y. & Takano, K., 1999. An Artificial Neural Network Approach for Broadband Seismic Phase Picking, *Bull. seism. Soc. Am.*, **89**(3), 670–680.
- Zucca, J. J., 1998. Forensic seismology supports the Comprehensive Test Ban Treaty, *Science & Technology Rev.*, LLNL, CA., Sept. 1998, pp. 4–11.

# Appendices





---

## COMBINED REAL-TIME DETECTOR

---

A combination of multiple algorithms into a real-time seismic event detection system is described in the flowchart of Figure [A.1](#). The system was developed during this thesis. It is currently used continuously for multiple permanent monitoring networks of varying size, one of them is the [DGMK](#) network operated by the [IfG](#). The system sends Emails containing state-of-health information, statistics and event alarms with locations from source-scanning as explained in chapter [6](#). For the [DGMK](#) network, the system was continuously cross-checked with a manual event screening. It found so far all events from the manual screening and could even detect more events which were not identified manually.

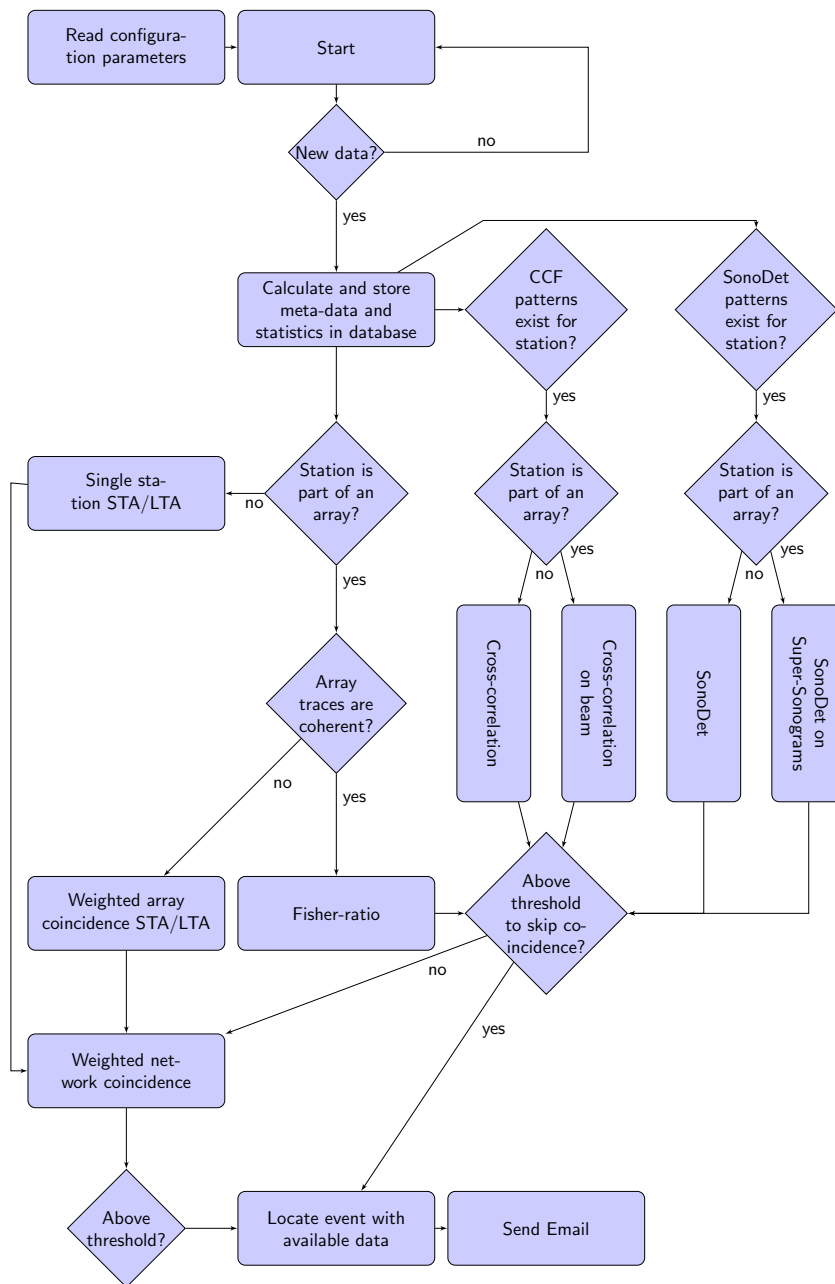


Figure A.1: Flowchart of coincidence processing with various detectors for DGMK network. Not shown are the real-time data acquisition steps from stations in the field. The template database for pattern recognition (CCF and SonoDet) can be updated after each event detection.

# B

---

## NOISE REMOVAL BY SIMPLIFIED SOURCE SCANNING DETECTION

---

Strong noise sources near seismic monitoring networks which can even trigger false positive detections at network coincidence detectors have often a fixed position of origin. The knowledge of this position can be exploited to detect them reliably even if single station noise signatures might be similar to sought after events. A simplified source scanning approach with only particular source grid points can be used. Source scanning is based on the time shifting of **CFs** based on the travel times of hypothetical sources. The source hypocenters are usually distributed over a three-dimensional cube in regular distances because only small a priori knowledge is available of future source locations. For known noise sources however the source location is known and the iteration over a 3D grid of source locations can be reduced to an iteration over few fixed grid points. Stacking **CFs** with the travel time offsets of these few points allows to presume a high confidence that a peak in the stack belongs to one of the given noise sources. Thereby these signals can be removed from detection results without risking false negatives. The knowledge about these noise source locations can also be incorporated into the source scanning algorithm to detect legitimate events by removing the appropriate grid points of noise sources from the 3D cube of source locations.

At the **DGMK** network, one particular type of noise signal which was detected by all stations of the network was recurring at irregular days during the long term monitoring. Beamforming at the array stations and comparing onset times between

the network stations showed that the signals had the velocity of acoustic waves. The noise signals only occurred during the day for several hours. Locating the signals with an velocity model for acoustic waves showed that the source came from a military practice area. By talking to local people in the region it could be confirmed that it came from artillery practice with the so called "Panzerhaubitze 2000". An example of the signals can be seen in Figure B.1. It turned out that during these practices it was very difficult to manually screen the data and even the coincidence STA/LTA detector was giving false positive detections due to overlapping acoustic events whose time difference of arrivals again did fit to seismic velocities.

Using the acoustic wave velocity model and the source location for source scanning provided a reliable detector of these events. The detections could then be incorporated into the manual screening by replacing the sonograms during short time detection intervals with the background noise of the current time frame as can be seen in Figure B.2. Using array beamforming techniques as for example the Fisher detector with acoustic wave propagation did not yield reliable results due to the low coherence between waveforms from the acoustic to seismic coupled signals.

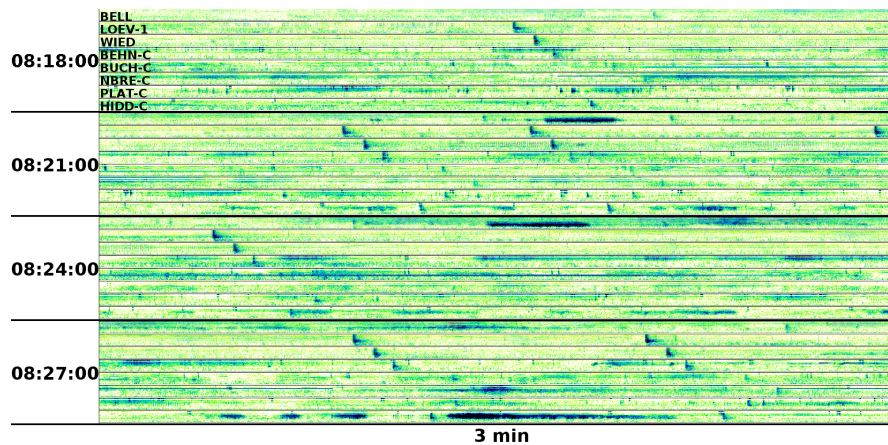


Figure B.1: The view shows super-sonograms of the 8 DGMK network stations. The high energy patterns are from acoustic waves from artillery practice from coupling into the ground. Screening data manually can be very difficult during practice times.

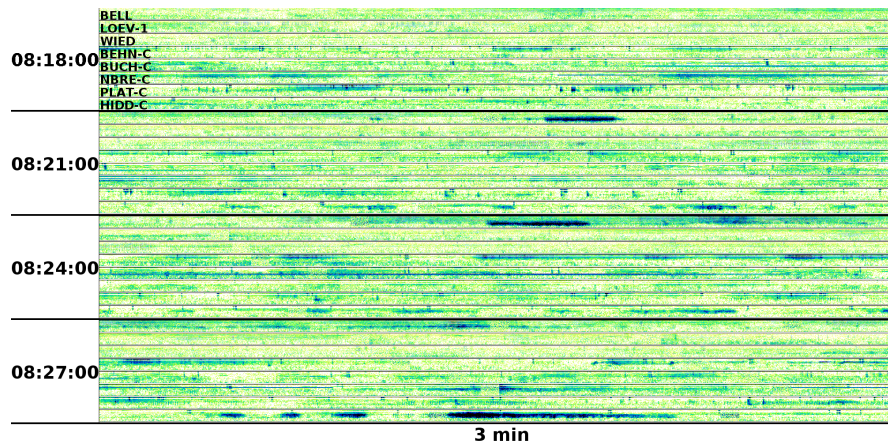


Figure B.2: Acoustic noise from artillery practice removed with source scanning detector (same time frame as in Figure B.1). The detector uses the acoustic wave velocity and the known origin from the artillery training area to stack STA/LTA CFs with the appropriate time delays from all stations. The sonograms at each detection are replaced with the current stationary noise of the row.





---

## VISUAL SEISMIC EVENT SCREENING BY SUPER-SONOGRAMS

---

- **Title:** Visual event screening of continuous seismic data by super-sonograms
- **Published in:** Pure and Applied Geophysics, 2012, Volume 171, Issue 3-5, Pages 549-559, DOI 10.1007/s00024-012-0618-x
- **Authors:** Sick, B.\*, Walter, M., and Joswig, M.
- **\*Corresponding author:** benjamin.sick@gmail.com

### C.1 ABSTRACT

In this study we present a new visualization method for human seismic data inspection called super-sonograms which maximizes the amount of time and stations visible at screen while retaining the possibility to detect short and low SNR signals. This visualization approach is integrated in a seismological software suite which is used in the seismic aftershock monitoring system (SAMS) of CTBTO on-site inspections (OSI) to detect suspicious events eventually representing aftershocks from an underground nuclear explosion (UNE). During an OSI huge amounts of continuous waveform data accumulate from up to 50 six-channel mini-arrays covering an inspection area of 1,000 square kilometers. Sought after events can have magnitudes as low as  $M_L - 2.0$ , and a duration of just a few seconds which makes it particularly hard to discover them in large, noisy datasets. Therefore, the data visualization is based on

non-linearly scaled, noise-adapted spectrograms, i.e. sonograms which help to distinguish weak signal energy from stationary background noise. Four single-trace sonograms per mini-array can be combined to super-sonograms since array aperture is small, and sonograms suppress differences of local site noise allowing an analyst to check fast on array-wide signal coherence. In this paper, we present the super-sonograms and the software on the basis of a dataset from a creeping, inhabited landslide in Austria where the same station layout is used as in an OSI. Detected signals are fracture processes in the sedimentary landslide, i.e. slidequakes, with  $M_L$   $-0.5$  to  $-2.5$  between July 2009 and July 2011. These signals are comparable in magnitude and duration to expected weak UNE aftershocks.

## C.2 INTRODUCTION

The seismic aftershock monitoring system (SAMS) of an on-site inspection (OSI) has to cover events within an area of up to 1,000 square kilometers (CTBTO, 1996). To meet these criteria the technique of *Nanoseismic Monitoring* (Joswig, 2008) is used and up to 50 seismic mini-arrays are installed for monitoring. A total of 40 inspectors are allowed in an OSI and an inspection can last up to 60 days with a maximum extension of 70 days (CTBTO, 1996). All data processing must be done onsite by the inspectors, and since event detections may inform the ongoing inspection, it is important to analyze the seismic data as fast as possible. Only few studies of aftershocks due to explosions are available, an overview can be found in Ford & Walter (2010). Jarpe et al. (1994) found that explosions from chemical and nuclear tests have similar aftershock rates but that magnitudes of aftershocks from explosions were smaller relative to aftershocks from earthquakes assuming similar magnitudes of the source event. Furthermore, manual processing of the continuous waveforms is essential. State of the art automatic detection algorithms are not useful in the OSI scenario as signatures of expected events are unknown a priori and signals from many different noise sources would lead to too many false

positive automatic detection picks. Training of sophisticated automatic processing tools to support manual analysis in such conditions is complicated and is the topic of current research. Seismological data from an OSI is large because of the many stations but little in the sense of recorded time. An automatic algorithm would have to take into account the many unknowns, like station specific characteristics as geology, weather influence and typical signals occurring in an inspection area (IA) at specific stations. Depending on regulations by the inspected state party (ISP), the geology and the time which is available, stations can not be buried deeply and station locations can not always be optimal (e.g. sediments instead of solid rock). This makes them especially exposed to local noise sources. Noise sources and regulations, e.g. traffic by military vehicles, might even be introduced deliberately by the ISP to compromise the measurements. An algorithm would have to be tuned separately for each mini-array with very little data (data accumulates after station deployment) and no real events (aftershocks of a UNE). By the manual analysis we enable expert analysts with year long experience with seismic signals to take into account all of these influences and possible error sources and make the decision to further investigate a signal or not. They are also the ones who deploy the stations and thus they know to a great detail what noise sources might be influencing the stations (e.g. a river, road or train track nearby, or the station is on a hill and more exposed to wind gusts and rain etc.). Events can be very sparse and one missed event could be the only hint to an UNE. The limited resources and tough time schedules led to the development of the new visualization technique of super-sonograms, specially suited for manual processing of large datasets with very low SNR events. The super-sonograms are incorporated in a new software suite called *NanoseismicSuite*.

### C.2.1 *Nanoseismic Monitoring*

The method of *Nanoseismic Monitoring* fills the gap between passive seismics and micro-seismic networks (Joswig, 2008). Data

acquisition is based on the application of seismic mini-arrays, which are suited for azimuth determination of an incoming signal and were used in numerous studies. Seismic arrays have a long-standing history in CTBT monitoring (e.g. Ringdal & Husebye 1982; Ringdal 1990) and much work was done on fundamental array design (e.g. Haubrich, 1968; Mykkeltveit et al., 1983; Harjes, 1990). However, sparse arrays with three or four stations are rarely considered (e.g. Suyehiro, 1967; Ward & Gregersen, 1973; Chiu et al., 1991; Kvaerna & Ringdal, 1992; Kennett et al., 2003) although they offer great improvement for automated processing at minor investment costs (e.g. Sokolowski & Miller, 1967; Joswig, 1990, 1993a). As the mini-arrays lead or navigate to the source of a signal, we established the term SNS - *Seismic Navigating System*, which consists of three vertical seismometers and one three-component seismometer for monitoring. Each mini-array is arranged as having the three-component station in the center and the three one-component vertical stations in a tripartite array around. In dependence of the epicentral distance of expected signals, the array aperture is usually between around 50 and 200 meters. The use of these mini-arrays combines array processing with three component processing and thus provides calculation of back azimuths, apparent velocities and particle motion. Array processing as time shifting and stacking is not yet integrated in the standard monitoring process. Furthermore, the mini-arrays are designed for a fast and easy installation by two persons which is crucial in an OSI. *Nanoseismic Monitoring* focuses on forensic seismology (Zucca, 1998; Douglas, 2007) with manual screening of data and sought after events just above the ambient noise level. Apart from OSI further applications are sinkhole monitoring (Wust-Bloch & Joswig, 2006), active fault mapping (Häge & Joswig, 2009) and monitoring of slope dynamics (Walter et al., 2009; Walter & Joswig, 2009; Walter et al., 2011a).

### C.2.2 Heumoes slope example dataset

Results of the Integrated Field Exercise 2008 (IFE08) in Kazakhstan where seismic data was recorded continuously by 30 seismic small arrays for 15 days can unfortunately not be presented in this study due to formal restrictions. The advantages of event screening seismic data by the analysis of super-sonograms are explained exemplary using seismic data recorded permanently by three mini-arrays at Heumoes slope, Austria. The creeping Heumoes slope is situated in the Vorarlberg Alps, Austria, around 25 km south of Bregenz (Figure C.1). The inhabited slope extends  $\sim 1.5$  km in east-west and  $\sim 600$  m in north-south direction and shows movement rates of a few centimeters per year at the surface (Lindenmaier et al., 2005). A permanent network consisting of three mini-arrays was installed from July 2009 for two years in order to observe slope-related signals caused by the movement of the slope (Figure C.1, Walter & Joswig, 2008; Walter et al., 2011b). The observed seismic signals with magnitudes between  $M_L = -0.7$  and  $M_L = -2.5$  are generated by brittle deformation of the unstable slope material, i.e. fracture processes or “slidequakes” (Gomberg et al., 2011). As the Heumoes slope is inhabited, the seismic recordings are dominated by anthropogenic noise sources. The differentiation between slope-related signals and anthropogenic or natural noise transients by noise forensics is essential (Douglas, 2007).

## C.3 SUPER-SONOGRAM EVENT SCREENING AND CLASSIFICATION

Automatic processing of the seismic data is not practicable at the moment because sought after signals in *Nanoseismic Monitoring* have such a low SNR and are often only detected at single mini-arrays. Furthermore, comprehensive training of an automatic detector would be difficult because fracture processes in the given slope are infrequent and signal patterns can vary significantly depending on origin of the event. Automatic picking algorithms would either miss crucial events (false nega-

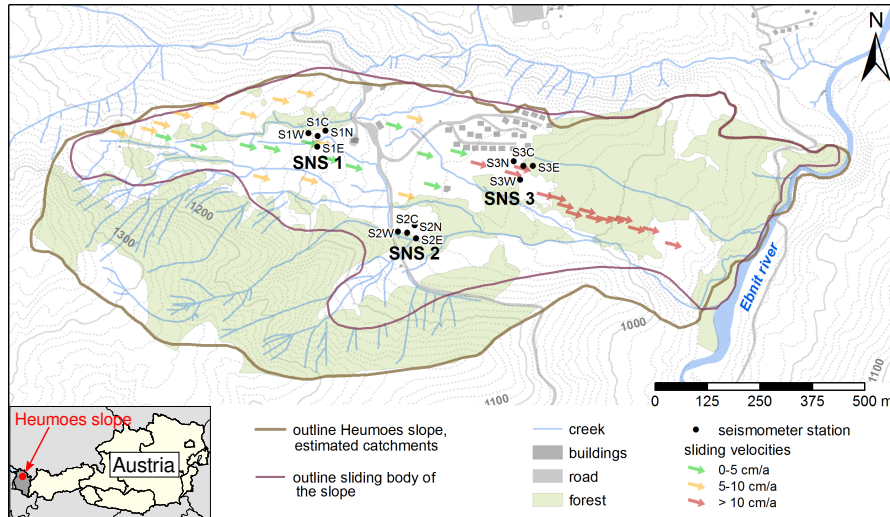


Figure C.1: Heumoes slope, sliding velocities and location of the three seismic mini-arrays SNS<sub>1</sub>, SNS<sub>2</sub>, SNS<sub>3</sub> and their stations (modified after [Lindenmaier et al., 2005](#)).

tives) or create an abundance of events coming from the various noise sources on the slope (false positives). An example can be found in [Spillmann et al. \(2007\)](#) where only  $\sim 0.0034$  percent of the 66.409 triggered events were slope-related. Research for automatic processing of such events is ongoing.

Manual processing on the other hand allows an experienced seismologist with a deep knowledge of the setting and noise sources of the given area to set potential events into a broader context and thus eliminate false positives while finding even events disturbed by noise bursts. The need for manual screening of continuous data encouraged the development of a new software suite which is capable of displaying large datasets on the screen while preserving the capability to detect very weak and short lasting events. The usually used seismograms (time-domain) were not sufficient anymore and instead energies of seismic data are visualized in form of spectrograms (time-frequency domain). The spectrograms are enhanced by multiple signal processing steps and are called sonograms ([Joswig, 1993b](#)).

### C.3.1 Sonogram calculation steps

The sonogram calculation steps are essential for the understanding of the resultant super-sonograms and are explained here after Joswig (1993b, 1995).

The time signal is processed by short-term-Fourier-transformation (STFT). It is split into segments of 256 samples  $x(\tau)$  which are tapered with a  $\sin^2(\tau)$  windowing function and transformed per fast-Fourier-transformation (FFT) to  $X(\omega)$  with a segment overlap of approximately 50%.

The resulting spectrograms are based on the power-spectral density (PSD) from the STFT and are filtered in 13 half-octave wide passbands (equation 23).

$$A(\omega, t) = \sum_{\text{half-octave}} X(\omega) X(\omega)^* \quad (23)$$

The amplitudes of the resultant time-frequency matrix are scaled logarithmic. If a log-normal noise distribution is assumed, the logarithmic scaled spectrogram has a Gaussian distribution of noise given by mean  $\mu(\omega)$  and variance  $\sigma(\omega)$ . Noise adaptation has to be outlier resistant and a more robust solution is to use the median  $M(\omega) = M_{50}$  instead of the mean and  $S(\omega) = M_{75} - M_{50}$  instead of the variance.  $M(\omega)$  and  $S(\omega)$  are both calculated for each frequency band allowing an individual adaptation. For the noise adaptation we subtract  $2^{M(\omega)}$  from our signal and allow only values greater than  $2^{M(\omega)+S(\omega)}$  (blanking). Therefore, we eliminate disturbing artefacts in our signal visualization (equation 24).

$$D(\omega, t) = \begin{cases} \log_2 \left( A(\omega, t) - 2^{M(\omega)} \right), & A(\omega, t) > 2^{M(\omega)+S(\omega)} \\ 0, & \text{else} \end{cases} \quad (24)$$

For further scaling by prewhitening we define the log noise variance (equation 25).

$$N_D(\omega) = \log_2 2^{M(\omega)+S(\omega)} - 2^{M(\omega)} \quad (25)$$

$D(\omega, t)$  and  $N_D(\omega)$  are each rounded to nearest integer values to suppress fine grain amplitude differences less than  $\sqrt{2}$ .

Subtracting the frequency-resolved noise variance  $N_D$  in the logarithmic scaled energy distribution performs a prewhitening where the significance of any local energy spot is rated and therefore color-coded as a multiple of the background noise variance (equation 26). This interpretation can be seen in the formulation of equation 27).

$$\text{SONO}(\omega, t) = \begin{cases} D(\omega, t) - N_D(\omega), & A(\omega, t) > 2^{M(\omega)+S(\omega)} \\ 0, & \text{else} \end{cases} \quad (26)$$

$$\text{SONO}(\omega, t) = \begin{cases} \log_2 \left( \frac{A(\omega, t) - 2^{M(\omega)}}{2^{M(\omega)+S(\omega)} - 2^{M(\omega)}} \right), & A(\omega, t) > 2^{M(\omega)+S(\omega)} \\ 0, & \text{else} \end{cases} \quad (27)$$

Sonograms were originally developed for automatic pattern recognition (Joswig, 1990) but are perfectly capable of assisting analysts in manual screening and identification of very small scale events especially in noisy environments. Sonograms filter disturbing stationary background noise and the half-octave band division of frequency bands is based on human perception of frequencies which enhances manual detections. Event patterns are prominent even when analyzing large datasets with varying noise conditions. Amplitudes are visualized with a specially developed color scale which emphasizes on contrasts (Figure C.2). Sonogram scaling makes use of values above the saturation of the color scale which can result in black areas of strong events. For detection purposes it is enough to recognize strong events as such, further analysis of e.g. amplitude ratios for a detailed classification of events can be done with seismograms with scaling on the maximum values. The individual processing steps for the sonogram calculation are illustrated in Figure C.2 on the basis of a weak local earthquake near the Heumoes

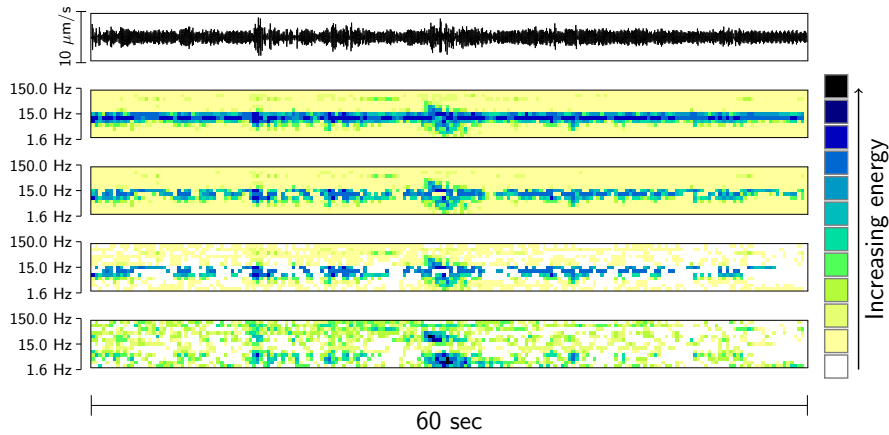


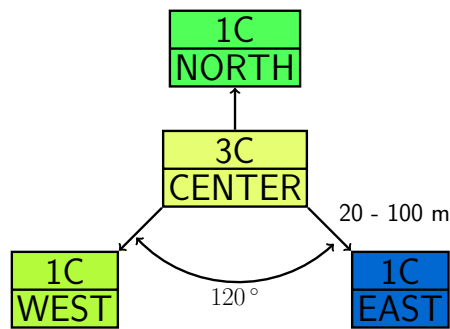
Figure C.2: Processing steps of sonogram calculation for a local earthquake in a noisy environment, from top to bottom: seismogram, power spectral density spectrogram with logarithmic amplitudes and half-octave frequency bands, noise adaptation, blanking and prewhitening ( $M_L$  1.0, distance 7.7 km, 2010/11/05 15:02:20 UTC).

slope. The elimination of disruptive dominating small band noise which is permanently present can be seen prominently in Figure C.2.

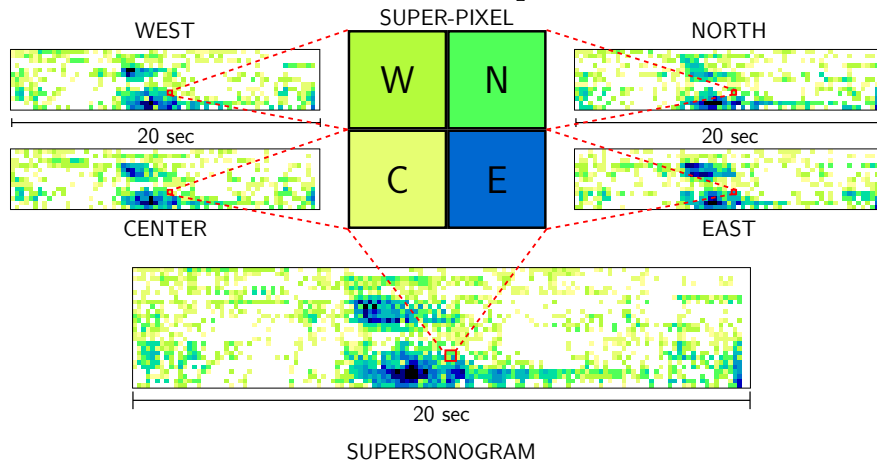
### c.3.2 Super-sonograms

Single stations of one mini-array are within 200 m of distance which makes it possible to combine the four vertical traces of one mini-array into a so called super-sonogram. The combination is done by using “super-pixels” at each time and frequency position. The horizontal traces of the three component stations are used later for the more detailed interpretation of signals. Each “super-pixel” of the super-sonogram consists of four pixels, each from one vertical trace of the mini-array. Figure C.3 shows how pixels of four ordinary sonograms create one “super-pixel” which is then used in the super-sonogram.

The super-sonogram visualization adds additional advantages to the array processing methods which were primarily introduced to estimate back-azimuth and apparent velocity. The



Layout of mini-array with one three-component (3C) central station and three vertical component (1C) stations.



Compilation of super-sonogram from four sonograms of a mini-array (same event as in Figure C.2). The pixels of each single sonogram create the “super-pixels” of the super-sonogram.

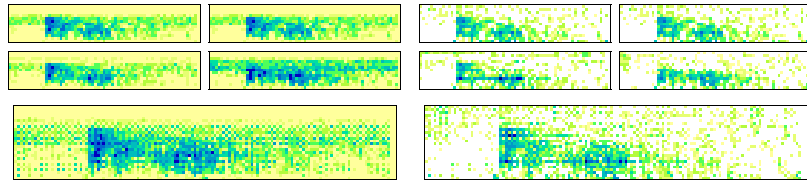
Figure C.3: Layout of mini-array and compilation of super-sonogram.

visualization helps out in the pure detection and differentiation of events from noise with fast coherence checks and acts as a preprocessing before events are inspected more thoroughly with beam-forming and localization. E.g. array-wide signal coherence can be checked very fast by looking just at one trace. Incoherent signals show up as spotted patterns while coherent ones create consistent areas of similar color. Furthermore, the amount of data which can be displayed on one screen increases significantly. Super-sonograms can be displayed on screen with a very small dimension and events are still prominent to an analyst. Additionally, faulty or very noisy data of single stations can be recognized immediately in comparison with other stations of the same array.

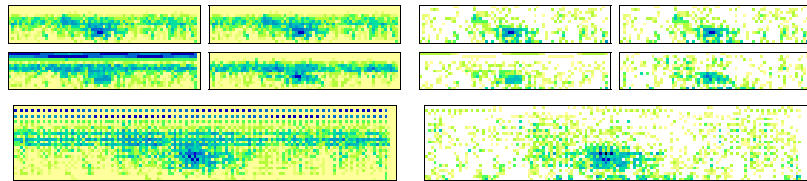
Tests with common spectrograms (Figure C.4) show that the combination of traces from different stations into one trace is only possible with the signal processing steps of the sonogram calculation. On the other hand, if regular spectrograms are combined to a super-sonogram, the varying noise conditions at each single station show up dominantly and obfuscate events (Figure C.4 top). Low SNR signals are not visible without the enhancements (Figure C.4 middle). With sonograms, the onset times of events get significantly clearer by better contrasts of pre and post onset time signals as well as e.g. the extension of low frequency parts of an impulsive i.e. broadband onset (Figure C.4 bottom).

### c.3.3 *Signal classification*

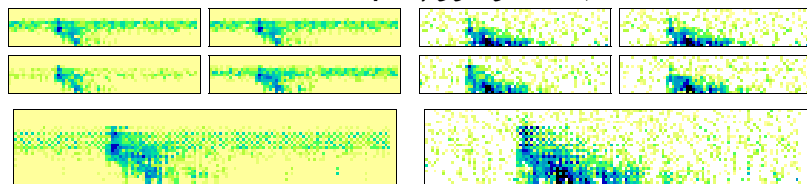
Sonograms allow an analyst to classify events by multiple factors partly known from conventional seismogram analysis. Energies of different frequencies, amplitudes, signal duration and different seismic onsets of phases are the main classification attributes. Additionally, the direct visualization of frequency contents allows e.g. the immediate recognition of moving signal sources. Signals of sources approaching a station are getting more broadband while those of leaving sources are getting more narrowband which can be seen in Figure C.6 bottom for a snowcat



Significantly different single station spectrograms on the left get much more similar through sonogram processing which makes super-sonogram creation possible ( $M_L$  1.2, distance 24.02 km, 2010/04/02 03:14:43 UTC).



The almost not visible event in the spectrograms on the left gets visible by lifting it from noise in the sonograms and the resulting super-sonogram ( $M_L$  0.7, distance 18.55 km, 2010/10/27 04:35:15 UTC).



Example of an improvement of a P-onset through better contrasts and completion of energies of lower frequencies of the impulsive i.e. broadband onset ( $M_L$  1.0, distance 4.94 km, 2010/03/23 15:58:50 UTC).

Figure C.4: Comparison of super-sonogram compilation of ordinary spectrograms without signal enhancing sonogram steps (left) versus sonograms (right). Figures consist of the four spectrograms/sonograms in the order given in Figure C.3 plus the resulting super-sonogram on the bottom. Signal length of all examples is 20 seconds.

moving on the Heumoes slope. By the use of super-sonograms in a large time-span display events can be furthermore analyzed by periodicity, number of stations and most importantly the event can be put in a broader context by looking at the data of other stations and other points of time with the same scaling. Anthropogenic noise can be identified easier and excluded by e.g. a repetition of signals of the same energy or/and a constant repeating frequency as shown in Figure C.5 for a water pump installed at the Heumoes slope. Regional and teleseismic seismicity need to be classified in an OSI to exclude it from UNEs while local seismicity can be the result from aftershocks of an UNE (Figure C.6 middle). In the case of landslide monitoring slidequakes and other slope-related events are of particular interest. Figure C.6 top shows one of the many registered events in the slope which is classified to be a slidequake. All examples show how different types of seismic sources create specific patterns in the super-sonograms and therefore help an analyst in manual screening.

#### C.4 SOFTWARE

The super-sonogram technique is integrated in a software suite called *NanoseismicSuite* which consists of four modules, *SeisServ*, *SonoView*, *TraceView* and *HypoLine* (Figure C.7). A basic description of each software module is given here, more information on the software can be found on the *Nanoseismic Monitoring* webpage<sup>1</sup>.

- *SeisServ*

*SeisServ* reads seismic data and meta-data in the Center for Seismic Studies (CSS) or MiniSEED format from files or an Oracle database. It provides this data to the other modules and allows editing of the meta-data, e.g. the geometry of seismic stations.

- *SonoView*

---

<sup>1</sup> <http://www.nanoseismic.net>

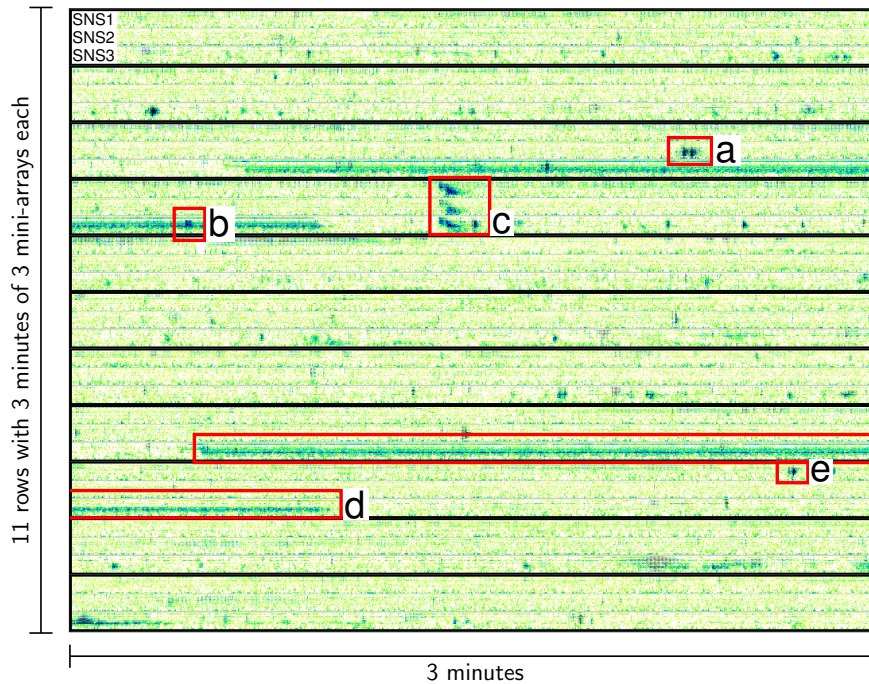
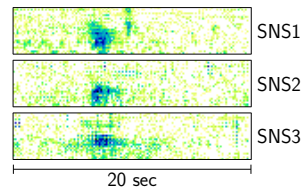
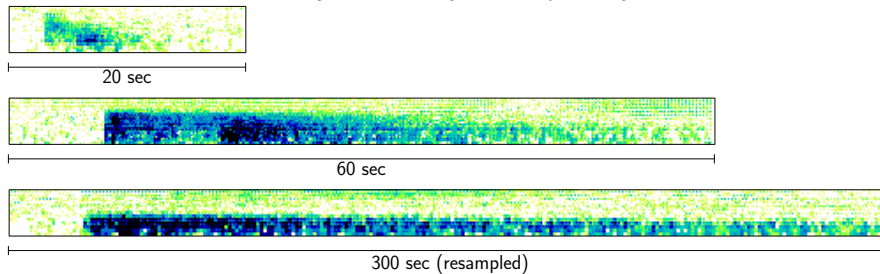


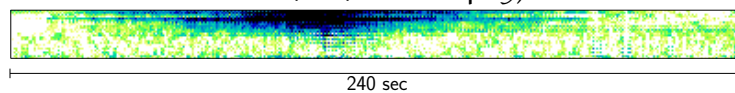
Figure C.5: Screenshot of the software module *SonoView* with super-sonograms of three mini-arrays of a larger timespan with recurring anthropogenic noise (start 2009/10/21 00:00:00 UTC). The screenshot shows eleven rows, each row contains three minutes of super-sonograms of all three mini-arrays. (a) Multiple frost heave events at SNS2. (b) Frost heave event in noise of SNS3. (c) Local earthquake ( $M_L$  0.3, distance 10.0 km) with frost heave event on SNS3 right after earthquake. (d) Anthropogenic noise transient caused by a pump installed near SNS3. (e) Frost heave event at SNS1.



Super-sonograms of slidequake at all mini-arrays ( $M_L = 1.8$ , distance 0.2 km from SNS1, 0.33 km from SNS2 and 0.35 km from SNS3, 2010/05/22 04:16:05 UTC).



Super-sonograms of natural seismicity at SNS1. From top to bottom: local earthquake ( $M_L$  0.9, distance 17.5 km, 2010/10/28 14:00:35), regional earthquake ( $M_L$  2.4, distance 68 km, 2009/11/02 12:14:40 UTC), teleseismic earthquake (Haiti region, 5 minutes super-sonogram resampled from 400 Hz to 100 Hz, 2010/01/12 22:04:05).



Super-sonogram with characteristic “cigar” shape of moving noise source (here snowcat on Heumoes slope, 4 minutes super-sonogram resampled from 400 Hz to 100 Hz, 2011/02/01 19:55:15 UTC).

Figure C.6: Examples of natural seismicity and noise.

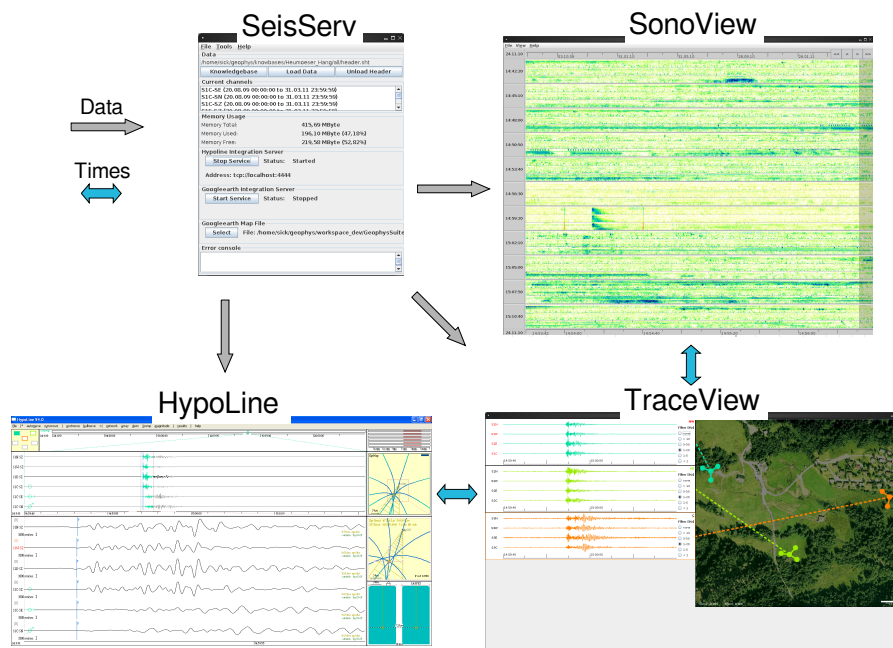


Figure C.7: *NanoseismicSuite* overview of components and interfaces. Arrows indicate data and timing interfaces. *SeisServ* provides data to *SonoView*, *TraceView* and *HypoLine* which synchronize current screening times with each other.

After loading the data, *SonoView* is the first application to use in a typical event screening scenario. It visualizes super-sonograms in a manner to maximize the visible data on one screen. An arbitrary amount of mini-arrays and time spans can be loaded. An analyst can scroll fast through the continuous data in *SonoView* and mark suspicious events for further processing steps.

- *TraceView*

Detected events from *SonoView* can be further analyzed in *TraceView* which visualizes the seismograms of these events together with a map of the measurement area with locations of the mini-arrays. It provides a two-dimensional neighbourhood overview of mini-arrays which can not be provided by the one-dimensional listing of *SonoView*. *TraceView* shows the seismograms of the currently selected mini-array and the five adjacent mini-arrays based on geographic context. Basic filters and scalings can be applied to the seismograms and geo-referenced images of the measurement area can be shown in the map (e.g. satellite images).

- *HypoLine*

The last application in the processing pipeline of the *Nano-seismicSuite* is *HypoLine* which is used for the localization and magnitude estimation of events. Accurate three-dimensional underground models of the measurement area are often not known a priori and localization is done by time difference of arrival (TDOA) hyperbolae and S-P distance circles based on one-dimensional velocity models. At the moment *HypoLine* supports the processing of data from up to six mini-arrays which it gets from *TraceView*. This subset of mini-arrays is no restriction for weak events because they are anyway only visible at the surrounding stations. For further processing of single events tools as e.g. Geotools, Seisan, Pitsa or SeismicHandler can be used. *HypoLine* allows a first coarse localization and identifica-

tion with interactive and graphical techniques for very weak events, where the influence of each parameter to event-location is displayed in real-time (Joswig, 2008).

## C.5 CONCLUSIONS AND DISCUSSIONS

The technique of super-sonograms and the corresponding software tools of the *NanoseismicSuite* are used in various areas of monitoring of low SNR events. Two years of seismic data recorded at Heumoes slope was processed with the software which allowed the screening of almost 100 slidequakes and a multitude of other slope dynamic events (Walter et al., 2009, 2011b). Additionally, data from another landslide in the southern alps of France is being processed with the *NanoseismicSuite* (Walter et al., 2009; Walter & Joswig, 2009; Walter et al., 2011a). For CTBTO purposes the software was first tested in the Integrated Field Exercise 2008 (IFE08) where the benefit of it became clear. It is now an official part of OSI SAMS and regularly used in CTBTO training cycles to train OSI SAMS team members as e.g. in the *OSI Advanced Training Course 2<sup>nd</sup> Training Cycle* (AC2TC) where the software was used in a training with IFE08 data as well as in the field in Hungary where recorded data from the field campaign was analyzed directly. Other areas of usage are the monitoring of induced seismicity (Häge et al., 2012) and sinkholes (Wust-Bloch & Joswig, 2006).

For future development it is planned to integrate automatic detection algorithms in the software to assist the manual processing by visual indications. Especially the field of pattern recognition provides promising algorithms (Joswig, 1996) and super-sonograms are predestined to be used here. Datasets can be screened partly manually and detected events can be used as templates to train automatic detection algorithms. Research with self-organizing maps (aka Kohonen maps, Kohonen 2001) to cluster events by unsupervised learning is ongoing. Self-organizing maps provide the capability to create an overview of the existing seismicity by prototypes of each event type. These prototypes can be used by an human analyst to estimate lo-

cal seismicity and as templates for automatic detections with pattern recognition.

## C.6 ACKNOWLEDGEMENTS

Early software development of the *NanoseismicSuite* was done mainly by Andreas Poszlovszki who created the modular object-oriented application basis which allowed the further extensive development by the main author into an application which is used now in many areas. Matthias Guggenmos and Andreas Eisermann also contributed code. The authors thank Patrick Blascheck and Eberhard Claar for their support developing and installing the permanent seismic network at Heumoes slope which is funded by DFG (German Research Foundation). Funding of the software development is provided by the Preparatory Commission for the Comprehensive Nuclear-Test-Ban Treaty Organization (CTBTO Prep Com) where Peter Labak provides the integration of the software into the OSI SAMS environment.

## REFERENCES

- Chiu, J. M., Steiner, G., Smalley Jr., R., & Johnston, A. C., 1991. PANDA: A simple, portable seismic array for local- to regional-scale seismic experiments, *Bull. seism. Soc. Am.*, **81**, 1000–1014.
- CTBTO, 1996. *Comprehensive Nuclear-Test-Ban Treaty (CTBT)*, Preparatory Commission for the Comprehensive Nuclear-Test-Ban Treaty Organization.
- Douglas, A., 2007. Forensic seismology revisited, *Surveys in Geophysics*, **28**(1), 1–31.
- Ford, S. R. & Walter, W. R., 2010. Aftershock Characteristics as a Means of Discriminating Explosions from Earthquakes, *Bull. seism. Soc. Am.*, **100**(1), 364–376.

- Gomberg, J., Schulz, W., Bodin, P., & Kean, J., 2011. Seismic and geodetic signatures of fault slip at the Slumgullion Landslide Natural Laboratory, *J. Geophys. Res.*, **116**(B09404), 20 pp.
- Häge, M. & Joswig, M., 2009. Spatiotemporal characterization of interswarm period seismicity in the focal area Nový Kostel (West Bohemia/Vogtland) by a short-term microseismic study, *Geophys. J. Int.*, **179**, 1071–1079.
- Häge, M., Blascheck, P., & Joswig, M., 2012. EGS hydraulic stimulation monitoring by surface arrays - location accuracy and completeness magnitude: the Basel Deep Heat Mining Project case study, *Journal of Seismology*.
- Harjes, H.-P., 1990. Design and siting of a new regional array in Central Europe, *Bull. seism. Soc. Am.*, **80**, 1801–1817.
- Haubrich, R. A., 1968. Array design, *Bull. seism. Soc. Am.*, **58**, 977–991.
- Jarpe, S., Goldstein, P., & Zucca, J. J., 1994. Comparison of the non-proliferation event aftershocks with other Nevada Test Site events, UCRL-JC-117754, *In: Non-proliferation Experiment Symposium, Rockville, Maryland, 19-21 April 1994*.
- Joswig, M., 1990. Pattern recognition for earthquake detection, *Bull. seism. Soc. Am.*, **80**(1), 170–186.
- Joswig, M., 1993a. Automated Seismogram Analysis for the Tripartite Bug Array: An Introduction, *Computers & Geosciences*, **19**(2), 203–206.
- Joswig, M., 1993b. Single-trace detection and array-wide coincidence association of local earthquakes and explosions, *Computers & Geosciences*, **19**(2), 207–221.
- Joswig, M., 1995. Artificial Intelligence Techniques applied to seismic signal analysis.pdf, *Dynamical systems and artificial intelligence applied to data banks in Geophysics*.
- Joswig, M., 1996. Pattern recognition techniques in seismic signal processing.pdf, *in: Proceedings of the 2nd Workshop on*

*Application of Artificial Intelligence Techniques in Seismology and Engineering Seismology*, **12**, 37–56.

Joswig, M., 2008. Nanoseismic monitoring fills the gap between microseismic networks and passive seismic, *First Break*, **26**, 117–124.

Kennett, B. L. N., Brown, D. J., Sambridge, M., & C., T., 2003. Signal Parameter Estimation for Sparse Arrays, *Bull. seism. Soc. Am.*, **93**, 1765–1772.

Kohonen, T., 2001. Self-organizing maps, *Springer Ser. Inf. Sci.*, **30**, 501 pp.

Kvaerna, T. & Ringdal, F., 1992. Integrated array and three-component processing using a seismic microarray, *Bull. seism. Soc. Am.*, **82**(2), 870–882.

Lindenmaier, F., Zehe, E., Dittfurth, A., & Ihringer, J., 2005. Process identification at a slow-moving landslide in the Vorarlberg Alps, *Hydrological Processes*, **19**, 1635–1651.

Mykkeltveit, S., Åstebøl, K., Doornbos, D. J., & Husebye, E., 1983. Seismic array configuration optimization, *Bull. seism. Soc. Am.*, **73**, 173–186.

Ringdal, F., 1990. Introduction to the special issue on regional seismic arrays and nuclear test ban verification, *Bull. seism. Soc. Am.*, **80**, 1775–1776.

Ringdal, F. & Husebye, E. S., 1982. Application of arrays in the detection, location, and identification of seismic events, *Bull. seism. Soc. Am.*, **72**, 201–224.

Sokolowski, T. J. & Miller, G. R., 1967. Automated epicenter locations from a quadripartite array, *Bull. seism. Soc. Am.*, **57**, 269—275.

Spillmann, T., Maurer, H., Green, A. G., Heincke, B., Willenberg, H., & Husen, S., 2007. Microseismic investigation of an unstable mountain slope in the Swiss Alps, *J. Geophys. Res.*, **112**(B07301), 25 pp.

- Suyehiro, S., 1967. A search for small, deep earthquakes using quadripartite stations in the Andes, *Bull. seism. Soc. Am.*, **57**, 447–461.
- Walter, M. & Joswig, M., 2008. Seismic monitoring of fracture processes generated by a creeping landslide in the Vorarlberg alps, *First Break*, **26**, 131–136.
- Walter, M. & Joswig, M., 2009. Seismic characterization of slope dynamics caused by softrock-landslides: The Super-Sauze case study, in Malet, J.-P., Remaître, A., Boogard, T. (Eds), *Proceedings of the International Conference on Landslide Processes: from geomorphologic mapping to dynamic modelling*, Strasbourg, CERG Editions.
- Walter, M., Niethammer, U., Rothmund, S., & Joswig, M., 2009. Joint analysis of the Super-Sauze (French Alps) mudslide by nanoseismic monitoring and UAV-based remote sensing, *First Break*, **27**(8), 75–82.
- Walter, M., Arnhardt, C., & Joswig, M., 2011a. Seismic monitoring of rockfalls, slide quakes, and fissure development at the Super-Sauze mudslide, French Alps, *Engineering Geology*, **128**, 12–22.
- Walter, M., Walser, M., & Joswig, M., 2011b. Mapping rainfall-triggered fracture processes, and seismic determination of landslide volume at the creeping Heumoes slope, *Vadose Zone Journal*, **10**(2), 487–495.
- Ward, P. L. & Gregersen, S., 1973. Comparison of earthquake locations determined with data from a network of stations and small tripartite arrays on Kilauea Volcano, Hawaii, *Bull. seism. Soc. Am.*, **63**, 679–711.
- Wust-Bloch, G. H. & Joswig, M., 2006. Pre-collapse identification of sinkholes in unconsolidated media at Dead Sea area by 'nanoseismic monitoring' (graphical jackknife location of weak sources by few, low-SNR records), *Geophys. J. Int.*, **167**, 1220–1232.

Zucca, J. J., 1998. Forensic seismology supports the Comprehensive Test Ban Treaty, *Science & Technology Rev.*, LLNL, CA., Sept. 1998, pp. 4-11.



# D

---

## LANDSLIDE AND SINKHOLE MONITORING BY SONOGRAM SCREENING

---

- **Title:** Near-surface fracture and impact discovery from landslides and sinkholes by sonogram screening
- **Published in:** First Break, 2013, Volume 31, Pages 95-101
- **Authors:** Sick, B.\*, Walter, M., and Joswig, M.
- **\*Corresponding author:** benjamin.sick@gmail.com

### D.1 ABSTRACT

Fracture and impact signals from near-surface geo-processes, like creeping landslides, pending rockfalls and premature sinkholes carry important information about formation stability and promise to enhance early warning approaches significantly. These fracture and impact signals appear like any other impulsive seismic signal. However, two aspects differ so much from e.g. local earthquake records, that for long time even their existence was unknown: (I) Low energy below  $M_L = -2$  from unknown sources regions, the network layout is mostly sub-optimal with source-receiver distances of several hundred to thousand meters, demanding signal detection with **SNR** near one, (II) Short signal duration, and a-priori unknown signatures result in frequent confusion of fracture signals with noise bursts. Therefore, noise forensics was necessary to learn and exclude signals from various impulsive disturbances; only then we recognized the searched-after signals. Obviously classical detector approaches, like **STA/LTA** are not suited to perform recognition

and discrimination with sufficient rate of success. Instead, we developed a hybrid scheme of visual inspection by seismologists based on noise-adapted, optimum spectral energy plots, i.e. sonograms. Selected applications from landslide monitoring in Austria and France, sinkhole mapping in Israel, and precursory fracture detection of a rockfall in Austria demonstrate the appropriateness of our approach.

## D.2 INTRODUCTION

Low-energy, a-priori unknown seismic signals of fractures and impacts carry important precursory information on geo-processes but must first be discovered. Most seismological campaigns to date focus on already known earthquake and tremor signals with sufficient SNR at known frequencies. Those signals are detected automatically, and can be distinguished from local noise bursts by coincidence analysis in any spaced sensor distribution. Automatic pattern recognition can identify signals of potential interest. In contrast, the goal of our campaigns was to discover previously unknown signals, at very low SNR. In this case automatic detectors can not be calibrated on known signals, and coincidence analysis is not applicable to exclude noise bursts because signals also show up at just one or two stations.

To demonstrate our approach of hybrid analysis we show examples of seismic signals from three study areas, two landslide and one sinkhole monitoring where sought-after signals were previously not known. The first landslide monitoring was done at the creeping Heumoes slope which is located in the northern Alpine Upland, in the Vorarlberg Alps, Austria, around 25 km south of Bregenz and shows average displacements of around 10 cm/yr. The landslide extends 1800 m in length and 600 m in width. The unstable slope material has an average thickness of  $\approx 20$  m (Lindenmaier et al., 2005). The second study area is the mudslide in Super-Sauze which is located in the Barcelonnette Basin in the Southern French Maritime Alps, approximately in the middle between the cities of Gap and Nice. The mudslide started to form in the 1960's and today it measures 850 m long.

The unstable slope has an estimated volume of 750 000 m<sup>3</sup> with a maximum thickness of 20 m, and shows significant dynamic behaviour with maximum displacement velocities of more than 3 cm/day (Amitrano et al., 2007). The sinkhole collapse examples originate from a study by (Wust-Bloch & Joswig, 2006) from the Dead Sea region in Israel.

To record weak, low SNR signals we enhanced the seismic network stations to mini-arrays (Seismic Navigating System – SNS). Each mini-array is comprised of a centre, 3-c seismometer (LE-3D sensor), and three outer 1-c seismometers (LE-1D), in 20 to 30 m distance to the central station. The advantage of using the mini-array configuration is that six channels require just one digitizer, one power supply, and allow for fast, even temporary field deployment. Nonetheless, the mini-array features all possibilities to determine back-azimuth and apparent velocity for reliable phase identification (Joswig, 2008). Measurements were done with three mini-arrays - continuously for two years at the Heumoes slope, by several multi-week campaigns at the Super-Sauze mudslide, and for a total of 400 hours during night time at Dead Sea sinkholes, Israel.

### D.3 VISUALIZATION OF CONTINUOUS SEISMIC DATA WITH SUPER-SONOGRAMS

After measurement one is faced with large amounts of digital data. It would seem likely to use automatic detection tools to process the vast amount of data, to filter out the relevant segments, and detect local or regional earthquakes. But our experience shows that for signals as weak as the sought-after slidequakes, firstly described by Gomberg et al. (1995), even state-of-the-art automatic detection algorithms can not replace the in-depth analysis by manual screening. This is especially true for new sites without a-priori knowledge on the expected signals. Here, automatic detectors either miss crucial events, or yield such large amount of false positive detections that screening them is as time consuming as the manual inspection in the first place. The manual inspection obviously benefits from the

human cognitive system, also taking into account the analyst's year-long experience, and his access to information beyond the seismic waveforms. An analyst is highly adaptive in recognizing temporal patterns, and therefore can eliminate false positives even if these noise signals have similar properties to the sought-after events. Temporal patterns might be based on daylight times, typical work hours, train schedules, temperatures, wind, seasonal changes, etc. Few of these patterns might be seen while analysing a list of automatic detections but this can never replace the continuous screening of all the data. However, screening of seismograms can make it very hard for an analyst to identify low SNR events, recognise coincidences between the many stations, and discover temporal patterns. Therefore, we developed a dedicated software tool "SonoView" which pre-processes the seismograms in an optimal manner for human, visual inspection. The software as well as the concept of Nanoseismic Monitoring (Joswig, 2008) was originally developed for On-Site-Inspections (OSI, see e.g. Zucca et al., 1995) of the CTBTO (Preparatory Commission for the Comprehensive Nuclear-Test-Ban Treaty Organization), and comprises the seismic aftershock monitoring system there (Sick et al., 2012). The challenge during an OSI is to detect aftershocks of underground nuclear explosions with local magnitudes as low as  $M_L = -2$  in an inspection area of 1,000 square kilometres with up to 50 mini-arrays (300 channels). Comparable to the investigation of the slope-related slidequakes from this study, optimized signal processing tools need to be applied during an OSI to screen such large seismic data-sets in near real-time. The OSI set-up is similar to our analysis in that the sought-after signals are very weak, and therefore visible only at few mini-arrays - comparable to our three mini-array setup. Instead of using a large amount of mini-arrays during an OSI, we often have to process a large time-span using a few mini-arrays. The underlying visualization for the manual screening is based on noise-adapted spectrograms of the power-spectral density (PSD), so called sonograms (Joswig, 1995). The sonograms use 13 half-octave frequency bands, a window length of 256 samples with around 50% overlap, remove stationary

noise by subtracting the mean and muting below one variance per frequency band, and finally prewhiten the whole image. For outlier resistant noise adaptation, statistics is based on fractiles, and amplitudes of the resultant time-frequency matrix are scaled logarithmically. The single processing steps for sonogram calculation are illustrated in Figure D.1 on basis of two seismograms from a weak, local earthquake near Heumoes slope. The cancellation of disruptive, dominating noise bands can be seen prominently.

Single stations of one mini-array are within 100 m of distance which allows the combination of the four vertical traces of one mini-array into a so called super-sonogram. The combination is done by using “super-pixels” at each time and frequency position. Each “super-pixel” of the super-sonogram consists of four pixels, each from one vertical trace of the mini-array. Figure D.2 shows how pixels of four sonograms create one “super-pixel” which is then used in the super-sonogram. Thanks to the noise adaptation, and array layout all traces exhibit very similar detectable energy thus giving smooth super-pixels. Thus, array-wide signal coherence can be checked very fast by looking just at one trace where incoherent signals show up as spotted patterns while coherent ones create consistent areas of similar colour. The amount of data which can be displayed on one screen without losing the ability to identify sought-after events increases significantly, and faulty or very noisy data of single stations can be recognized immediately in comparison with other stations of the same array.

#### D.4 NOISE FORENSICS

Sought-after signals have amplitudes close to the background noise, and they are only detected at few stations. Thus, many noise signals can initially be classified as possible events of interest. The first task after data recording was always to identify any possible noise source on basis of the sonograms. The visual inspection with super-sonograms allowed the classification and identification of signals according to a multitude of

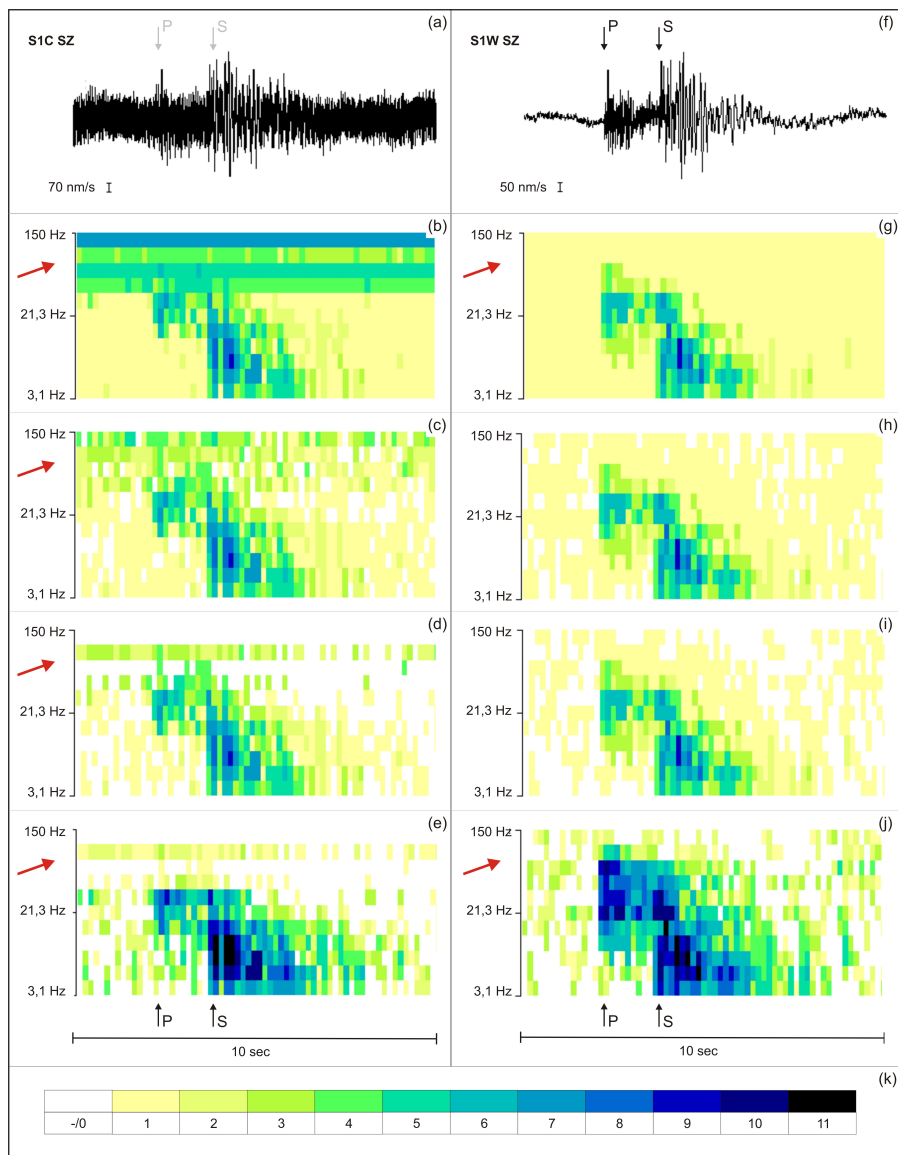


Figure D.1: Step-by-step sonogram generation of a weak local earthquake signal ( $M_L = 0.3$  distance 10 km) at Heumoes slope under bad (station S1C, a – e) and good noise conditions (station S1W, f – j): unfiltered seismograms (a and f), spectrograms (b and g), noise-adaption (c and h), muting (d and i), prewhitening (e and j) and logarithmic energy-colour scale (k).

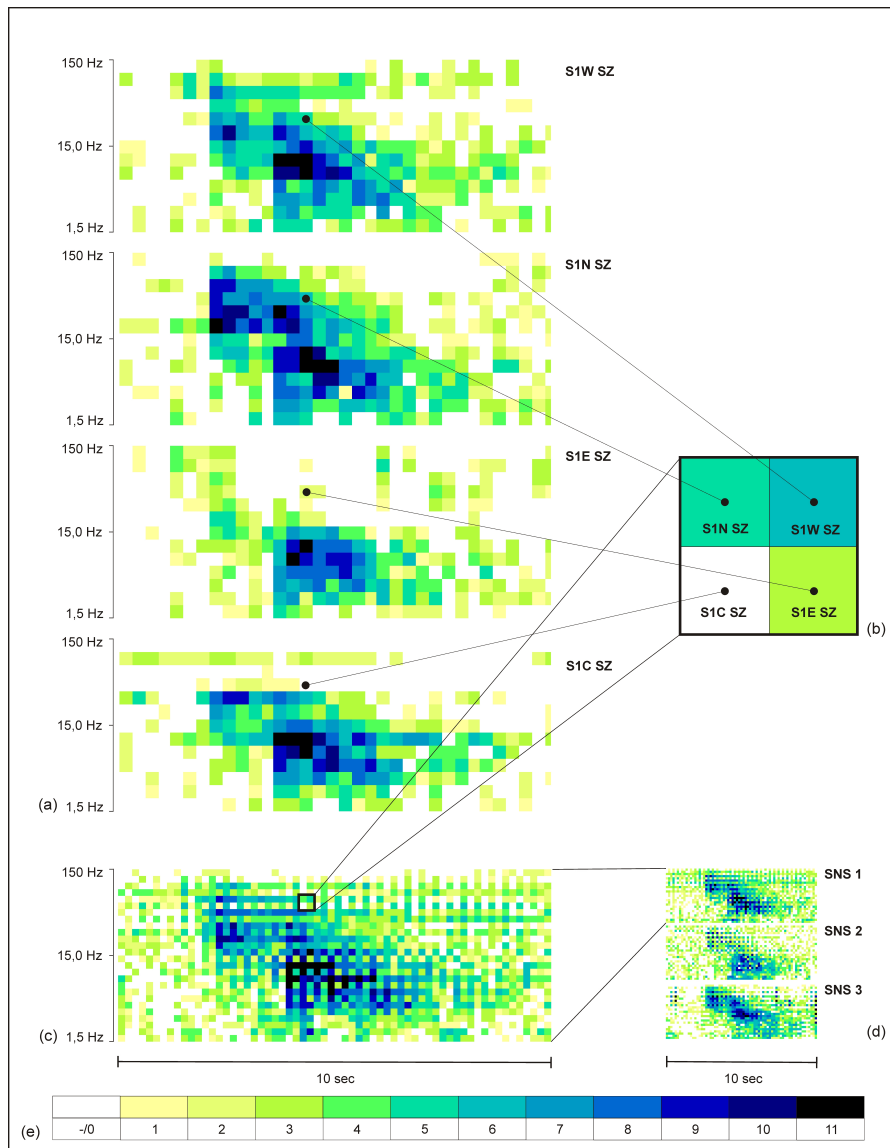


Figure D.2: Generation of super-sonograms from the registration of a weak local earthquake at Heumoos slope (Figure 1): sonograms of the stations S<sub>1</sub>W, S<sub>1</sub>N, S<sub>1</sub>E und S<sub>1</sub>C (a), super-pixel with the colour-scaled energy of the single registrations (b), generated super-sonogram of one mini-array (c), super-sonograms of three mini-arrays in original resolution as used in SonoView (d) as well as the logarithmic energy-colour scale (e).

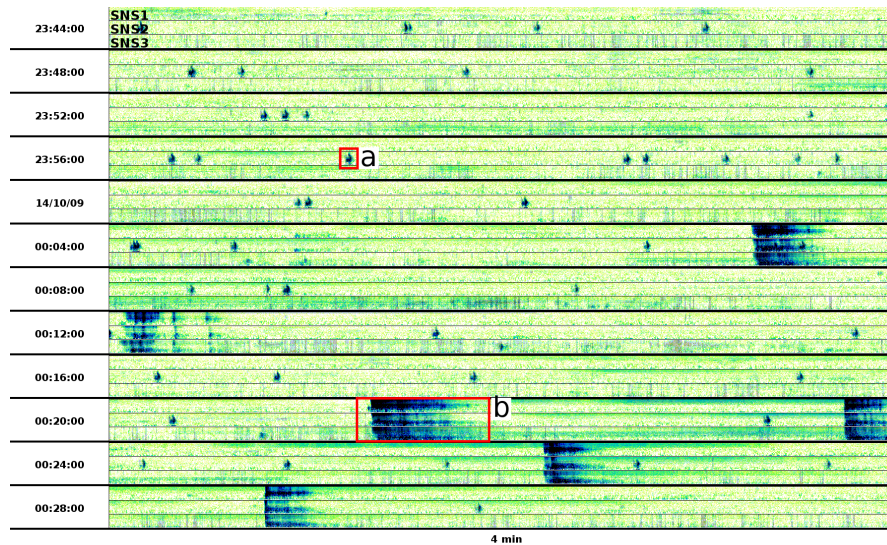


Figure D.3: Screenshot of SonoView showing 12 rows with 3 super-sonograms and 4 minutes of continuously recorded seismic data each (48 minutes in total), starting 2009-10-13, 23:44:00 UTC. (a) example of a frost heave event at SNS2. (b) example of natural noise transient caused by thunder.

criteria, mainly: signal length, frequency content, amplitude ratios, apparent velocity, SNR, coherence across one and between mini-arrays, phase separation, ts-tp time, and eventual repetition characteristics over larger time windows. Figure D.3 shows super-sonograms from the three mini-arrays installed at the Heumoes slope with two different reoccurring noise types. One of the event types originates from thunder featuring apparent velocities of acoustic waves. The other signal is more difficult to identify: “episodes” of this signal reoccurred multiple times during the two year measurement in winter time, and the signal was always visible at only one mini-array. By correlating signal appearance with the freezing cycles at the slope it was possible to identify these signals as frost-heave events within the upper soil layer (Walter, 2013).

Another example of noise sources identified at the Heumoes slope is given in Figure D.4. These signals appeared during daytime in winter and originated from the ski lift which is installed on the slope, and the snow cat which operates there. The ski lift signal reappears every four seconds and originates

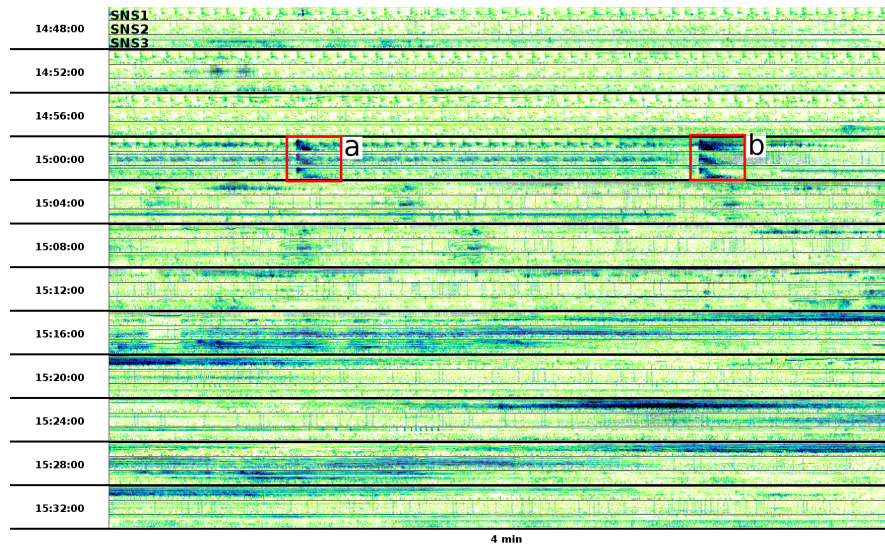


Figure D.4: SonoView screenshot starting 2011-03-09, 14:48:00 UTC showing two local earthquakes (a, b) with  $M_L = 1.4$  distance 9.7 km and  $M_L = 1.5$  distance 8.2 km respectively in the noise of a recurring signal coming from a ski lift (ca. 14:48 h – 15:04 h). After the events, the lift stops and the snowcat runs.

from an impact of the handles of the drag lift seats during operation. The snow cat signal has the typical “cigar”-like, constant-frequent shape in the sonograms which comes from the approaching (increase in amplitudes) and withdrawal (decrease of amplitudes) of the snow cat to and away from the sensors. Hidden in the noise of the ski lift are two local earthquakes which can still be identified clearly by means of their different patterns in the super-sonograms.

Apart from the above mentioned noise signals, a multitude of other, often reoccurring anthropogenic signals were encountered which come mainly from habitation, winter sport, hiking and agriculture. These signals include, e.g., water pump operations, car traffic, aerial overflight, and animals or people walking in the proximity of the sensors.

## D.5 DISCOVERED SIGNALS-OF-INTEREST

After ruling out the noise signals it was possible to discover a multitude of low SNR signals on the two different landslides, i.e.

weak earthquakes and several slope-related signals (slidequakes, tremor-like scratch or shrink signals, and rockfall impacts).

Almost 300 local earthquakes were recorded in the two years of continuous recording at the Heumoes slope, and visually identified using SonoView; more than 95% with magnitudes between  $M_L = -1.1$  and  $M_L = 3.2$  could be located. An example of three local earthquakes is shown in Figure D.5 by three mini-arrays, and thus twelve vertical channels for three minutes, and bandpass-filtered 5 to 50 Hz. Despite appropriate filter settings the local earthquake (a) is barely visible on a few channels. It can also be seen how the noise transient (b) scales down the signal of SNS2. Below the seismograms, the same data plus additional three minutes of data as super-sonograms is shown. Although event (a) is still weak in the compact and space saving super-sonograms, the typical patterns of a local earthquake are visible, and the coherence across the network can be seen which enables an analyst to discover it fast.

At Heumoes slope, a total of 121 slidequakes  $M_L = -2.5$  to  $M_L = -0.5$  were discovered and located (39 during field campaigns between 2005 and 2008, and 82 during continuous seismic monitoring between July 2009 and May 2011). A signal example of these slidequakes is shown in Figure D.6. We located the vast majority of slidequakes clustered in the central section of the landslide featuring the lowest surface displacement rates. Refraction seismics revealed a significant upwarping of the bedrock in this slope area oriented perpendicularly to the general slope movement. We hypothesize this upwarping to act as a barrier for slope movement thus slowing down the surface displacement rates (Walter et al., 2011b). Consistent with this idea, slidequakes occur at or near the interface between the barrier and landslide body. By chance, and outside the scope of our research work monitoring slidequake generation at the Heumoes slope at some hundred meters source-station distance, the permanent network recorded an unexpected, large and fast-running rockfall event with an estimated volume of 15000 cubic metres at the gorge Rappenlochschlucht in about 5 km distance to the seismic stations (Figure D.9). By analyzing the event with

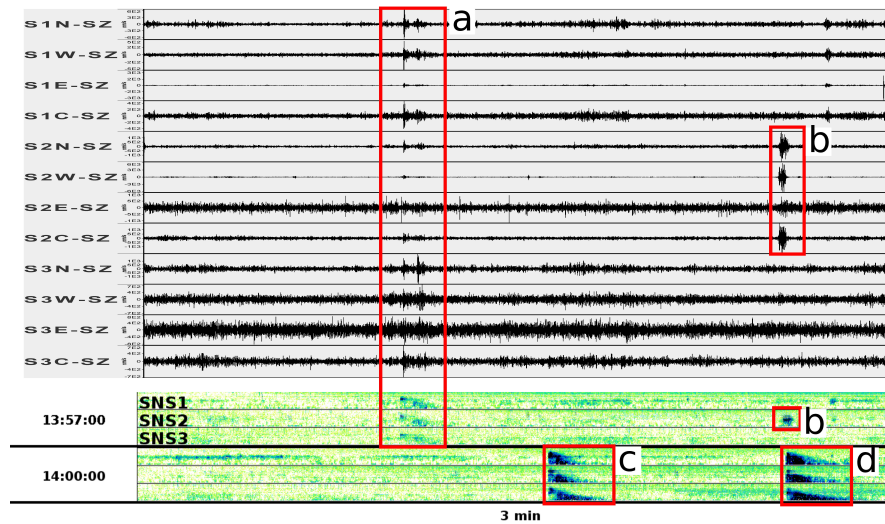


Figure D.5: Comparison of seismogram and super-sonogram view from data of the Heumoes slope starting at 2010-09-08, 13:57:00 UTC. The top shows three minutes (13:57:00 – 14:00:00) of seismograms filtered with a bandpass with corner frequencies 5 and 50 Hz of all vertical channels. The bottom shows two rows, with each row containing three minutes of super-sonograms with all vertical channels. (a) local earthquake  $M_L = 1.1$  in a distance of 21 km with very low SNR but consistent patterns in the super-sonograms. (b) noise transient. (c-d) local earthquakes with higher SNR ( $M_L = 1.6$  distance 12 km and  $M_L = 1.7$  distance 10 km respectively).

SonoView, several preceding, smaller rockfall events associated with precursory fracture activity could be identified minutes and hours before the main event (Walter et al., 2012).

At the Super-Sauze mudslide, France, 34 slidequakes  $M_L = -3.2$  to  $M_L = -1.3$  were located during a 10-day field campaign in 2008, mostly clustering in the mid-part of the slope (Walter et al., 2011a, Figure D.7). In contrast to Heumoes slope, the mid-part of the Super-Sauze mudslide features the highest superficial displacement rates. The analysis of bedrock topography reveals a system of crests that border the entire landslide, and channel the mudslide material in several gullies (Malet et al., 2005). These crests are oriented in-line to slope movement, and the majority of slidequake locations not only relates to these crests generally, but also correlates to the gullies with highest displacement rates at the slope surface.

At the Dead-Sea region, Israel, sinkholes occurred regularly, and lined-up down to sea shores. Prior to the final collapse, and long before superficial subsidence got obvious, dozens of low-energy impact signals  $M_L = -3$  to  $M_L = -1.5$  were detected in distances up to several hundred metres (Figure D.8, Wust-Bloch and Joswig, 2006). Spectral discrimination unveiled impact into brine, and onto aggregated scree material. Thus, the monitoring could even provide a measure of sinkhole ‘maturity’ proceeding from the initial brine state in washed-out salt sediments to the solid-impact behaviour after sufficient detachment of roof material.

## D.6 CONCLUSIONS

By SonoView, we provide a tool-set for in-depth, visual analysis of passive seismic, near-surface measurements. The tool-set is essential for the discovery of short-duration, low SNR events with a-priori unknown signatures. The hybrid approach of a noise-adapted display and human diagnosis, and the compact visualization by super-sonograms enables analysts to inspect continuous seismic data efficiently, and to find events which would have perished with automatic approaches. Four single-trace

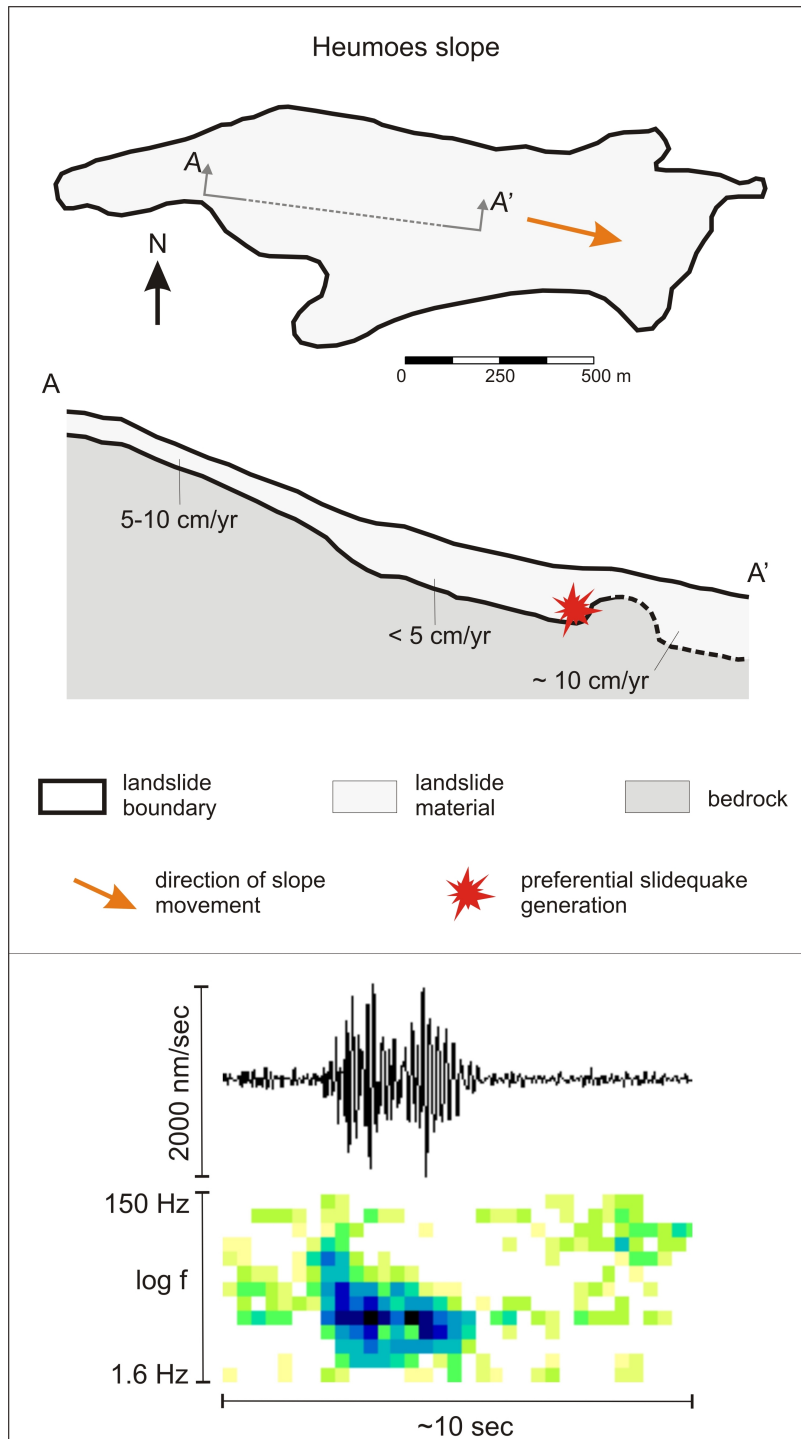


Figure D.6: Top: Schematic illustration of preferential slidequake generation at Heumoes slope. Bottom: slidequake observed at Heumoes slope ( $M_L = -1.4$  in 180 m distance). Modified after [Walter \(2013\)](#).

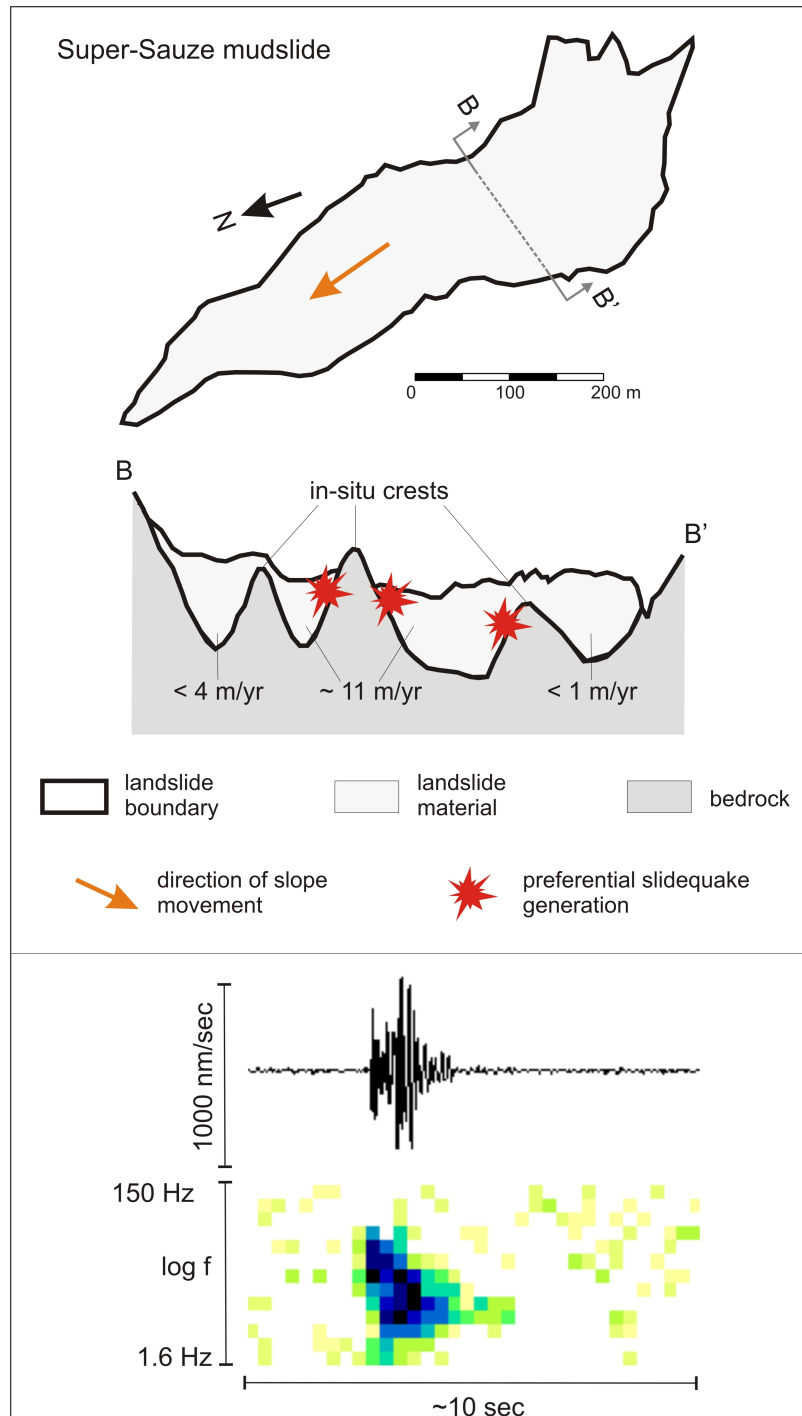


Figure D.7: Top: Schematic illustration of preferential slidequake generation at the Super-Sauze mudslide. Bottom: slidequake observed in Super-Sauze ( $M_L = -2.4$  in 100 m distance). Modified after [Walter \(2013\)](#).

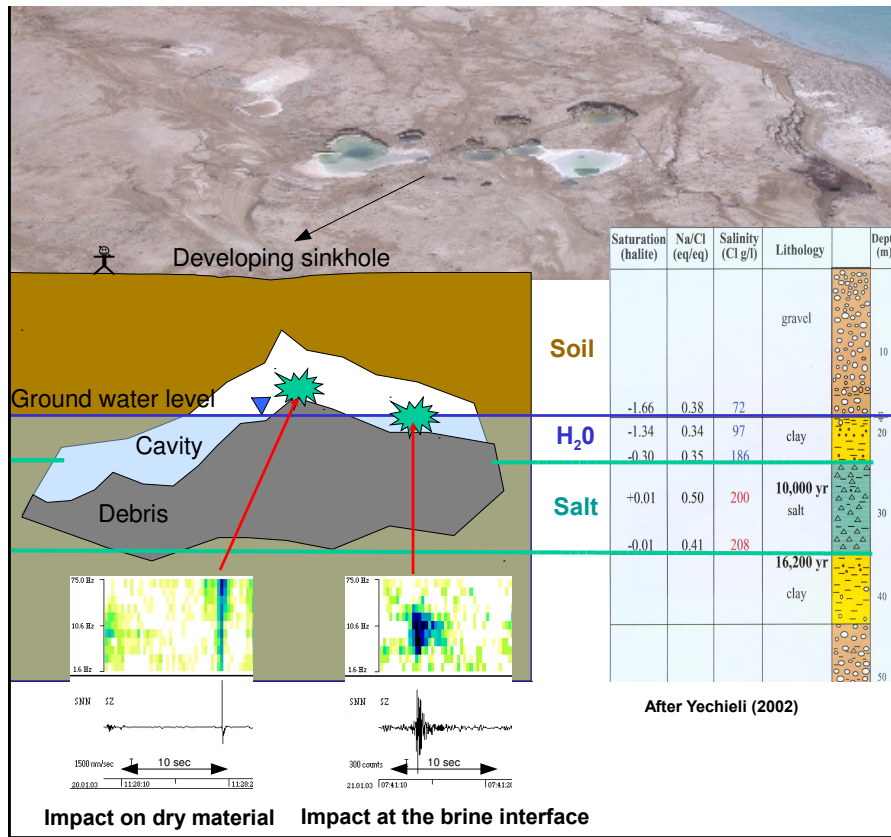


Figure D.8: Schematic diagram of a sinkhole and mature cavity in the subsurface according to local borehole log (Yechieli, 2002). Groundwater depth is below 20 m and salt is found between 23 and 35 m depth. The sonogram analysis allows the discrimination between dry impacts and impacts in brine-filled cavities, therefore, monitoring pre-collapse sinkhole activity. Modified after Wust-Bloch & Joswig (2006).

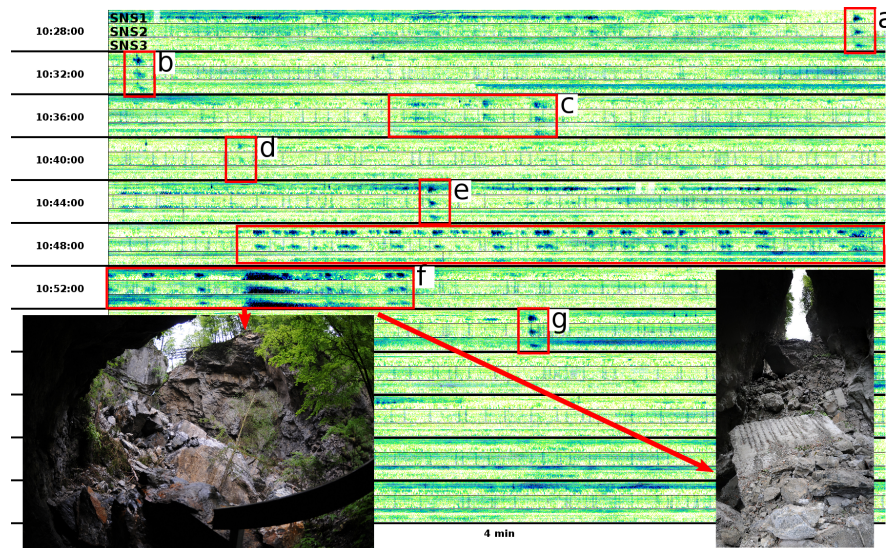


Figure D.9: SonoView screenshot starting at 2011-05-10, 10:28:00 UTC of rockfall registration at Heumoes slope. Events (a) – (e) are precursory fracture signals, (f) is the main rockfall event and (g) is a fracture signal after the main rockfall. The two photographs show the rubble of the rockfall and the destroyed bridge (photos: Friedrich Böhringer).

sonograms per mini-array can be combined to super-sonograms since array aperture is small, and sonograms suppress differences in site noise. Thus an analyst can check fast on array-wide signal coherence. SonoView is part of Nanoseismic Monitoring, a ‘seismic microscope’ to study fracture occurrence in landslides and rockfalls, discover impact signals from sinkholes, map active faults in short-duration field campaigns, monitor induced seismicity, and support nuclear arms control.

#### D.7 ACKNOWLEDGEMENTS

We are thankful to the German Research Foundation (DFG) for their financial support for the studies at Heumoes slope and in Super-Sauze within the research unit FOR-581.

## REFERENCES

- Amitrano, D., Gaffet, S., Malet, J.-P., & Maquaire, O., 2007. Understanding mudslides through micro-seismic monitoring: the Super-Sauze (South-East French Alps) case study, *Bulletin de la Société Géologique de France*, **178**(2), 149–157.
- Gomberg, J., Bodin, P., Savage, W., & Jackson, M. E., 1995. Landslide faults and tectonic faults, analogs?: The Slumgullion earthflow, Colorado, *Geology*, **23**(1), 41–44.
- Joswig, M., 1995. Automated classification of local earthquake data in the BUG small array, *Geophys. J. Int.*, **120**, 262–286.
- Joswig, M., 2008. Nanoseismic monitoring fills the gap between microseismic networks and passive seismic, *First Break*, **26**, 117–124.
- Lindenmaier, F., Zehe, E., Dittfurth, A., & Ihringer, J., 2005. Process identification at a slow-moving landslide in the Vorarlberg Alps, *Hydrological Processes*, **19**, 1635–1651.
- Malet, J.-P., van Asch, T., van Beek, R., & Maquaire, O., 2005. Forecasting the behaviour of complex landslides with a spatially distributed hydrological model, *Natural Hazards and Earth System Sciences*, **5**(1), 71–85.
- Sick, B., Walter, M., & Joswig, M., 2012. Visual Event Screening of Continuous Seismic Data by Supersonograms, *Pure and Applied Geophysics*, **171**(3-5), 549–559.
- Walter, M., 2013. *Seismische Untersuchungen von Lockergesteins-Hangrutschungen und ihr Beitrag zum ganzheitlichen Verständnis der Hangdynamik*, Ph.D. thesis.
- Walter, M., Arnhardt, C., & Joswig, M., 2011a. Seismic monitoring of rockfalls, slide quakes, and fissure development at the Super-Sauze mudslide, French Alps, *Engineering Geology*, **128**, 12–22.

Walter, M., Walser, M., & Joswig, M., 2011b. Mapping rainfall-triggered fracture processes, and seismic determination of landslide volume at the creeping Heumoes slope, *Vadose Zone Journal*, **10**(2), 487–495.

Walter, M., Schwaderer, U., & Joswig, M., 2012. Seismic monitoring of precursory fracture signals from a destructive rockfall in the Vorarlberg Alps, Austria, *Natural Hazards and Earth System Science*, **12**(11), 3545–3555.

Wust-Bloch, G. H. & Joswig, M., 2006. Pre-collapse identification of sinkholes in unconsolidated media at Dead Sea area by 'nanoseismic monitoring' (graphical jackknife location of weak sources by few, low-SNR records), *Geophys. J. Int.*, **167**, 1220–1232.

Yechieli, Y., 2002. Borehole Hever 2: Geological and hydrological findings, *Geological Survey of Israel*, **GSI/8/2002**, 8.

Zucca, J., Carrigan, C., Goldstein, P., Jarpe, S., Sweeney, J., & Pickles, W., 1995. Signatures of testing: On-Site Inspection Technologies. Lawrence Livermore National Laboratory, UCRL-JC-119213., Tech. rep.





# F

---

## LIST OF PUBLICATIONS

---

Part of the work presented here has already been published:

1. Chapter 5: Sick, B., Guggenmos, M., and Joswig, M. (2015). Chances and limits of single-station seismic event clustering by unsupervised pattern recognition. *Geophys. J. Int.*, 201(3), 1801–1813. <https://doi.org/10.1093/gji/ggv126>
2. Chapter 6: Sick, B., and Joswig, M. (2017). Combining network and array waveform coherence for automatic location: examples from induced seismicity monitoring. *Geophys. J. Int.*, 208(3), 1373–1388. <https://doi.org/10.1093/gji/ggw468>
3. Appendix C: Sick, B., Walter, M., and Joswig, M. (2012). Visual Event Screening of Continuous Seismic Data by Supersonograms. *Pure and Applied Geophysics*, 171(3–5), 549–559. <http://doi.org/10.1007/s00024-012-0618-x>
4. Appendix D: Sick, B., Walter, M., and Joswig, M. (2013). Near-surface fracture and impact discovery from landslides and sinkholes by sonogram screening. *First Break*, 31, 95–101.



---

## CURRICULUM VITAE

---

### Personal information

Surname(s) / First name(s)

**Sick, Benjamin (Dipl.-Ing.)**

Email(s)

benjamin.sick@gmail.com

### Work experience

Dates

October 2016 - ongoing

Occupation or position held

Developer Algorithm Design - Research & Development for Advanced Driver Assistance Systems

Employer

ZF Friedrichshafen

Dates

October 2010 - September 2016 (before since July 2009 research assistant)

Occupation or position held

Research associate

Employer

University of Stuttgart, Institute for Geophysics

Dates

October 2009 – September 2010

Occupation or position held

Internship followed by student trainee

Employer

DMT GmbH & Co. KG

Dates

November 2008 – May 2009

Occupation or position held

International internship

Employer

Advanced IS and IT Research Center (Adetti-IUL), Lisbon, Portugal

Dates

March 2006 - October 2008

Occupation or position held

Research assistant

Employer

University of Stuttgart, Institute for political economics and law

### Education

Dates

November 2010 - September 2016

Title of qualification awarded

PhD, Doktor-Ingenieur, ongoing

Institution

University of Stuttgart, Institute for Geophysics

Dates

September 2014 - August 2015

Title of qualification awarded

Young Scientist research award

Institution

United Nations Comprehensive Nuclear-Test-Ban Treaty Organization (CTBTO)

Dates

October 2004 - September 2010

Title of qualification awarded

Diplom (top 20% of the year), equivalent to M.Sc.

Institution

University of Stuttgart, Institute for Signal Processing and System Theory and Institute for Geophysics

Dates

February 2007 – June 2007

Title of qualification awarded

Finished with distinction

Institution

University of Adelaide, School of Computer Science, Adelaide, Australia



---

## ERKLÄRUNG

---

Hiermit versichere ich, dass ich die vorliegende Arbeit selbstständig angefertigt und keine anderen als die angegebenen Quellen und Hilfsmittel verwendet habe.

Stuttgart, den 31. Mai 2017

---

BENJAMIN SICK